

**LATTICE BOLTZMANN STUDY OF NEAR-WALL
MULTI-PHASE AND MULTI-COMPONENT FLOWS**

HUANG, JUNJIE

NATIONAL UNIVERSITY OF SINGAPORE

2009

**LATTICE BOLTZMANN STUDY OF NEAR-WALL
MULTI-PHASE AND MULTI-COMPONENT FLOWS**

HUANG, JUNJIE

(B. Eng., Tsinghua University, China)

A THESIS SUBMITTED

FOR THE DEGREE OF DOCTOR OF PHILOSOPHY

DEPARTMENT OF MECHANICAL ENGINEERING

NATIONAL UNIVERSITY OF SINGAPORE

2009

Acknowledgements

First of all, I am deeply grateful to my supervisors, Professor Chang Shu and Professor Yong Tian Chew, for their continuous guidance, supervision and enjoyable discussions during this work. I also owe a debt of gratitude to Dr. Xiao Dong Niu, Dr. Yan Peng, Dr. Hong Wei Zheng, and Dr. Kun Qu for their instructions and discussions.

In addition, the National University of Singapore has provided me various supports, including the research scholarship, the abundant library resources, and the advanced computing facilities as well a good environment, which are essential to the completion of this work. I want to thank both the university and the many staffs from the libraries, the mechanical engineering department and the computer center, whose efforts have contributed to the above mentioned factors.

Finally I would like to thank, from the bottom of my heart, my parents for their endless love, understanding and encouragement.

Table of Contents

Acknowledgements	i
Table of Contents	ii
Summary	ix
List of Tables	xi
List of Figures	xii
Nomenclature	xix

Chapter I. Introduction	1
1.1 Overview of MPMC flows	2
1.1.1 The phenomena	2
1.1.2 Governing equations and dimensionless numbers	3
1.1.3 Other important factors	6
1.2 Modeling and simulation of MPMC flows	7
1.2.1 Discrete particle methods	8
1.2.1.1 MD simulation	8
1.2.1.2 DPD and SPH simulations	9
1.2.2 Continuum methods	11
1.2.2.1 VOF and LS methods	11
1.2.2.2 Diffuse interface methods	12
1.2.2.3 Some remarks on the continuum methods	13
1.2.3 General remarks and outlook	14
1.3 LBM studies of near-wall MPMC flows	15
1.3.1 LBM for MPMC flows	16
1.3.2 LBM simulations of wetting and CL dynamics	17
1.3.2.1 Wetting and CL dynamics on smooth surfaces	17
1.3.2.2 Wetting and CL dynamics on rough surfaces	18
1.3.3 Summary and some gaps of previous studies	19
1.4 Objectives of this study	20
Chapter II. LBM and Its Modeling of MPMC Flows	24
2.1 LBM - an introduction	24
2.1.1 Basic theory and formulation	24

2.1.1.1	Brief derivation of LBE	25
2.1.1.2	Reference quantities, dimensionless numbers and compressibility	31
2.1.2	BCs in LBM	34
2.1.2.1	BCs at solid walls	35
2.1.2.2	BCs at the inlets and outlets for periodic problems	37
2.1.3	Initial conditions in LBM	37
2.2	FE Based LBM for MPMC Flows	38
2.2.1	FE theory for liquid-vapor systems near critical points	38
2.2.2	FE theory for immiscible binary fluid systems	42
2.2.2.1	A loose induction from FE theory for LV systems	42
2.2.2.2	Remarks on the order parameter	45
2.2.3	Lattice Boltzmann formulation for immiscible binary fluids	46
2.2.3.1	Lattice Boltzmann formulation - implementation A	48
2.2.3.2	Lattice Boltzmann formulation - implementation B	50
2.2.3.3	Chapman-Enskog expansion and the macroscopic equations	51
2.2.4	LBM for multi-phase flows with large density ratios	52
2.3	Modeling of wetting and CL dynamics	53
2.3.1	Wetting in LV systems	54
2.3.2	Wetting in binary fluid systems	56
2.3.3	Wetting in LDR-LBM	57
2.3.4	Implementation of wetting boundary condition	57
	Chapter III. Lattice Boltzmann Simulations and Validations	63
3.1	Lattice Boltzmann simulation procedure	63
3.2	Some remarks on LBM simulations	64

3.2.1	On simulations of steady and unsteady flows	64
3.2.2	On the stability	65
3.2.3	On the convergence	66
3.3	Validation for single phase flows	68
3.3.1	Couette flows	69
3.3.2	Poiseuille flows	70
3.3.3	Pressure driven flows in a 3D rectangular channel	71
3.3.4	Driven cavity flows	72
3.4	Validation for MPMC flows	73
3.4.1	Laplace's law verification	73
3.4.2	Surface layers near hydrophilic and hydrophobic walls	74
3.4.3	Static CA study	76
3.4.4	Capillary wave study	77
3.4.5	Droplet in a shear flow	78
3.4.6	Tests of convergence	80
3.5	Parallel implementation and performance	81
3.5.1	Parallel implementation of LBM simulations	81
3.5.2	Performance of parallel LBM codes	82
3.6	Summary	82
 Chapter IV. Investigation of MPMC Flows near Rough Walls		94
4.1	The <i>Lotus Effect</i>	94
4.2	WBC on <i>rough</i> surfaces	96
4.3	Two-dimensional study of a droplet driven by a body force over a grooved wall	98

4.3.1 General description of the problem	98
4.3.2 Effects of surface tension	99
4.3.3 Effects of lower wall wettability	100
4.3.4 Effects of body force direction	102
4.3.5 Effects of density ratio	103
4.3.6 Effects of groove width and depth for neutral-wetting and hydrophobic walls	105
4.3.7 Hydrophilic grooved walls: a detailed look	106
4.3.7.1 Effects of groove width and depth for hydrophilic walls	106
4.3.7.2 Critical CA	107
4.3.7.3 Critical groove width and depth	107
4.3.7.4 Droplet motions over subsequent grooves	109
4.3.8 Some analyses of the flow field	109
4.3.9 Some comparisons with previous work	110
4.4 Effects of the grooves	111
4.5 Three-dimensional study of droplet spreading and dewetting on a textured surface	112
4.5.1 Droplet near one pillar	112
4.5.2 Droplet near multiple pillars	113
4.6 Summary	114
Chapter V. Mobility in DIM Simulations of Binary Fluids	128
5.1 Brief review of mobility in DIM simulations of binary fluids	128
5.2 Aims of this chapter	130
5.3 Sitting droplet subject to a shear flow	131

5.4 Chemically driven binary fluids	133
5.4.1 Droplet dewetting	133
5.4.1.1 Two-dimensional droplet dewetting	133
5.4.1.2 Three-dimensional droplet dewetting	141
5.4.2 Droplets on a chemically heterogeneous wall	142
5.5 Summary and some remarks	144
Chapter VI. Droplet Manipulation by Controlling Substrate	157
Wettability	
6.1 Droplet manipulation techniques in digital microfluidics	157
6.2 Simulations of droplet motion on substrates with spatiotemporally controlled wettability	158
6.2.1 Descriptions of the problem and simulation	159
6.2.2 The parameters	161
6.2.3 Comparison of droplet motions under different controls	162
6.2.4 Effects of the switch frequency and confined stripe size	165
6.2.5 Effects of initial droplet position	169
6.3 Some further discussions and remarks	171
6.4 Summary	173
Chapter VII. Bubble Entrapment during Droplet Impact	181
7.1 Introduction on bubble entrapment in droplet impact	181
7.2 Problem description and simulation setup	184
7.3 Results and discussion	185
7.3.1 Types I and II: Entrapment during slow impact	186

7.3.2 Type III: Entrapment during fast impact	191
7.3.3 Type IV: Hybrid type entrapment	192
7.3.4 Preliminary look at the entrapment condition	193
7.4 Summary	194
Chapter VIII. Conclusion and Future Work	208
8.1 The effects of surface topography and wettability	208
8.2 The mobility effects	209
8.3 Droplet manipulation by surface wettability control	210
8.4 Bubble entrapment during droplet impact	211
8.5 Concluding remarks and future work	212
References	215
Appendix	227

Summary

Recent developments of lab-on-a-chip devices call for better understanding of small scale multi-phase and multi-component (MPMC) flows for the optimal design, fabrication and operation of these devices. In this thesis, the lattice Boltzmann method (LBM) was used to investigate a range of MPMC flows near various substrates mainly at small scales, with the focuses on the “Lotus Effect”, mobility in diffuse interface modeling (DIM), substrate control for droplet manipulation and bubble entrapment during droplet impact.

First, a 2D droplet moving in a channel made of one smooth and one grooved wall was studied. It was found that the wettability and the topography of the groove affected the flow much more under small scales than under macroscopic scales. With the grooved surface being sufficiently hydrophobic, the droplet was lifted and completely attached to the other wall, resulting in significantly reduced drag. For hydrophilic grooved surfaces, the effects of the two factors were found coupled with each other and a variety of interesting phenomena resulting from them were captured. Some of the simulations are expected to be helpful in elucidating the “Lotus Effect”. Next, the mobility in DIM was found to be closely related to the slip velocity of the three-phase lines, and it was discovered that it may even determine the routes through which a near-wall MPMC system evolves. Such mobility-dependent bifurcations were studied in detail through droplet dewetting, and also illustrated by droplet motions on a heterogeneous surface. Thirdly, droplets on surfaces with given wettability distributions and temporal variations were investigated in order to devise fast droplet manipulation methods. Several kinds of droplet behaviors were found under different

substrate controls. When proper hydrophobic confinement and wettability switch were applied, rapid transport of droplets toward a desired direction was achieved. Key factors for such droplet transport were explored and their relations were identified. Finally, droplet impacts onto homogeneous surfaces were investigated. Several types of bubble entrapment during such processes were discovered and analyzed, and conditions for entrapment prevention were preliminarily estimated.

In conclusion, investigations of several kinds of near-wall MPMC flow problems and some simulation issues on DIM have been carried out by using LBM. The results suggest that LBM is a fairly useful tool in the modeling and simulation of MPMC flows, especially those found in digital microfluidics involving complex physics and surface chemistry. They may also provide better understanding of MPMC flows over complicated surfaces in nature such as lotus leaves, and for some industrial applications involving droplets.

List of Tables

Table 1.1	Important factors in MPMC flows	23
Table 2.1	Weights in the discrete equilibrium distributions	60
Table 3.1	Parameters for simulation in Laplace law verification	83
Table 4.1	Common parameters for most 2D simulations near a grooved wall	116
Table 4.2	Some parameters for the 3D simulation near a single pillar	116
Table 4.3	Some common parameters for 3D simulations near a pillar array	116
Table 5.1	Common parameters for simulations of a sitting droplet subject to a shear flow	146
Table 5.2	Common parameters for simulations of droplet dewetting	146
Table 5.3	Common parameters for simulations of droplets on heterogeneous substrates	146
Table 6.1	Common parameters for the droplet manipulation problem	174
Table 7.1	Key parameters for the cases in Types I-IV of bubble entrapment	195
Table 7.2	Some simulation parameters for all cases in Types I-IV	195

List of Figures

Fig. 2.1	D2Q9 velocity model	60
Fig. 2.2	D3Q15 velocity model	60
Fig. 2.3	Illustration of BB on the lower wall	61
Fig. 2.4	Typical density profile across a flat interface	61
Fig. 2.5	Illustration of WBC implementation on a flat wall	62
Fig. 3.1	Illustration of the Couette Flow	83
Fig. 3.2	Comparison of Couette flow velocity profile	83
Fig. 3.3	Comparison of Poiseuille flow velocity profile	84
Fig. 3.4	Comparison of velocity profiles along two center lines ($z = H_z$ and $y = H_y$) for flows in a 3D rectangular channel	84
Fig. 3.5	Illustration of the driven cavity flow	84
Fig. 3.6	Comparison of the convergence history (the evolution of $ \vec{u} _{res}$) (LBM v.s. vorticity-stream function formulation)	85
Fig. 3.7	Comparison of velocity profiles along the two center lines, $y = 0.5$ and $x = 0.5$, for the driven cavity flow (LBM v.s vorticity-stream function formulation)	85
Fig. 3.8	Evolution of the deviation in surface tension for a stationary droplet	86
Fig. 3.9	Evolution of the maximum and minimum values of the order parameter	86
Fig. 3.10	The center order parameter profiles before and after the equilibration	87
Fig. 3.11	Comparison of order parameter profiles for the surface layers near a hydrophobic wall	87
Fig. 3.12	Comparison of order parameter profiles for the surface layers near a hydrophilic wall	88

Fig. 3.13	Illustration on the calculation of θ from R_x and H_y	88
Fig. 3.14	Static CA validation (numerical v.s. theoretical)	89
Fig. 3.15	Problem setup for capillary wave study	89
Fig. 3.16	Comparison of the interface position evolution for a capillary wave by three different simulations and the analytical solution	90
Fig. 3.17	Illustration of the droplet in a shear flow	90
Fig. 3.18	Comparison of the variation of the deformation parameter with the capillary number for a sheared droplet	91
Fig. 3.19	Initial condition in the convergence test for droplet spreading	91
Fig. 3.20	Comparison of the interface regions for three simulations of droplet spreading with different mesh sizes	92
Fig. 3.21	Comparison of the flow fields for three simulations of droplet spreading with different mesh sizes	92
Fig. 3.22	Illustration of domain decomposition along horizontal direction for the parallel implementation of LBM	93
Fig. 3.23	Variation of the computational time with the number of nodes used for the evaluation of a parallel LBM code	93
Fig. 4.1	Transition points at the intersections of two orthogonal walls	117
Fig. 4.2	Illustration of the initial condition of 2D flows inside a grooved channel	117
Fig. 4.3	Comparison of the liquid velocity evolution under different surface tensions	117
Fig. 4.4	Comparison of snapshots of the liquid positions and configurations every 10^5 steps under different surface tensions	118
Fig. 4.5	Comparison of the liquid velocity evolution under different wettabilities of the lower wall	118
Fig. 4.6	Comparison of snapshots of the liquid positions and configurations at time step 6×10^5 under different wettabilities of the lower wall	119

Fig. 4.7	Enlarged view of local and apparent CAs at time step 6×10^5 for $\theta = 60^\circ$	119
Fig. 4.8	Comparison of the liquid velocity evolution under different forces for $\theta = 45^\circ, 90^\circ$ and 135°	120
Fig. 4.9	Advancing interfaces at $t = 0.5, 1, 1.5, 2, 2.5, 3, 3.5, 4$ ($\times 10^5$) under different forces for $\theta = 45^\circ$ and 90°	120
Fig. 4.10	Comparison of the liquid velocity evolution under different density ratios for $\theta = 45^\circ$ and 105°	121
Fig. 4.11	Interface positions at $t = 10^6$ under different density ratios ($\theta = 45^\circ$)	121
Fig. 4.12	Comparison of the liquid velocity evolution under different groove geometries for $\theta = 90^\circ$ and 135°	122
Fig. 4.13	Comparison of snapshots of the liquid positions and configurations every 2×10^5 steps under different groove widths and depths for $\theta = 45^\circ$	122
Fig. 4.14	Comparison of the liquid velocity evolution under different groove geometries for $\theta = 45^\circ$	123
Fig. 4.15	Advancing interfaces at $t = 2, 2.5, 3, 3.5$ ($\times 10^5$) below and beyond the critical contact angle	123
Fig. 4.16	Advancing interface positions at $t = 2, 2.5, 3, 3.5$ ($\times 10^5$) below and beyond the critical groove width	124
Fig. 4.17	Advancing interface positions at $t = 2, 2.5, 3, 3.5$ ($\times 10^5$) below and beyond the critical groove depth	124
Fig. 4.18	Advancing and receding interface positions at late stages ($t = 8, 8.5, 9, 9.5, 10$ ($\times 10^5$))	125
Fig. 4.19	Contour of velocity component u at $t = 10 \times 10^5$ for $H_{groove} = 18$ in critical groove depth study	125
Fig. 4.20	Flow field at $t = 5 \times 10^5$ with $\theta = 135^\circ, 23 \times 15$ and a horizontal body force in the study of effects of different body forces	126
Fig. 4.21	Comparison of the liquid velocity evolution for flat and grooved walls	126

Fig. 4.22	Drop evolution near a single pillar	127
Fig. 4.23	Drop configurations on a pillar array after 10^5 time steps	127
Fig. 4.24	Interface evolutions in the middle $y - z$ plane every 2.5×10^4 time steps	127
Fig. 5.1	Initial condition for a sitting droplet under shear	146
Fig. 5.2	Comparison of droplet configurations in steady state with different mobilities under small capillary numbers	146
Fig. 5.3	Comparison of droplet velocity evolutions with different mobilities under small capillary numbers	147
Fig. 5.4	Variation of the steady droplet velocity with the mobility \tilde{M}	147
Fig. 5.5	Steady flow field (relative to the droplet) around a droplet for $\tilde{M} = 10$	147
Fig. 5.6	Snapshots of droplet shapes every 10^3 steps after the wall wettability is suddenly switched from neutral wetting to very hydrophobic	148
Fig. 5.7	Evolution of the dynamic CA at time intervals shown in Fig. 5.6	150
Fig. 5.8	Evolution of the average center y -coordinate (\bar{y}_{drop}) and the average vertical velocity (\bar{v}_{drop}) of the droplet under different mobilities	150
Fig. 5.9	Evolution of the kinetic energy of the droplet (KE_{drop}) and the whole flow field (KE_{total}) under different mobilities	151
Fig. 5.10	Evolution of R_x on the wall for different mobilities	151
Fig. 5.11	Evolution of the CL velocity for different mobilities	152
Fig. 5.12	Bifurcation diagram of the evolution of R_x under different mobilities	152
Fig. 5.13	Variation of the initial CL velocity with the mobility	153
Fig. 5.14	Variation of the critical mobility with the initial CA difference	153
Fig. 5.15	Variation of the critical mobility with the surface tension	153

Fig. 5.16	Snapshots of the 3D droplet at the end of simulation (Time: 10, 000) for $\theta = 145^\circ$	154
Fig. 5.17	Bifurcation diagram of evolution of R_x under different mobilities for a 3D droplet	154
Fig. 5.18	Wettability distribution on the heterogeneous wall at $z = 0$	154
Fig. 5.19	Snapshots of droplet shapes for $\tilde{M} = 2$ and for $\tilde{M} = 20$ on chemically heterogeneous walls	155
Fig. 5.20	Evolution of the average droplet velocity $ \bar{u} _d$ for $\tilde{M} = 2$ and $\tilde{M} = 20$	156
Fig. 6.1	Initial condition and problem setup for droplet manipulation	174
Fig. 6.2	Two types of surface potential distribution (in $-\tilde{\omega}$) of the substrate	174
Fig. 6.3	The surface potential distribution (in $-\tilde{\omega}$) of the substrate in case (iii)	175
Fig. 6.4	Evolution of the droplet velocity and the velocities at different positions	175
Fig. 6.5	The droplet shape and the TPL distribution every 9×10^3 steps for case (ii)	176
Fig. 6.6	The droplet shape and the TPL distribution every 9×10^3 steps for case (iii)	176
Fig. 6.7	Droplet position evolution $x_d(t)$ under different T_{switch} (12, 15, 16, 17, 18, 21, 22, 23, 24, $27(\times 10^3)$) with $W_{conf} = 20$	177
Fig. 6.8	Evolution of the droplet velocity and the velocities at different positions (after achieving continuous motions) under different T_{switch} (16, 17, $18(\times 10^3)$) with $W_{conf} = 20$	177
Fig. 6.9	Evolution of the droplet velocity and the velocities at different positions (after achieving continuous motions) under different T_{switch} (13, 14, $15(\times 10^3)$) with $W_{conf} = 30$	178
Fig. 6.10	Comparison of droplet position evolutions under four “local-optimal” conditions	178

Fig. 6.11	Comparison of droplet velocity at different positions under four “local-optimal” conditions	178
Fig. 6.12	Variations of the “local-optimal” period for wettability switch T_{switch} and the respective maximum droplet velocity U_{max} with the size of confined stripe W_{conf}	179
Fig. 6.13	Comparison of droplet velocity evolutions for different initial droplet positions $X_C = 30, 34, 45, 56, 60$	179
Fig. 6.14	Comparison of droplet position evolutions for different initial droplet positions $X_C = 30, 34, 45, 56, 60$	180
Fig. 7.1	Illustration of the initial condition for droplet impact	195
Fig. 7.2	Snapshots of the bottom plane (Type I; Case 1)	196
Fig. 7.3	Snapshots of the middle $x - z$ plane (Type I; Case 1)	196
Fig. 7.4	Snapshots of the middle $x - z$ plane (Type I; Case 2)	197
Fig. 7.5	Enlarged views of the flow fields in the middle $x - z$ plane at selected time (Type I; Case 1)	197
Fig. 7.6	Enlarged view of the flow fields in the middle $x - z$ plane at selected time (Type I; Case 2)	198
Fig. 7.7	Evolution of the inner and outer diameter of the circles on the bottom plane (Type I; Cases 1 & 2)	198
Fig. 7.8	Snapshots of the middle $x - z$ plane (Type II; Case 1)	199
Fig. 7.9	Snapshots of the bottom plane (Type II; Case 1)	200
Fig. 7.10	Snapshots of the middle $x - z$ plane (Type II; Case 2)	201
Fig. 7.11	Snapshots of the bottom plane (Type II; Case 2)	202
Fig. 7.12	Enlarged view of the flow fields in the middle $x - z$ plane at selected time (Type II; Case 1)	202
Fig. 7.13	Enlarged view of the flow fields in the middle $x - z$ plane at selected time (Type II; Case 2)	203
Fig. 7.14	Pressure distribution along the center line at the bottom plane for Types I and II	203

Fig. 7.15	Snapshots of the middle $x - z$ plane (left column) and the bottom plane (right column) (Type III)	204
Fig. 7.16	Snapshots of the middle $x - z$ plane (left column) and the bottom plane (right column) (Type IV)	205
Fig. 7.17	$Re - We$ and $Oh - We$ maps for all droplet impact cases studied	207

Nomenclature

- **Abbreviations**

2D / 3D	Two / Three Dimensions (Dimensional)
AC	Artificial Compressibility
BB	Bounce Back
BC	Boundary Condition
BGK	Bhatnagar-Gross-Krook
C-LBM	Color Based Lattice Boltzmann Model
CA / CAs	Contact Angle / Contact Angles
CHE	Cahn-Hilliard Equation
CL / CLs	Contact Line / Contact Lines
Col.	Collision
D2Q9	Two Dimension Nine Velocity
D3Q15	Three Dimension Fifteen Velocity
DF	Distribution Function
DIM	Diffuse Interface Method (Model)
DPD	Dissipative Particle Dynamics
E	East
EDF	Equilibrium Distribution Function
FE	Free Energy
FE-LBM	FE Based Lattice Boltzmann Model
FE1	FE Model for Liquid-Vapor Systems
FE2	FE Model for Binary Fluids Systems
FE2-LBM	Lattice Boltzmann Model for FE2

FE2-LBM-A / B	Implementation A / B of FE2-LBM
FEM	Finite Element Method
FT	Front Tracking (Method)
LBE	Lattice Boltzmann Equation
LBM	Lattice Boltzmann Method (Model)
LDR-LBM	LBM for Multi-phase Flows with Large Density Ratios
LGA	Lattice Gas Automata
LHS	Left Hand Side
LS	Level Set (Method)
LU	Lattice Unit(s)
LV	Liquid-Vapor
MD	Molecular Dynamics (Simulation)
MPI	Message Passing Interface
MPMC	Multi-Phase and / or Multi-Component
MRT	Multiple Relaxation Time
N	North
NE	North-East
NSCH	Navier-Stokes-Cahn-Hilliard
NSE	Navier-Stokes Equations
NW	North-West
P-LBM	Potential Based Lattice Boltzmann Model
RHS	Right Hand Side
S	South
SE	South-East
SPH	Smoothed Particle Hydrodynamics

Str.	Streaming
SW	South-West
TPL / TPLs	Three-Phase-Line / Three-Phase-Lines
VOF	Volume of Fluid (Method)
W	West
WBC	Wetting Boundary Condition
WG	Wettability Gradient

- **Subscripts**

$\alpha, \beta, \gamma, \chi, \zeta$	Indices for spatial coordinates
A, B, L, G	To denote the property of the fluid $A, B, Liquid, Gas$
c	To denote quantities associated with the droplet <i>center</i>
c	1) To denote <i>characteristic</i> quantities 2) To denote the property of the fluid near the <i>critical</i> point
$conf$	To denote the properties of the hydrophobic <i>confining</i> stripes
cr	To denote the critical quantity (for mobility)
cw	To denote the quantities associated with a capillary wave
CL	To denote the quantities associated with the CL
d	To denote the quantities associated with the <i>droplet</i>
$groove$	To denote the quantities of the <i>groove</i>

IN / OUT	To denote the quantities at the inlet / outlet
i	Index of the lattice velocity
$i,j / i,j,k$	Indices of discretization points in the $(x-, y-)$ / $(x-, y-, z-)$ directions)
in / out	1) To denote the quantities inside / outside the droplet 2) To denote the inner/outer circle in the bottom plane in bubble entrapment study
l	1) To denote the quantities of the liquid phase 2) To denote the quantities of the lower wall
$liquid$	To denote the quantities of the liquid segment
lv	1) To denote the quantities of the liquid-vapor system 2) To denote the liquid-vapor interface
max / min	To denote the maximum / minimum values
n	To denote the normal direction
s	To denote the values taken on the surface
sl	To denote the solid-liquid interface
sv	To denote the solid-vapor interface
t	To denote the tangential direction
u	To denote the quantities of the upper wall
v	To denote the quantities of the vapor phase
x / y	To denote the $x- / y-$ direction
∞	To denote the quantities infinitely far away

- **Superscripts**

b	To denote the <i>bulk</i> quantities
$crit$	To denote the <i>critical</i> quantities (for CA, groove width, and depth)
eq	To denote the quantities at <i>equilibrium</i> states
(n)	To denote the terms at the n^{th} order
n	To denote the quantities at time step t^n

- **Fundamental constants**

κ_B	Boltzmann constant
D	Dimension of the spatial space

- **Basic coordinates**

t	Time coordinate
	Spatial coordinate (in tangential direction)
$\vec{x} / x_\alpha / (x, y, z)$	Spatial coordinates
n	Spatial coordinate (in normal direction)
$\vec{\xi} / \xi_\alpha$	Velocity space coordinates

- **Mathematical operators**

∇	Gradient operator in physical space
$\nabla_{\vec{\xi}}$	Gradient operator in velocity space
$\nabla \cdot$	Divergence operator in physical space

$\partial_t / \frac{\partial}{\partial t}$	1) Partial derivative with respect to time
	2) Partial derivative with respect to the spatial coordinate in tangential direction t
∂_{t_0}	Partial derivative with respect to time at the zeroth order
∂_{t_1}	Partial derivative with respect to time at the first order
∂_α	Partial derivative with respect to the spatial coordinate x_α
$\frac{\partial}{\partial n}$	Partial derivative with respect to the spatial coordinate in normal direction n
$\frac{\partial}{\partial x}, \frac{\partial}{\partial y}, \frac{\partial}{\partial z}$	Partial derivative with respect to the spatial coordinate x, y, z
$\nabla^2 / \partial_{\alpha\alpha}$	Laplacian operator
$\frac{\partial^2}{\partial n^2}$	2 nd order partial derivative with respect to the spatial coordinate in normal direction n
$\frac{\partial^2}{\partial t^2}$	2 nd order partial derivative with respect to the spatial coordinate in tangential direction t
$\frac{\partial^2}{\partial x^2}, \frac{\partial^2}{\partial y^2}, \frac{\partial^2}{\partial z^2}$	2 nd order partial derivative with respect to the spatial coordinate x, y, z
\sum_i	Summation over the discrete velocity directions
\otimes	Tensor product

$ $	1) Module of a vector
	2) Absolute value of a number
$O()$	Order of ()

- **Mathematical functions**

$\exp(x) / e^x$	Exponential function
$\sin(x)$	Sine function
$\cos(x)$	Cosine function
$\tanh(x)$	Hyperbolic tangent function
$\operatorname{erfc}(x) = \frac{2}{\sqrt{\pi}} \int_x^{\infty} e^{-t^2} dt$	Complementary error function
$N(\phi)$	A function defined to calculate the averages

- **Other parameters, quantities or variables (in Green letters)**

α_k	Coefficients in the analytical solution of 3D channel flow
$\Delta\phi$	Spacing between two neighbouring contour lines in ϕ
$\Delta\theta$	1) Deviation in the measured CA from theoretical CA 2) Difference between the initial CA and static CA in the study of droplet dewetting
$\delta_{\alpha\beta}$	Kronecker delta (\vec{I} in subscript form)
δ_t	(Lattice) Time step
δ_x	(Lattice) Grid size
ε	1) Small parameter in Chapman-Enskog expansion

	2) Criterion to determine the steady state
	3) Interface thickness scaled (by a macroscopic length)
$\varepsilon_{in} / \varepsilon_{out}$	Deviation of ϕ inside / outside the drop
$\varepsilon_{in}^{eq} / \varepsilon_{out}^{eq}$	Equilibrium deviation of ϕ inside / outside the drop
$\bar{\varepsilon}$	Scaled viscosity in the analytical solution of the capillary wave
ϕ	1) Order parameter field in DIM 2) Level set function in LS methods
$\phi_1, \phi_2, \phi_3, \phi_4$	Solutions of the order parameter at the wall
ϕ_ρ	Intermediate symbol in induction of FE2 model
ϕ_σ	Order parameter on the wall
ϕ_{in} / ϕ_{out}	Order parameter inside / outside the drop
ϕ_s	Order parameter on the solid boundary
ϕ^*	Coefficient related to the density difference in LDR-LBM
$\phi_{in}^{eq} / \phi_{out}^{eq}$	Equilibrium order parameter inside / outside the drop
γ	Specific heat ratio
$\dot{\gamma}$	Shear rate
η	Dynamic viscosity
φ	Surface FE density (per unit area)
κ	Coefficient in the interfacial energy
κ_ρ	Intermediate symbol in induction of FE2 model
λ	Wavelength of the capillary wave

μ	Chemical potential field
μ^b	Bulk chemical potential
$\bar{\mu}$	Chemical potential in $\psi(\rho, T)$
ν	Kinematic viscosity
ν_A / ν_B	Kinematic viscosity of fluid A / B
ν_L / ν_G	Kinematic viscosity of the liquid / gas
ν_r	Reference kinematic viscosity
$\bar{\Pi}$	Non-equilibrium stress tensor
$\Pi_{\beta\alpha}^{(1)}$	Non-equilibrium stress tensor at the first order
θ	CA
θ_{conf}	CA of the hydrophobic confining patch
θ_{dyn}	Dynamic CA
$\theta_{philic} / \theta_{phobic}$	CA of the hydrophilic / hydrophobic patch
ρ	Mass density field
$\rho_1, \rho_2, \rho_3, \rho_4$	Solutions of the density at the wall
ρ_σ	Density at the wall
ρ_A / ρ_B	(Constant) Density of fluid A / B
ρ_c	1) Characteristic density 2) Density at the critical point
$\rho_{i,j} / \rho_{i,j,k}$	Density at the point $(i, j) / (i, j, k)$
ρ_L / ρ_G	(Constant) Density of the liquid / gas
ρ_l / ρ_v	Equilibrium liquid /vapor density near critical points

ρ_r	Reference density
$\bar{\rho}$	Constant average density
$\tilde{\rho}$	Dimensionless variable related to ρ near critical points
σ	Surface tension (coefficient)
$\sigma_{lv}^* / \sigma_{sv} / \sigma_{sl}$	Surface tension between the liquid and vapor / solid and vapor / solid and liquid
σ_{num}	Numerically calculated surface tension
$\tau / \tau_f / \tau_g$	Relaxation parameters in LBE
τ_{lv}	Dimensionless parameter related to T near critical points
τ_R^*	Intermediate parameter in derivation of LBE
Ω	Collision integral
ω	Coefficient related to $\tilde{\omega}$
ω_0	Oscillation frequency of the capillary wave for inviscid flows
$\tilde{\omega}$	Dimensionless coefficient that determines CA
$\tilde{\omega}_{conf}$	Wettability parameter for the hydrophobic confining patch
$\tilde{\omega}_{max} / \tilde{\omega}_{min}$	Wettability parameter for the hydrophilic / hydrophobic patch
ψ	Bulk FE density

- **Other parameters, quantities or variables (in Roman letters)**

A / B 1) Fluid A / B

2) Coefficients in the EDF

A_i, B_i	Coefficients in the EDF
A_p	Amplitude of the initial perturbation in the capillary wave
a	Coefficient in the bulk FE
a_ρ	Intermediate symbol in the induction of FE2 model
a_{cw}	Dimensionless interface displacement in the capillary wave
Bo	Bond number
b	Number of nonzero lattice velocities
C	Volume fraction function in VOF method
C_1, C_2	Constants in the relation between critical mobility and surface tension
Ca	Capillary number
Ch	Cahn number
c	Magnitude of the orthogonal lattice velocities
c_s	Isothermal sound speed
D_d	Diameter of the drop
D_f	Deformation parameter
D_{in} / D_{out}	Diameter of the inner/outer circle in the bottom plane in bubble entrapment study
$E^{(n)}$	Lattice tensor of rank n
e	Internal energy density field

\vec{e}_i	Lattice velocity (vector) set
F	FE functional of a system
f	(Continuous) One-particle DF for ρ, \vec{u}
f_i	Discrete DF with \vec{e}_i for ρ, \vec{u}
$f_i^{(1)}$	DF at the first order for f_i
f_i^{eq}	Discrete EDF with \vec{e}_i for ρ, \vec{u}
$f_{i_{IN}} / f_{i_{OUT}}$	DF on the buffer nodes at the inlet / outlet boundary
\tilde{f}_i	Post-collision DF for f_i
$\bar{f}_i, \bar{f}_i^{eq}$	Intermediate functions in deriving LBE
$\bar{\bar{G}} / G_{\alpha\beta}$	Intermediate stress tensor in FE2-LBM-A
g	Magnitude of the body force
\vec{g} / g_α	Body force vector
g	(Continuous) One-particle DF for ϕ
g_i	Discrete DF with \vec{e}_i for ϕ
$g_i^{(1)}$	DF at the first order for f_i
g_i^{eq}	Discrete EDF with \vec{e}_i for ϕ
\tilde{g}_i	Post-collision DF for g_i
H	Distance between the lower and upper walls
H_y	1) Half width of a 3D channel in the y – direction 2) Height of a 2D droplet
H_z	Half width of a 3D channel in the z – direction
h	Initial perturbation to the interface

\vec{I}	Second order unit tensor
i	Index of the lattice velocity
\vec{i}_t, \vec{j}_n	Base vectors in the (t, n) coordinate system
\vec{i}_x, \vec{j}_y	Base vectors in the (x, y) coordinate system
$[K] / K_{ij}$	Scattering matrix in the boundary conditions for DF
KE_d	Kinetic energy of the droplet
KE_{total}	Kinetic energy of the whole system
k	1) Index in the analytical solution of 3D channel flow 2) Wavenumber in capillary wave study
k_1, k_2	Constants in the relation between slip velocity and mobility
k_r	Intermediate variable to calculate the CA
L	1) Characteristic length 2) Intermediate variable to derive the stress tensor in FE1
L_c	Characteristic length
L_x / L_y	Length of the domain in the $x - / y -$ direction
l_{CL}	Size of the inner region near the CL
l_T	Half interface thickness
M	Mobility
Ma / Ma_{LBM}	Mach number / LBM Mach number
M_T	Total mass of the system
\tilde{M}	Dimensionless constant related to M

\tilde{M}_{cr}	Critical mobility in droplet dewetting study
m	Mass of one gas molecule
n	Number density field
\vec{n}	Unit normal vector at the wall
Oh	Ohnesorge number
Pe	Peclet number
\vec{p}^{th}	Full pressure tensor
p	Pressure field
p_c	Pressure at the critical point
p_r	Reference pressure
p_{tot}	Total pressure
p^b	Bulk pressure
p^{hydro}	Hydrodynamic pressure
\bar{p}	1) (Constant) Average pressure 2) Pressure in $\psi(\rho, T)$ (function of temperature only)
R	Gas constant
R_d	Droplet radius
Re	Reynolds number
R_L	Major axis of the deformed droplet (assumed ellipse)
R_B	Minor axis of the deformed droplet (assumed ellipse)
R_x	1) Half of the distance between two three phase points for a 2D droplet on a solid wall 2) Half of the distance between two three phase points

in the middle $x - z$ plane for a 3D droplet
on a solid wall

r	Distance away from the droplet center
r_v	Kinematic viscosity ratio
r_ρ	Density ratio
S	(Pressure-like) Field to enforce incompressibility
S_{spread}	Spreading parameter
t'	Scaled time in the analytical solution of the capillary wave
T	(Constant) Temperature
T_c	Temperature at the critical point
T_{comm}	Time used on <i>communication</i> in parallel implementation
T_{comp}	Time used on <i>computation</i> in parallel implementation
T_{equil}	Time for the droplet to equilibrate initially in the study of droplet manipulation
T_{switch}	Period to switch the wettabilities of different patches in the study of droplet manipulation
\vec{T}_{SS}	Reversible part of the stress tensor
U	1) Velocity of the upper wall in a 2D driven cavity 2) Velocity of the upper wall in the study of a shear driven droplet
U_c	Characteristic velocity

U_d	(Constant) Drop velocity in x – direction under steady state
U_l	Velocity the lower wall
U_u	Velocity the upper wall
U_z	(Initial) Droplet impact velocity (in z – direction)
$\bar{u} / (u, v, w)$	(Mass averaged) Fluid velocity field
u_d	Instantaneous average droplet velocity in x – direction
u_{liquid}	Velocity of the liquid segment
u_{max}	Maximum velocity
\vec{u}_w	Wall velocity (vector)
$ \vec{u} _d$	Average droplet velocity magnitude
$ \vec{u} _{res}$	Change of the velocity field between consecutive steps
V	Domain for volume integration
V_{CL}	CL velocity
v_d	Average velocity of the drop in y – direction
W	Interface thickness
$W_{conf} / \tilde{W}_{conf}$	Width / Relative width of the confining stripe
We	Webber number
W_{lv}	A function of density and temperature in $\psi(\rho, T)$
w_d	Average droplet velocity in z – direction
w_i	Weight with \vec{e}_i
x_d	Average droplet position in x – direction

$\bar{X}_c / (X_c, Y_c, Z_c)$	(Initial) Drop center position
y_d	Average droplet position in y – direction
y_l	y – coordinate of the lower wall
y_{mid}	y – coordinate of the middle horizontal line
y_u	y – coordinate of the upper wall
Z_1, Z_2, Z_3, Z_4	Functions of z_1, z_2, z_3, z_4
z_1, z_2, z_3, z_4	Roots of an algebraic equation related to capillary wave study

Chapter I

Introduction

There has been a fast growth in lab-on-a-chip technologies over the past decade due to their huge impacts on chemical and biological analyses (Stone et al. 2004). One of the important issues to be addressed in such systems is the near-wall multi-phase and multi-component (MPMC) flows at the scales of micron or even nanometer level. Due to the small scale, the surface to volume ratio in such flows is much larger than that in their macroscopic counterparts. As a consequence, the interfacial properties and boundary walls play dominant roles in determining the flow characteristics (Darhuber & Troian 2005, Squires & Quake 2005), and the thorough understanding of them is crucial to the optimal design and manufacturing of micro devices. However, the small scale poses considerable difficulties in detecting and measuring the dynamical quantities, such as the velocity fields and the evolving interface shapes. Thus, it is especially desirable to gain some useful information and even deep insights about these flows through physical modelings and computer simulations.

In this chapter, an overview of the MPMC flows is first provided. After that, different approaches and methods for the modeling and simulation of near-wall MPMC flows are reviewed. Next, specific reviews of the lattice Boltzmann methods (LBM) for these flows are given. They are followed by the aims of the present research. This chapter is ended by highlighting several contributions arising from this work.

1.1 Overview of MPMC flows

First an overview of MPMC flows is provided. The physical phenomena, the governing equations using the continuum descriptions, and the important factors in these flows are briefly introduced as follows.

1.1.1 The phenomena

MPMC flows are easily seen in nature and have applications in many industries (e.g., chemical engineering, pharmaceuticals, food science and cosmetics) and in everyday life (e.g., the ink jet printing process) (de Gennes et al. 2004). The commonly encountered MPMC phenomena include bubbles in a liquid matrix, droplets¹ in air, emulsions (e.g., water-in-oil and oil-in-water systems), and double emulsions (e.g., water-in-oil-in-water and oil-in-water-in-oil systems). Aside from single component two phase flows near critical points, the two phases or components are normally separated by an interface of thickness much smaller than the size of the bubble or droplet. The surface tension² affects the flows by acting on the interfaces and their neighbouring parts. From the microscopic point of view, the surface tension is due to the different interactions between the fluid molecules of the same type and of different types (de Gennes et al. 2004). In contrast to bulk fluid molecules, molecules in the interfacial regions suffer from inhomogeneous forces. Under this effect, the interfacial area always tends to be minimized. To accurately describe these flows, it is necessary to properly incorporate the surface tension effect into the model.

¹ Droplets are drops of very small sizes. In this thesis, “drop” and “droplet” are not strictly distinguished and may be used interchangeably.

² In this thesis, for convenience, the term “surface tension” is used generally to denote the interfacial tension force of various interfaces (e.g., gas-liquid, liquid-liquid, liquid-solid, etc.), and at some places it is also used to denote the surface tension coefficient (i.e., the specific value).

1.1.2 Governing equations and dimensionless numbers

It would be useful to first look at the governing equations of MPMC flows in continuum models because they help to provide a general impression on the important factors that affect these flows. For simplicity, only isothermal incompressible flows are considered in this work. Before presenting the equations, it is worth having a quick review on two types of continuum modeling approaches.

Among the continuum models, there is a sharp interface approach (also known as “interface tracking” in numerical modeling), in which interfaces are viewed as surfaces with zero thickness, and multiple sets of governing equations are applied in each phase or component, and the interfacial conditions are used as boundary conditions. This approach can provide very accurate results for cases without topological changes, and it forms the foundation of the front tracking (FT) methods (Unverdi & Tryggvason 1992)³. However, such an approach encounters singularity problems when topological changes (e.g., formation of droplets from a flat interface, breakup of bubbles) occur. Under those situations, artificial treatments are required. Here the governing equations and the relevant boundary conditions across interfaces in this approach will not be further discussed. The main focus is put on another type of approach.

Contrary to the tracking philosophy, there exists another type of approach which uses a continuous function to distinguish different fluids (to be called “indicator function” thereafter). This type of approach appears to be able to deal with topological changes

³ The pure front-tracking method uses Lagrangian points to represent the interfaces. However, in the numerical implementations the interfaces may not be strictly treated as sharp; smoothing at the scale of grid size can be applied and an indicator function can be used as well (Unverdi & Tryggvason 1992). This is similar to some other methods described below.

naturally. The indicator function can be chosen as the volume fraction of one of the two phases/components, as in the volume-of-fluid (VOF) method (Scardovelli & Zaleski 1999), the signed distance to the interface, as in the level-set (LS) method (Osher & Fedkiw 2002), or the density/mass fraction of one phase or component (also called “order parameter” later), as in the diffuse interface models (DIM) (Anderson et al. 1998). In this type of approach, there is only one set of unified governing equations and the interfaces are implicitly captured (known as “interface capturing”).

Because of the high relevance to the present work and also for conciseness, the governing equations for a two-component fluid system (for convenience, the two fluids are called “fluid- *A*” and “fluid- *B*”) of the same density and viscosity in the diffuse interface model will be discussed in detail. This set consists of three equations which reflect the mass conservation, Newton’s second law (as applied to the fluids), and the evolution of the order parameter through convection and diffusion⁴ (Jacqmin 1999):

$$\nabla \cdot \vec{u} = 0, \quad (1.1a)$$

$$\partial_t \vec{u} + (\vec{u} \cdot \nabla) \vec{u} = -\nabla S + \nu \nabla^2 \vec{u} - \phi \nabla \mu, \quad (1.1b)$$

$$\partial_t \phi + (\vec{u} \cdot \nabla) \phi = M \nabla^2 \mu. \quad (1.1c)$$

Here \vec{u} is the fluid velocity, ϕ is the order parameter (function of the mass fraction of “fluid- *A*”), μ is the chemical potential, ν is the kinematic viscosity, M is the mobility (assumed to be constant), and S is used to enforce incompressibility yet not the pressure. The term $-\phi \nabla \mu$ represents the surface tension effect in DIM and may be related to the surface tension σ in some form depending on the choice of free

⁴ Note that in Eq. (1.1b) the last term is due to the surface tension force which contains the surface tension coefficient. More details will be given in Chapter II and III.

energy (FE) (details to be given in Chapter II). The third equation is known as the Cahn-Hilliard equation (CHE). For simplicity, this system of equations will be abbreviated as the NSCH (Navier-Stokes-Cahn-Hilliard) equations later. After being non-dimensionalized with a characteristic density ρ_c , a characteristic length L_c and a characteristic velocity U_c , they become (for simplicity the same set of symbols are used for the dimensionless variables)

$$\nabla \cdot \vec{u} = 0, \quad (1.2a)$$

$$\partial_t \vec{u} + (\vec{u} \cdot \nabla) \vec{u} = -\nabla S + \text{Re}^{-1} \nabla^2 \vec{u} - (\text{Re} Ca)^{-1} \phi \nabla \mu, \quad (1.2b)$$

$$\partial_t \phi + (\vec{u} \cdot \nabla) \phi = \text{Pe}^{-1} \nabla^2 \mu. \quad (1.2c)$$

where Re is the Reynolds number,

$$\text{Re} = \rho_c U_c L_c / \eta, \quad (1.3)$$

($\eta = \rho_c \nu$ is the dynamic viscosity), Ca is the Capillary number,

$$Ca = \eta U_c / \sigma, \quad (1.4)$$

and Pe is the Peclet number (note that the definition of Pe is not unique; some different definition is to be given later),

$$Pe = U_c L_c^2 / M \sigma. \quad (1.5)$$

From the above equations, it is easy to find that in the physical problem itself there are two important dimensionless numbers: the Reynolds number which reflects the ratio of inertia force to viscous force, and the Capillary number which reflects the ratio of the viscous force over the surface tension force. It should be noted that the Peclet number is only relevant to DIM in which a convection-diffusion equation is used for the order parameter. Sometimes, the Webber number, defined as

$$We = \rho_c U_c^2 L_c / \sigma, \quad (1.6)$$

is also used, but it is not independent; in fact it can be related to the Reynolds number and Capillary number as $We = Ca Re$. Thus the Webber number actually reflects the ratio of inertia force to the surface tension force. For some problems, the Ohnesorge number, defined as

$$Oh = \eta / \sqrt{\rho_c \sigma L_c}, \quad (1.7)$$

may be useful and it is easy to verify that $Oh = We^{1/2} Re^{-1}$.

1.1.3 Other important factors

Until now, only the parameters for a simplified multi-component flow problem are listed. In reality, many other factors may be present, some of which can be reflected through dimensionless numbers whereas others can not.

In the presence of external body forces such as the gravity force or a uniform electrical force, the Bond number, defined as

$$Bo = \rho_c L_c^2 g / \sigma, \quad (1.8)$$

is often used where g is the body force density (e.g., gravitational constant for gravity force). When the flows are near solid walls, as mentioned at the beginning, the wall property can affect the flow significantly under small scales. Then, there comes another parameter, that is, the contact angle (CA) θ (as measured in one of the fluid, say, fluid- A). It characterizes the different interactions between the wall and the two fluids. Smaller θ indicates stronger attraction between the wall and fluid- A than that between the wall and fluid- B . Furthermore, if the wall is not smooth, either in the topographical or the chemical sense, it may be necessary to suitably model such heterogeneities in order to obtain correct fluid behaviors in simulations. Finally, when

the two fluids have different densities and viscosities, the density ratio, $r_\rho = \rho_A / \rho_B$, and the (kinematic) viscosity ratio, $r_\nu = \nu_A / \nu_B$, can be important to determine the flow characters under certain situations. All the above factors are summarized in Table 1.1.

1.2 Modeling and simulation of MPMC flows

In last section, a general view on the MPMC flows and various factors affecting them have been provided. This section comprehensively reviews how to model and simulate them.

To numerically solve the governing equations given above is one of the mostly used strategies to study MPMC flows. But this may not be easy, especially for small scale problems. The reason is because, as mentioned above, MPMC flows usually involve scales of large contrasts, such as the interface thickness and the characteristic length in the flow, and the microscopic relaxation time (toward local equilibrium in the interfacial region) and the characteristic time for the flow. Detailed information at the finest scale is extremely difficult to be realistically included in the continuum modeling. Various methods besides the continuum modeling exist in the literature. All of them, including the continuum methods, are reviewed in the following.

Note that for the interest of the present work, special focus is given on the near-wall MPMC flows at small scales. Before the reviews, two general components in the near-wall MPMC flows deserve to be highlighted again: the first is the interface between different phases or components, often characterized by the surface or surface tension and its geometrical curvature; the second is the interaction between the fluids

and the solid walls, often termed wetting (both static and dynamic). Failure to include either of them in an appropriate manner will lead to the uselessness of the whole method.

Essentially two main approaches exist in the literature for the modeling and simulation of MPMC flows. Besides the continuum one (including FT, VOF, LS, and DIM), there are discrete particle methods of Lagrangian type. This category includes the methods of the molecular dynamics (MD) simulation, the dissipative particle dynamics (DPD) and the smoothed particle hydrodynamics (SPH). In addition, there is lattice Boltzmann method (LBM) which falls somewhere in between, but probably closer to the continuum one.

1.2.1 Discrete particle methods

Conceptually, the discrete particle methods can be further divided into the microscopic approach, namely MD simulations, and the mesoscopic approach, which involves coarse graining at the mesoscopic level. The DPD and SPH methods belong to the latter.

1.2.1.1 MD simulation

MD simulation is by far the most accurate and genuine, and it provides most detailed information about the system being studied. It starts from the molecules that constitute the fluids. The position and velocity of each individual molecule are evolved according to the Newton's law. The macroscopic variables, including the density, velocity and temperature, are obtained by some proper statistical averaging (Rapaport 1995). MD simulations have been used to study the effects of wetting

properties on the boundary conditions at a solid wall by Barrata & Bocquet (1999), the dynamics of wetting of a water droplet on a textured surface composed of carbon atoms by Lundgren et al. (2003), and most recently the wetting on rough and heterogeneous surfaces at nanoscale by Lundgren et al. (2007). The interface and wetting are generally easier to model in MD - both are characterized by some certain interaction potentials between the molecules. Although MD is straightforward and fundamentally accurate, it often demands large amount of computational resource and time. Consequently the systems that can be investigated by MD are extremely small and contain very limited number of molecules; the time span of a single MD simulation is extremely short as well.

1.2.1.2 DPD and SPH simulations

DPD simulations are quite similar to the MD simulations. The differences lie in the averaging at certain mesoscopic level. DPD particles are much larger than the real molecules of the fluid; in fact, each DPD particle represents a cluster of fluid molecules and has internal degrees of freedom. Nevertheless, these large particles are evolved almost in the same way as that in MD except additional forces are included. Usually the forces acting on DPD particles consist of three parts: a conservative force, a dissipative force and a random force. The latter two, namely the dissipative and random forces, are due to the coarse graining and can be derived from statistical mechanics along a “bottom up” path (Flekkoy & Coveney 1999). DPD simulations have been applied to study a drop on a solid wall subject to simple shear by Jones et al. (1999), and most recently to simulate multi-phase flows in a fracture junction by Liu et al. (2007a) and in microchannel networks by Liu et al. (2007b).

In addition to DPD, the method of SPH, which originates from the study of astronomical hydrodynamics, has found its application in the study of MPMC flows. SPH also uses certain number of particles to represent the fluid system and they obey the Newton's second law as well. Different from DPD, SPH follows a "top down" path in the sense that the forces acting on SPH particles are derived by some specific SPH approximations of the force terms in the Navier-Stokes equations (Liu & Liu 2003). Recently SPH has been extended and applied to the MPMC flows near solid walls in which wetting is important (Tartakovsky & Meakin 2005).

It is noted that both DPD and SPH studies of the near-wall MPMC flows are relatively new and most cases that have been studied using them are not quite complicated. In both methods, the fluids have some degree of compressibility, and the incompressibility condition is only approximately satisfied. This is understandable considering the fact that incompressible flow is just a mathematical model for fluids with very large sound speeds, and real fluids are always compressible even at a very low degree. LBM shares this kind of quasi-compressibility with these two particle methods. The accuracy of DPD and SPH has not been demonstrated sufficiently, possibly because this is still one aspect that needs to be greatly improved in future. In general, the accuracy of the mesoscopic particle methods depends on the size of the particles chosen in the simulation. The proper choice seems to be somewhat an art: too large particle size compromises the accuracy whereas too small particle size increases the computation cost.

1.2.2 Continuum methods

As briefly discussed earlier, the continuum methods aim to solve the set of the partial differential equations (PDEs) that govern the fluid flows using Eulerian grids (fixed or sometimes dynamically adapted). In the following, only the application of the VOF, LS and DIM methods in the study of near wall MPMC flows are reviewed.

1.2.2.1 VOF and LS methods

The VOF method uses the volume fraction of one of the fluid phases or components (denoted as C) to characterize the interfaces. In the bulk region (of a pure fluid), C is equal to zero or unity; across the interfacial region, it varies smoothly in $[0,1]$. The normal direction and the curvature of the interface are calculated from derivatives of this smoothed volume fraction function. The surface tension force is applied using these two computed quantities, and its magnitude is proportional to the surface tension σ . The balance of forces across the interface is purely reflected in the pressure field, and not in C . Thus besides an indicator, the major role of the volume fraction function is for the enforcement of the surface tension effect, and it is not obviously related to any physical energy. The volume fraction function is purely advected by the velocity field, i.e., it obeys the equation: $\partial_t C + (\vec{u} \cdot \nabla) C = 0$. Thus, it may be necessary to use various sophisticated schemes in numerical advections. Renardy et al. (2001) gave detailed discussions on how to apply the VOF method for the investigation of MPMC fluids involving contact line (CL) dynamics. They compared two different ways to include wetting in VOF: one extrapolated the volume fraction to the outside of the computation domain and use the known equilibrium CA to prescribe the interface normal at the wall; the other was to extend further the concept of volume fraction to the solids and thus to deal with the CL area as a three-

phase problem. In addition, a suitable slip model with some slip length was used so that the singularity problem with the CLs was relieved. They argued that the first approach was better in VOF. Their investigations mainly focused on the numerical implementations and they only showed a few simple cases in two dimensions (2D) such as a drop under shear and a rising drop.

Similar to the volume fraction function in the VOF method, the level set function ϕ used in the LS method is not endowed with physical meaning, either. It is defined as the signed distance away from the interface and is purely a geometrical variable. The role of ϕ in LS is similar to C in VOF and they actually are evolved according to the same equation except that in LS a re-initialization procedure may be required. The way to include wetting and CL dynamics in LS is similar to the first approach described above in VOF. That is, the interface normal on the solid boundary is determined from the CA. By incorporating a model on the dynamic CA dependent on the CL velocity, Spelt (2005) extended the LS method for MPMC flow simulations involving moving CLs with the hysteresis effect taken into account. Later it was applied to study shear flows over 2D droplets, also by Spelt (2006).

1.2.2.2 Diffuse interface methods

DIM originates from the theory for near-critical fluids, in which the fluid system is fundamentally viewed as a whole and the indicator function is associated with the energy of the system. In DIM the interfacial region has its own physics inside; but as the interface width becomes smaller and smaller (compared with the macroscopic length), it can be mathematically proved that DIM approaches the original sharp interface equations (Anderson et al. 1998, Liu & Shen 2003). Wetting and CL

dynamics are included in DIM through a surface energy term. Some important basic issues in numerical simulations using DIM have been studied by Jacqmin (1999), and the CL dynamics in DIM has been excellently analyzed for a simple 2D problem by Jacqmin (2000). Quite recently, it has been applied to study capillarity driven droplet spreading by Khatavkar et al. (2007a) and droplet impact on a surface by Khatavkar et al. (2007b). More detailed introductions about the theories in DIM will be presented in Chapter II.

1.2.2.3 Some remarks on the continuum methods

All of the above continuum methods have seen certain success in the study of MPMC flows. However, VOF and LS may be categorized into one type since both of them use an indicator function without significant physical meanings; DIM is another different type because the order parameter in DIM may be related to some physics such as the free energy and the equation of state. The reason why different methods using different indicator functions can simulate the same problem and get the same results is probably because they all approach the same sharp interface limit under which only the interface shape and the surface tension forces are important. Hence, it would be desirable to make the interface thickness (in VOF and LS, the size of the smoothing region) as small as possible. This makes the adaptive meshing technique especially attractive in the study of MPMC flows. Recently it has been applied in DIM to study drop dynamics in non-Newtonian fluids by Yue et al. (2006). But in this thesis, such techniques have not been incorporated. On the other hand, the above discussions hold for macroscopic systems (and probably also for mesoscopic ones); when the system scale is too small (for instance, in the submicron regime) or when the fluids are near the critical points, the true interface thickness may not be regarded as

infinitely small any longer. Under those situations, normal regular meshes may be sufficient, and DIM would probably be a better candidate due to its physical origin. In fact, DIM has been used as a tool for direct simulations of nanoscale fluid systems by Jacqmin (2000).

As to the modeling of wetting and CL dynamics, VOF and LS often rely on explicitly finding the interface position and impose the CA or some sophisticated predetermined model on the interface near the wall; DIM addresses this issue in a seemingly more natural way by adding the surface energy contribution. In this aspect, VOF and LS appear to follow the “top-down” path because the CA or hysteresis models may be determined experimentally; DIM seems to be closer to the “bottom-up” concept because the coefficient in the surface energy might be extracted from molecular simulations (though it may use the CA as an input as well).

1.2.3 General remarks and outlook

After the above reviews of various methods, it is worth noting that there are simply *different ways* to tackle the *same problem*. As long as the modeling is correct and the simulation results are accurate, they should reach the same final solution. But in practice, this may not be exactly the case. For purely discrete particle methods, it is difficult to completely eliminate the fluctuations in the macroscopic quantities. Thus, the solutions obtained by MD and DPD often show some small irregularities and are not as smooth as those obtained through continuum methods or quasi-particle methods. Increasing the total simulation time (for the time averaging of steady problems) or the total number of simulations (for the ensemble averaging of unsteady problems) may help to alleviate the undesirable fluctuations, but that would also

increase the computational burden. At the same time, it would be fair to say that fluctuations always exist in real problems, but they are usually not very important for systems of the macroscopic and mesoscopic scales. On the other hand, the continuum and quasi-particle methods can provide nice results without fluctuations, but they may become insufficient to describe the physical problem in some part of the domain (e.g., CLs) or even the whole domain (e.g., very high Knudsen number gas flows). Thus, the two approaches actually complement with each other and it would be desirable to smartly combine both to form some hybrid methods, which forms the core idea of some multiscale modeling strategies. Excellent reviews and outlook of multiscale modeling have been given by E & Engquist (2003). Further discussions about this type of multiscale modeling are beyond the scope of this thesis. Here the focus is on LBM - a quasi-particle method which has its origin in kinetic theory and might hold the promise to be more easily combined with the *pure* particle methods as an effective multiscale modeling solution, which has been preliminarily demonstrated in a recent attempt to develop hybrid LBM-MD simulations by Dupuis et al. (2007). The review of LBM literature for near-wall MPMC flows is provided in the following section, and detailed introductions about the specific LBM used in the current work will be given in the next chapter.

1.3 LBM studies of near-wall MPMC flows

Historically, LBM evolved from the Lattice Gas Automata (LGA) with some defects of LGA being overcome (Chen & Doolen 1998, Succi 2001). One of the most popular and well established applications of LBM is the computations of low Reynolds number incompressible flows. In such applications, LBM resembles the artificial compressibility (AC) method (He et al. 2002). Probably the greatest potential of LBM

lies in the study of MPMC flows (especially in porous media) due to its relatively simple incorporation of interfacial physics and its simple treatment of complex boundaries (Succi 2001). In the following, various lattice Boltzmann models for MPMC flows are briefly tracked first; then efforts are concentrated on summarizing their studies of wetting and CL dynamics.

1.3.1 LBM for MPMC flows

Developments of LBM, including models for MPMC flows, appear fairly empirical when compared with the continuum methods probably due to its origin from LGA. The proposals of new models were often lack of very strict mathematical procedures though later some attempts were made to base the derivations more strictly on some theories in statistical mechanics. Yet this might not be the most important issue because the somewhat empirically developed models have worked reasonably well in many simulations. In the LBM community, the mostly used models include the color based model (C-LBM) (Gunstensen & Rothman 1991), the potential based model (P-LBM) (Shan & Chen 1993, Shan & Chen 1994) and FE based model (FE-LBM) (Swift et al. 1995, Swift et al. 1996). Thus, studies of near-wall MPMC flows using these three types of approaches are mainly reviewed in the following. Other models derived more strictly from Enskog theory (Luo 1998, Luo & Girimaji 2003, Guo & Zhao 2005) will not be discussed further here because these models seem to be still in the early development stage and the wall effects on flows have not been included yet⁵.

⁵ This does not imply that they are less important than, or inferior to other models reviewed here.

1.3.2 LBM simulations of wetting and CL dynamics

As mentioned earlier, in the presence of solid boundaries, modeling MPMC flows should incorporate the interactions between the solid substrates and the fluids of two phases or components properly. All the three models (C-LBM, P-LBM, and FE-LBM) have been extended to study such three-phase interactions. The problems that have been studied vary from very simple ones, like the density profile near the wall and the static CA of a droplet, to more complicated cases such as CL dynamics, capillary rise in confined geometries, and to even more complex cases including fluid slip near walls with alternating hydrophilic-hydrophobic patterns, droplets near walls with roughness characterized by certain grooves or pillars and MPMC flows near walls with both chemical and geometrical heterogeneities.

1.3.2.1 Wetting and CL dynamics on smooth surfaces

Latva-Kokko & Rothman (2005) proposed a color-based lattice Boltzmann model to study the capillary rise in confined geometries with minimal CA hysteresis. However, the color model deals with the interfaces in a somewhat artificial way, thus it looks more phenomenological and seems to lack a solid physical basis. Benzi et al. (2006) systematically studied the wetting and CA modeling in P-LBM. Detailed analyses, derivations as well as numerical results were provided for the density profile and CA determination; they further used the model to study the velocity slip near a wall with hydrophilic-hydrophobic patterns and obtained the effective slip lengths very close to previous hydrodynamic slip models. However, probably due to the not-so-natural mean field potential, P-LBM shares some similar problems with C-LBM: that is, it is not quite physically sound; in fact its thermodynamic inconsistency has been known for some time.

Different from these two models, Briant et al. (2002) included the wetting in LBM based on the FE concept. The FE-LBM may be viewed as a special implementation of the DIM discussed earlier, thus it inherits the general advantages of DIM, for instance, the use of the FE makes it appear physically sounder and capable to include the three phase interactions in a more consistent way. But their initial work was rather simple because they only studied a steady interface profile of a shear driven two phase flow between two parallel plates. Later the modeling and simulation of CL dynamics in FE-LBM were further developed by Briant et al. (2004) and by Briant & Yeomans (2004). In the two pieces of work, both near-critical liquid-vapor and binary fluid systems were studied, and comprehensive investigations of the inner region of the three-phase point, including the chemical potential field, were provided; besides, good comparisons with some other classical approaches for the contact-line problem were shown. Although incisive and very important, these studies remained fundamental and simple - the CA at the wall was fixed to be 90 degrees and the flows were all shear driven.

1.3.2.2 Wetting and CL dynamics on rough surfaces

Verberg et al. (2004) applied the FE-LBM to study the pattern formation in binary fluid systems confined between two grooved walls with chemical heterogeneities. The flows were either driven by shearing the two walls or by a pressure difference between the inlet and outlet. Interesting and diverse processes were observed. But this study was just qualitative, and quantitative information about the droplet shape evolutions and velocities was not provided.

Recently Dupuis & Yeomans (2005) investigated the droplets on superhydrophobic substrates with an FE-LBM. The superhydrophobicity was achieved by a nonwetttable wall with an array of square micro pillars. Two static equilibrium states of a droplet as well as transitions between them were successfully simulated. However, the droplet was confined to stay static or at most to move only in the vertical direction. Although some insights about droplet behaviors near textured surfaces have been obtained in their study, there is still plenty of space in exploring the dynamics of these systems. More recently, Zhang & Kwok (2006) investigated the dynamics of a liquid drop driven by a body force inside a channel having grooved hydrophobic⁶ surfaces also using a slightly different FE-LBM (Zhang et al. 2004). They managed to capture a stick-jump-slip behavior of the drop and provided the advancing and receding angles together with comparisons with those predicted by some other theories. But in their study only hydrophobic surfaces were investigated. However, it has been postulated by Herminghaus (2000) that hydrophilic surfaces with similar microstructures may achieve apparent hydrophobicity as well. Hence it would be interesting to study drop motions in rough hydrophilic channels and compare them with their hydrophobic counterparts.

1.3.3 Summary and some gaps of previous studies

In summary, to date, various lattice Boltzmann models have been developed for MPMC flows, and they have been extended to include the surface wall effects having given wettabilities as well. Some studies have even addressed the most complicated problems, namely flows near rough walls with chemical heterogeneities. However, there are still some limitations in previous works:

⁶ Note that the terms “hydrophobic” and hydrophilic” are in a relative sense and in the present study the “neutral-wetting” case with the static CA being 90 degrees is used as a baseline.

- Most studies investigated relatively simple cases, often steady problems;
- For those studying more complex flows, the results were either qualitative or restricted to some certain parameter regimes (e.g. hydrophobic walls only);
- The roles of some important simulation parameters such as the mobility in the binary fluid model have not been fully investigated.
- Some special interesting phenomena (e.g., bubble entrapment) in MPMC flows have not been well studied.

Note that more in-depth reviews of these aspects will be provided later in each individual chapter that addresses one of the issues.

1.4 Objectives of this study

The overall objective of this study was to further investigate both some fundamental aspects and some practically important cases of the near-wall MPMC flows mainly at small scales by the FE based lattice Boltzmann models. More specifically, this work aims:

- To study the effects of surface roughness on mechanically driven flows, not only for hydrophobic walls but also for hydrophilic ones;
- To study the role of mobility in capillarity-driven flows, especially its relation with the CL velocity and its effects on the evolution of such flow systems;
- To explore the feasibility of using numerical simulations as a designing tool for the manipulation of droplets through spatiotemporally controlled substrate wettability;
- To investigate various “bubble” entrapment phenomena during droplet impact on homogeneous surfaces.

It is noted that the study of the near-wall MPMC flows is a very active and diverse research field and many factors, such as temperature, compressibility, phase transition, chemical reaction, magnetic field and tiny solid particles, may affect the flow characteristics. However, it would be virtually impossible to consider all of them in a single thesis. In the present work, only the “pure” isothermal and incompressible MPMC flows will be studied and the effects of evaporation and condensation, chemical reaction, magnetic field and solid colloids are beyond the scope of this study. In some flow problems, the non-Newtonian rheology can play important roles; but it is not included in this research either.

LBM was chosen due to its ease in implementation of parallel computing, fair efficiency in computation of incompressible flows, and most importantly, its feasibility to incorporate the interfacial physics and the surface chemistry of the walls, even with certain roughness characterized by grooves or pillars. The most basic aspects of this method, including the theories, formulations and implementations, and the FE based models for MPMC flows will be presented in the next chapter in order to provide a clear illustration of the lattice Boltzmann modeling strategy as well as its suitability for the present study.

Besides widening and deepening our knowledge of various phenomena in MPMC flows, this study could provide some guidelines on the design of micro- and nano-fluidic devices (especially the substrates), and on the manipulation of extremely small volume of liquids by electrical or optical means in lab-on-a-chip systems. It may also provide some insights, for example, the relation between the mobility and the slip velocity at the three-phase point, on the diffuse interface modeling of MPMC flows as

well as on the dynamics of such MPMC systems. Finally, this work would be helpful to understand the so-called “Lotus Effect”, namely the superhydrophobicity of some plant leaves and some insect legs, because these biological surfaces are found to possess micro- or nano- structures and several cases studied later are just simplified models of the flows over them.

Table 1.1. Important factors in MPMC flows

Name	Expression	Relation to others
Reynolds number	$Re = \rho_c U_c L_c / \eta$	
Capillary number	$Ca = \eta U_c / \sigma$	
Webber number	$We = \rho_c U_c^2 L_c / \sigma$	$We = Ca Re$
Ohnesorge number	$Oh = \eta / \sqrt{\rho_c \sigma L_c}$	$Oh = We^{1/2} Re^{-1}$
Bond number	$Bo = \rho_c L_c^2 g / \sigma$	
Contact angle	θ	
Density ratio	$r_\rho = \rho_A / \rho_B$	
Viscosity ratio	$r_\nu = \nu_A / \nu_B$	

Chapter II

LBM and Its Modeling of MPMC Flows

In this chapter, the basics of LBM and the FE-based LBM are first introduced. After that, LBM modeling of wetting and CL dynamics, also in the FE framework, is given in detail.

2.1 LBM - an introduction

First, the simplest and also the most primitive LBM for single phase and nearly incompressible flows is introduced in this section. The key elements of LBM, such as its origin from kinetic theory, lattice velocity models, properties of the lattice tensors, its use of the artificial-compressibility methodology and the boundary and initial conditions, are reviewed.

2.1.1 Basic theory and formulation

Although originally developed from LGA, the lattice Boltzmann equation (LBE) has also been found to be derivable from the Boltzmann equation under the small Mach number assumption with suitable discretizations in the velocity space and coupled discretizations in space and time. For consistency and completeness, the formal procedure to derive the LBE from the Boltzmann equation is briefly described as follows. Note that more rigorous procedures and many of the formulas given below can be found in the work by He & Luo (1997a).

2.1.1.1 Brief derivation of LBE

The starting point to derive the LBE is the Boltzmann equation for a dilute gas.

Assuming no external body forces, it may be written in a general form as

$$\partial_t f + \vec{\xi} \cdot \nabla f = \Omega(f, \hat{f}), \quad (2.1)$$

where $f = f(\vec{x}, \vec{\xi}, t)$ is the one-particle distribution function (DF) in the physical and velocity space, the left hand side (LHS) represents the effect of the streaming and the right hand side (RHS), often named ‘‘collision integral’’, represents the change due to collisions between gas molecules. For monatomic gases, the mass density ρ , the momentum $\rho \vec{u}$, and the internal energy density ρe (e is the internal energy per unit mass) can be obtained as the moments of the DF,

$$\rho = m \int f d\vec{\xi}, \quad (2.2a)$$

$$\rho \vec{u} = m \int \vec{\xi} f d\vec{\xi}, \quad (2.2b)$$

$$\rho e = \rho \left(\frac{1}{2} D R T \right) = \frac{1}{2} m \int |\vec{\xi} - \vec{u}|^2 f d\vec{\xi}, \quad (2.2c)$$

where m is the mass of a single gas molecule, D is the dimension of the space, $R = k_B/m$ is the gas constant with k_B being the Boltzmann constant, and T is the temperature. The mass density ρ is related to the number density n as $\rho = mn$. Here it is worth mentioning that the pressure is calculated from the density ρ and temperature T as (i.e., the equation of state for ideal gases)

$$p = \rho R T. \quad (2.3)$$

Usually the number of molecules, the momentum and the energy are all conserved in collision, and the collision integral $\Omega(f, \hat{f})$ has the following properties

$$\int \Omega(f, \hat{f}) d\vec{\xi} = 0, \quad (2.4a)$$

$$\int \bar{\xi} \Omega(f, \hat{f}) d\bar{\xi} = 0, \quad (2.4b)$$

$$\frac{1}{2} \int |\bar{\xi}|^2 \Omega(f, \hat{f}) d\bar{\xi} = 0, \quad (2.4c)$$

where 1 , $\bar{\xi}$ and $\frac{1}{2}|\bar{\xi}|^2$ are called ‘‘collision invariants’’. It can further be proved that $\frac{1}{2}|\bar{\xi} - \bar{u}|^2$ is also collision invariant. Thus, the density ρ , the momentum $\rho\bar{u}$ and the temperature T are all conserved variables. The three quantities uniquely determine the local thermal equilibrium state under which the DF is given by the Maxwellian

$$f^{eq} = \frac{1}{m} \frac{\rho}{(2\pi RT)^{D/2}} \exp\left[-\frac{1}{2RT} |\bar{\xi} - \bar{u}|^2\right]. \quad (2.5)$$

Because the full collision integral is very complicated, the Bhatnagar-Gross-Krook (BGK) single-relaxation-time (SRT) model is often used as an alternative in many problems (Bhatnagar et al. 1954),

$$\Omega(f, f) = -(1/\tau)(f - f^{eq}), \quad (2.6)$$

where τ is the relaxation time. In kinetic theory, τ is normally related to the dynamic viscosity η and the pressure p , and the relation is found through the Chapman-Enskog multiscale analysis (Chapman 1990),

$$\tau = \eta/p. \quad (2.7)$$

In order to derive the LBE, the first step is to discretize the continuous velocity space. For instance, in 2D, if the D2Q9 model (see Fig. 2.1) is employed, the velocity space is discretized into nine discrete points \bar{e}_i ($i = 0, 1, \dots, 8$) which can be expressed as

$$\bar{e}_i = \begin{cases} 0 & (i = 0) \\ (\cos[(i-1)\pi/4], \sin[(i-1)\pi/4])c & (i = 1, \dots, 8) \end{cases}. \quad (2.8)$$

In 3D, the D3Q15 model (see Fig. 2.2) can be used. The discrete velocities for this model, \bar{e}_i ($i = 0, 1, \dots, 14$), can be written in matrix form as

$$\begin{aligned}
& [\bar{e}_0 \quad \bar{e}_1 \quad \bar{e}_2 \quad \bar{e}_3 \quad \bar{e}_4 \quad \bar{e}_5 \quad \bar{e}_6 \quad \bar{e}_7 \quad \bar{e}_8 \quad \bar{e}_9 \quad \bar{e}_{10} \quad \bar{e}_{11} \quad \bar{e}_{12} \quad \bar{e}_{13} \quad \bar{e}_{14}] \\
& = \begin{bmatrix} 0 & 1 & -1 & 0 & 0 & 0 & 0 & 1 & -1 & -1 & 1 & -1 & 1 & 1 & -1 \\ 0 & 0 & 0 & 1 & -1 & 0 & 0 & 1 & -1 & 1 & -1 & -1 & 1 & -1 & 1 \\ 0 & 0 & 0 & 0 & 0 & 1 & -1 & 1 & -1 & 1 & -1 & 1 & -1 & 1 & -1 \end{bmatrix} c. \quad (2.9)
\end{aligned}$$

In the above $c = \sqrt{3RT}$ is the ‘‘lattice velocity’’. The D2Q9 model includes the zero velocity and velocities in horizontal, vertical and diagonal directions, and it satisfies the requirements that guarantee the recovery of Navier-Stokes equations (see below for details) (Succi 2001). The D3Q15 model is one of the few models in three dimensions that satisfy similar requirements; other more complex models include D3Q19 and D3Q27, but they are not used here. After the discretization of the velocity space, the DF changes from the continuous $f(\bar{x}, \bar{\xi}, t)$ to discrete $f_i(\bar{x}, \bar{e}_i, t)$. Then the discrete BGK Boltzmann equation can be written as

$$\partial_t f_i + \bar{e}_i \cdot \nabla f_i = -(1/\tau)(f_i - f_i^{eq}) \quad (i = 0, 1, \dots, b), \quad (2.10)$$

where b denotes the number of nonzero lattice velocities ($b = 8$ for D2Q9, and $b = 14$ for D3Q15). These equations are essentially $b + 1$ coupled partial differential equations. The discrete equilibrium DFs f_i^{eq} can be obtained by expanding the Maxwellian with low Mach number approximation. Truncated at the second order (to $O((|\bar{u}|/c)^2)$), they can be expressed in a general form as,

$$f_i^{eq} = w_i \rho \left[1 + \frac{1}{c_s^2} (\bar{e}_i \cdot \bar{u}) + \frac{1}{2c_s^4} (\bar{u} \otimes \bar{u}) : (\bar{e}_i \otimes \bar{e}_i - c_s^2 \bar{I}) \right], \quad (2.11)$$

where \bar{I} is the second-rank unit tensor, ‘‘ \otimes ’’ denotes tensor product (e.g., combining two vectors into one second-rank tensor), ‘‘:’’ represents contraction product between tensors, $c_s \equiv \sqrt{RT}$ ($= c/\sqrt{3}$ for D2Q9 and D3Q15) is the isothermal sound speed conventionally defined in LBM, and w_i is the weight associated with the discrete

velocity \vec{e}_i . Table 2.1 gives the weights for the D2Q9 and D3Q15 models. The macroscopic variables can be calculated from the discrete moments of the discrete DFs as

$$\rho = \sum_i f_i, \quad (2.12a)$$

$$\rho \vec{u} = \sum_i \vec{e}_i f_i, \quad (2.12b)$$

where the sum \sum_i is taken over all discrete velocities ($i=0, \dots, b$). Note that for simplicity it is assumed $m=1$ which leads to $\rho = n$. It can be shown that (Nourgaliev et al., 2003) the discrete equilibrium DFs f_i^{eq} satisfy the following conditions

$$\sum_i f_i^{eq} = \rho, \quad (2.13a)$$

$$\sum_i e_{i\alpha} f_i^{eq} = \rho u_\alpha, \quad (2.13b)$$

$$\sum_i e_{i\alpha} e_{i\beta} f_i^{eq} = \rho u_\alpha u_\beta + \rho c_s^2 \delta_{\alpha\beta}, \quad (2.13c)$$

$$\sum_i e_{i\alpha} e_{i\beta} e_{i\gamma} f_i^{eq} = \rho c_s^2 (\delta_{\alpha\beta} u_\gamma + \delta_{\alpha\gamma} u_\beta + \delta_{\beta\gamma} u_\alpha), \quad (2.13d)$$

due to the properties of the lattices

$$E^{(0)} = \sum_i w_i = 1, \quad (2.14a)$$

$$E^{(1)} = \sum_i w_i e_{i\alpha} = 0, \quad (2.14b)$$

$$E^{(2)} = \sum_i w_i e_{i\alpha} e_{i\beta} = c_s^2 \delta_{\alpha\beta}, \quad (2.14c)$$

$$E^{(3)} = \sum_i w_i e_{i\alpha} e_{i\beta} e_{i\gamma} = 0, \quad (2.14d)$$

$$E^{(4)} = \sum_i w_i e_{i\alpha} e_{i\beta} e_{i\gamma} e_{i\chi} = c_s^4 \Delta_{\alpha\beta\gamma\chi} = c_s^4 (\delta_{\alpha\beta} \delta_{\gamma\chi} + \delta_{\alpha\gamma} \delta_{\beta\chi} + \delta_{\alpha\chi} \delta_{\beta\gamma}), \quad (2.14e)$$

$$E^{(5)} = \sum_i w_i e_{i\alpha} e_{i\beta} e_{i\gamma} e_{i\chi} e_{i\zeta} = 0. \quad (2.14f)$$

Here $E^{(n)}$ is called the lattice tensor of rank n . It is noted that for convenience and also for clarity the subscript forms are used in Eqs. (2.13, b-d) and (2.14, b-f). Later they will appear again in some other formulas, and Einstein summation applies for repeated Greek indices only (i.e., no summation over the repeated index i for lattice velocity).

In theory, there are no restrictions on which numerical method should be used to solve the discrete BGK Boltzmann equation. Common techniques, such as the finite difference method (FDM), finite volume method (FVM) and finite element method (FEM), may all be applied. But here only the simplest version, using the most popular lattice type discretization, is presented. The lattice Boltzmann equation results from coupled discretizations in space and time. First the discretization in time is performed: Eq. (2.10) can be integrated from t to $t + \delta_t$, which results in

$$f_i(\bar{x} + \bar{e}_i \delta_t, t + \delta_t) - f_i(\bar{x}, t) = -(1/\tau) \int_t^{t+\delta_t} (f_i - f_i^{eq}) dt. \quad (2.15)$$

To achieve the second order accuracy, the trapezoidal approximation is employed for the RHS (Dellar 2001), which leads to

$$f_i(\bar{x} + \bar{e}_i \delta_t, t + \delta_t) - f_i(\bar{x}, t) = -\frac{\delta_t}{2\tau} \left\{ [f_i(\bar{x}, t) - f_i^{eq}(\bar{x}, t)] + [f_i(\bar{x} + \bar{e}_i \delta_t, t + \delta_t) - f_i^{eq}(\bar{x} + \bar{e}_i \delta_t, t + \delta_t)] \right\}. \quad (2.16)$$

With a new variable introduced as follows,

$$\bar{f}_i = f_i + \frac{\delta_t}{2\tau} (f_i - f_i^{eq}), \quad (2.17)$$

it is straightforward to obtain the explicit evolution equation for \bar{f}_i as

$$\bar{f}_i(\bar{x} + \bar{e}_i \delta_t, t + \delta_t) - \bar{f}_i(\bar{x}, t) = -\frac{\delta_t}{\tau + 0.5\delta_t} [\bar{f}_i(\bar{x}, t) - \bar{f}_i^{eq}(\bar{x}, t)], \quad (2.18)$$

where $\bar{f}_i^{eq} = f_i^{eq}$ (Dellar 2001). Now another relaxation parameter for \bar{f}_i can be defined,

$$\tau_R^* = 0.5 + \tau/\delta_i, \quad (2.19)$$

and then it can be verified that \bar{f}_i corresponds to f_i in common LBM and τ_R^* is related to the viscosity as

$$(\tau_R^* - 0.5)\delta_i = \eta/p = \eta/(\rho RT) = \nu/c_s^2. \quad (2.20)$$

In using \bar{f}_i , the macroscopic variables are obtained by the following relations (Dellar 2001)

$$\sum_i \bar{f}_i = \sum_i f_i + \frac{\delta_t}{2\tau} \sum_i (f_i - f_i^{eq}) = \sum_i f_i = \rho, \quad (2.21a)$$

$$\sum_i \bar{e}_i \bar{f}_i = \sum_i \bar{e}_i f_i + \frac{\delta_t}{2\tau} \sum_i \bar{e}_i (f_i - f_i^{eq}) = \sum_i \bar{e}_i f_i = \rho \bar{u}, \quad (2.21b)$$

$$p = \rho c_s^2, \quad (2.21c)$$

$$\sum_i (\bar{e}_i \otimes \bar{e}_i) (\bar{f}_i - \bar{f}_i^{eq}) = \left(1 + \frac{\delta_t}{2\tau}\right) \sum_i (\bar{e}_i \otimes \bar{e}_i) (f_i - f_i^{eq}) = \left(1 + \frac{\delta_t}{2\tau}\right) (-\bar{\Pi}), \quad (2.21d)$$

where $\bar{\Pi}$ is the viscous stress tensor. This formulation (in \bar{f}_i) is adopted in the present work. For brevity, the over bar will be omitted, and τ (instead of τ_R^*) is used.

After these simplifications, Eq. (2.18) becomes

$$f_i(\bar{x} + \bar{e}_i \delta_i, t + \delta_t) - f_i(\bar{x}, t) = -(1/\tau) [f_i(\bar{x}, t) - f_i^{eq}(\bar{x}, t)], \quad (2.22)$$

which is exactly the same as the LBE mostly used in the literature.

Until now, the spatial discretization has not been performed yet. It is most convenient to choose the regular lattice sites which exactly match the points $(\bar{x}, \bar{x} + \bar{e}_i \delta_i, \dots)$.

This is the formulation used in most previous LBM studies and also in this work.

However, it is noted that other spatial discretization strategies, such as the interpolation-supplemented LBM by He et al. (1996) and the Taylor-series-expansion- and Least-square-based LBM by Shu et al. (2001), may also be used, and they may perform much better for certain cases. However, the implementations and further studies in this aspect are out of the scope of the present work.

For the simplest version, the lattice Boltzmann equation is usually implemented through two separate steps, namely, collision and streaming (Col.-Str.):

$$\text{Collision: } \tilde{f}_i(\bar{x}, t) = f_i(\bar{x}, t) - \frac{1}{\tau} [f_i(\bar{x}, t) - f_i^{eq}(\bar{x}, t)], \quad (2.23)$$

$$\text{Streaming: } f_i(\bar{x} + \bar{e}_i \delta_t, t + \delta_t) = \tilde{f}_i(\bar{x}, t). \quad (2.24)$$

The collision step is completely local and the streaming step involves pure shift of DFs between neighbouring sites. The simplicity of LBM is clearly reflected by the Col.-Str. steps. But attention needs to be paid on the boundary sites. The issue of boundary conditions (BCs) will be discussed later in Subsection 2.1.2.

2.1.1.2 Reference quantities, dimensionless numbers and compressibility

In the LBM framework, it is a common practice to use the lattice velocity c and the lattice length δ_x as the reference quantities for the velocity and length. Consequently, the reference time is given by

$$\delta_t = \delta_x / c. \quad (2.25)$$

Then all other variables in length and time will be measured in δ_x and δ_t , which are normally called the “lattice units” (LU). Under such a system, the (dimensionless) sound speed in D2Q9 and D3Q15 is $c_s^* = 1/\sqrt{3}$. It should be noted that for the simulations in this thesis, LU is always used unless otherwise specified. It would be

useful to make some comparisons between LU and the units used in other particle methods. The use of LU in LBM is actually similar to MD simulations in which the reference quantities are chosen as those constants in the interaction potential (so-called MD units) (Rapaport 1995); and it also bears similarity to DPD simulations in which the reference quantities are picked in such a way that the DPD particles are of unit mass, the cut-off distance for the interaction potential is unit and the temperature satisfies $k_B T = 1$ (so-called DPD units) (Groot & Warren 1997).

The above reference quantities of LU result in the following reference kinematic viscosity $\nu_r = c \delta_x = c^2 \delta_t$, and then the (dimensionless) kinematic viscosity expressed in LU is (for D2Q9 and D3Q15)

$$\nu^* = (c_s^*)^2 (\tau - 0.5) = \frac{1}{3} (\tau - 0.5). \quad (2.26)$$

Suppose that the (dimensionless) characteristic velocity is U_c^* and the (dimensionless) characteristic length is L_c^* (both in LU), then it is found that the Reynolds number is

$$\text{Re} = \frac{U_c^* L_c^*}{\nu^*} = \frac{3U_c^* L_c^*}{\tau - 0.5}. \quad (2.27)$$

It is straightforward to inverse Eq. (2.27) to find the dimensionless relaxation parameter τ from the Reynolds number as

$$\tau = 0.5 + \frac{3U_c^* L_c^*}{\text{Re}}. \quad (2.28)$$

For brevity, the superscript $*$ is usually omitted. In addition, a *LBM Mach number* can be defined as

$$\text{Ma}_{LBM} = \frac{U_c}{c_s}. \quad (2.29)$$

It is easy to find that Ma_{LBM} is related to the normal Mach number as

$$Ma_{LBM} = \sqrt{\gamma} Ma, \quad (2.30)$$

where γ is the specific heat ratio of the gas. The difference is due to the definition of sound speed: in LBM isothermal condition is assumed whereas under other situations the isentropic flow condition is normally assumed. Nevertheless, they are of the same order.

It is worth giving some discussions on how LBM approximately solves the incompressible flow problems and the cautions to be taken in such simulations. Incompressibility is commonly expressed as

$$\nabla \cdot \vec{u} = 0, \quad (2.31)$$

which results from the condition

$$(1/\rho)d\rho/dt = 0. \quad (2.32)$$

Here the simplified case with $\rho = const$ is discussed. As mentioned above, LBM resembles the AC method when used to compute incompressible flows. Hence, Ma_{LBM} should be small (ideally approaching zero), so that the incompressibility condition is well satisfied. Assuming that the reference density is ρ_r , the reference pressure is then given by

$$p_r = \rho_r c^2. \quad (2.33)$$

For single phase incompressible flows, the absolute values of the density and pressure are not important because they vary in a small range around their averages, for instance,

$$\rho = \bar{\rho}(1 + O(Ma^2)), \quad p = \bar{p}(1 + O(Ma^2)). \quad (2.34a, b)$$

It is practicable to choose their averages to be, say, $\bar{\rho} = 3$ and $\bar{p} = 1$ (for $c = \sqrt{3}c_s$).

Models reducing compressibility errors have been proposed by He & Luo (1997b) to

better simulate the incompressible flows in which the equilibrium DFs are modified to be

$$f_i^{eq} = w_i \left\{ \rho + \bar{\rho} \left[\frac{1}{c_s^2} (\vec{e}_i \cdot \vec{u}) + \frac{1}{2c_s^4} (\vec{u} \otimes \vec{u}) : (\vec{e}_i \otimes \vec{e}_i - c_s^2 \vec{I}) \right] \right\}. \quad (2.35)$$

Although choosing a larger sound speed reduces the compressibility error, it should be also noted that a larger sound speed implies smaller time step and thus compromises the computational efficiency. Hence, the sound speed should be properly adjusted in order to achieve accurate and efficient simulations.

To summarize, in LBM simulations of single phase incompressible flows, there are two important dimensionless parameters, one of which (the Reynolds number) reflects the flow physics of the problem whereas the other (the Mach number) may be regarded as a computational parameter that can be adjusted to achieve a optimum balance in the accuracy and efficiency.

2.1.2 BCs in LBM

LBM simulations are always carried out inside a finite domain. Hence, proper conditions need to be specified on the boundaries of the domain. The main variables in LBM are the discrete DFs. Therefore, BCs in LBM essentially specify how to determine the incoming DFs either from the outgoing DFs or from the given conditions for macroscopic variables (e.g., the velocity, the pressure). Simulations of MPMC flows require additional conditions that will be discussed later in this chapter. According to the interaction type at the boundary (fluid-solid or fluid-fluid), BCs can be categorized into (Yu et al. 2005):

- (a) BCs at solid walls;

(b) BCs at open boundaries.

In the first type, BCs is to model the effect of solids outside the domain on the fluid flows being simulated. The second type can be further categorized into a few subtypes:

(b1) BCs for a periodic problem;

(b2) BCs at a fluid reservoir (with uniform pressure, velocity, etc.);

(b3) BCs resulted from a suitable cut-off of the infinite domain;

(b4) BCs at symmetric lines or planes.

Comprehensive discussions of all the above BCs require considerable space. In what follows, only (a) and (b1) will be described in detail using the D2Q9 model for illustration.

2.1.2.1 BCs at solid walls

For clarity, two types of nodes in LBM, namely the *fluid nodes* and the *buffer nodes*, are first introduced. As implicated by the name, the buffer nodes are for buffer use only and are not involved in the Col.-Str. processes. Col.-Str. processes happen only on the fluids nodes and they can be further divided into the *bulk fluid nodes* and the *boundary fluid nodes*. A bulk fluid node does not have any buffer nodes as its neighbours; in other words, all its neighbouring nodes are fluid nodes. In contrast, the neighbours of a boundary fluid node consist of both buffer nodes and fluid nodes. It is noted that, unless specified otherwise, the *by-link* cases are assumed, in which the wall is $\delta_x/2$ away from the boundary fluid nodes.

Consider a typical Col.-Str. process for a boundary node near the lower wall. After collision, all the DFs are updated from f_i to \tilde{f}_i which can be grouped into (see Fig. 2.1 for the numbering of lattice velocities):

(Col.-Group-1) \tilde{f}_i ($i = 0, \dots, 5$) (DFs streaming to neighbouring fluid nodes);

(Col.-Group-2) \tilde{f}_i ($i = 6, 7, 8$) (DFs hitting the wall).

The DFs required in the streaming step can also be divided into two groups:

(Str.-Group-1) f_i ($i = 0, 1, 5, \dots, 8$);

(Str.-Group-2) f_i ($i = 2, 3, 4$).

(Str.-Group-1) are directly obtained from the post-collision DFs of the neighbouring nodes, i.e.,

$$f_i(\bar{x}, t) = \tilde{f}_i(\bar{x} - \bar{e}_i \delta_t, t - \delta_t) \quad (i = 0, 1, 5, \dots, 8). \quad (2.36)$$

(Str.-Group-2) can be obtained for the post-collision DFs that will “hit the wall”, i.e., (Col.-Group-2). The boundary condition on a stationary wall is essentially the mapping from (Col.-Group-2) to (Str.-Group-2) which can be in general written as (Sbragaglia & Succi 2004)

$$\begin{bmatrix} f_2(\bar{x}, t + \delta_t) \\ f_3(\bar{x}, t + \delta_t) \\ f_4(\bar{x}, t + \delta_t) \end{bmatrix} = \begin{bmatrix} \mathbf{K}_{11} & \mathbf{K}_{12} & \mathbf{K}_{13} \\ \mathbf{K}_{21} & \mathbf{K}_{22} & \mathbf{K}_{23} \\ \mathbf{K}_{31} & \mathbf{K}_{32} & \mathbf{K}_{33} \end{bmatrix} \begin{bmatrix} \tilde{f}_6(\bar{x}, t) \\ \tilde{f}_7(\bar{x}, t) \\ \tilde{f}_8(\bar{x}, t) \end{bmatrix} = [\mathbf{K}] \begin{bmatrix} \tilde{f}_6(\bar{x}, t) \\ \tilde{f}_7(\bar{x}, t) \\ \tilde{f}_8(\bar{x}, t) \end{bmatrix}, \quad (2.37)$$

where the matrix $[\mathbf{K}]$ may be regarded as the “discrete scattering kernel”. Of course this mapping should include certain constraints such as mass conservation. In the following only the commonly used bounce back (BB) scheme is described.

Conventionally, the BB scheme is used to enforce the no-slip condition (see Fig. 2.3 for illustration and Fig. 2.1 for lattice velocity numbering). In the BB scheme, one assumes that the outgoing DFs first hit the wall and then are bounced back along the opposite directions with the same lattice speed. The interaction time with the wall is assumed to be zero. For the BB scheme, Eq. (2.37) can be simplified as

$$\begin{bmatrix} f_2(\bar{x}, t + \delta_t) \\ f_3(\bar{x}, t + \delta_t) \\ f_4(\bar{x}, t + \delta_t) \end{bmatrix} = \begin{bmatrix} \tilde{f}_6(\bar{x}, t) \\ \tilde{f}_7(\bar{x}, t) \\ \tilde{f}_8(\bar{x}, t) \end{bmatrix}. \quad (2.38)$$

For a moving wall, the bounced DFs gain additional momentum after interacting with the wall. For the situation shown in Fig. 2.3, if the wall is moving with the velocity \vec{u}_w , Eq. (2.38) is modified to be (Mei et al. 1999)

$$\begin{bmatrix} f_2(\bar{x}, t + \delta_t) \\ f_3(\bar{x}, t + \delta_t) \\ f_4(\bar{x}, t + \delta_t) \end{bmatrix} = \begin{bmatrix} \tilde{f}_6(\bar{x}, t) \\ \tilde{f}_7(\bar{x}, t) \\ \tilde{f}_8(\bar{x}, t) \end{bmatrix} + \frac{6\rho}{c^2} \begin{bmatrix} w_6 \vec{e}_2 \cdot \vec{u}_w \\ w_7 \vec{e}_3 \cdot \vec{u}_w \\ w_8 \vec{e}_4 \cdot \vec{u}_w \end{bmatrix}. \quad (2.39)$$

2.1.2.2 BCs at the inlets and outlets for periodic problems

BCs on solid boundaries may be complete for a few problems (for instance, the driven-cavity). But BCs for inlets and outlets are commonly encountered as well (for example, flows inside a channel). At inlets and outlets, there exist fluxes of the fluid variables (density, momentum, etc.). The simplest BCs in this category are the periodic BCs. Suppose a 2D problem is periodic, say, in the x – direction with $x = 0$ being the left end, and $x = L$, the right end. Then the periodic BCs for the DFs read,

$$f_{i_{IN}} \Big|_{x=0} = f_{i_{OUT}} \Big|_{x=L}, \quad f_{i_{IN}} \Big|_{x=L} = f_{i_{OUT}} \Big|_{x=0} \quad (2.40a, b)$$

where $i_{IN} = 1, 2, 8$ at $x = 0$ (correspondingly, $i_{OUT} = 1, 2, 8$ at $x = L$), and $i_{IN} = 4, 5, 6$ at $x = L$ (correspondingly, $i_{OUT} = 4, 5, 6$ at $x = 0$) for the D2Q9 model.

2.1.3 Initial conditions in LBM

Initial conditions are another important issue in LBM simulations, either for steady problems or unsteady problems. For steady flows, LBM acts as a special type of solver for the time-independent equations and the initial conditions may affect the

speed of convergence. For unsteady flows, LBM specifies how the system evolves, and the initial conditions should conform to the physical initial states. In LBM, it is common to set the initial DFs equal to the equilibrium DFs calculated from the given initial macroscopic fields (e.g., the density and velocity fields) (Skordos 1993). In the presence of velocity gradients, it is a better practice to include the first order correction of the non-equilibrium DFs. But in this thesis, it is not implemented because for most cases the initial velocity field is just uniformly zero.

2.2 FE based LBM for MPMC flows

In the above, the fundamentals of LBM simulations have been presented. Next LBM based on the FE concept for MPMC flows will be introduced. It is noted that the FE theory is independent of LBM, and LBM may be viewed as a special implementation used to simulate the MPMC fluid systems. Other types of methods (for instance, the FEM solutions of the NSCH equations) can also be employed to study such systems. But LBM possesses certain advantages as already discussed at the end of Chapter I.

2.2.1 FE theory for liquid-vapor systems near critical points

First it is useful to give some introductions on the FE theory for single component liquid-vapor (LV) systems near critical points (to be denoted as FE1) because it provides the core ideas of DIM and may serve as the basis for other models. More thorough descriptions about the theory can be found in the work by Papatzacos (2002).

For a single-component LV system (e.g., water and water-vapor), suppose that the critical point of the fluid is characterized by the critical pressure p_c , the critical density ρ_c and the critical temperature T_c . When the system temperature T is lower

than, but close to, the critical temperature (i.e., $T < T_c$ and $|1 - (T/T_c)| \ll 1$), the liquid and vapor phases can coexist and the pseudo *van der Waals* (VW) model can be applied to describe such a fluid system. For convenience, two small dimensionless variables, relevant to the non-dimensional temperature and density respectively, are defined as follows

$$\tau_{lv} \equiv 4(1 - (T/T_c)), \quad (2.41)$$

$$\tilde{\rho} \equiv (\rho/\rho_c) - 1. \quad (2.42)$$

The *Helmholtz FE per unit volume* is given by

$$\psi(\rho, T) = W_{lv}(\rho, T) + \bar{\mu}(T)\rho - \bar{p}(T), \quad (2.43)$$

where $\bar{\mu}(T)$ is the chemical potential, $\bar{p}(T)$ is the pressure of the bulk fluid given by

$$\bar{p}(T) = p_c(1 - \tau_{lv})^2, \quad (2.44)$$

and

$$W_{lv}(\rho, T) = p_c(\tilde{\rho}^2 - \tau_{lv})^2, \quad (2.45)$$

is a function of the density and temperature. Across a flat interface, the densities of the liquid and vapor phases, ρ_l and ρ_v , are the values of ρ giving $W_{lv} = 0$:

$$\rho_l = \rho_c(1 + \sqrt{\tau_{lv}}), \quad \rho_v = \rho_c(1 - \sqrt{\tau_{lv}}). \quad (2.46a, b)$$

The equation of state can be obtained from the definition of *bulk pressure*

$$p^b = \rho(\partial\psi/\partial\rho) - \psi, \quad (2.47)$$

and it is straightforward to get,

$$p^b = p_c(\tilde{\rho} + 1)^2(3\tilde{\rho}^2 - 2\tilde{\rho} + 1 - 2\tau_{lv}). \quad (2.48)$$

The *bulk chemical potential* is defined by

$$\mu^b = \partial\psi/\partial\rho, \quad (2.49)$$

and is found to be,

$$\mu^b = 4p_c \rho_c^{-1} \tilde{\rho} (\tilde{\rho}^2 - \tau_{lv}) + \bar{\mu}(T). \quad (2.50)$$

It is noted that when the temperature is assumed to be uniform (isothermal flows) it is unnecessary to determine $\bar{\mu}$ for it is simply a constant. In general, when solid boundaries are not present, the *Helmholtz FE functional* can be written as

$$F = \int_V (\psi + (1/2)\kappa |\nabla \rho|^2) dV \quad (2.51)$$

where V is the volume of the system and κ is a constant. Minimizing F with the constant-mass constraint $\int_V \rho dV = M_T$ (M_T is the total mass), one gets the Euler-Lagrange variational equation

$$(\partial \psi / \partial \rho) - \bar{\mu} - \kappa \nabla^2 \rho = 0 \quad (2.52)$$

which holds *throughout the whole domain*. In the bulk region (of either a pure liquid or vapor), one has $\nabla^2 \rho = 0$ and $\mu^b = \partial \psi / \partial \rho = \bar{\mu}$. It is worth noting that the chemical potential

$$\bar{\mu} = (\partial \psi / \partial \rho) - \kappa \nabla^2 \rho \quad (2.53)$$

is a constant when the system is in equilibrium. For a one-dimensional problem, say, in x – direction, Eq. (2.52) can be integrated once, leading to

$$\psi(\rho) - \bar{\mu}\rho + \bar{p} - (1/2)\kappa(d\rho/dx)^2 = 0 \quad (2.54)$$

Substituting Eq. (2.43) into Eq. (2.54), one finds

$$W_{lv}(\rho) = (1/2)\kappa(d\rho/dx)^2 \quad (2.55)$$

With the given form of the function $W_{lv}(\rho)$, the surface tension can be calculated according to its definition,

$$\sigma_{lv} = \kappa \int_{-\infty}^{\infty} (d\rho/dx)^2 dx = (4/3)\rho_c \sqrt{2\kappa p_c} \tau_{lv}^{3/2} \quad (2.56)$$

(Note here the subscript is added to emphasize that it is for the liquid-vapor system, but usually it is omitted.) And if in addition $d\rho/dx > 0$, one can further find a particular solution of the function $\rho(x)$ as

$$\rho(x) = \rho_c \left(1 + \sqrt{\tau_{lv}} \tanh(x/l_T) \right), \quad (2.57)$$

where

$$l_T = \rho_c \sqrt{\kappa / (2\tau_{lv} p_c)} = W/2, \quad (2.58)$$

with W defined as the interface width. Fig. 2.4 shows a typical density profile across a flat interface based on the above model using $W = 4$. Note that it is often convenient to also define a sharp interface as the surface (line) where $\rho = (\rho_l + \rho_v)/2$ ($= \rho_c$ for a flat interface) although in fact the interfacial region usually spans a few grid points.

For general problems in any dimensions, there exists a conservation law according to Noether's theorem due to the fact that the FE functional F and the mass constraint are independent of the spatial coordinates (Anderson et al. 1998),

$$\nabla \cdot \vec{T}_{SS} = 0, \quad (2.59)$$

where \vec{T}_{SS} is a second-rank tensor given by

$$\vec{T}_{SS} = L\vec{I} - (\nabla\rho) \otimes (\partial L / \partial (\nabla\rho)), \quad (2.60)$$

with L given by

$$L = \psi(\rho) + (1/2)\kappa|\nabla\rho|^2 - \bar{\mu}\rho. \quad (2.61)$$

Thus, the tensor \vec{T}_{SS} is,

$$\vec{T}_{SS} = \left(-p^b + \kappa\rho\nabla^2\rho + (1/2)\kappa|\nabla\rho|^2 \right) \vec{I} - \kappa(\nabla\rho) \otimes (\nabla\rho). \quad (2.62)$$

After some further straightforward calculations, it can be found that,

$$\nabla \cdot \vec{T}_{SS} = -[\nabla(\rho\bar{\mu}) - \bar{\mu}(\nabla\rho)] = -\rho\nabla\bar{\mu} = 0. \quad (2.63)$$

For dynamic cases, when the body forces are excluded, the governing equations for the isothermal single component LV systems are given by

$$\partial_t \rho + \nabla \cdot (\rho\bar{u}) = 0, \quad (2.64a)$$

$$\partial_t (\rho\bar{u}) + \nabla \cdot (\rho\bar{u} \otimes \bar{u}) = \nabla \cdot (\vec{T}_{SS} + \vec{\Pi}), \quad (2.64b)$$

where $\vec{\Pi}$ is the viscous (dissipative) stress tensor given by

$$\vec{\Pi} = \eta(\nabla\bar{u} + (\nabla\bar{u})^T). \quad (2.65)$$

It can be seen that \vec{T}_{SS} represents the reversible part of the stress tensor.

2.2.2 FE theory for immiscible binary fluid systems

Considering that the LV systems are made of the same kind of molecules whereas binary fluid systems consist two different kinds of molecules (e.g., water and silicon oil), it may be fair to say that the two types of systems differ fundamentally in this aspect. Nevertheless, the FE theory for immiscible binary fluid systems (denoted as FE2) normally seen in the literature is very similar to the above one for LV systems near critical points.

2.2.2.1 A loose induction from FE theory for LV systems

If the following compound variables are defined,

$$\phi_\rho \equiv (1/\sqrt{\tau_{lv}})(\rho/\rho_c - 1), \quad (2.66)$$

$$a_\rho \equiv p_c \tau_{lv}^2, \quad (2.67)$$

$$\kappa_\rho \equiv \kappa(\rho_c \sqrt{\tau_{lv}})^2, \quad (2.68)$$

and further the two terms $\bar{\mu}(T)\rho$ and $-\bar{p}(T)$ are neglected from the Helmholtz FE density, the results below can be obtained (note that there are no strict justifications for this simplification, and here it is just made to show the connections between the two FE models for liquid-vapor and binary fluid systems),

(1) Across a flat interface,

$$\phi_\rho|_l = 1, \quad \phi_\rho|_v = -1; \quad (2.69a, b)$$

(2) The simplified bulk FE density is,

$$\psi(\phi_\rho) = a_\rho(\phi_\rho^2 - 1)^2; \quad (2.70)$$

(3) The simplified FE functional is,

$$F = \int_V \left(\psi(\phi_\rho) + (\kappa_\rho/2) |\nabla \phi_\rho|^2 \right) dV; \quad (2.71)$$

(4) The surface tension is,

$$\sigma = (4/3) \sqrt{2\kappa_\rho a_\rho}; \quad (2.72)$$

(5) The interface width is,

$$W = \sqrt{2\kappa_\rho/a_\rho}. \quad (2.73)$$

When ϕ_ρ is reinterpreted as an order parameter to distinguish the two fluid components, then these results just provide exactly the same FE theory intensively used for immiscible binary fluids with uniform density. But after the above replacements and simplifications, some other formulas also change. Note the subscript “ ρ ” will be omitted for binary fluid systems. Now the chemical potential μ is calculated by taking the variation of the FE functional with respect to the order parameter,

$$\mu = \delta F / \delta \phi = \psi'(\phi) - \kappa \nabla^2 \phi = 4a\phi(\phi^2 - 1) - \kappa \nabla^2 \phi. \quad (2.74)$$

If the bulk pressure (sometimes also called “thermodynamic pressure”, see the work

by Lee & Lin (2005)) in FE2 is defined in a way similar to FE1 as,

$$p^b = \phi\psi'(\phi) - \psi(\phi) \quad (2.75)$$

then the reversible stress tensor in FE2 is,

$$\vec{T}_{ss} = \left(-p^b + \kappa\phi\nabla^2\phi + (1/2)\kappa|\nabla\phi|^2 \right) \vec{I} - \kappa(\nabla\phi) \otimes (\nabla\phi) \quad (2.76)$$

and similarly it can be found that,

$$\nabla \cdot \vec{T}_{ss} = -[\nabla(\phi\mu) - \mu(\nabla\phi)] = -\phi\nabla\mu = 0 \quad (2.77)$$

For a flat interface, the analytical solution of the interface profile is

$$\phi(x) = \tanh(x/(W/2)), \quad (2.78)$$

Similar to FE1, it is also a common practice to define a sharp interface as the surface (or lines) on which $\phi = 0$. From Eqs. (2.72) and (2.73), the coefficients a and κ can be expressed in terms of σ and W as,

$$a = (3\sigma)/(4W) \quad (2.79)$$

$$\kappa = 3\sigma W/8 \quad (2.80)$$

However, as observed from the two different sets of governing equations, Eqs. (1.1, a-c) and Eqs. (2.64, a & b), there exists a significant difference between FE1 and FE2. FE1 has only one mass conservation equation for the density, whereas FE2 has an additional equation to govern the evolution of the order parameter. In FE1, the density also plays the role of the order parameter and the pressure in the momentum equation is exactly obtained from the EOS. In FE2 for incompressible binary fluids, it is necessary to enforce the incompressibility condition, Eq. (1.1a). As discussed in Subsection 2.1.1.2, this is realized through the AC-like methodology in LBM. The details are provided in the next section.

2.2.2.2 Remarks on the order parameter

It would render the model clearer if a few further remarks are made upon the order parameter ϕ . Although across a flat interface ϕ changes from -1 to 1 indicating a transition from one pure fluid to the other, the order parameter can take other values (close to -1 or 1) in the bulk fluid when the interfaces have nonzero curvatures. For instance, the order parameters inside and outside a stationary droplet in equilibrium could be $\phi_{in} = 1 + \varepsilon_{in}$ and $\phi_{out} = -(1 - \varepsilon_{out})$ with ε_{in} and ε_{out} having some small positive values. Note that ε_{in} and ε_{out} are nearly constant “far” away (e.g., $2W$ away) from the interface (with typical variations less than 0.5%). This may be understood as a requirement either to minimize the FE functional or to satisfy the Laplace’s law on the relation between the pressure difference across the interface and the surface tension. Such a phenomenon was called “overshoots” and “undershoots” and was regarded inherent to the DIM using the above form of bulk FE (Jacqmin 1999). Hence, if the initial ϕ field for a droplet (of a radius R_d and with its center positioned at \vec{X}_C) is specified as,

$$\phi(r) = -\tanh((r - R_d)/(W/2)), \quad (2.81)$$

with

$$r = \sqrt{\sum_{\alpha=1}^D (x_\alpha - X_{C\alpha})^2}, \quad (2.82)$$

being the distance away from the droplet center (here D is the dimension of space and $D = 2$ or 3), then the ϕ field will evolve toward an equilibrium distribution with

$\phi_{in}^{eq} = 1 + \varepsilon_{in}^{eq}$ and $\phi_{out}^{eq} = -(1 - \varepsilon_{out}^{eq})$ that satisfy the Laplace law,

$$p_{in}^b(\phi_{in}^{eq}) - p_{out}^b(\phi_{out}^{eq}) = \sigma / [(D - 1)R_d]. \quad (2.83)$$

During this process, the droplet shrinks a bit. Only recently, this issue has been investigated systematically by Yue et al. (2007). It is noted that such a phenomenon has also been observed in the LBM simulations of the present work and some results will be given later.

The above discussions give a concrete explanation on why the order parameter in DIM is different from other indicator functions such as the volume fraction in VOF and the signed distance function in LS (as mentioned in Subsection 1.2.2.3). But one may be questioned that how on earth to interpret the order parameter deviating from the bulk value: can it be the mass fraction of one component? The answer might be: it may not be exactly interpreted as the mass fraction or concentration; but rather, the DIM views the binary fluids as some sort of mixture for which phase transition may even occur under certain situations. Ultimately, DIM is just a model that mimics the real systems well provided that some conditions are satisfied. Thus, it may not be quite meaningful to ask for the strict physical explanations.

2.2.3 Lattice Boltzmann formulation for immiscible binary fluids

Now the lattice Boltzmann formulation for solving the set of governing equations (Eqs. (1.1, a-c)), denoted as FE2-LBM, is presented as follows. It is noted that here the term “solving” differs from other direct discretization techniques; it is in the LBM way - to recover the macroscopic equations in the long-time and long-wavelength limits.

In FE2-LBM, the FE is almost identical to that defined in Eq. (2.71) above except that an additional term is inserted into the volume integration to approximately enforce the incompressibility condition (Kendon et al. 2001, Verberg et al. 2004),

$$F(\phi, \nabla \phi) = \int_V \left(\rho c_s^2 \ln \rho + \psi(\phi) + (\kappa/2) |\nabla \phi|^2 \right) dV. \quad (2.84)$$

It is noted that the density ρ in the above formula is dimensionless and it varies near unity (recall that here the binary fluid system is assumed to have uniform density).

After the insertion of the term $\rho c_s^2 \ln \rho$, the full pressure in FE2 is,

$$\vec{P}^{th} = -\vec{T}_{SS} + p^{hydro} \vec{I} \quad (2.85)$$

with the hydrodynamic pressure p^{hydro} (note the name follows Lee & Lin (2005)) being,

$$p^{hydro} = \rho c_s^2 \quad (2.86)$$

and the divergence of the full pressure is,

$$\nabla \cdot \vec{P}^{th} = \nabla \cdot \left(-\vec{T}_{SS} + p^{hydro} \vec{I} \right) = \phi \nabla \mu + \nabla p^{hydro} \quad (2.87)$$

Note that the forcing term due to the pressure that appears in the RHS of the momentum equation is $-\nabla \cdot \vec{P}^{th}$. Then, it becomes clear that the hydrodynamic pressure p^{hydro} matches the term S in Eq. (1.1b).

LBM allows different implementations within the above FE framework. Although different sub-models may differ in specific coefficients, they all approximately recover the same macroscopic equations when the Chapman-Enskog procedure is applied. Here two sub-models are described.

2.2.3.1 Lattice Boltzmann formulation - implementation A

The first sub-model (denoted as FE2-LBM-A) is based on the work by Kendon et al. (2001). LBEs in the model read,

$$f_i(\bar{x} + \bar{e}_i \delta_t, t + \delta_t) - f_i(\bar{x}, t) = -(1/\tau_f) [f_i(\bar{x}, t) - f_i^{eq}(\bar{x}, t)] \quad (2.88)$$

$$g_i(\bar{x} + \bar{e}_i \delta_t, t + \delta_t) - g_i(\bar{x}, t) = -(1/\tau_g) [g_i(\bar{x}, t) - g_i^{eq}(\bar{x}, t)] \quad (2.89)$$

where f_i are the DFs for the hydrodynamic fields, g_i are the DFs for the order parameter field. In Eqs. (2.88) and (2.89), τ_f and τ_g are the relaxation parameters related to the kinematic viscosity and the mobility respectively; the equilibrium DFs, f_i^{eq} and g_i^{eq} , are calculated from the density ρ , the velocity u_α and the order parameter ϕ (plus its gradient, $\nabla\phi$, and its Laplacian, $\nabla^2\phi$) as follows,

$$f_i^{eq} = w_i \left\{ A_i + \rho \left[\frac{1}{c_s^2} (\bar{e}_i \cdot \bar{u}) + \frac{1}{2c_s^4} (\bar{e}_i \otimes \bar{e}_i - c_s^2 \bar{I}) : (\bar{u} \otimes \bar{u}) \right] + (\bar{e}_i \otimes \bar{e}_i) : \bar{G} \right\} \quad (2.90)$$

$$g_i^{eq} = w_i \left\{ B_i + \phi \left[\frac{1}{c_s^2} (\bar{e}_i \cdot \bar{u}) + \frac{1}{2c_s^4} (\bar{e}_i \otimes \bar{e}_i - c_s^2 \bar{I}) : (\bar{u} \otimes \bar{u}) \right] \right\} \quad (2.91)$$

with the coefficients A_i and B_i given by,

$$A_i = \begin{cases} (1/c_s^2) (P_{\gamma\gamma}^{th}/D) = A & (i > 0) \\ w_0^{-1} [\rho - (1 - w_0)A] & (i = 0) \end{cases} \quad (2.92)$$

$$B_i = \begin{cases} \tilde{M}\mu/c_s^2 = B & (i > 0) \\ w_0^{-1} [\phi - (1 - w_0)B] & (i = 0) \end{cases} \quad (2.93)$$

and the components of the tensor \bar{G} are,

$$G_{\alpha\beta} = \frac{1}{2c_s^4} \left(P_{\alpha\beta}^{th} - \frac{1}{D} P_{\gamma\gamma}^{th} \delta_{\alpha\beta} \right) \quad (2.94)$$

Here \tilde{M} is a parameter related to the mobility M as $M = (\tau_g - 1/2)\tilde{M}\delta_t$ and in the simulations, the second relaxation parameter is chosen as $\tau_g = 1$ leading to

$M = (1/2)\tilde{M}\delta_i$. It is noted that unless specified otherwise, this relaxation parameter is always chosen to be this value in all models involving the distribution functions for the order parameter; also for convenience, the specific mobility values used in simulation are always given in terms of \tilde{M} later in this thesis.

Recall that $\tilde{P}^{th} = -\tilde{T}_{SS} + p^{hydro}\tilde{I}$ is the full pressure, then the coefficients A and $G_{\alpha\beta}$ can be explicitly computed out,

$$A = \frac{1}{c_s^2} \frac{P_{\gamma\gamma}^{th}}{D} = \frac{1}{c_s^2} \left\{ (\rho c_s^2 + \phi\mu) - \left[\psi(\phi) + \left(\frac{1}{2} - \frac{1}{D} \right) \kappa (\partial_\alpha \phi)(\partial_\alpha \phi) \right] \right\} \quad (2.95)$$

$$G_{\alpha\beta} = \frac{1}{2c_s^4} \left(P_{\alpha\beta}^{th} - \frac{1}{D} P_{\gamma\gamma}^{th} \delta_{\alpha\beta} \right) = \frac{\kappa}{2c_s^4} \left[(\partial_\alpha \phi)(\partial_\beta \phi) - \frac{1}{D} (\partial_\gamma \phi)(\partial_\gamma \phi) \delta_{\alpha\beta} \right] \quad (2.96)$$

It can be verified that the above equilibrium DFs, f_i^{eq} and g_i^{eq} , satisfy

$$\sum_i f_i^{eq} = \rho \quad (2.97a)$$

$$\sum_i e_{i\alpha} f_i^{eq} = \rho u_\alpha \quad (2.97b)$$

$$\sum_i e_{i\alpha} e_{i\beta} f_i^{eq} = \rho u_\alpha u_\beta + P_{\alpha\beta}^{th} \quad (2.97c)$$

$$\sum_i e_{i\alpha} e_{i\beta} e_{i\gamma} f_i^{eq} = \rho c_s^2 (\delta_{\alpha\beta} u_\gamma + \delta_{\alpha\gamma} u_\beta + \delta_{\beta\gamma} u_\alpha) \quad (2.97d)$$

$$\sum_i g_i^{eq} = \phi \quad (2.98a)$$

$$\sum_i e_{i\alpha} g_i^{eq} = \phi u_\alpha \quad (2.98b)$$

$$\sum_i e_{i\alpha} e_{i\beta} g_i^{eq} = \tilde{M}\mu\delta_{\alpha\beta} + \phi u_\alpha u_\beta \quad (2.98c)$$

It is seen that in FE2-LBM-A, the basic strategy is to construct appropriate equilibrium DFs according to the full pressure tensor.

2.2.3.2 Lattice Boltzmann formulation - implementation B

The sub-model used in the present work (FE2-LBM-B) is slightly different from FE2-LBM-A. It essentially makes use of the relation in Eq. (2.77),

$$\nabla \cdot \vec{T}_{ss} = -[\nabla(\phi\mu) - \mu(\nabla\phi)] = -\phi\nabla\mu.$$

Because the chemical potential μ contains the term $\nabla^2\phi$ which is a second order derivative, $\nabla\mu$ involves the third order derivative. The term $\phi\nabla\mu$ may be better dealt with in the following way: first, it is split into two terms, $\nabla(\phi\mu)$ and $-\mu(\nabla\phi)$; then the term $\nabla(\phi\mu)$ is put into the equilibrium DFs whereas the term $-\mu(\nabla\phi)$ is put on the RHS of the LBEs as a body force. Such an implementation was previously used by Zheng et al. (2006) in a model for large density ratio multi-phase flows (to be described later) and is adopted in most simulations of present work. In accordance to the above implementation, the first LBE for FE2-LBM-B is modified to be

$$f_i(\vec{x} + \vec{e}_i\delta_t, t + \delta_t) - f_i(\vec{x}, t) = -(f_i(\vec{x}, t) - f_i^{eq}(\vec{x}, t))/\tau_f + \delta_t w_i \vec{e}_{i\alpha} (\mu \partial_\alpha \phi) / c_s^2, \quad (2.99)$$

and the modified equilibrium DFs are,

$$f_i^{eq} = w_i \left\{ A_i + \rho \left[\frac{1}{c_s^2} (\vec{e}_i \cdot \vec{u}) + \frac{1}{2c_s^4} (\vec{e}_i \otimes \vec{e}_i - c_s^2 \vec{I}) : (\vec{u} \otimes \vec{u}) \right] \right\} \quad (2.100)$$

with the coefficient A now given by,

$$A = (\rho c_s^2 + \phi\mu) / c_s^2 \quad (2.101)$$

Then, the second order moments of f_i^{eq} satisfy the following modified relation,

$$\sum_i e_{i\alpha} e_{i\beta} f_i^{eq} = \rho u_\alpha u_\beta + (\rho c_s^2 + \phi\mu) \delta_{\alpha\beta} \quad (2.102)$$

The modified equilibrium DFs in Eq. (2.100) no longer contain the terms involving the tensor \vec{G} and the coefficient A is much simplified as well. Such modifications seem to improve the model to some degree (some tests show that they can improve

the isotropy of interfacial region and reduce some undesired numerical artifact like the spurious currents, most probably due to the simplifications of the coefficients, which may help to remove certain discretization errors).

2.2.3.3 Chapman-Enskog expansion and the macroscopic equations

In applying the multiscale Chapman-Enskog expansion on Eqs. (2.99) and (2.89) as follows,

$$f_i(\bar{x} + \bar{e}_i \delta_t, t + \delta_t) = f_i(\bar{x}, t) + \varepsilon(\partial_t + e_{i\alpha} \partial_\alpha) f_i + \frac{1}{2} \varepsilon^2 (\partial_t + e_{i\alpha} \partial_\alpha) (\partial_t + e_{i\beta} \partial_\beta) f_i + O(\varepsilon^3) \quad (2.103)$$

$$f_i = f_i^{eq} + \varepsilon f_i^{(1)} + O(\varepsilon^2) \quad (2.104)$$

$$g_i(\bar{x} + \bar{e}_i \delta_t, t + \delta_t) = g_i(\bar{x}, t) + \varepsilon(\partial_t + e_{i\alpha} \partial_\alpha) g_i + \frac{1}{2} \varepsilon^2 (\partial_t + e_{i\alpha} \partial_\alpha) (\partial_t + e_{i\beta} \partial_\beta) g_i + O(\varepsilon^3) \quad (2.105)$$

$$g_i = g_i^{eq} + \varepsilon g_i^{(1)} + O(\varepsilon^2) \quad (2.106)$$

$$\partial_t = \partial_{t_0} + \varepsilon \partial_{t_1} + O(\varepsilon^2) \quad (2.107)$$

with $\varepsilon = \delta_t$ being small compared to the macroscopic time scales, it can be found that the macroscopic equations are (detailed derivations are given in the Appendix),

$$\partial_t \rho + \partial_\alpha (\rho u_\alpha) = 0 \quad (2.108a)$$

$$\partial_t (\rho u_\alpha) + \partial_\beta (\rho u_\alpha u_\beta + \rho c_s^2 \delta_{\alpha\beta}) = \partial_\beta [\eta (\partial_\beta u_\alpha + \partial_\alpha u_\beta)] - \phi \partial_\alpha \mu \quad (2.108b)$$

$$\partial_t \phi + \partial_\alpha (\phi u_\alpha) = M \partial_{\alpha\alpha} \phi \quad (2.108c)$$

It is noted that the continuity equation is slightly different from Eq. (1.1a). This reason is already mentioned above. That is, LBM assumes that the fluid is slightly compressible and makes use of the fact that the incompressible condition is approximately satisfied when the Mach number is small.

2.2.4 LBM for multi-phase flows with large density ratios

For some problems investigated in this study, the model for large density ratio multi-phase flows (denoted as LDR-LBM) by Zheng et al. (2006) is used. Note that the specifics for the model described here are not completely the same as those by Zheng et al. (2006); besides that model has been extended to include wetting in the present work. In the following it is briefly recaptured.

Similar to previous LBM developed for large-density-ratio problems (Inamuro et al. 2004, Lee & Lin 2005), it was based on the FE concept and was for a liquid-gas system with the (constant) liquid and gas densities being ρ_L and ρ_G respectively. The FE functional in this model is very similar to that in FE2 (except the definitions (or interpretations) of the order parameter and density),

$$F = \int_V [\psi(\phi) + (\kappa/2)(\partial_\alpha \phi)(\partial_\alpha \phi) + c_s^2 \rho \ln \rho] dV \quad (2.109)$$

where ϕ is the order parameter related to the density difference and ρ is the average density. The bulk FE $\psi(\phi)$ also has a double-well form (but the equilibrium values are $\pm \phi^*$ instead of ± 1 in FE2),

$$\psi(\phi) = a(\phi^2 - \phi^{*2})^2 \quad (2.110)$$

For a flat interface, the analytical solution of the interface profile is,

$$\phi(x) = \phi^* \tanh(x/(W/2)), \quad (2.111)$$

with the interface thickness W given by,

$$W = (1/\phi^*) \sqrt{2\kappa/a}, \quad (2.112)$$

And the surface tension can be calculated as,

$$\sigma = \int_{-\infty}^{\infty} \kappa (d\phi/dx)^2 dx = (4\sqrt{2\kappa a}/3)(\phi^*)^3 \quad (2.113)$$

The LBEs are almost the same as those in FE2-LBM-B. Since the use of this model in the present work involves an external body force, the LBEs for the hydrodynamic fields are modified to be,

$$f_i(\vec{x} + \vec{e}_i \delta_t, t + \delta_t) - f_i(\vec{x}, t) = -\left(f_i(\vec{x}, t) - f_i^{eq}(\vec{x}, t)\right) / \tau_f + \delta_t w_i \vec{e}_{i\alpha} (\mu \partial_\alpha \phi + \rho g_\alpha) / c_s^2 \quad (2.114)$$

where g_α is the component of the body force density in the x_α direction.

2.3 Modeling of wetting and CL dynamics

In last section, the general framework of modeling MPMC flows using the FE concept has been laid. In this section, the next two issues will be addressed: (1) how to include the wetting and CL dynamics in the above framework; (2) how to incorporate them in LBM.

Wetting has been intensively studied in surface chemistry. It is still a fast-marching field despite its long history. It essentially studies the interactions between two fundamentally different phases: fluid and solid. Commonly the fluid contains two phases or components (though it is also possible that only one phase is present, or in the other limit, many fluid phases exist). Quite a number of factors affect wetting such as the temperature, surface roughness, electrical fields, local pH values and even the configurations of the fluid molecules. Although sometimes the deformation of solid is taken into account, it is usually negligible and is not considered in this thesis. The main focus in the present work is, of course, on how the fluid is affected by the solid. For convenience, the regions where interfaces between fluids (of two different phases and components) meet the solid boundaries are called “three-phase-line” (TPL).

The following FE theories for wetting assume that the solid wall is ideally smooth and has the same wetting property everywhere. In accordance to the above subsection, LV systems will first be addressed and next, FE2-LBM and then LDR-LBM.

2.3.1 Wetting in LV systems

To include wetting in the FE framework for LV systems, a surface energy term is added, leading to the modified FE functional,

$$F = \int_V \left(\psi + (1/2)\kappa|\nabla\rho|^2 \right) dV + \int_S \phi(\rho_\sigma) dS \quad (2.115)$$

where S denotes the surface of the wall, ρ_σ is the fluid density at the wall, and $\phi(\rho_\sigma)$ is the surface energy density (per unit area) which, for simplicity, is usually assumed to be (Papatzacos 2002, Briant et al. 2002)

$$\phi(\rho_\sigma) = -\omega\rho_\sigma \quad (2.116)$$

Here ω is a parameter related to the wetting property. Now minimizing the whole FE functional including the surface energy contribution, the natural boundary condition can be obtained, in addition to Eq. (2.52),

$$\kappa\vec{n} \cdot (\nabla\rho)_S = \kappa(\partial\rho/\partial n)_S = -\omega \quad (2.117)$$

where \vec{n} is the unit normal at the wall pointing into the fluid. For one-dimensional problems, if ω is within a certain range (details on how to determine the range can be found in (Papatzacos 2002) and are omitted here for brevity), four solutions for the boundary fluid density ρ_σ can be found,

$$\rho_1/\rho_c = 1 - \sqrt{\tau_{lv} \sqrt{1+|\tilde{\omega}|}}, \quad \rho_2/\rho_c = 1 - \sqrt{\tau_{lv} \sqrt{1-|\tilde{\omega}|}}, \quad (2.118a, b)$$

$$\rho_3/\rho_c = 1 + \sqrt{\tau_{lv} \sqrt{1-|\tilde{\omega}|}}, \quad \rho_4/\rho_c = 1 + \sqrt{\tau_{lv} \sqrt{1+|\tilde{\omega}|}}, \quad (2.118c, d)$$

where the dimensionless parameter $\tilde{\omega}$ is given by,

$$\tilde{\omega} = \omega / (\tau_{lv} \sqrt{2\kappa p_c}). \quad (2.119)$$

When $\omega \leq 0$, the normal gradient of the density at the wall is positive, thus the surface fluid density is smaller than the bulk fluid; ρ_σ at the boundary takes the value ρ_1 if the bulk fluid is a vapor, and ρ_3 if the bulk fluid is a liquid. This means that the wall is hydrophobic and favors the vapor phase. The surface tension between the solid and vapor, σ_{sv} , and that between the solid and liquid, σ_{sl} , are calculated as

$$\sigma_{sv} = -\omega\rho_1 + \int_{\rho_1}^{\rho_v} \sqrt{2\kappa W_{lv}(\rho)} d\rho, \quad (2.120a)$$

$$\sigma_{sl} = -\omega\rho_3 + \int_{\rho_3}^{\rho_l} \sqrt{2\kappa W_{lv}(\rho)} d\rho, \quad (2.120b)$$

respectively. When $\omega > 0$, the normal gradient of the density at the wall is negative, thus the surface fluid density is larger than the bulk fluid; ρ_σ at the boundary takes the value ρ_2 if the bulk fluid is a vapor, and ρ_4 if the bulk fluid is a liquid. This implies that the wall is hydrophilic and favors the liquid phase. For this case, the surface tensions σ_{sv} and σ_{sl} are computed as,

$$\sigma_{sv} = -\omega\rho_2 + \int_{\rho_v}^{\rho_2} \sqrt{2\kappa W_{lv}(\rho)} d\rho, \quad (2.121a)$$

$$\sigma_{sl} = -\omega\rho_4 + \int_{\rho_l}^{\rho_4} \sqrt{2\kappa W_{lv}(\rho)} d\rho. \quad (2.121b)$$

According to Young's equation, the CA measured in the liquid part is calculated as,

$$\cos \theta = (\sigma_{sv} - \sigma_{sl}) / \sigma_{lv}. \quad (2.122)$$

For either $\omega \leq 0$ or $\omega > 0$, it is found that,

$$\cos \theta = (1/2) \left[\left(\sqrt{1 + \tilde{\omega}} \right)^3 - \left(\sqrt{1 - \tilde{\omega}} \right)^3 \right], \quad (2.123)$$

from Eq. (2.56), and either Eqs. (2.120, a & b) or Eqs. (2.121, a & b). Thus, the wall property is uniquely determined by the dimensionless parameter $\tilde{\omega}$.

2.3.2 Wetting in binary fluid systems

Wetting in binary fluid systems is modeled in a way similar to the above. That is, the surface energy contribution is further added, leading to the following FE functional (Briant & Yeomans 2004),

$$F = \int_V \left(\psi(\phi) + (\kappa/2) |\nabla \phi|^2 \right) dV + \int_S \varphi(\phi_\sigma) dS, \quad (2.124)$$

with $\varphi(\phi_\sigma)$ being the surface energy density which is assumed to be,

$$\varphi(\phi_\sigma) = -\omega \phi_\sigma. \quad (2.125)$$

Minimizing the whole FE functional including the surface energy, the natural boundary condition can be obtained, similar to Eq. (2.117),

$$\bar{\kappa} \cdot (\nabla \phi)_S = \kappa (\partial \phi / \partial n)_S = -\omega \quad (2.126)$$

By similar derivations, it is possible to find four solutions for the order parameter at the wall as,

$$\phi_1 = -\sqrt{1+|\tilde{\omega}|}, \quad \phi_2 = -\sqrt{1-|\tilde{\omega}|}, \quad (2.127a, b)$$

$$\phi_3 = \sqrt{1-|\tilde{\omega}|}, \quad \phi_4 = \sqrt{1+|\tilde{\omega}|}. \quad (2.127c, d)$$

with the dimensionless parameter $\tilde{\omega}$ now defined as,

$$\tilde{\omega} = \omega / (\sqrt{2\kappa a}). \quad (2.128)$$

The CA measured in the fluid with $\phi > 0$ is found to be the same as Eq. (2.123).

2.3.3 Wetting in LDR-LBM

Wetting in the LDR model is almost the same except that the additional parameter ϕ^* needs to be taken into account. After the inclusion of the following surface energy $\varphi(\phi_\sigma) = -\omega\phi_\sigma$ in Eq. (2.109), the functional minimization procedure leads to, $\kappa\vec{n} \cdot (\nabla\phi)_s = -\omega$, and the CA (measured in the liquid with $\phi > 0$) is also given by Eq. (2.123). The differences are due to ϕ^* . Now the four solutions for the order parameter at the wall are,

$$\phi_1 = -\phi^* \sqrt{1+|\tilde{\omega}|}, \quad \phi_2 = -\phi^* \sqrt{1-|\tilde{\omega}|}, \quad (2.129a, b)$$

$$\phi_3 = \phi^* \sqrt{1-|\tilde{\omega}|}, \quad \phi_4 = \phi^* \sqrt{1+|\tilde{\omega}|}. \quad (2.129c, d)$$

and the dimensionless coefficient $\tilde{\omega}$ is given by,

$$\tilde{\omega} = \omega / \left(\sqrt{2\kappa\alpha} (\phi^*)^2 \right). \quad (2.130)$$

2.3.4 Implementation of wetting boundary condition

The implementation of the wetting boundary condition (WBC) follows the way used by Briant et al. (2002). Since WBC is very similar in all the FE1, FE2 and LDR models, only the WBC for the LV system is introduced and the following formulas are given in terms of the density ρ . From Eq. (2.117), WBC is essentially the enforcement of a given normal gradient of the density (order parameter) on the wall,

$$\left(\frac{\partial\rho}{\partial n} \right)_s = -\frac{\omega}{\kappa}, \quad (2.131)$$

Take a two dimensional horizontal wall at the lower side as an example (see Fig. 2.5). The following formulas, which are at least second order accurate, are used to evaluate the derivatives

$$\left. \frac{\partial \rho}{\partial x} \right|_{i,j} \approx \frac{\rho_{i+1,j} - \rho_{i-1,j}}{2\delta_x}, \quad \left. \frac{\partial \rho}{\partial y} \right|_{i,j} = -\frac{\omega}{\kappa} \quad (2.132a, b)$$

$$\left. \frac{\partial^2 \rho}{\partial x^2} \right|_{i,j} \approx \frac{\rho_{i+1,j} - 2\rho_{i,j} + \rho_{i-1,j}}{\delta_x^2} \quad (2.133a)$$

$$\left. \frac{\partial^2 \rho}{\partial y^2} \right|_{i,j} \approx \frac{1}{4\delta_x^2} \left(\frac{6\omega}{\kappa} \delta_x + \rho_{i,j+2} + 4\rho_{i,j+1} - 5\rho_{i,j} \right) \quad (2.133b)$$

where in evaluating $\left. \frac{\partial^2 \rho}{\partial y^2} \right|_{i,j}$ the following biased difference schemes,

$$\left. \frac{\partial^2 \rho}{\partial y^2} \right|_{i,j} \approx \frac{1}{2\delta_x} \left(-3 \left. \frac{\partial \rho}{\partial y} \right|_{i,j} + 4 \left. \frac{\partial \rho}{\partial y} \right|_{i,j+1} - \left. \frac{\partial \rho}{\partial y} \right|_{i,j+2} \right), \quad (2.134a)$$

$$\left. \frac{\partial \rho}{\partial y} \right|_{i,j+2} \approx \frac{3\rho_{i,j+2} - 4\rho_{i,j+1} + \rho_{i,j}}{2\delta_x}, \quad (2.134b)$$

and the central difference scheme

$$\left. \frac{\partial \rho}{\partial y} \right|_{i,j+1} \approx \frac{\rho_{i,j+2} - \rho_{i,j}}{2\delta_x}, \quad (2.135)$$

are used. For horizontal walls at the upper side and vertical walls, similar formulas can easily be derived. Attention is required when the normal direction \bar{n} is opposite to the y or x direction. The Laplacian is calculated as

$$\nabla^2 \rho = \frac{\partial^2 \rho}{\partial x^2} + \frac{\partial^2 \rho}{\partial y^2}. \quad (2.136)$$

Extensions to three dimensions are straightforward. Suppose that the wall is in the $x - y$ plane at $z = 0$, the following formulas can be used,

$$\left. \frac{\partial \rho}{\partial x} \right|_{i,j,k} \approx \frac{\rho_{i+1,j,k} - \rho_{i-1,j,k}}{2\delta_x}, \quad \left. \frac{\partial \rho}{\partial y} \right|_{i,j,k} \approx \frac{\rho_{i,j+1,k} - \rho_{i,j-1,k}}{2\delta_x}, \quad \left. \frac{\partial \rho}{\partial z} \right|_{i,j,k} = -\frac{\omega}{\kappa}, \quad (2.137a, b, c)$$

$$\left. \frac{\partial^2 \rho}{\partial x^2} \right|_{i,j,k} \approx \frac{\rho_{i+1,j,k} - 2\rho_{i,j,k} + \rho_{i-1,j,k}}{\delta_x^2}, \quad \left. \frac{\partial^2 \rho}{\partial y^2} \right|_{i,j,k} \approx \frac{\rho_{i,j+1,k} - 2\rho_{i,j,k} + \rho_{i,j-1,k}}{\delta_x^2}, \quad (2.138a, b)$$

$$\left. \frac{\partial^2 \rho}{\partial z^2} \right|_{i,j,k} \approx \frac{1}{4\delta_x^2} \left(\frac{6\omega}{\kappa} \delta_x + \rho_{i,j,k+2} + 4\rho_{i,j,k+1} - 5\rho_{i,j,k} \right), \quad (2.138c)$$

These derivatives are required in the calculations of the chemical potential or some other coefficients that appear in the equilibrium DFs (or the force term in FE2-LBM-B and LDR-LBM). For all these formulas, the uniform mesh spacing (δ_x) in all directions is assumed.

It is noted that when the normal BBL scheme is applied for the boundary nodes, the above scheme will introduce additional errors of order $\delta_x/2$ because the condition for the normal gradient is supposed to hold at the wall. But such deviations should be very small and may be neglected when the mesh is fine enough.

Table 2.1. Weights in the discrete equilibrium distributions

Velocity model	$w_0 (\vec{e}_0 = 0)$	$w_i (\vec{e}_i = c)$	$w_i (\vec{e}_i = \sqrt{2}c)$	$w_i (\vec{e}_i = \sqrt{3}c)$
D2Q9	4/9	1/9	1/36	NA
D3Q15	2/9	1/9	NA	1/72

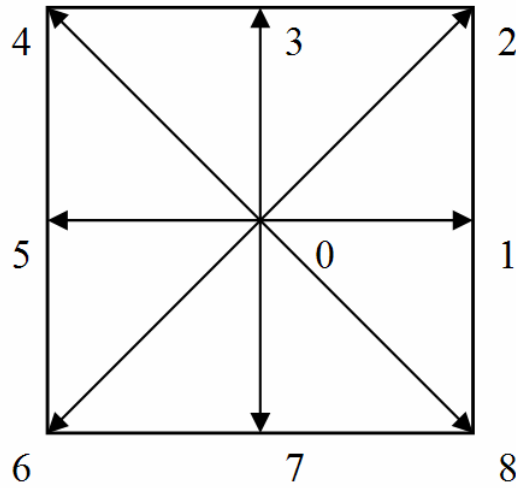


Fig. 2.1. D2Q9 velocity model

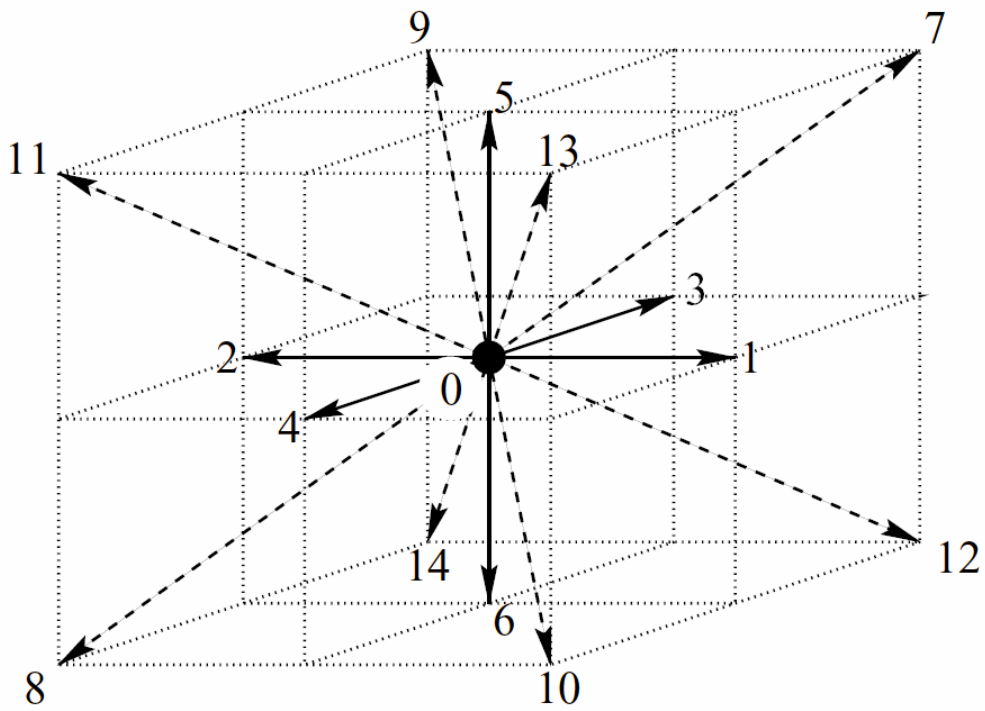


Fig. 2.2. D3Q15 velocity model

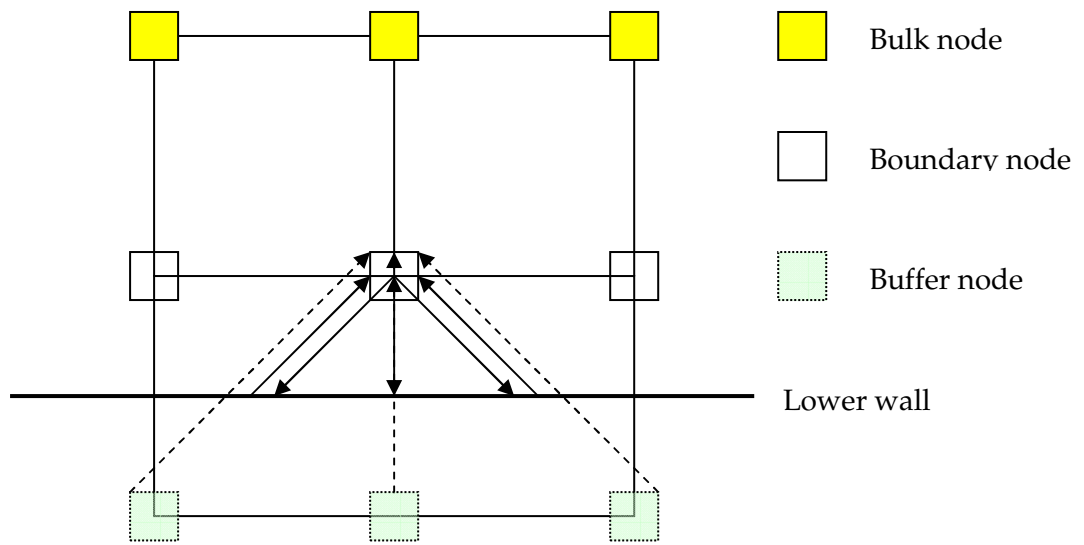


Fig. 2.3. Illustration of BB on the lower wall

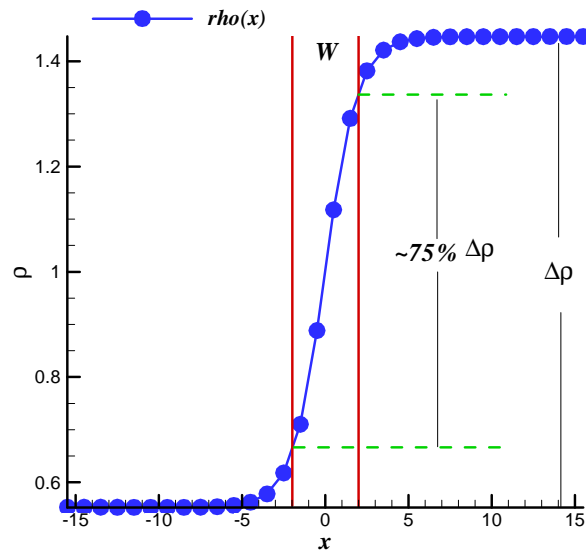


Fig. 2.4. Typical density profile across a flat interface

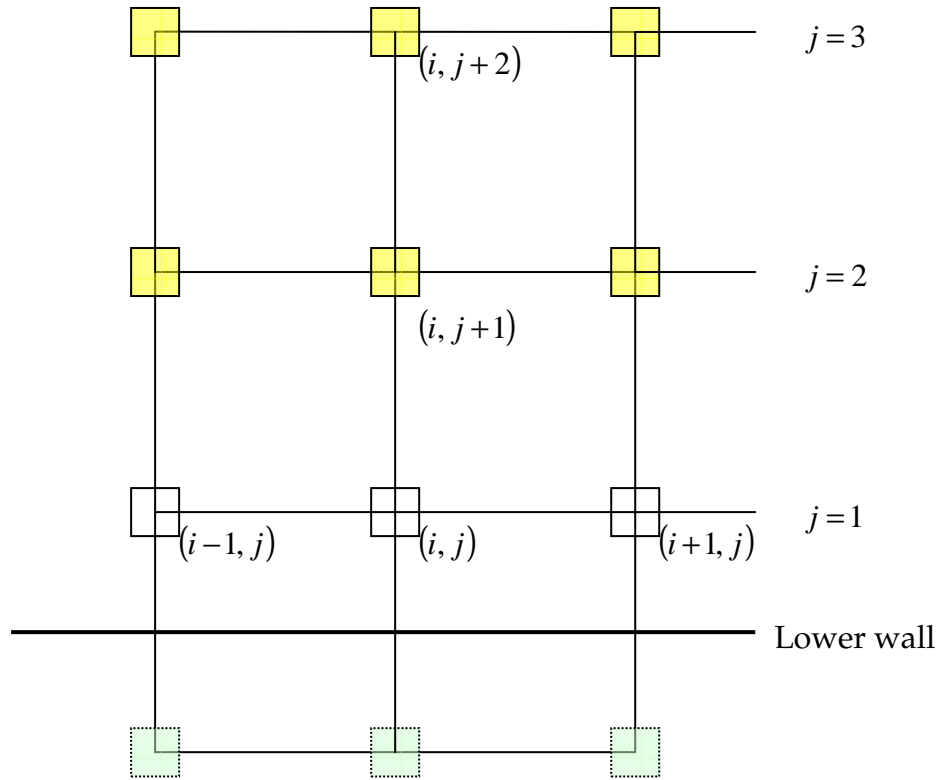


Fig. 2.5. Illustration of WBC implementation on a flat wall

Chapter III

Lattice Boltzmann Simulations and Validations

In the last chapter, the basic theory of LBM and the FE based lattice Boltzmann modeling of MPMC flows including wetting have been presented. In this chapter, the lattice Boltzmann simulation procedure is first detailed. After that, a few remarks are made on how it solves steady and unsteady flow problems, on its stability, and then on the issue of convergence. Subsequently, some prototypical problems are investigated by using some of the models introduced before in order to validate both the models and the corresponding codes. Finally the parallel implementation of LBM simulation and its performance are addressed.

3.1 Lattice Boltzmann simulation procedure

A full computation cycle of a typical simulation using FE2-LBM-B is given as follows,

(1) Collision:

$$f_i(\bar{x}, t^+) = [1 - (1/\tau_f)]f_i(\bar{x}, t) + (1/\tau_f)f_i^{eq}(\bar{x}, t) + \delta_i w_i \bar{e}_{i\alpha} (\mu \partial_\alpha \phi) / c_s^2,$$

$$g_i(\bar{x}, t^+) = [1 - (1/\tau_g)]g_i(\bar{x}, t) + (1/\tau_g)g_i^{eq}(\bar{x}, t);$$

(2) Applying BCs for f_i , g_i ;

(3) Streaming:

$$f_i(\bar{x} + \bar{e}_i \delta_t, t + \delta_t) = f_i(\bar{x}, t^+),$$

$$g_i(\bar{x} + \bar{e}_i \delta_t, t + \delta_t) = g_i(\bar{x}, t^+);$$

- (4) Calculating of macroscopic variables: ρ , u_α , ϕ , $\partial_\alpha\phi$, μ and specifying $\partial_\alpha\phi$ on the solid boundaries;
- (5) Calculating of equilibrium DFs: f_i^{eq} and g_i^{eq} ;
- (6) Check if a prescribed criterion is satisfied (e.g., reaching the given number of steps or a steady state). If it is satisfied, the computation is terminated; otherwise, go to step (1).

3.2 Some remarks on LBM simulations

Before the validations results are shown, some remarks are worth mentioning here.

3.2.1 On simulations of steady and unsteady flows

As mentioned in Subsection 2.1.3, when LBM is used to study steady flows, it is simply a special solver to obtain the converged solutions in space, and the intermediate solutions are not important. In these simulations, there are no intrinsic time scales for the system evolution. Hence, as discussed in Subsection 2.1.1.2, it usually only requires that the lattice sound speed should be chosen in such a way that the compressibility error is minimized and the efficiency is not too low at the same time. By contrast, unsteady flows have one or even many characteristic time scales. For instance, in the capillary wave problem studied later, there is a characteristic time scale, namely, the period for interface oscillation. In this type of simulations, LBM is required to resolve not only the spatial functions, but also their time evolutions. Thus, when choosing the lattice sound speed, one must bear in mind the additional requirement that the time step resulting from the choice should be considerably smaller than the minimum characteristic time scale. If the time step is too large, one may sacrifice the accuracy, and sometimes the computation may even blow up. Note

that here only the standard LBM is considered, in which the time step is tied to the grid spacing and the lattice sound speed. Of course, this is not necessarily required in general.

3.2.2 On the stability

The usual LBM are subject to a few stability requirements. According to Sterling & Chen (1996), there are certain conditions that are imposed on the relaxation parameter and the LBM Mach number for a stable computation.

First, the relaxation parameter (as given in Eq. (2.19)) must be greater than 0.5. In that limit, the viscosity tends to become zero. It is noted that the analysis by Sterling & Chen (1996) was based on a uniform mean flow. In the computations of more complex flows, the requirement is more stringent. In general, the simulation tends to become unstable when the viscosity becomes very low (even before reaching the limit of zero). Some other more sophisticated models using multiple relaxation times (MRT) (Lallemand & Luo 2000) may be able to reach lower limit of the viscosity than the single relaxation time model. But they are not used in this thesis because they are much more complicated and also due to the time limit. In fact, MRT models for MPMC fluid flows are developed just quite recently by McCracken & Abraham (2005) and by Premnath & Abraham (2007). The second condition requires that the maximum velocity (tied to the LBM Mach number) cannot go beyond certain limit. The specific value of this limit depends on other parameters, including the lattice model and the relaxation parameter (Sterling & Chen 1996). The typical values given by Sterling & Chen (1996) are larger than 0.3, which is often regarded as the limit of

the requirement by incompressibility approximation. In all simulations, the maximum velocity is much smaller than this value, thus this condition is well observed.

3.2.3 On the convergence

As mentioned earlier, when used for MPMC fluid systems, LBM may be viewed (though not strictly) as a special implementation of the DIM. Thus, the discussions on the convergence properties of the direct numerical solutions of the governing equations of DIM may apply for LBM as well. Jacqmin (1999) has pointed out that the convergence of numerical solutions of DIM equations to the corresponding sharp interface solutions depends on, in addition to the grid size δ_x , the interface thickness W , and the mobility M . It can be regarded as the combination of two convergence issues: (1) the convergence of the DIM equations to the sharp interface equations as both W and M approach zero; (2) the convergence of the discrete numerical solutions to the continuum solutions of the DIM equations. The second point is just the same as the usual numerical solutions. But the overall convergence property depends on both, and it is much more delicate than the second.

First, some discussions are provided on the first issue. As noted in Subsection 1.1.2, the Peclet number, $Pe = U_c L_c^2 / M \sigma$, is an additional parameter special to DIM. Besides, when the bulk FE in Chapter II is used, the interface thickness W may be analytically related to the coefficients in the chemical potential μ ; then the momentum and Cahn-Hilliard equations in dimensionless form can be rewritten explicitly as,

$$\partial_t \vec{u} + (\vec{u} \cdot \nabla) \vec{u} = -\nabla S + \text{Re}^{-1} \nabla^2 \vec{u} - (\text{Re} Ca)^{-1} \phi \nabla \{ Ch^{-1} [3\phi(\phi^2 - 1)] - Ch(3\nabla^2 \phi / 8) \} \quad (3.1)$$

$$\partial_t \phi + (\vec{u} \cdot \nabla) \phi = Pe^{-1} \nabla^2 \{ Ch^{-1} [3\phi(\phi^2 - 1)] - Ch(3\nabla^2 \phi/8) \} \quad (3.2)$$

where

$$Ch = W/L_c \quad (3.3)$$

is the Cahn number. Both W and M are relevant only in the interfacial region, and Ch and Pe determine how the “microscopic” length and dynamics of the interface compare with the macroscopic or mesoscopic ones. It may be more appropriate to look at the effects of Ch and Pe (which may be viewed as some kind of “dimensionless W and M ”). For fluid simulations at large scales, Ch should be as small as possible (ideally, $W \rightarrow 0$) and Pe should be as large as possible (ideally, $M \rightarrow 0$). In the above two limits, the forcing term in Eq. (3.1) becomes a singular one that mimics the surface tension force, and the RHS of Eq. (3.2) vanishes, making it a pure advection equation. At the same time, the rates for the two parameters to approach zero should be properly adjusted by considering the “micro-dynamics” inside the interfacial region and its interaction with the flow. This is a quite complex issue. More comprehensive analyses about it are given by Jacqmin (1999). Note that as mentioned in Chapter I, sometimes the Peclet number can be defined differently as (written in terms of the present symbols), $U_c L_c W / M \sigma$, which is related to the present one as $U_c L_c W / M \sigma = Pe Ch$. If that definition is adopted, then the RHS of Eq. (3.2) will take a different form as follows, $Pe^{-1} \nabla^2 [3\phi(\phi^2 - 1) - Ch^2(3\nabla^2 \phi/8)]$.

According to Jacqmin (1999), it is difficult to know how the solution error compares with the truncation error. The actual overall convergence property can be determined (probably solely) through numerical tests for individual problems.

It should be pointed out that the convergence of the numerical solutions only applies for the continuum approach, in which the systems are viewed as continuous fields. Even for normal fluid systems at macroscopic scale, it is often not economic to use a very fine mesh. In the simulations presented later, meshes of intermediate size are normally used to achieve a good balance between accuracy and efficiency (sometimes the accuracy may be compromised). When the system scales down to micrometer or even nanometer level, it may be no longer appropriate to reduce the grid size and interface thickness infinitely because they can be not-that-small as compared with the system size or some notable parts of the system (such as the grooves or pillars on rough surfaces). It is in the small scale systems that the continuum description meets the discrete molecular description.

Although the target macroscopic equations of LBM are the same as DIM, LBM contains some elements that are not present in DIM or different from DIM. That makes the convergence analysis even more complicated, especially for small scale flows. As pointed out by Sbragaglia et al. (2006), the continuum description of LBM is still unknown when strong surface fluctuations are present. Hence, the problems are especially challenging and many issues remain open, including the numerical convergence.

3.3 Validations for single phase flows

Next, simulation results of several typical problems are given for validation purposes. First, the MPMC codes are used to study some single phase incompressible flows to verify that they reduce to the simpler simulators when only one phase is present. Theoretically, single phase flows are special cases of MPMC flows. Thus, MPMC

models presented above should be able to simulate single phase flow problems. In fact, MPMC models include more factors in single phase flow simulations, for instance, the wetting property of the wall, which becomes more important as the systems scale down. But in the following, the wetting property is fixed to be neutral wetting so that the results can be compared with those obtained from pure single phase codes. The Couette, Poiseuille and driven cavity flows are simulated by the FE2-LBM-B, LDR-LBM and FE2-LBM-B respectively. In all these simulations, the initial order parameter fields were set to be uniform with $\phi = 1$ for FE2-LBM-B or $\phi = \phi^*$ for LDR-LBM.

3.3.1 Couette flows

The problem is depicted in Fig. 3.1. The upper wall at $y = y_u$ is moving constantly with U_u and the lower wall at $y = y_l$, U_l . The flow is independent of x . Hence the velocity field is simplified as

$$\vec{u} = u(y)\vec{i}_x, \quad (3.4)$$

and the full Navier-Stokes equations are simplified as

$$\frac{d^2u}{dy^2} = 0. \quad (3.5)$$

The boundary conditions are

$$u|_{y=y_l} = U_l, \quad u|_{y=y_u} = U_u. \quad (3.6a, b)$$

The velocity profile is a linear function of y ,

$$u(y) = U_l + \frac{U_u - U_l}{y_u - y_l}(y - y_l). \quad (3.7)$$

In the simulations (by the FE2-LBM-B model), a mesh of size 10×40 was used, and the upper and lower wall velocities were $U_u = 0.01$ and $U_l = -0.01$ respectively. Fig.

3.2 compares the velocity profile from simulation with that from Eq. (3.7). It is obvious that the numerical solution matches the analytical one.

3.3.2 Poiseuille flows

The basic setup for the Poiseuille flow study is almost the same as shown in Fig. 3.1. But now both the upper and lower walls are stationary and a uniform force field is applied in the x – direction,

$$\vec{g} = g\vec{i}_x. \quad (3.8)$$

For such a problem, the velocity profile is also a function of y . The simplified NSEs read,

$$\nu \frac{d^2 u}{dy^2} + g = 0. \quad (3.9)$$

The boundary conditions are

$$u|_{y=y_l} = 0, \quad u|_{y=y_u} = 0. \quad (3.10a, b)$$

Then, the analytical solution is found to be,

$$u(y) = \frac{g}{2\nu} (y_u - y)(y - y_l), \quad (3.11)$$

with the maximum velocity being,

$$u_{\max} = u\left(\frac{y_l + y_u}{2}\right) = \frac{g}{8\nu} (y_u - y_l)^2. \quad (3.12)$$

In the simulations (by the LDR-LBM model), a mesh of size 10×32 was used, the magnitude of the body force was $g = 10^{-5}$, and the kinematic viscosity, $\nu = 0.125$. Fig. 3.3 gives the comparison between the numerical and analytical solutions. It is easily found that they agree with each other.

3.3.3 Pressure driven flows in a 3D rectangular channel

The Couette and Poiseuille flows are the simplest two cases that have linear and parabolic velocity profiles respectively. Next a more complicated case is studied. It is the flow inside a 3D rectangular channel driven by a uniform pressure difference. The channel is infinitely long in x -direction, $2H_y$ wide in y -direction, and $2H_z$ high in z -direction. The pressure difference is in x -direction, and for simplicity, is modeled as a body force (its magnitude denoted as ρg). For this problem, there exists an analytical solution for the velocity profile in the $y-z$ plane (van der Graaf et al. 2006)

$$u(y, z) = \frac{(2H_z)^2 \rho g}{8\eta} \times \left[1 - \left(\frac{z - H_z}{H_z} \right)^2 + 4 \sum_{k=1}^{\infty} \frac{(-1)^k}{\alpha_k^3} \frac{\cosh(\alpha_k (y - H_y)/H_z)}{\cosh(\alpha_k H_y/H_z)} \cos(\alpha_k (z - H_z)/H_z) \right] \quad (3.13)$$

where $\alpha_k = \frac{2k-1}{2} \pi$ ($k=1,2,\dots$). Note that the coordinates y and z are in the following ranges: $0 < y < 2H_y$, $0 < z < 2H_z$. The terms of the infinite series decrease quickly as the index k increases, thus in calculation only the first five terms are kept. Since the solutions are independent of x , periodic boundary is used in this direction. The model is FE2-LBM-B. Figs. 3.4 (a & b) compare the velocity profiles along two center lines ($z = H_z$ and $y = H_y$) with the analytical solutions. The mesh is $3 \times 20 \times 40$, the pressure gradient, $\rho g = 10^{-6}$, and the viscosity, $\eta = 0.1$. Again, very good agreements between them were obtained.

3.3.4 Driven cavity flows

To test the ability of the codes to study even more complex single phase problems, the 2D driven cavity problem is chosen. The problem setup is shown in Fig. 3.5. The left, right and lower walls are stationary and the upper wall moves at a constant velocity U . For such a problem, no simplifications can be made on the NSEs.

A case with the Reynolds number $Re = 1000$ was studied by the FE2-LBM-B code with a mesh 128×128 , and another set of code using the vorticity-stream function formulation of the NSEs with a mesh 127×127 ⁷. To decide whether steady states are reached, the following criterion was used,

$$|\vec{u}|_{res} < \varepsilon \quad (3.14)$$

where ε is a small parameter (chosen to be 10^{-6} here), and the quantity $|\vec{u}|_{res}$ reflecting the change of the velocity field in two consecutive steps ($t = t^n, t^{n+1}$) is defined as,

$$|\vec{u}|_{res} = \frac{\sum_{i,j} \left| \|\vec{u}_{i,j}^{n+1}\| - \|\vec{u}_{i,j}^n\| \right|}{\sum_{i,j} \|\vec{u}_{i,j}^{n+1}\|} \quad (3.15)$$

with $|\vec{u}| = \sqrt{u^2 + v^2}$ being the module of the velocity. Fig. 3.6 compares the evolution of $|\vec{u}|_{res}$ by the two methods. It is seen that the vorticity-stream function formulation reaches the steady state faster and takes less computation time than LBM. As mentioned in Chapter I, this problem with LBM may be somewhat alleviated when a smaller sound speed is chosen. Once the steady state is reached, the two methods provide very close results as shown in Fig. 3.7 which compares the velocity profiles

⁷ On each time step, the discrete Fourier transforms were used as a solver; thus, no iteration was needed.

along the central horizontal and vertical lines respectively. Note that in Fig. 3.7 the spatial coordinates are scaled by the side length.

3.4 Validations for MPMC flows

In the above, a few validation cases were provided for single phase flow problems and good comparisons with either the analytical solutions or the numerical solutions by other methods have been obtained. Now some more cases will be investigated in the MPMC framework. They include:

- (1) the Laplace law verification for a stationary droplet,
- (2) the surface layers near hydrophilic and hydrophobic walls,
- (3) the study of static CAs,
- (4) the capillary waves,
- (5) a droplet in a shear flow.

Note that in the first three cases, the systems are stationary, and in the other two, flows are present.

3.4.1 Laplace's law verification

The verification of Laplace law for a stationary droplet or bubble is a basic and the mostly used validation case for MPMC fluid systems. The Laplace law has already been given in Eq. (2.83). Here only some results are presented. The initial setup is simple: in the center of a square domain, there is a circular droplet. The parameters for the simulations are given in Table 3.1, and Fig. 3.8 shows the evolution of the deviation in surface tension, $\Delta\sigma/\sigma$, where $\Delta\sigma = \sigma_{num} - \sigma$ is the absolute deviation (with σ_{num} being the numerical surface tension calculated from Eq. (2.83)). The specific model is FE2-LBM-B.

From Fig. 3.8, it is seen that the relative deviation was -100% at the beginning. This is because the order parameter field was initialized by Eq. (2.81), thus

$$\phi_{in} \approx 1, \phi_{out} \approx -1 \quad (3.16)$$

which lead to a negligible pressure difference and thus $\sigma_{num} = 0$. During the numerical evolution, the order parameter field is relaxed toward the equilibrium state in which the order parameters satisfy the condition given by Eq. (2.83). Note that the inside and outside order parameters were sampled at the droplet center and some point that is $R_d + 2W$ away from the center respectively, thus both are safely outside the interfacial region. The evolutions of the maximum and minimum values of ϕ are plotted in Figs. 3.9 (a & b) respectively, and the profiles along the center horizontal line $y = y_{mid}$ at the beginning and the end are shown in Fig. 3.10. From these figures, some fundamental features of DIM mentioned before are clearly reflected.

3.4.2 Surface layers near hydrophilic and hydrophobic walls

When the wall is not neutral wetting ($\tilde{\omega} \neq 0$), the density or order parameter at the wall, ρ_σ or ϕ_σ , is different from the value in the bulk region. This means that, even if only one fluid phase or component is present, there is a near-wall transition layer developed for hydrophilic and hydrophobic walls. Such a layer is the interface between the fluid phase and the solid phase, and it also has a thickness of several grid points (similar to W). For a suitably given $\tilde{\omega}$ and a certain bulk fluid, there exists analytical solutions for this surface layer. For example, when the bulk fluid (infinitely far away from the wall) corresponds to $\phi = 1$ and the parameter $\tilde{\omega}$ is negative, the analytical solution is

$$\phi = \tanh\left\{\left(2x/W\right) + \tanh^{-1}(\phi_\sigma)\right\} \quad (3.17)$$

with the order parameter at the wall given by

$$\phi_\sigma = \phi_3 = \sqrt{1 - |\tilde{\omega}|}. \quad (3.18)$$

Note that the above results may be obtained in a way similar to that in deriving Eqs. (2.57) and (2.118) during which Eq. (2.54) and (2.55) are used. More details are found in (Papatzacos 2002) and the analogy between FE1 and FE2 is reflected through Eqs. (2.66-73). In what follows, simulation results of this example are compared with the analytical solutions for the FE2-LBM-B model. The problem is actually one-dimensional but here the two-dimensional model (specifically, D2Q9) is used with only three grid points in the other side (along y -direction). The parameter that determines the wettability is $\tilde{\omega} = -0.334933$, which would correspond to a CA $\theta = 120^\circ$ if both components are present. On the wall with given wettability, the way previously described is used to enforce the wetting condition; on the other side, to mimic the situation infinitely far away, the following conditions are imposed,

$$\phi|_\infty = 1, \nabla\phi|_\infty = 0, \nabla^2\phi|_\infty = 0; \quad (3.19a, b, c)$$

$$\rho|_\infty = 1, \vec{u}|_\infty = 0; \quad (3.20a, b)$$

$$f_i|_\infty = f_i^{eq}|_\infty, g_i|_\infty = g_i^{eq}|_\infty; \quad (3.21a, b)$$

for the order parameter field, the hydrodynamic field and the DFs respectively, where the equilibrium DFs are calculated using the given macroscopic conditions. Figs. 3.11 (a & b) compare the LBM results with the analytical ones for $W = 3$ and $W = 9$ respectively. It is found that the numerical solutions agree with the analytical ones fairly well and the agreement becomes better as the interface thickness increases. Similarly, in Figs. 3.12 (a & b), comparisons for the hydrophilic case $\tilde{\omega} = 0.334933$ ($\theta = 60^\circ$) are shown. As mentioned earlier, in many simulations the interface should be made as thin (compared to the characteristic length scale) as possible, thus it is not

practicable to use an interface as thick as spanning nine grid points. Fortunately, an interface with $W = 3$ appears to be already sufficiently thick.

3.4.3 Static CA study

As given by Eq. (2.123), when two phases or components are near the solid wall, the CA is related to the parameter $\tilde{\omega}$. Both FE2-LBM-B and LDR-LBM have been validated for this problem. Here the results for LDR-LBM are given. The initial condition is a semicircular stationary droplet sitting along the center line on the lower wall. The upper wall is neutral wetting, and on the left and right sides periodic boundaries are assumed. After the system reaches its equilibrium state, the droplet takes an arc shape (for example, see Fig. 3.13). For convenience, R_x is used to denote half of the distance between the two three-phase points on the lower wall and H_y denotes the height of the droplet. Then, the CA θ can be calculated using R_x and H_y as,

$$\theta = \pi - \cos^{-1} \left(\frac{1 - k_r^2}{1 + k_r^2} \right) \quad (3.22)$$

with $k_r = R_x/H_y$. In the above formula, θ is expressed in radian. Quite a number of tests have been done in the range $[15^0, 165^0]$ and with an spacing of 15^0 . The initial droplet radius is 25. The mesh is 101×50 for the cases with θ in the range $[45^0, 135^0]$, and 201×80 for the other cases. The comparisons of the CAs calculated by Eq. (3.22) using the numerically measured R_x and H_y with the theoretical values calculated from Eq. (2.123) are given in Fig. 3.14. It is seen that all of them are in good agreements (the deviation $\Delta\theta < 3^0$) with each other except for $\theta = 15^0$ and 165^0 .

The reason for the deviations may be that when the CA is closer to 0° or 180° , it becomes more difficult to resolve the details in the interfacial region.

3.4.4 Capillary wave study

Next, a benchmark problem for dynamic MPMC fluid systems - the capillary wave generated by perturbing a flat interface - is studied. The problem is shown in Fig. 3.15. The distances from the upper and lower walls to the unperturbed fluid interface are both H and the width of the domain is λ . For simplicity, the upper and lower fluids are assumed to have the same density and viscosity. At the beginning ($t = 0$), a sinusoidal perturbation is applied as,

$$h(x) = A_p \sin(kx) \quad (3.23)$$

where $k = 2\pi/\lambda$ is the wavenumber and A_p is the amplitude (being small). When H is much larger than λ and the fluids are both inviscid, the frequency ω_0 of the interface oscillation can be obtained as,

$$\omega_0 = \sqrt{\sigma k^3 / (2\rho)} \quad (3.24)$$

When the fluids are slightly viscous, the oscillation will be damped. Under some conditions, an approximate analytical solution can be obtained for the displacement a_{cw} scaled by the initial (maximum) value as (note here only the simplified solution for equal density fluids is given and more general solutions can be found in the work by Kim (2005)),

$$a_{cw}(t') = \sum_{i=1}^4 \frac{z_i \omega_0^2}{Z_i (z_i^2 - \bar{\varepsilon} \omega_0)} \exp\left[\frac{(z_i^2 - \bar{\varepsilon} \omega_0) t'}{\omega_0}\right] \operatorname{erfc}\left(z_i \sqrt{\frac{t'}{\omega_0}}\right) \quad (3.25)$$

where

$$t' = \omega_0 t, \quad \bar{\varepsilon} = \nu k^2 / \omega_0 \quad (3.26)$$

are the scaled time and dimensionless viscosity, z_i are the four roots of the algebraic equation,

$$z^4 - \sqrt{\bar{\varepsilon}\omega_0} z^3 - \bar{\varepsilon}\omega_0 z^2 + (\sqrt{\bar{\varepsilon}\omega_0})^3 z + \omega_0^2 = 0 \quad (3.27)$$

and

$$Z_1 = (z_2 - z_1)(z_3 - z_1)(z_4 - z_1), \quad Z_2 = (z_3 - z_2)(z_4 - z_2)(z_1 - z_2), \quad (3.28a, b)$$

$$Z_3 = (z_4 - z_3)(z_1 - z_3)(z_2 - z_3), \quad Z_4 = (z_1 - z_4)(z_2 - z_4)(z_3 - z_4), \quad (3.28c, d)$$

During the computation, the interface position (defined as the point where $\phi = 0$) along the vertical line $x = \lambda/4$ was monitored. To determine the position accurately, linear interpolation scheme was used. Fig. 3.16 compares the analytical results with the numerically captured interface evolutions using (1) a mesh 128^2 with $W = 5$, $\tilde{M} = 10$; (2) a mesh 256^2 with $W = 5$, $\tilde{M} = 20$; (3) a mesh 512^2 with $W = 6$, $\tilde{M} = 20$. It is seen that initially (for the first half period) all the numerical solutions agree with the analytical one very well, and the deviations become larger as time increases. Note that this trend was also observed by Kim (2005) when the NSCH equations were directly solved. According to Kim (2005) and references therein, the error between the numerical and analytical results is affected by the ratio δ_x/A_p (i.e., the ratio between the mesh size and the wave amplitude). As time increases, the amplitude of the wave becomes smaller and it becomes more difficult to resolve the interface positions accurately. The results on finer meshes seem to be better.

3.4.5 Droplet in a shear flow

Finally, a 3D droplet between two parallel moving walls is studied. More details about this problem can be found in the work by van der Graaf et al. (2006). The initial condition is shown in Fig. 3.17. The droplet radius is R . The upper and lower walls,

separated by a distance H , are moving at U_u and U_l respectively. This induces a shear flow between them and the shear rate $\dot{\gamma}$ is given by,

$$\dot{\gamma} = (U_u - U_l)/H \quad (3.29)$$

Then the Capillary number for this problem is specifically defined as,

$$Ca = \eta\dot{\gamma}R/\sigma \quad (3.30)$$

The shearing causes the droplet to deform. When Ca is small, the droplet can reach a steady state in which it takes an elliptic shape. Suppose the major axis of the ellipse is R_L and the minor, R_B , then the deformation parameter D_f is calculated by,

$$D_f = (R_L - R_B)/(R_L + R_B) \quad (3.31)$$

Under very low Ca in an unbounded shear flow, there exists a theoretical relation between the deformation parameter and the Capillary number (see the work by van der Graaf et al. (2006) and references therein),

$$D_f = 35Ca/32 \quad (3.32)$$

Note that the relation given here is for the special cases in which the two fluids have the same viscosity. A series of simulations for Ca in $[0.05, 0.3]$ with a spacing 0.05 have been performed using the FE2-LBM-B model. The mesh is $80 \times 40 \times 40$ (same as one of the test series by van der Graaf et al. (2006)), and the droplet radius is 10. The deformation parameter was manually measured using the image tools in GIMP⁸ after the order parameter field reaches steady. The results are shown in Fig. 3.18. For comparison, the theoretic results from Eq. (3.32) and those by van der Graaf et al. (2006) are also plotted. Note that both simulation results differ from the theoretical ones, probably because the assumption that the two shearing walls are infinitely far away is not satisfied and the boundary walls have non-negligible effects on the flow.

⁸ <http://www.gimp.org>

But it is seen that the present results agree well with those by van der Graaf et al. (2006) when Ca is small (e.g., in $[0.05,0.2]$). For larger Ca , D_f obtained by the present simulation increases faster. Considering that there exists a critical Ca (about 0.4 as given by van der Graaf et al. (2006)) under which the droplet breaks up, one may tend to postulate that the $D_f - Ca$ relation becomes nonlinear for large Ca . From this point of view, the present results seem to reflect such a transition better. It is noted that in the present work, the data was extracted when the change in the order parameter field became sufficiently small whereas in the work by van der Graaf et al. (2006) the data was extracted after certain number of steps. Differences between the two sets of simulations may also be due to that not all the parameters (e.g., the Cahn number and the Peclet number) match exactly. But the above evidences should be sufficient to verify that the present model and code work well for this problem.

3.4.6 Test of convergence

In the above study of capillary wave, some results on different meshes have been presented. To further investigate the convergence issue, a droplet spreading on hydrophilic surfaces was studied using FE2-LBM-B model. Initially there is a semicircular droplet (with CA 90° ; see Fig. 3.19) sitting on a hydrophilic substrate with equilibrium CA 15° . The droplet tends to spread on this substrate towards its equilibrium state. Three different meshes with increasing resolutions, 200×100 , 400×200 , and 800×400 , were used to calculate this problem. The nominal interface thickness W and mobility \tilde{M} remain the same ($W = 3$ and $\tilde{M} = 10$). Fig. 3.20 compares the contour of the order parameter field in the range $[-0.8,0.8]$ with neighbouring lines separated by $\Delta\phi = 0.2$ for the three test cases. It is obvious that on

a finer mesh the interface apparently become thinner, and it is seen that the interfacial regions on the finer meshes almost fall within those on the coarse meshes, indicating a good convergence property. In addition, the velocity vectors for the three cases are shown in Fig. 3.21. It is found that the flow fields on different meshes look almost the same as well. It is noted that in the above figures the time and space have been properly rescaled so that the comparisons are made at the same time and on the same coordinate.

3.5 Parallel implementation and performance

The underlying theories of LBM have been introduced in the above. In this subsection, a practical issue, the parallel implementation and performance of LBM, will be addressed. LBM is very suitable for parallel computation, and its implementation is relatively simple due to the intrinsic properties of the collision and streaming procedures (Succi 2001). Through numerical tests, LBM has been found to be able to achieve very nice speedup, especially for some 3D problems.

3.5.1 Parallel implementation of LBM simulations

The parallel implementation of LBM uses the domain decomposition strategy. It is illustrated in Fig. 3.22 for a division in the x -direction. After the whole domain is divided into several subdomains, the LBM procedures are carried out in each subdomain, but the distribution functions (and the order parameter for MPMC fluids) from neighbouring subdomains are required as boundary conditions at each time step. The exchange of the information is realized using the Message Passing Interface (MPI) library⁹ (available for both C and FORTRAN).

⁹ <http://www-unix.mcs.anl.gov/mpi>

3.5.2 Performance of parallel LBM codes

Like in most parallel computations, the performance of a parallel LBM code depends on the ratio of the computation time over the communication time, T_{comp}/T_{comm} , which is related to a number of factors including the numerical algorithm and problem geometry. As compared with serial computations, the communication time is additional. Larger T_{comp}/T_{comm} means smaller percentage of the communication time, and the speedup becomes better. The above division in the x -direction is most suitable for a problem with large aspect ratios ($L_x/L_y \gg 1$, and $L_x/L_z \gg 1$). For a given problem using the above decompositions, when the number of subdomains (of equal size) increases, the size of each subdomain decreases which reduces the computation time. Then, the ideal speedup becomes difficult to reach. Thus, for each individual problem with a specific decomposition, there is an optimal number of subdomains. Fig. 3.23 gives an example for the variation of computation time with the number of subdomains in the simulation of a 3D droplet by FE2-LBM-B. Note that in the simulations using the parallel codes, the optimal number of nodes was first determined by running the specific simulation for a relatively short time (e.g., 1000 time steps). Then, it was picked for the complete simulation.

3.6 Summary

To summarize, the details of LBM simulation and implementation have been described and they are verified through comparisons with analytical results or other simulation work for a number of problems. Some other key issues, such as stability and convergence, have also been briefly addressed.

Table 3.1. Parameters for simulation in Laplace law verification

Parameter	Value
Domain side length	65
Surface Tension	0.001
Interface Width	3
Kinematic Viscosity	0.01
Mobility	10
Initial droplet radius	16

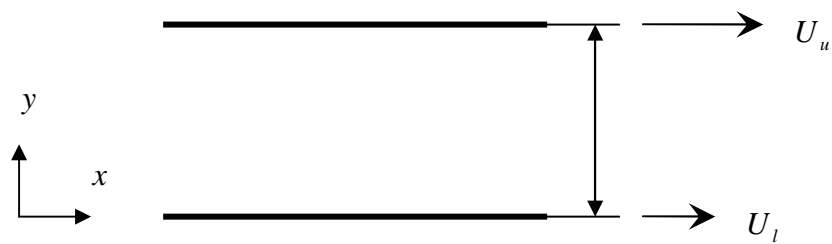


Fig. 3.1. Illustration of the Couette flow

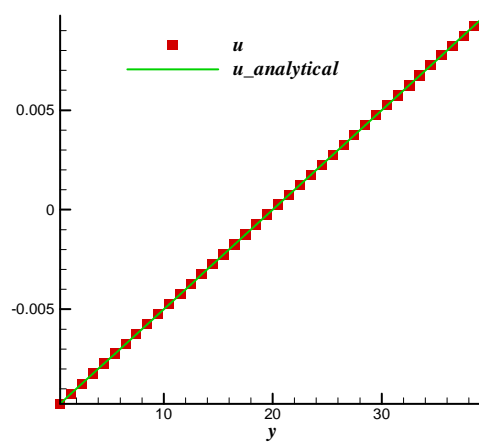


Fig. 3.2. Comparison of Couette flow velocity profile (numerical: symbol; analytical: line)

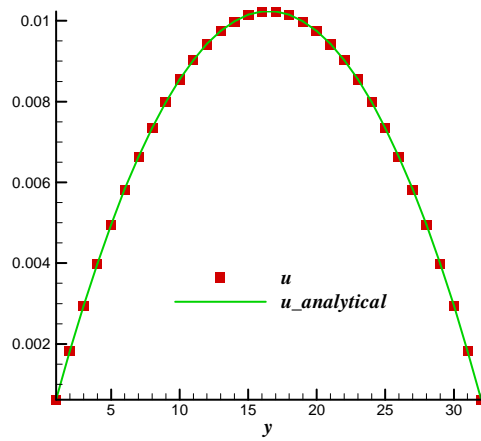


Fig. 3.3. Comparison of Poiseuille flow velocity profile (numerical: symbol; analytical: line)

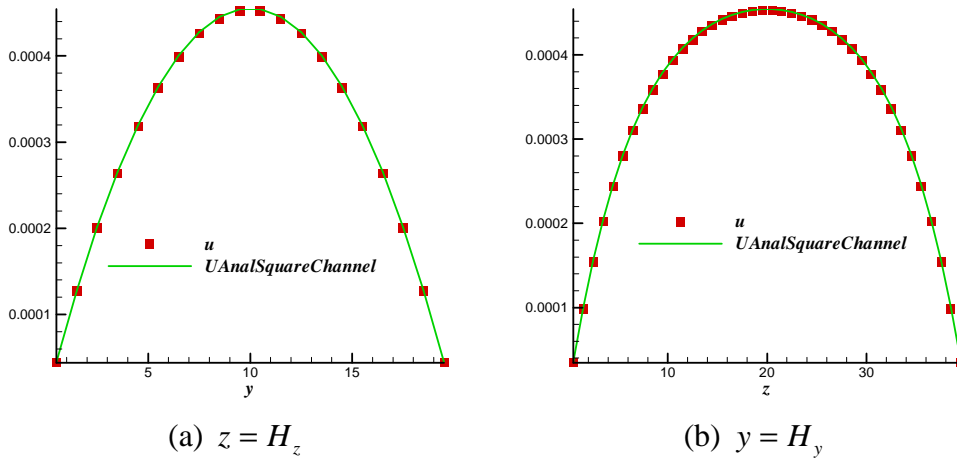


Fig. 3.4. Comparison of velocity profiles along two center lines ($z = H_z$ and $y = H_y$) for flows in a 3D rectangular channel (numerical: symbol; analytical: line)

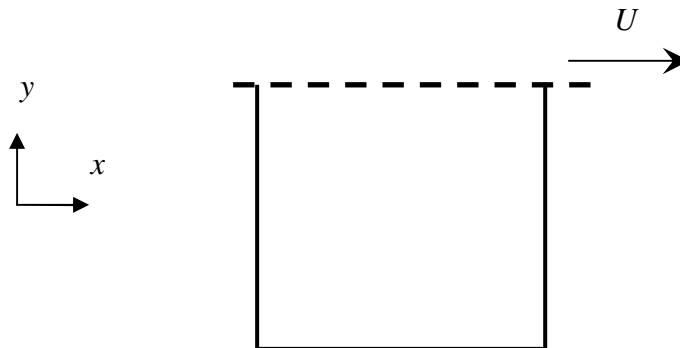


Fig. 3.5. Illustration of the driven cavity flow

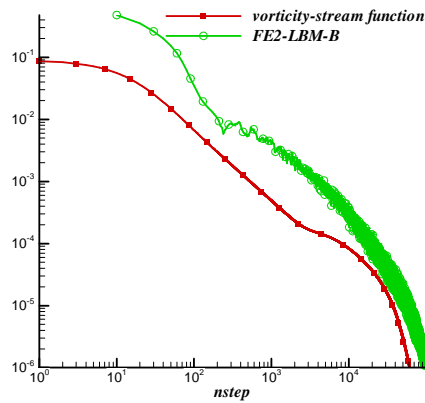


Fig. 3.6. Comparison of the convergence history (the evolution of $|\vec{u}|_{res}$) (LBM v.s. the vorticity-stream function formulation)

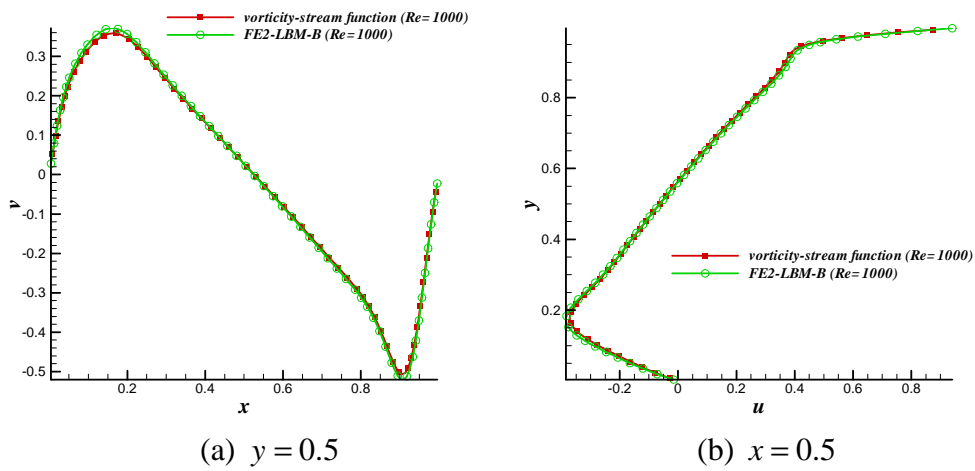


Fig. 3.7. Comparison of velocity profiles along the two center lines, $y=0.5$ and $x=0.5$, for the driven cavity flow (LBM v.s. vorticity-stream function formulation)

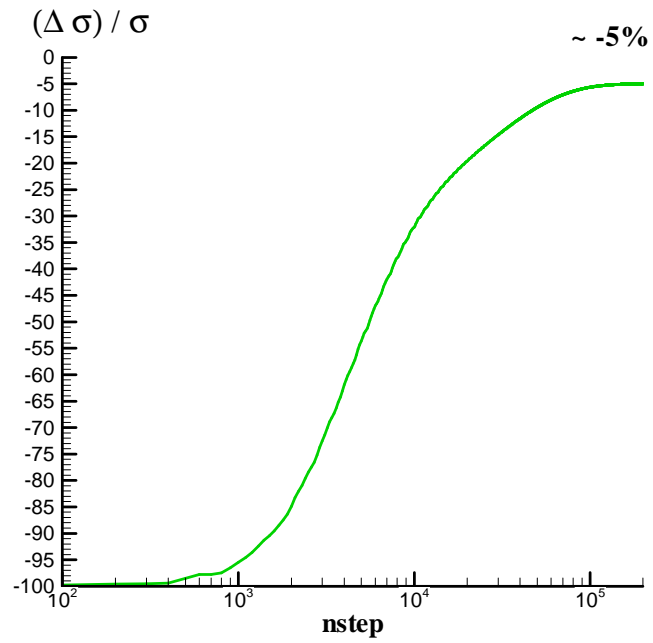


Fig. 3.8. Evolution of the deviation in surface tension for a stationary droplet

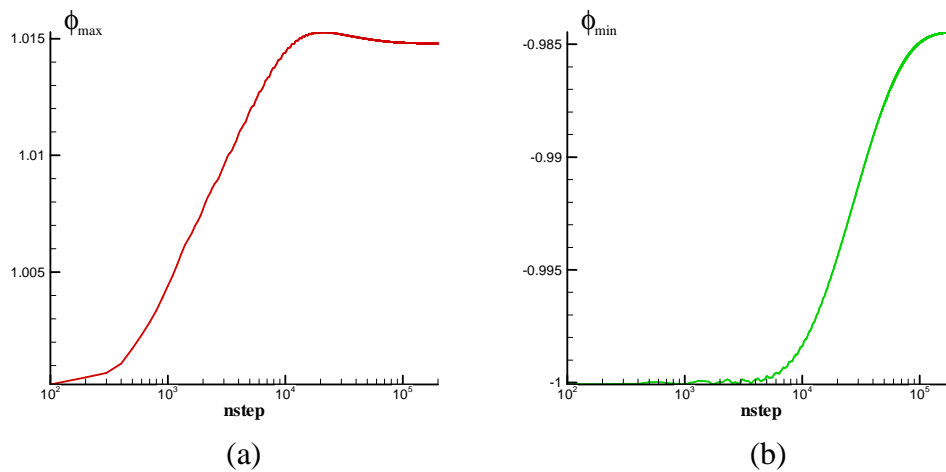


Fig. 3.9. Evolution of the maximum and minimum values of the order parameter

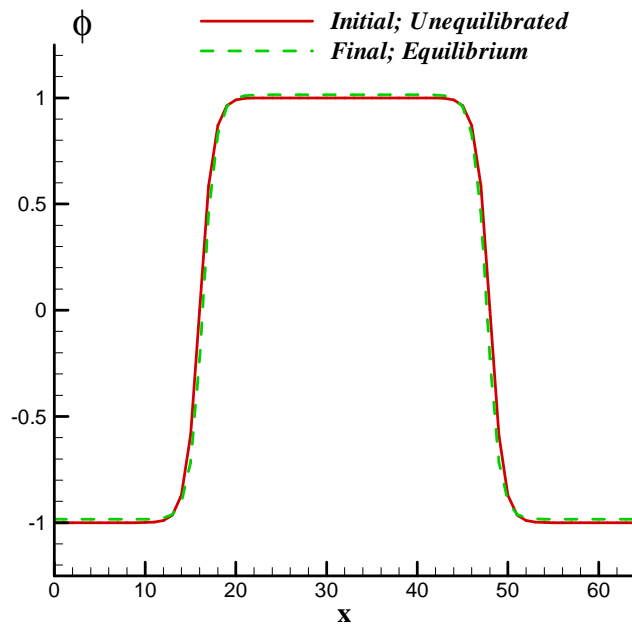


Fig. 3.10. The center order parameter profiles before and after the equilibration

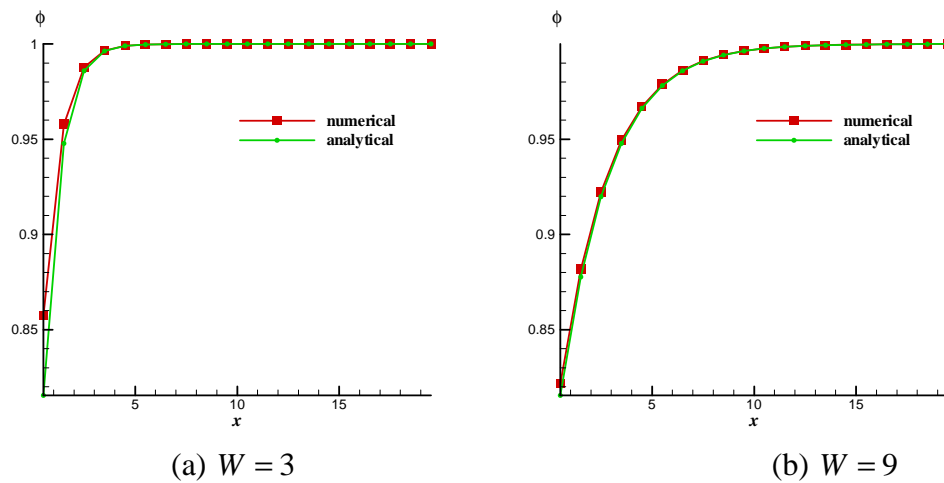


Fig. 3.11. Comparison of order parameter profiles for the surface layers near a hydrophobic wall

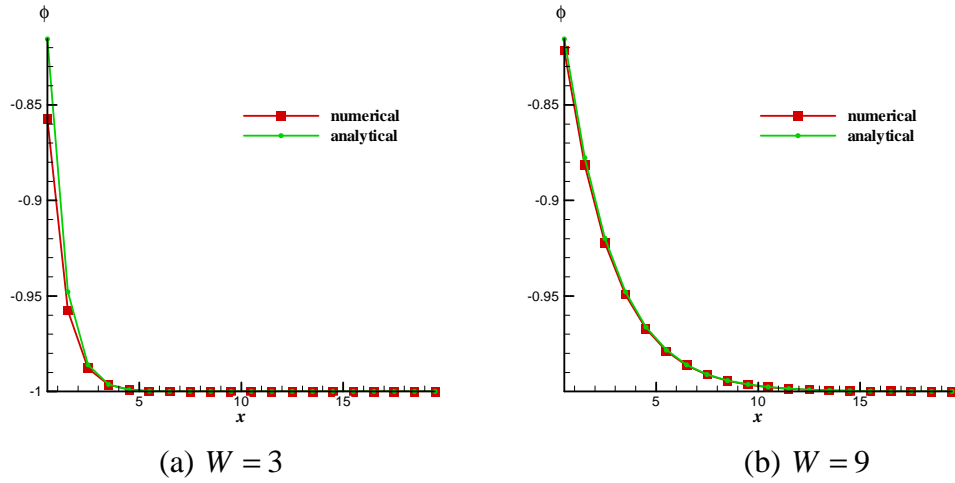


Fig. 3.12. Comparison of order parameter profiles for the surface layers near a hydrophilic wall

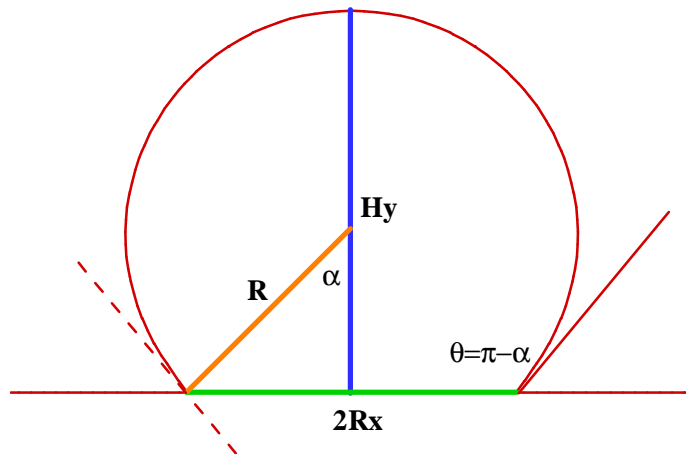


Fig. 3.13. Illustration on the calculation of θ from R_x and H_y

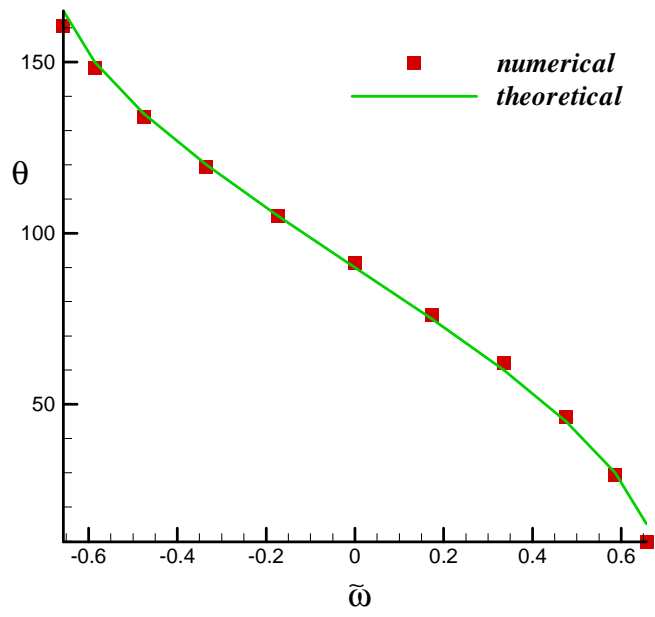


Fig. 3.14. Static CA validation (numerical v.s. theoretical)

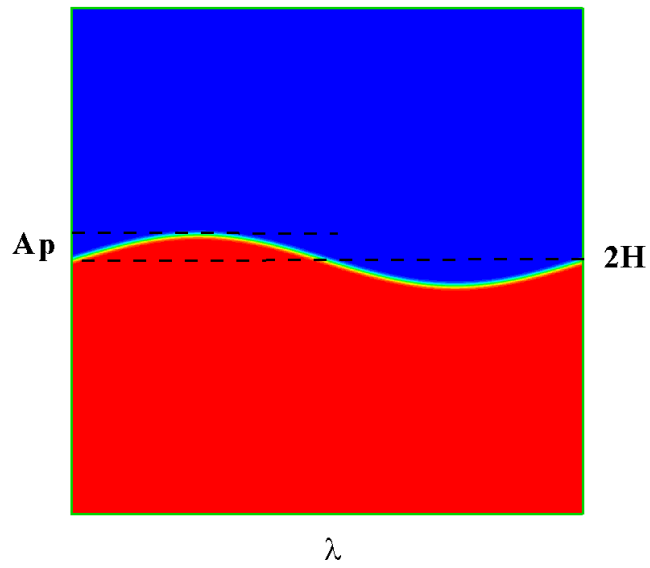


Fig. 3.15. Problem setup for capillary wave study

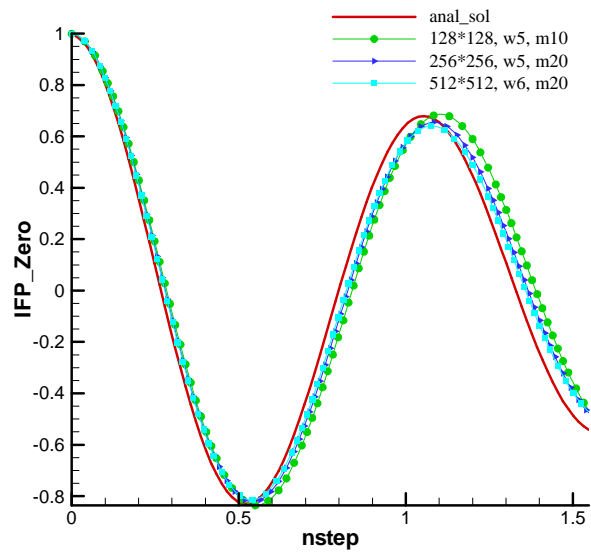


Fig. 3.16. Comparison of the interface position evolution for a capillary wave by three different simulations and the analytical solution

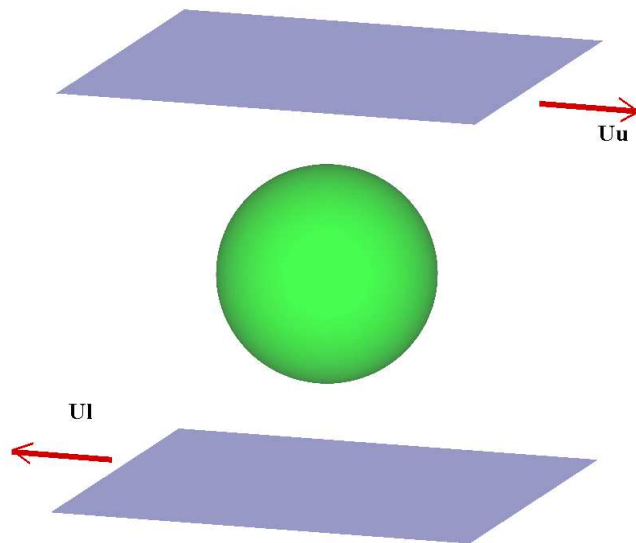


Fig. 3.17. Illustration of the droplet in a shear flow

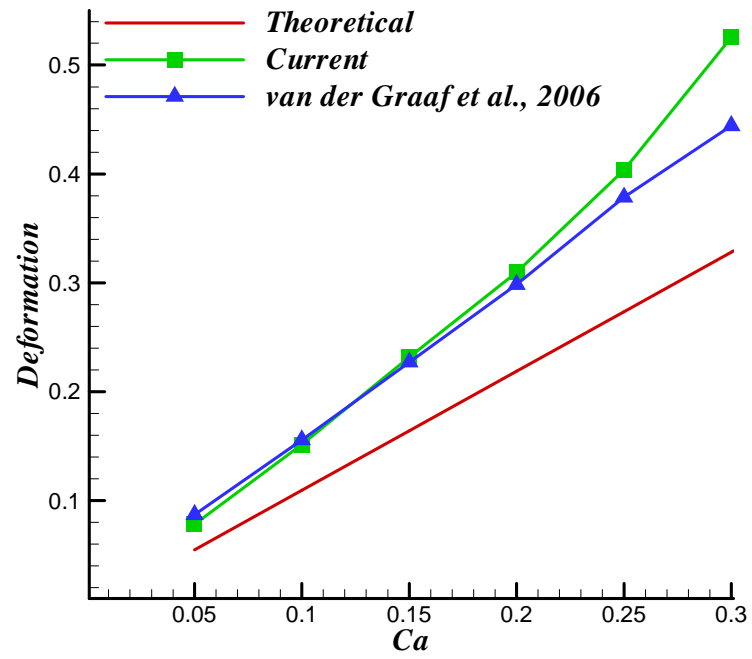


Fig. 3.18. Comparison of the variation of the deformation parameter with the capillary number for a sheared droplet

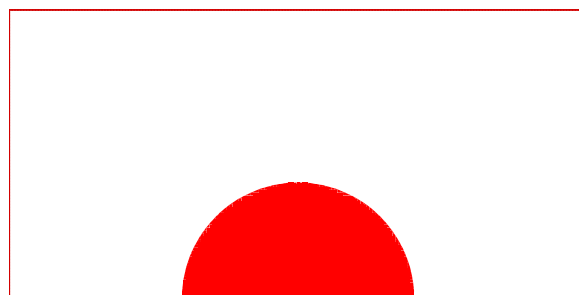


Fig. 3.19. Initial condition in the convergence test for droplet spreading

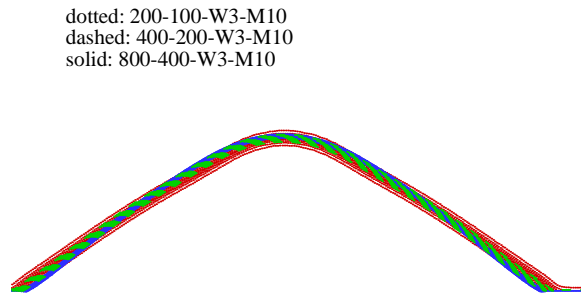


Fig. 3.20. Comparison of the interface regions for three simulations of droplet spreading with different mesh sizes

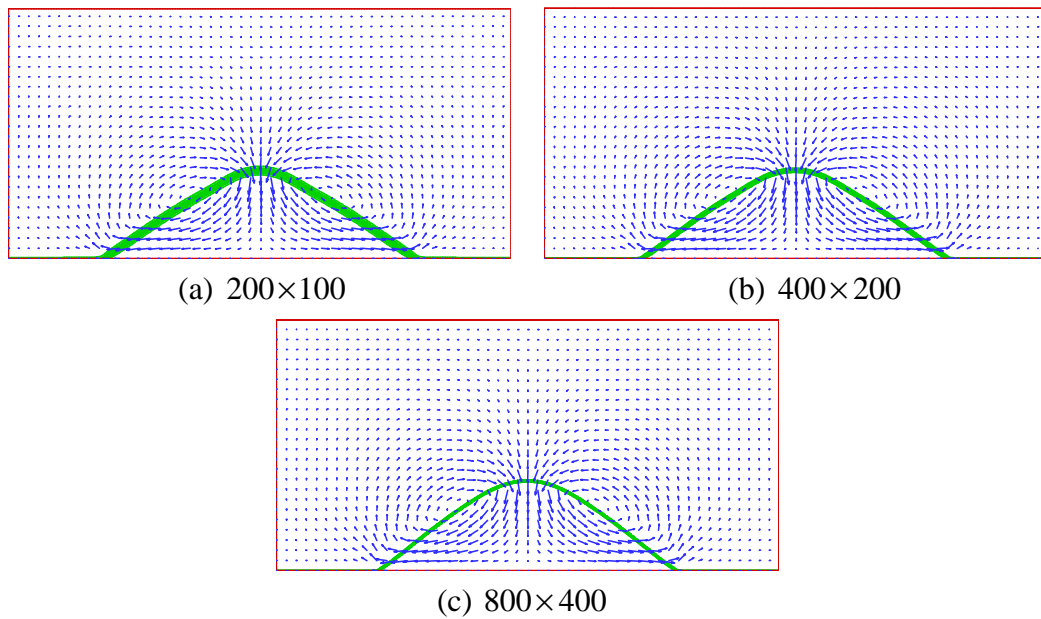


Fig. 3.21. Comparison of the flow fields for three simulations of droplet spreading with different mesh sizes

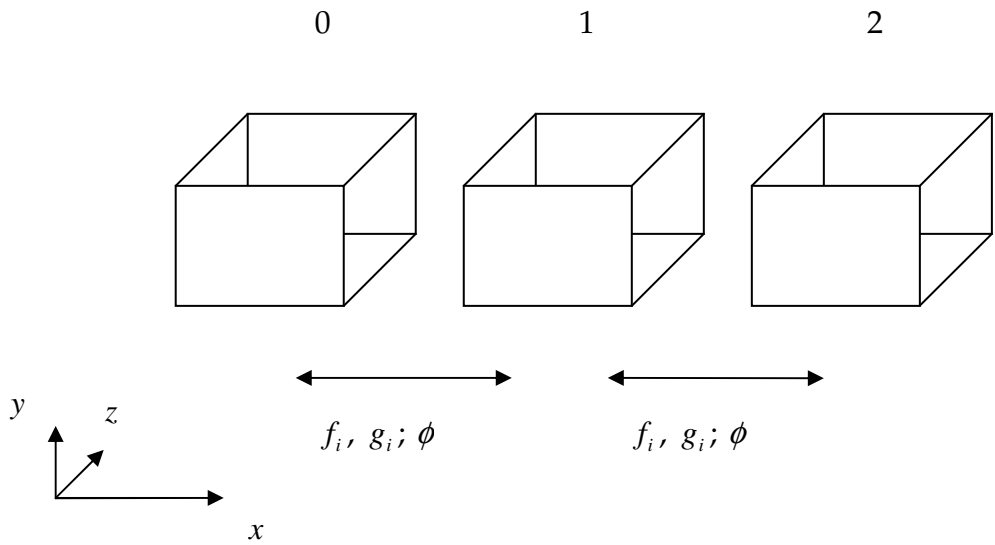


Fig. 3.22. Illustration of domain decomposition along horizontal direction for the parallel implementation of LBM

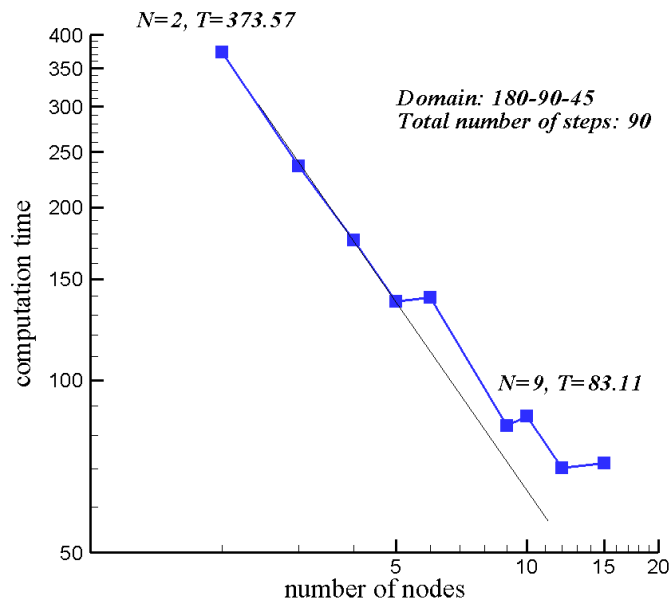


Fig. 3.23. Variation of the computational time with the number of nodes used for the evaluation of a parallel LBM code

Chapter IV

Investigation of MPMC Flows near Rough Walls¹⁰

In the last chapter, many benchmark problems have been studied with the lattice Boltzmann models used in this thesis (specifically, FE2-LBM-B and LDR-LBM). Those results have confirmed that the models and codes can perform reasonably well. In this chapter, the LDR-LBM model will be used to investigate primarily the effects of surface roughness and wettability on the flows. This work was initially inspired by the interesting phenomenon called *Lotus Effect*.

4.1 The *Lotus Effect*

In recent years more and more researchers become interested in the *Lotus Effect* (Barthlott & Neinhuis 1997, Patankar 2004, Marmur 2004, Furstner et al. 2005). Water droplets on surfaces with Lotus Effect show very high CAs, and they are easy to roll off and experience small hysteresis (Barthlott & Neinhuis 1997). Some preliminary studies have found that, besides the interfacial and wetting properties, the micro- and nano-scale structures on lotus leaves may be essential for this intriguing phenomenon (Patanekar 2004). This justifies the topography of the wall to be another important factor.

¹⁰ Materials in this chapter have been published in

[1] Y. T. Chew, J. J. Huang, C. Shu and H. W. Zheng. Proceedings of “Enhancement and Promotion of Computational Methods in Engineering and Science X” (2006).

[2] J. J. Huang, C. Shu, Y. T. Chew and H. W. Zheng. International Journal of Modern Physics C, 18 (4), pp. 492-500 (2007).

[3] J. J. Huang, C. Shu and Y. T. Chew. Physics of Fluids 21, pp. 022103 (2009).

It has been reported that roughness may apparently increase the hydrophobicity or hydrophilicity of the surface. Considerable efforts have been spent on fabricating and investigating superhydrophobic surfaces with certain small scale structures such as pillar arrays (Yoshimitsu et al. 2002, Jopp et al. 2004, He et al. 2004). The Cassie-Baxter's theory (Cassie & Baxter 1944) and Wenzel's theory (Wenzel 1949) are two well known theories which may explain the superhydrophobicity of such textured surfaces for droplets filling in or suspended on these structures respectively (though their validity is still questionable). It is noted that most of previous studies on this kind of problem were presented in the surface chemistry community, and they focused mainly on the measurements of static CAs, receding and advancing angles, and in the theoretical aspect, on calculations of apparent CA through minimization of the system FE under certain static configurations (Johnson & Dettre 1964, Eick et al. 1975, Patankar 2003, McHale et al. 2004a). For the effects of roughness on hydrophilic surfaces, it has been observed by McHale et al. (2004b) that drop spreading was greatly enhanced on rough hydrophilic surfaces and these surfaces may be called *superhydrophilic* as well. Regarding lotus leaves, it has been generally believed that they are intrinsically hydrophobic and the small scale roughness further increases their hydrophobicity. However, some other researchers recently proposed that in contradiction to previous perceptions, the raw materials of lotus leaves are hydrophilic (Cheng & Rodak 2005). The underlying physics might be the so-called "roughness-induced non-wetting" (that is, the apparent hydrophobicity is due to the small structures) (Herminghaus 2000).

In order to obtain a comprehensive understanding of these surfaces and possibly resolve the conflicting issues, it would be desirable to study the flows over surfaces

with different wettabilities and small structures, besides measuring some static and (limited) dynamic quantities. In this chapter, both 2D and 3D studies of droplet motions on rough surfaces (with rectangular grooves in 2D and square pillars in 3D) having different wettabilities are reported. Before the results are given, the issue on how to implement the wetting boundary condition (WBC) on such surfaces is first addressed.

4.2 WBC on *rough* surfaces

When the surface is not smooth, the WBC needs to be modified, specifically on the corner points where singularities of the surface curvature occur. Here only boundary nodes at the intersection of two perpendicular lines, encountered in 2D grooved channels, are discussed in detail (e.g., see Fig. 4.1). Note that the situations for similar nodes in 3D surfaces with pillars are much more complicated and are not illustrated here. The way to deal with them is through a simple *coordinate transformation*. That is, it is imagined that there virtually exist inclined planes (the dashed lines in Fig. 4.1) as a transition between the horizontal and vertical planes. On the transitional nodes, the normal and tangential gradients of the density are first evaluated in the inclined coordinate system (t, n) , and then transformed into the usual coordinate system (x, y) ; the Laplacian is just evaluated in (t, n) . The transformation of the derivatives between the (x, y) and (t, n) coordinates can be written as

$$\begin{bmatrix} \frac{\partial}{\partial x} \\ \frac{\partial}{\partial y} \end{bmatrix} = \begin{bmatrix} \frac{\partial t}{\partial x} & \frac{\partial n}{\partial x} \\ \frac{\partial t}{\partial y} & \frac{\partial n}{\partial y} \end{bmatrix} \begin{bmatrix} \frac{\partial}{\partial t} \\ \frac{\partial}{\partial n} \end{bmatrix} \quad (4.1)$$

For the upper corner points in Fig. 4.1, the relation between the two coordinate systems can be written as,

$$\begin{bmatrix} \vec{i}_t \\ \vec{j}_n \end{bmatrix} = \begin{bmatrix} \cos(-45^\circ) & \sin(-45^\circ) \\ \cos 45^\circ & \sin 45^\circ \end{bmatrix} \begin{bmatrix} \vec{i}_x \\ \vec{j}_y \end{bmatrix} \quad (4.2)$$

then the transformation matrix can be explicitly written as,

$$\begin{bmatrix} \frac{\partial t}{\partial x} & \frac{\partial n}{\partial x} \\ \frac{\partial t}{\partial y} & \frac{\partial n}{\partial y} \end{bmatrix} = \frac{1}{\sqrt{2}} \begin{bmatrix} 1 & 1 \\ -1 & 1 \end{bmatrix} \quad (4.3)$$

For this point,

$$\left. \frac{\partial \phi}{\partial t} \right|_{i,j} \approx \frac{1}{2\sqrt{2}\delta_x} (\phi_{i+1,j-1} - \phi_{i-1,j+1}) \quad (4.4a)$$

$$\left. \frac{\partial \phi}{\partial n} \right|_{i,j} = -\frac{\omega}{\kappa} \quad (4.4b)$$

and the Laplacian $\nabla^2 \phi$ is evaluated as,

$$\nabla^2 \phi = \frac{\partial^2 \phi}{\partial t^2} + \frac{\partial^2 \phi}{\partial n^2} \quad (4.5)$$

with

$$\left. \frac{\partial^2 \phi}{\partial t^2} \right|_{i,j} \approx \frac{1}{2\delta_x^2} (\phi_{i+1,j-1} - 2\phi_{i,j} + \phi_{i-1,j+1}) \quad (4.6a)$$

$$\left. \frac{\partial^2 \phi}{\partial n^2} \right|_{i,j} \approx \frac{1}{8\delta_x^2} \left(\frac{6\omega}{\kappa} (\sqrt{2}\delta_x) + \phi_{i+2,j+2} + 4\phi_{i+1,j+1} - 5\phi_{i,j} \right) \quad (4.6b)$$

For the lower transition points, the neighbouring points at $i+1, j-1$ and $i-1, j+1$ are out of the domain, some additional approximations need to be used, specifically, they are

$$\phi_{i+1,j-1} \approx \phi_{i+1,j}, \quad \phi_{i-1,j+1} \approx \phi_{i,j+1} \quad (4.7a, b)$$

In the simulation, when the transition points are encountered, these formulas are used to replace those similar to Eqs. (2.131) to (2.138) in the calculations of the chemical potential and the force term in LDR-LBM.

Such a way seems to be able to regularize the geometrical singularities naturally and has not resulted in any nonphysical phenomena in numerical simulations. Of course it is not expected that the finest structures of the surface are accurately resolved; after all, truncations at the grid size level are somehow made in such an implementation.

4.3 Two-dimensional study of a droplet driven by a body force over a grooved wall

In this section, simulation results of a 2D droplet moving over a grooved wall will be presented.

4.3.1 General description of the problem

The initial condition is illustrated in Fig. 4.2. The darkest part represents the liquid, the lightest parts represent the gas, and the parts with darkness in between represent the solid walls or solid between grooves. Initially the liquid is stationary on the flat part of the channel and takes a rectangular shape. A constant body force of magnitude g is applied in the liquid region ($\phi > 0$) to drive the droplet to move over the grooved part. In Fig. 4.2, only an inclined force is shown, and the inclination angle is, -45° , with respect to x direction. Another horizontal force (i.e., inclination angle 0°) is also tested. For both, the magnitude of the horizontal component is $10^{-6}/\sqrt{2}$. On the left and right sides periodic boundary conditions are applied. Some common parameters (in LU) for most simulations are listed in Table 4.1. Note that the upper wall is kept stationary and neutral wetting ($\tilde{\omega} = 0$, $\theta = 90^\circ$). The size of the initial liquid segment is 135×55 .

In this study, the main focus is on the flow pattern and the average velocity of the droplet, which is calculated by

$$u_{liquid} = \frac{\sum_{i,j} u_{i,j} N(\phi_{i,j})}{\sum_{i,j} N(\phi_{i,j})} \quad (4.8)$$

where the function $N(\phi)$ is defined as

$$N(\phi) = \begin{cases} 1 & (\phi > 0) \\ 0 & (\phi \leq 0) \end{cases} \quad (4.9)$$

The important dimensionless parameters, the Reynolds number and capillary number, are estimated using the liquid properties (viscosity $\nu_L = 0.005$, surface tension $\sigma = 0.001$), the channel height of the flat part (55) and a typical velocity of the droplet (4×10^{-4}). Then, it is found that $Re = 4.4$, $Ca = 2 \times 10^{-3}$. These indicate a rough regime which most of the following 2D simulations fall in. Here it may be helpful to provide some more information on the lattice units (LU) so that the conversions of variables between the physical system and the simulation system using LU are clear for MPMC flows. As introduced in Subsection 2.1.1.2, in LBM the lengths are measured by δ_x and the velocities are measured by the lattice velocity c . That sets the time unit as $\delta_t = \delta_x / c$, and the kinematic viscosities are thus measured by $c\delta_x$. In addition, for MPMC flows a reference density ρ_r is introduced (here using the liquid density), and then the surface tension is measured by $\rho_r c^2 \delta_x$.

4.3.2 Effects of surface tension

In this subsection, the effects of surface tension on the flow pattern are investigated. For conciseness only the results for all the walls being neutral wetting ($\theta = 90^\circ$) are presented, and the inclined force is applied. Fig. 4.3 shows the comparisons of the evolution of liquid velocity with time for $\sigma = 10^{-4}$, 10^{-3} and 2.5×10^{-3} . Fig. 4.4 gives

the snapshots of the liquid position and configuration every 10^5 steps for the three cases. Using the average velocities at $t = 2 \times 10^5$, rough estimations of the capillary numbers give $Ca \approx 6.35 \times 10^{-2}$, 1.36×10^{-3} and 1.68×10^{-4} for the three cases.

From Fig. 4.3, it is seen that the droplet velocity keeps increasing when $\sigma = 10^{-4}$ whereas for $\sigma = 10^{-3}$ and 2.5×10^{-3} it first increases, then almost reaches a constant and after that it keeps decreasing. Such differences can be understood based on Fig. 4.4. When the surface tension is small, the liquid experiences some fingering process and finally detaches from the wall surface due to the change of the channel geometry from the flat to the grooved part. This is an outcome of both the body force and the pinning at the transition point under the given conditions. Having less contact with the wall and thus experiencing very small drag, the droplet is accelerated quickly. In contrast, when the surface tension increases, it is unlikely to see the fingering and the pinning at the transition greatly decelerates the droplet as found for the two cases with $\sigma = 10^{-3}$ and 2.5×10^{-3} . In fact when $\sigma = 2.5 \times 10^{-3}$, the droplet is almost stuck at the transition point. These results have clearly demonstrated that as the scale becomes smaller the surface tension and wall geometry become more and more important in determining the flow characteristics.

4.3.3 Effects of lower wall wettability

The effects of lower wall wettability with the groove size fixed as 23×15 are presented here. The inclined force is used. The wettability of the lower wall was varied to be hydrophilic ($\theta \approx 45^\circ, 60^\circ$), neutral wetting ($\theta = 90^\circ$) and hydrophobic ($\theta \approx 120^\circ, 135^\circ$).

Fig. 4.5 gives the comparison of the average liquid velocity under different wettabilities of the lower wall. A general trend observed from Fig. 4.5 is that the drag on the droplet decreases as the hydrophobicity of the lower wall increases. Fig. 4.6 shows the comparisons of the snapshots of the liquid positions and configurations at $t = 6 \times 10^5$ for the five cases. It is seen that as the hydrophobicity increases the contact area between the drop and the lower grooved wall decreases. This may explain the above drag variation with the wettability.

For the most hydrophilic case ($\theta \approx 45^\circ$), the liquid almost completely fills the grooves. For $\theta \approx 60^\circ$ the liquid no longer spreads deep enough to reach the bottom side of the groove and some concave arcs (as seen from the liquid side) are formed between the left and right sides of the grooves. For this case, even when the lower wall is hydrophilic, the apparent advancing angle appears much greater than 90° . This is in line with the idea of “roughness-induced non-wetting” under a dynamic situation. It is noted that this does not contradict with the hydrophilic property of the wall. In fact, if measured locally (down to the sub-groove scale), the CAs are still less than 90° (see Fig. 4.7). Of course, whether such a phenomenon occurs should depend on the specific geometry of the groove. This issue will be investigated later. For the neutral wetting case ($\theta = 90^\circ$), the droplet only “skips” over the top sides of the “islands” between neighboring grooves. When the hydrophobicity increases to $\theta \approx 120^\circ$, the droplet touches only some of the “islands” (not shown here) during the course over the grooved parts. When it is not in touch with the “islands”, the amplitude of the oscillation in the velocity is reduced (see Fig. 4.5). For the most hydrophobic case ($\theta \approx 135^\circ$), the liquid is lifted and attaches the upper wall completely.

4.3.4 Effects of body force direction

To investigate how the direction of the body force affects the simulation outcome, the two ways of applying the body force ((1) inclined at 45° with magnitude 10^{-6} ; (2) horizontal with magnitude $10^{-6}/\sqrt{2}$) are compared. As mentioned above, the horizontal component is kept the same whereas in the first case there is a vertical component that may affect the contact between the droplet and grooved wall. It is noted that here the droplet weight is not considered explicitly. Since it is found in the simulations that the force effects may be quite different under different wetting conditions, the results under three different wall wettabilities ($\theta = 45^\circ, 90^\circ$ and 135°) are presented here.

Fig. 4.8 shows the droplet velocity evolutions for the six cases. When the wall is very hydrophilic, the droplet moves faster under the inclined force than the horizontal one. But for neutral-wetting and hydrophobic walls, the horizontal force drives the droplet to move faster. These observations are rather interesting. By noting that the downward component of the inclined force facilitates the contact between the droplet and the lower wall and thus may increase the drag, it is not difficult to explain the cases with $\theta = 90^\circ$ and 135° , but the hydrophilic case is a bit counter-intuitive. A plausible understanding could be reached after a close look at the droplet-groove interaction (see Fig. 4.9). Fig. 4.9 compares how the droplet moves across the first few grooves for the hydrophilic and neutral-wetting cases. When the lower wall is not very hydrophilic, the droplet just moves over the grooves. Hence, the less the contact, the faster the droplet runs. But if the wall is sufficiently hydrophilic, the droplet spreads into the grooves and reaches the bottom surface. During its passing over a groove, the advancing interface experiences substantial reconfigurations, in contrast to the less-

hydrophilic cases. Such a process seems to accelerate the droplet (see the corresponding “bumps” on Fig. 4.8) and under similar conditions the droplet-wall contact becomes a plus. That may be the reason why the droplet moves faster under the action of the inclined force for $\theta = 45^\circ$.

Another important finding is that: for the hydrophilic case the inclined force helps the droplet overcome the pinning at the transition point (from flat to grooved part). This is probably because the vertical component of the force tends to cause the downward motion of the interface and with it the energy barrier at the transition point is easier to overcome. Obviously, the force may affect the droplet motion significantly. However, it is not viable to try all the possibilities. In the following subsections, only one of the two ways of applying the force will be focused.

4.3.5 Effects of density ratio

As mentioned above, the study in this chapter is based on a model for multi-phase flows with large density ratio by Zheng et al. (2006); thus it allows the study on the effects of density ratio over a wide range. Before carrying out any specific investigations, it is helpful to analyze a liquid droplet immersed in a gas medium in the presence of a uniform force field g (e.g., gravity). Suppose that the droplet volume is V_L . At zero velocity, the net force acting on it is estimated to be $\rho_L V_L g - \rho_G V_L g$. When ρ_L is much larger than ρ_G , one may apply a force on the liquid part only with the force density modified to be $(1 - \rho_G / \rho_L)g$ to study the droplet motion. In the following, not only is the gas density ρ_G modified (ρ_L fixed to be 1), but also the magnitude of driving force is changed accordingly. Three gas

densities were tested, $\rho_G = 0.001, 0.01$ and 0.1 (for which the density ratios are 1000, 100 and 10 respectively). The corresponding force densities were $0.999g (\approx g)$, $0.99g$ and $0.9g$. The inclined force was used. The CAs tested include $\theta = 45^\circ, 90^\circ$ and 105° , but only the typical results for $\theta = 45^\circ$ and 105° are shown below.

Fig. 4.10 shows the average liquid velocities under the above different density ratios for $\theta = 45^\circ$ and 105° . It is seen that the liquid velocity is slightly lower when $\rho_G = 0.01$ than $\rho_G = 0.001$, but there is a notable decrease when $\rho_G = 0.1$. However, if speaking of order of magnitude, the decrease of density ratio does not lead to significant change of droplet velocity. On the other hand, the change of lower wall wettability seems to cause much larger variations (e.g., see the cases for $\theta = 45^\circ$ and 105° in Fig. 4.10).

When the density ratio is varied, there may be appreciable differences in the interface positions at a given time. Fig. 4.11 compares the interface snapshots for the three density ratios at 10^6 time steps for $\theta = 45^\circ$. The difference in the advancing interface between $\rho_G = 0.001$ and 0.1 appears to be the largest. At the same time, it is interesting to note that the interfaces inside the grooves (after the liquid passes them) have only negligible differences. This indicates that the density ratio mainly affects the speed of the droplet. Of course, these discussions are held in the present modeling framework. Under other conditions or setups, the density ratio could become a more critical factor.

4.3.6 Effects of groove width and depth for neutral-wetting and hydrophobic walls

To investigate the effects of groove width, W_{groove} , and depth, H_{groove} , the following two values (23, 16) for the W_{groove} , and (15, 5) for the H_{groove} with neutral-wetting and hydrophobic walls have been tested (only $\theta \approx 135^\circ$ is presented for the hydrophobic case), and the inclined force is used. Including the previous test, there are totally three cases being compared ($W_{groove} \times H_{groove} = 23 \times 15$, 16×15 and 16×5). It has been found that the groove geometry only affects the droplet motion slightly when the lower wall is not so hydrophilic.

When the lower wall is neutral-wetting, the droplet only touches the top sides of the solid islands between the grooves, irrespective of the groove geometry. From Fig. 4.12, one can see that the change in the width has relatively stronger effects than the change in the depth. This is not unexpected because the liquid does not penetrate into the grooves, thus avoiding direct effects of the depth. It is also seen that the droplet moves faster when the width increases. This may be due to the fact that it has less total contact area with the wall for wider grooves.

As the hydrophobicity of the lower wall further increases ($\theta \approx 135^\circ$), the droplet completely attaches to the upper wall which is always kept at neutral-wetting. As found in Fig. 4.12, the changes in groove size do not affect the liquid motion much as the liquid has in fact no direct contact with the lower wall. Because the liquid-gas interface is very close to the lower wall and the interface has a finite thickness in the present model, certain small amount of difference is still recognizable especially for different groove widths.

4.3.7 Hydrophilic grooved walls: a detailed look

When the lower wall is grooved, as previously exhibited, the droplet-wall interaction is enhanced and there exist more enriched phenomena. In this subsection, detailed studies of such flows are given.

4.3.7.1 Effects of groove width and depth for hydrophilic walls

The above three cases ($W_{groove} \times H_{groove} = 23 \times 15, 16 \times 15$ and 16×5) are studied. Fig. 4.13 shows the comparison of the image sequences every 2×10^5 time steps. It is seen from Fig. 4.13(b) that when the groove width changes from 23 to 16, the droplet only penetrates slightly into the groove and no longer touches the bottom (similar to the case in the last section with $\theta \approx 60^\circ$ and groove dimension of 23×15). This results in reduction of the drag because the liquid velocity increases, as seen in Fig. 4.14. It is interesting to see that when the depth of the groove is further reduced to be 5, the droplet fills the whole grooves again even though the groove width is 16. Unlike the case with width 23, the periodic acceleration of the droplet becomes much more notable. In fact, as shown in Fig. 4.14, the maximum velocity of the droplet in each cycle almost reaches the initial maximum. The reason may be that it takes less time for advancing three-phase line to move across the vertical part of the groove when the groove depth decreases, and thus it reaches the bottom of the grooves earlier and benefits more from the spreading on the hydrophilic bottom surfaces. This is similar to the scenario of enhanced drop spreading on superhydrophilic surfaces in (McHale et al. 2004b). From these observations, it might be fair to conclude that by this driving mechanism whether rough hydrophilic surfaces expedites or impedes the droplet motion depends on the specific geometry (probably on the aspect ratio of the groove depth and width).

Based on the results shown above and also those reported by Reddy et al. (2005), it is expected that both the degree of lower wall hydrophilicity and the groove geometry are crucial to determine the degree of droplet filling in the grooves. Next, further numerical experiments aiming to clarify this issue are reported. First the groove geometry was fixed and the low wall CA θ was varied to find the critical value beyond which the droplet would touch the bottom of the groove. And then θ was kept constant and the groove width and depth were changed. The main focus is on the motion across the first groove. Later evolutions involving subsequent grooves are just briefly discussed. Also note that the inclined force is applied.

4.3.7.2 Critical CA

Firstly, the groove is fixed to have a dimension of 23×15 . By testing different lower wall CAs, the regime in which the critical CA lies is gradually narrowed down. The narrowest that has been reached is $51.20^\circ < \theta^{crit} < 52.48^\circ$. Fig. 4.15 shows how the advancing interfaces move across the first groove. Similar to what were observed before, for $\theta = 52.48^\circ$ (the less hydrophilic one), the droplet attaches to the right side of the first groove before it touches the bottom surface; whereas for $\theta = 51.20^\circ$ (the more hydrophilic case), it reaches the bottom surface first and shows considerable reconfigurations, resulting in an entrapped bubble inside the groove.

4.3.7.3 Critical groove width and depth

Next the CA is fixed to be $\theta = 45^\circ$, and so is the depth of the groove ($H_{groove} = 15$). Then the groove width is varied. By similar practices, the critical width has been identified to be in the region $19 < W_{groove}^{crit} < 20$. The advancing interface snapshots of

its passing the first groove for $W_{groove} = 19$ and $W_{groove} = 20$ are given in Fig. 4.16. At $t = 2, 2.5 (\times 10^5)$, the difference is rather negligibly small; but after the time the droplet reaches the left-lower corner points (with $W_{groove} = 20$), there are larger and larger disparities. This indicates that the droplet is somehow able to detect the geometry ahead of its arrival of the site of groove difference. This appears to be rather counter-intuitive. The reason could be that the slight difference in the groove geometry is reflected through the minor difference in the gas motion in the groove (e.g., the speed and amount of gases to be discharged out of the groove) and this in turn differentiates the advancing interface evolution.

Finally, both the lower wall CA and the groove width are fixed ($\theta = 45^\circ$, $W_{groove} = 23$), and the groove depth is changed. Similar investigations have found that the critical depth to be in $17 < H_{groove}^{crit} < 18$. The relevant comparisons are shown in Fig. 4.17. By the same arguments as above, the disparities might be explained.

If one roughly take the critical values for the groove width and depth as $W_{groove}^{crit} \approx 19.5$ and $H_{groove}^{crit} \approx 17.5$, then it is easy to find that the aspect ratio of groove, W_{groove}/H_{groove} , for the two critical cases are 1.3 and 1.31. This may imply that the aspect ratio is a more crucial and general factor (Huang et al. 2009a). It is expected that its critical values should vary under different conditions (e.g., Capillary number, relative droplet size with respect to the channel depth, etc.). But once other conditions are specified the critical aspect ratio could be fixed. Of course, further more simulations are required to confirm it.

4.3.7.4 Droplet motions over subsequent grooves

In the above investigations of the critical values, the attention was focused only on the first groove. Although under many situations the interface configurations are almost the same in all the grooves, it is not necessary for this to always hold. In fact, it has been observed that near certain critical conditions even though the droplet does not fill the first groove, it can spread to the groove bottom surface when it reaches some subsequent grooves. Fig. 4.18 gives two examples: one is taken from the critical wettability study for fixed groove geometry and the other is from the study of critical groove depth. The reason for both filling seems to be similar. That is, when the receding interface was about to leave the flat part of the channel, the droplet was subject to more drag which slows it down. This allows sufficient time for the advancing interface to spread into the groove. Considering that they are already quite close to the critical condition, the magnitude of the disturbance required is not quite large. Thus, the change from one configuration to another is not difficult.

4.3.8 Some analyses of the flow field

Finally, some flow patterns are analyzed in order to gain a deeper understanding of the flows. The first one is from the critical groove depth study (with $H_{groove} = 18$) at the time, $t = 10 \times 10^5$. Since the motion is mainly horizontal, the contour for the velocity component, u , is selected. The interfaces are shown as the background (see Fig. 4.19). From Fig. 4.19, one can observe, besides the major droplet motion, two other important features: the first is the discharge of gas from the groove in which the advancing interface fills; the other is the large velocity changes near the top corners of the solid “islands” immersed in the droplet. By considering that the present flow is dominantly horizontal and the viscous stresses mostly come from the gradient in u , it

seems fair to draw a qualitative conclusion that high stresses exist in such regions near the top of solid “islands”. The second is a flow field in the study of different ways of applying the body force. Specifically, the instantaneous “streamline” at the time $t = 5 \times 10^5$ is checked. The applied force is horizontal and the lower wall is hydrophobic (with $\theta = 135^\circ$). The field is given in two different reference frames: one is static (see Fig. 4.20(a)) and the other is moving with the droplet (at its instant average velocity) (see Fig. 4.20(b)). In Fig. 4.20(a), it is easy to find some vortices in some grooves rotating in the clockwise direction. These are understandable because under the hydrophobic condition the droplet has no direct contact with the lower surface and the flow may be divided into upper and lower parts. The flow inside the grooves is similar to the standard driven cavity flow. From Fig. 4.20(b), in the moving frame, certain circulation patterns are observed inside the droplet and outside it as well (note that the outer circulation is split into two parts due to the periodic boundary condition used). It seems not easy to imagine these patterns directly by intuition. Only by numerical simulations could they be visualized. Besides, underneath the droplet, a thin layer of gas is seen passing from right to left.

4.3.9 Some comparisons with previous work

It may be important to compare the present results with those by Reddy et al. (2005). In their work, the Reynolds number was several order of magnitudes smaller than the present work, and the channel height was of comparable size with or even smaller than the groove dimension. Although in both work the entrapment of gas bubbles is related to the instability of stretched interfaces, the findings by Reddy et al. (2005) does not apply here. As previously observed, in the present work, the motion of droplet is sufficiently fast. Therefore, even when the advancing interface passes the

inner corner of the groove, it is still possible to see gas bubbles entrapped. The present work focuses on the effects of wettability and groove geometry. This is in line with the spirit of Seemann et al. (2005), in which the morphologies of three-dimensional static droplets on micro-grooved surfaces were investigated mainly by experiments and also by some numerical simulations. Note that an intriguing diagram simply based on the aspect ratio of the groove and the CA was obtained by Seemann et al. (2005). Depending on the two factors, liquid on micro-grooved surfaces (with groove depth between $0.1\sim 0.9\ \mu m$ and groove width between $0.4\sim 3\ \mu m$) may display different morphologies such as droplets, filaments, pinned wedges or corner wedges: for instance, a large CA and a large aspect ratio (note that the aspect ratio used in the present work is the inverse of that by Seemann et al. (2005)) tend to lead to the formation of droplets whereas filaments or wedges are likely to be observed under small CAs and small aspect ratios (Seemann et al. 2005). This is in favor of some preliminary findings above and the postulations about droplets moving over hydrophilic walls though the present work studies dynamic interfaces.

4.4 Effects of the grooves

Having studied the droplet motion in grooved channels, it would be interesting to make some comparisons between the droplets moving inside the grooved channel and in a smooth channel without the grooved parts so that the effects of the grooves can be elicited. Here the groove dimension is 23×15 , and the inclined force is applied. The typical three values for CA ($\theta = 45^\circ$, 90° , and 135°) are chosen. The comparisons of the average liquid velocity are shown in Fig. 4.21. It is noted that the same range and scale for the u_{liquid} axis are used in all the sub-figures. From Fig. 4.21, it can be seen that the effects of geometrical change on the droplet are obvious, and it is also

observed that they are different for different wettabilities. When the wall is flat, the evolution of the droplet velocity for different wettabilities follows a similar trend and the differences of the final velocity are not very large. However, when the groove is present, the differences become much more noticeable. For hydrophilic walls, the groove greatly decelerates the droplet as compared with the flat case and the deceleration is most prominent when the droplet is in the transition from the flat to the grooved parts, indicating a significant pinning effect. By contrast, for the hydrophobic walls, under the given conditions, the pinning at the transition point results in a lifting force and makes the droplet attach to the upper wall. Consequently, a lubrication layer forms between the droplet and lower wall. This significantly increases the droplet velocity as compared with the case over a smooth wall.

4.5 Three-dimensional study of droplet spreading and dewetting on a textured surface

In this section, preliminary investigations of 3D droplet motions near walls with one pillar and pillar arrays are reported. Unlike the above 2D cases, no body force is applied to drive the droplet, and motions are caused purely by surface tension forces in the 3D cases.

4.5.1 Droplet near one pillar

First a droplet near a single square pillar is studied. Initially the droplet is in a non-equilibrium state. In other words, the total energy of the system is not minimized. Due to the specific geometry and wetting property the droplet will move towards an equilibrium state under the action of the surface tension force. For this case, the solid wall is neutral wetting ($\tilde{\omega} = 0$, $\theta = 90^\circ$). The initial droplet radius is about 7.5. Some

other parameters are given in Table 4.2. The initial and final (after 10^4 steps) states are shown in Figs. 4.22 (a & b). The apparent CA is larger than 90° finally.

4.5.2 Droplet near multiple pillars

In this subsection, a droplet near a 5×5 pillar array is investigated. Three cases with the same initial condition but different wetting properties for the lower wall have been simulated. The parameter controlling wetting, $\tilde{\omega}$, takes the value 0.477, 0 and -0.477 which correspond to the theoretical CA being $\theta \approx 45^\circ$, 90° and 135° . Some other parameters are listed in Table 4.3. The initial droplet radius is about 12.5. The droplet configurations after 10^5 steps are given in Fig. 4.23, and the interface evolutions in the middle $y-z$ plane are shown in Fig. 4.24 for every 2.5×10^4 steps.

From Figs. 4.23 and 4.24, one can find the different behaviors of the droplet as described below. For the hydrophilic case the droplet tends to spread over the wall surfaces and the final droplet becomes very flat, similar to that on a flat wettable surface. Such spreading seems to be even enhanced due to the presence of the pillars as seen from the evolution of the interface. Normally on a flat wall, the speed for the droplet approaching its equilibrium configuration decreases; however, in Fig. 4.24(a), significant changes still occur at consecutive sampling times even after long time evolution. For the neutral wetting and hydrophobic cases, the change of the interface position becomes smaller and smaller, indicating that it is approaching true static equilibrium. It is also interesting to note that finally the droplet is in contact with nine nearest pillars in the neutral wetting case whereas it is only in contact with five nearest pillars in the hydrophobic case. As the hydrophobicity increases, it might be expected that the droplet would just sit on one pillar similar to the above situation for a single pillar.

4.6 Summary

In summary, both 2D and 3D droplets near rough surfaces have been studied by LBM. In the 2D study, the impacts of the adhesion and geometrical properties of the surface on the flow pattern and droplet velocity have been explored in detail. It has been found that the droplet can move faster on grooved hydrophobic surfaces than on their hydrophilic counterparts. Under certain conditions, the dynamic “roughness-induced non-wetting” has been captured for hydrophilic surface. The effects of density ratio have also been studied and it is found that it affects the droplet velocity but not in a very significant way. For rough hydrophilic walls the effects of the surface wettability and topography are found to be highly coupled with each other. The critical CA, grooved width and depth for the droplet to assume one of two different shapes in groove have been found under certain respective conditions. Based on the results, the aspect ratio of the groove is suggested to be a critical factor to determine the droplet motion. Some detailed analyses of the flow fields have been given for better understanding of the droplet motion, as well as the flow. In addition, a few comparisons between the droplet motions over grooved and smoothed channels have been provided to illustrate how the presence of groove affects the motion. Finally, 3D droplet behaviors near textured walls have also been preliminarily studied. The increase of apparent CA on textured hydrophobic walls has been observed and droplet motions from an initial non-equilibrium state to an equilibrium state under different wall wettabilities have been well captured. It should be noted that for the 3D cases the domain size is not so large and the resolution for the droplet and surface structures may be insufficient. To perform more realistic simulations (e.g., 3D droplet motion along a certain direction on texture surface), it is necessary to extend the domain size

as well as simulation time significantly. Due to the limited time and computational resource, that is left for future work.

Table 4.1. Common parameters for most 2D simulations near a grooved wall

Parameters	Values
Liquid Density	1
Gas Density	0.001
Surface Tension	0.001
Interface Width	3
Kinematic Viscosity of Gas	0.1
Kinematic Viscosity of Liquid	0.005
Distance between Neighbouring Grooves	28
Total Length	450
Magnitude of body force	10^{-6}
Inclination angle of body force	-45°

Table 4.2. Some parameters for the 3D simulation near a single pillar

Parameters	Value
Liquid Density ρ_L	1.5
Gas Density ρ_G	0.5
Surface Tension σ	0.001
Interface Width W	3
Kinematic Viscosity ν	0.005
Pillar Height	8
Pillar Side Length	10
Grid Size	$31 \times 31 \times 30$

Table 4.3. Some common parameters for 3D simulations near a pillar array

Parameters	Values
Liquid Density ρ_L	1
Gas Density ρ_G	0.001
Surface Tension σ	0.0001
Interface Width W	3
Kinematic Viscosity ν	0.01
Pillar Height	7
Pillar Side Length	6
Distance between Neighbouring Pillars	4
Grid Size	$51 \times 51 \times 35$

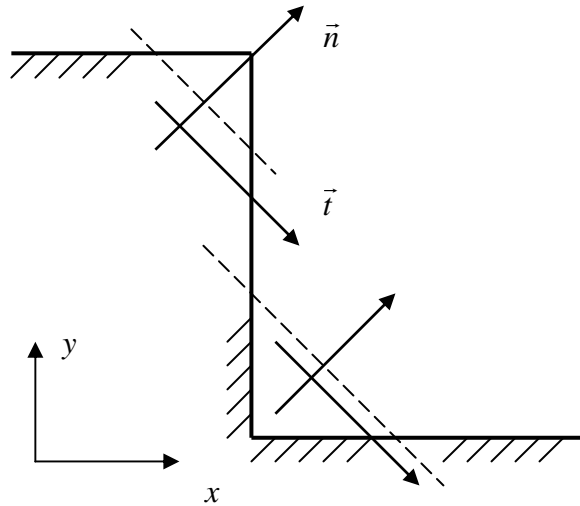


Fig. 4.1. Transition points at the intersections of two orthogonal walls

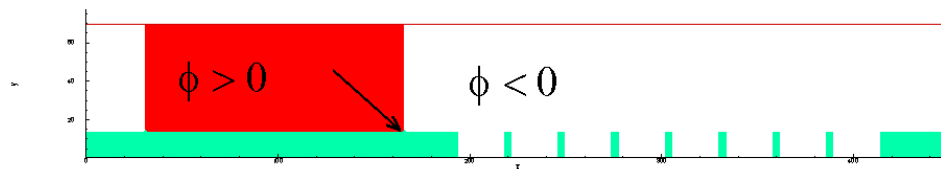


Fig. 4.2. Illustration of the initial condition of 2D flows inside a grooved channel

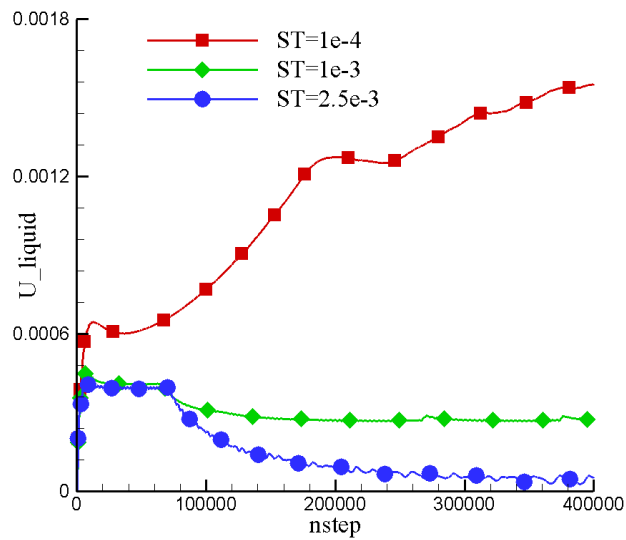


Fig. 4.3. Comparison of the liquid velocity evolution under different surface tensions

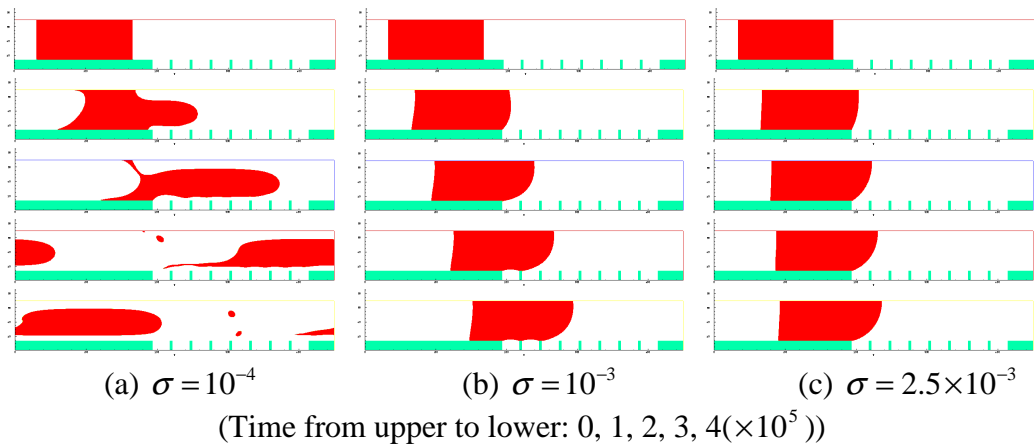


Fig. 4.4. Comparison of snapshots of the liquid positions and configurations every 10^5 steps under different surface tensions

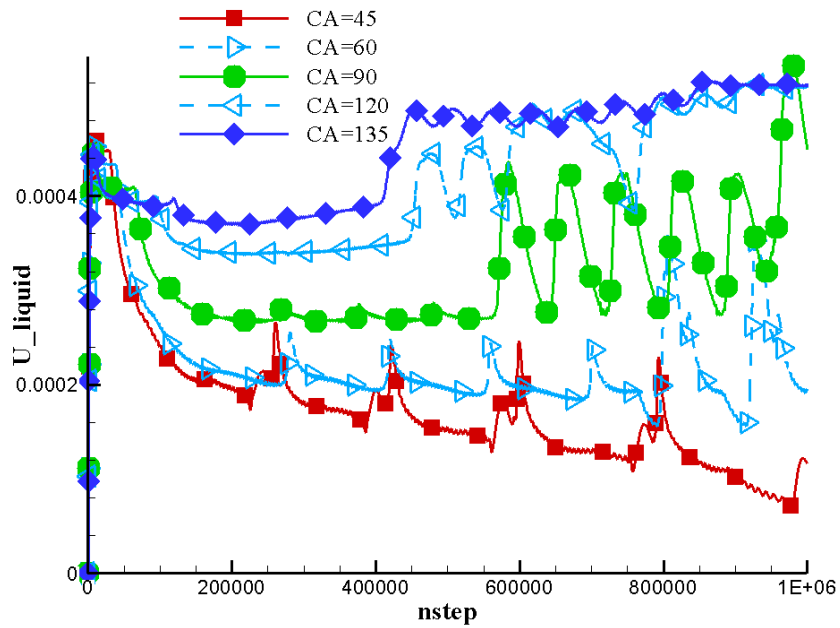
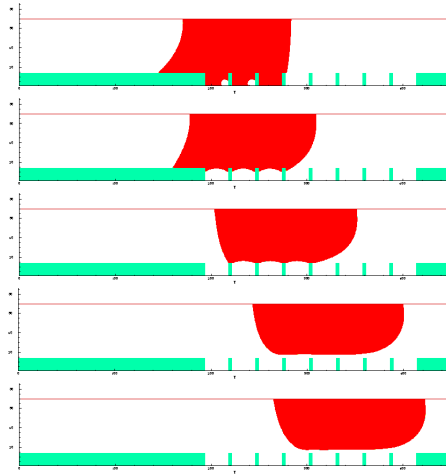


Fig. 4.5. Comparison of the liquid velocity evolution under different wettabilities of the lower wall



(CA from upper to lower: $\theta = 45^\circ$, 60° , 90° , 120° and 135°)

Fig. 4.6. Comparison of snapshots of the liquid positions and configurations at time step 6×10^5 under different wettabilities of the lower wall

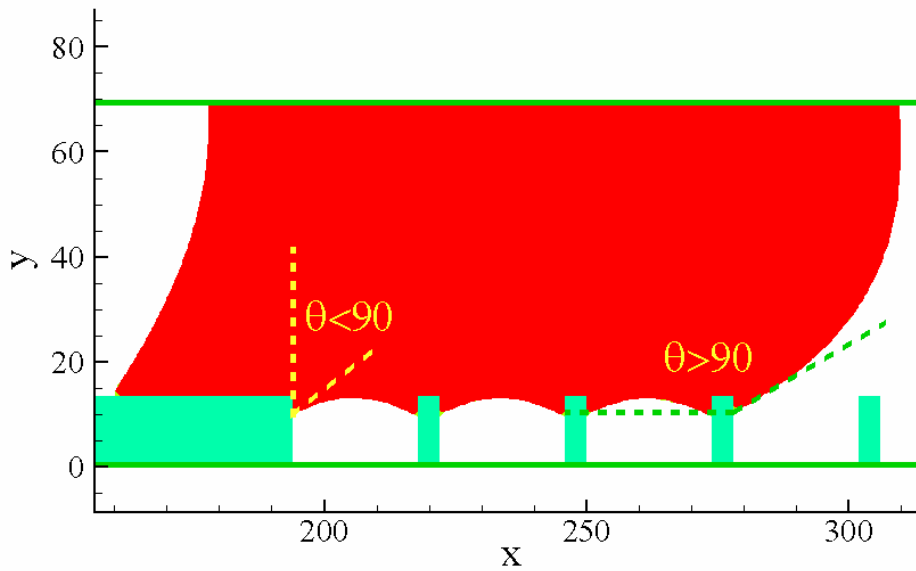


Fig. 4.7. Enlarged view of local and apparent CAs at time step 6×10^5 for $\theta = 60^\circ$

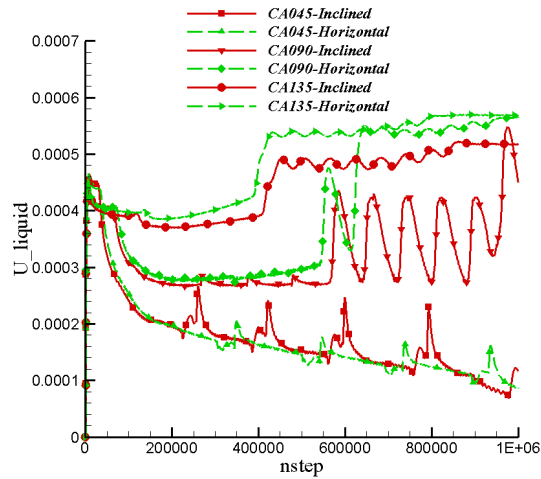


Fig. 4.8. Comparison of the liquid velocity evolution under different forces for $\theta = 45^\circ$, 90° and 135°

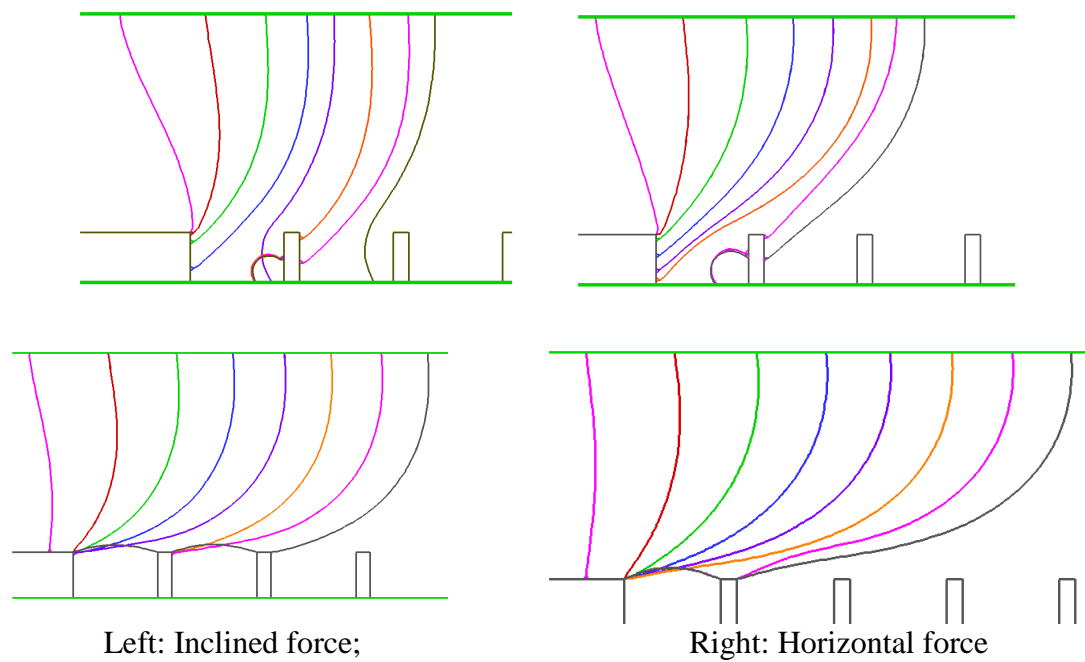


Fig. 4.9. Advancing interfaces at $t = 0.5, 1, 1.5, 2, 2.5, 3, 3.5, 4 (\times 10^5)$ under different forces for $\theta = 45^\circ$ (upper row) and 90° (lower row)

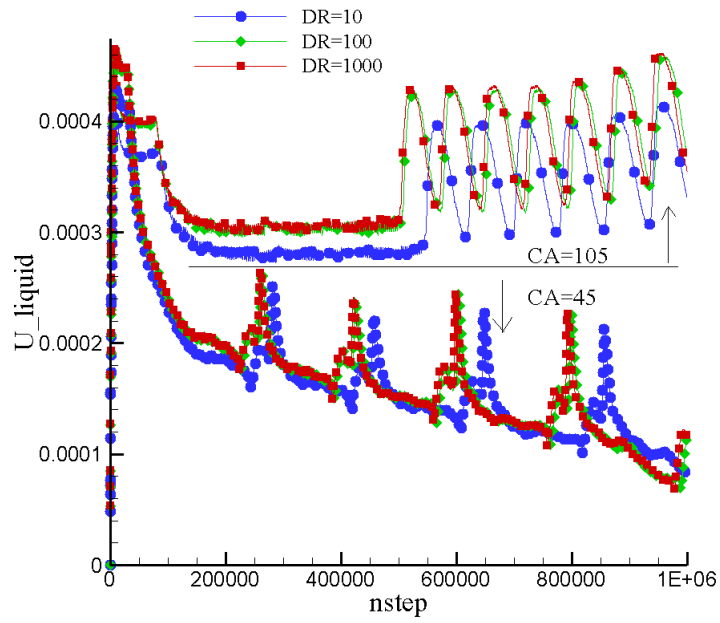


Fig. 4.10. Comparison of the liquid velocity evolution under different density ratios for $\theta = 45^\circ$ and 105°

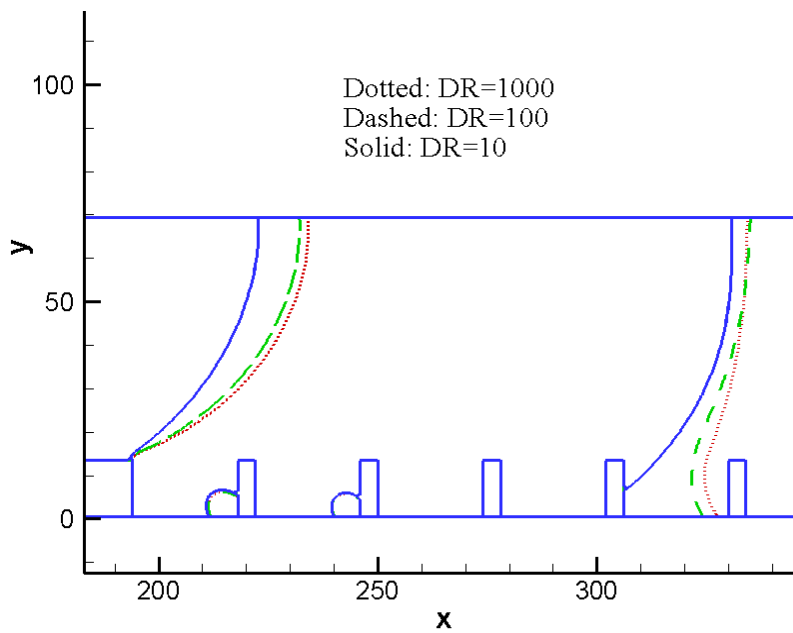


Fig. 4.11. Interface positions at $t = 10^6$ under different density ratios ($\theta = 45^\circ$)

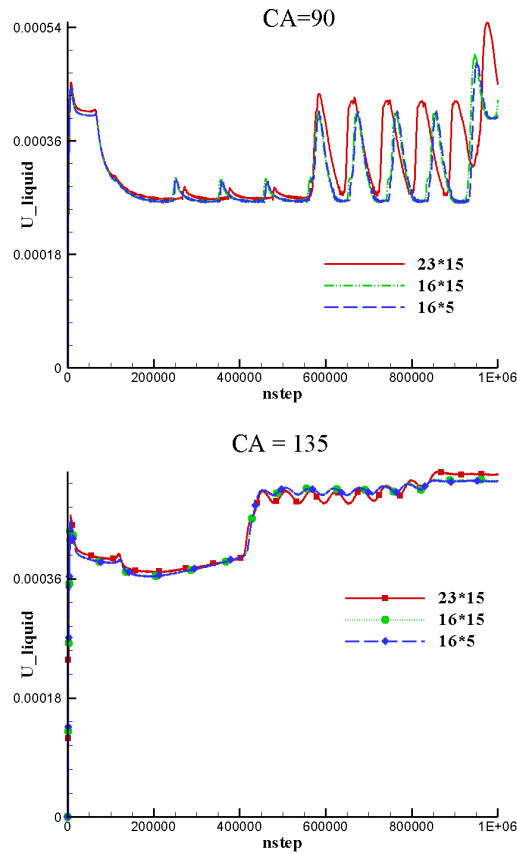


Fig. 4.12. Comparison of the liquid velocity evolution under different groove geometries for $\theta = 90^\circ$ and 135°

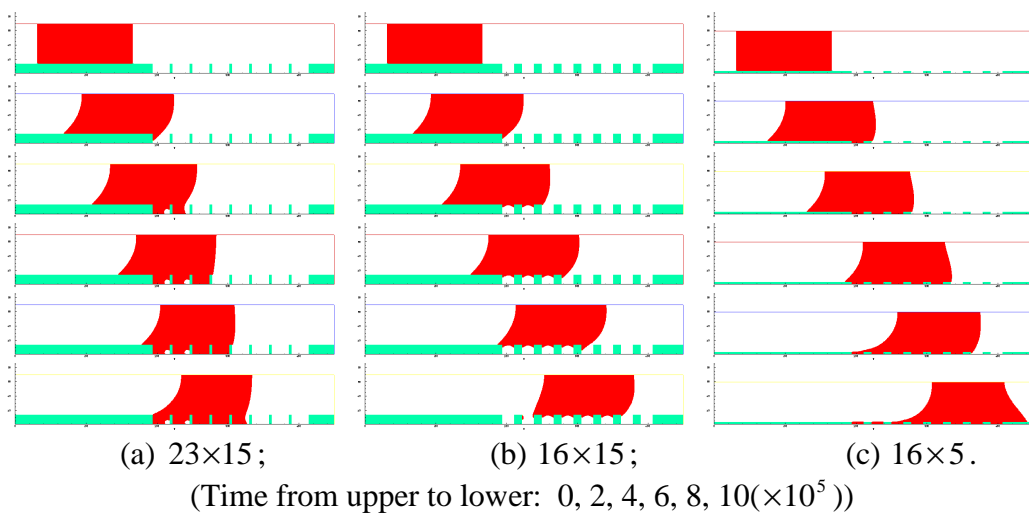


Fig. 4.13. Comparison of snapshots of the liquid positions and configurations every 2×10^5 steps under different groove widths and depths for $\theta = 45^\circ$

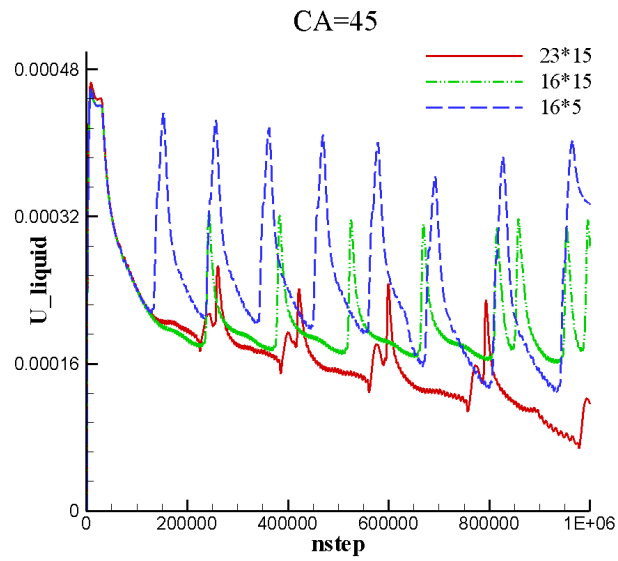


Fig. 4.14. Comparison of the liquid velocity evolution under different groove geometries for $\theta = 45^\circ$

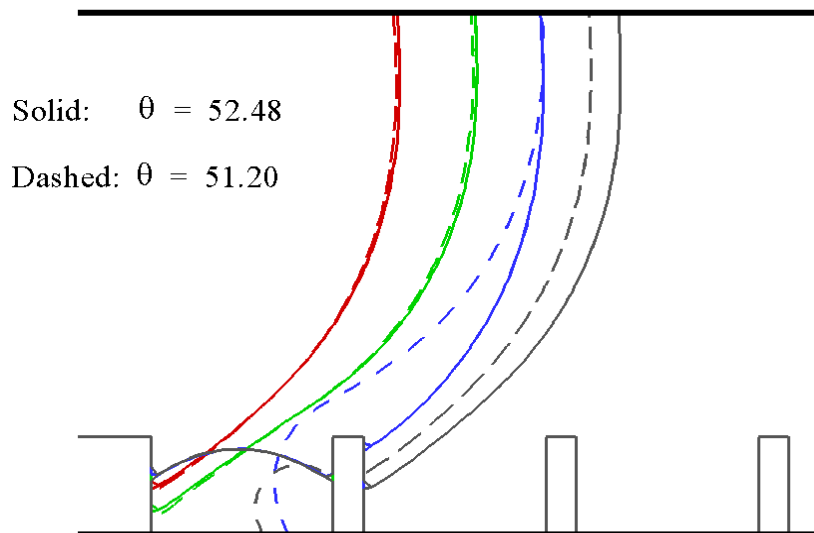


Fig. 4.15. Advancing interfaces at $t = 2, 2.5, 3, 3.5 (\times 10^5)$ below and beyond the critical contact angle

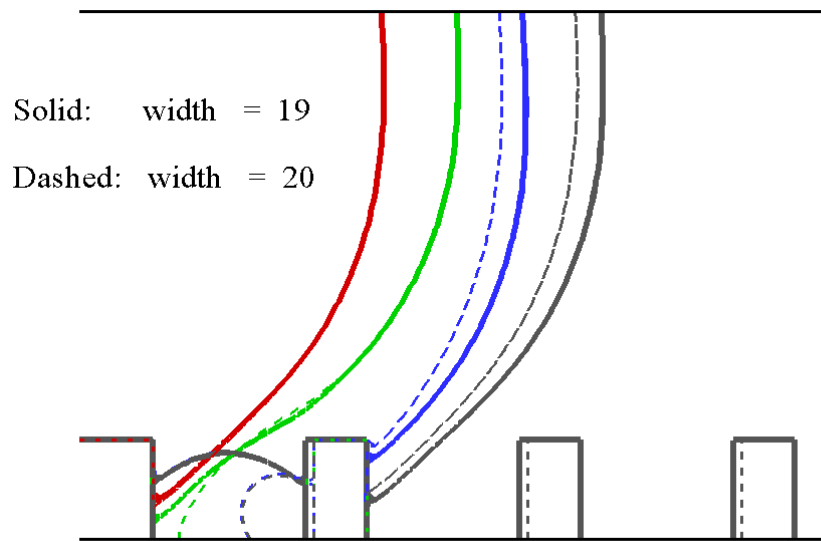


Fig. 4.16. Advancing interface positions at $t = 2, 2.5, 3, 3.5 (\times 10^5)$ below and beyond the critical groove width

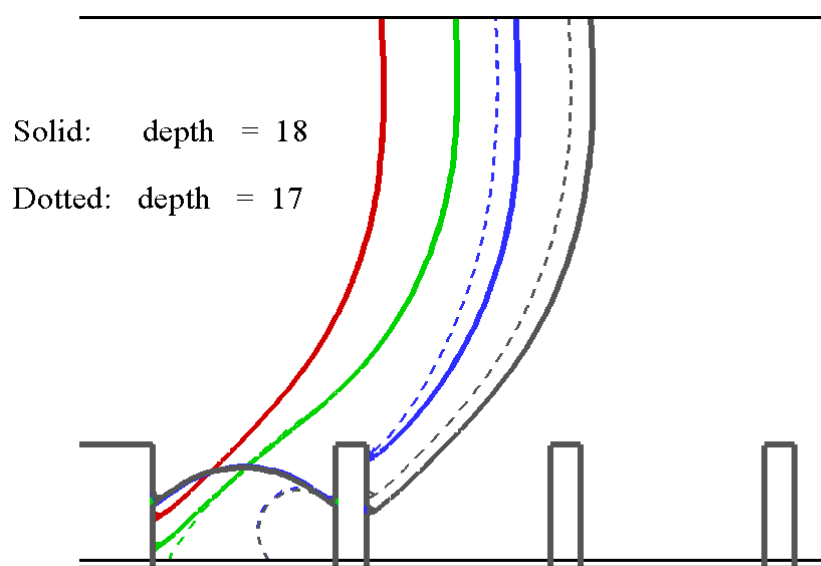


Fig. 4.17. Advancing interface positions at $t = 2, 2.5, 3, 3.5 (\times 10^5)$ below and beyond the critical groove depth

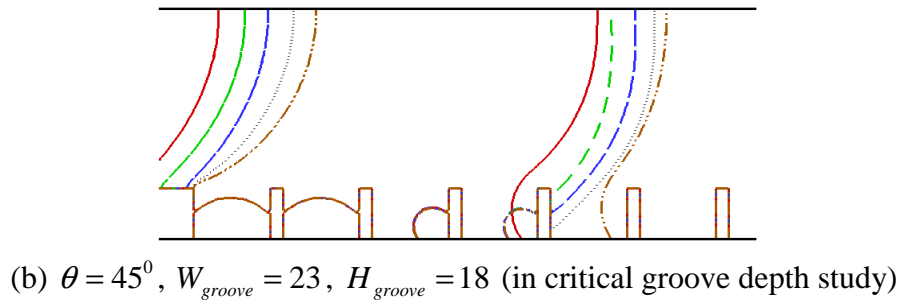
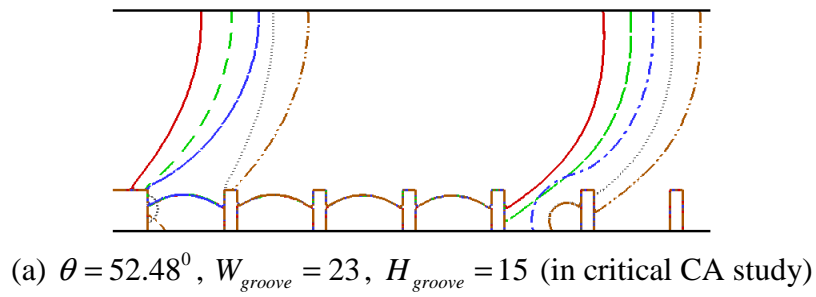


Fig. 4.18. Advancing (right cluster) and receding (left cluster) interface positions at late stages ($t = 8, 8.5, 9, 9.5, 10(\times 10^5)$) from left to right for each cluster

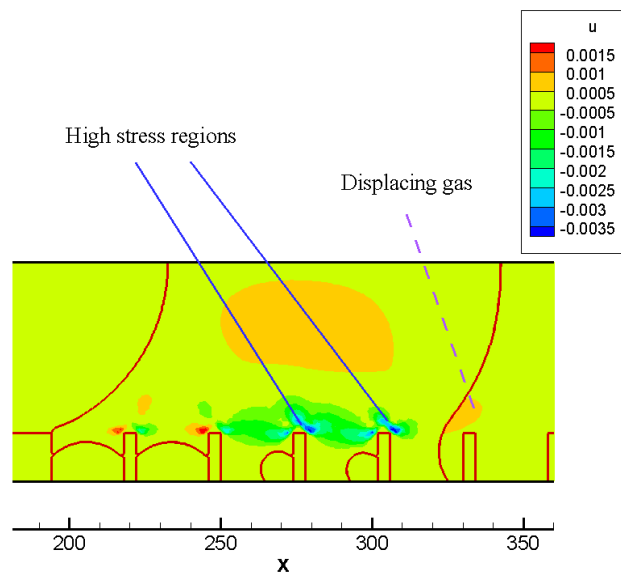
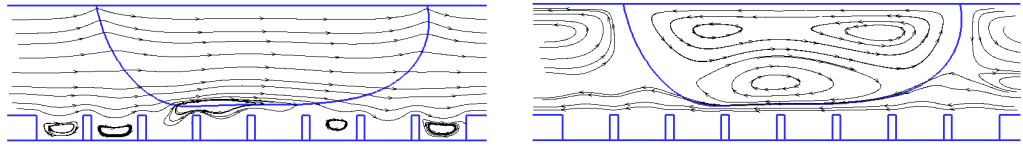
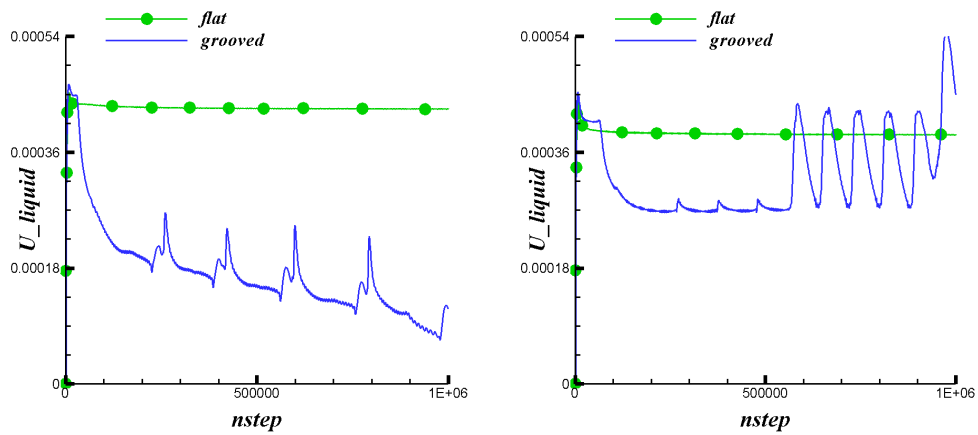


Fig. 4.19. Contour of velocity component u at $t = 10 \times 10^5$ for $H_{groove} = 18$ in critical groove depth study



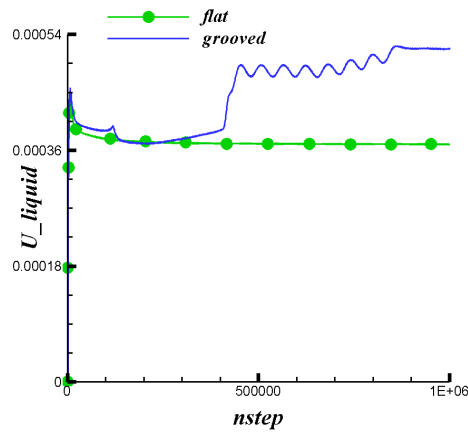
(a) Seen in the absolute reference frame; (b) Seen in a frame moving with the droplet.

Fig. 4.20. Flow field at $t = 5 \times 10^5$ with $\theta = 135^\circ$, 23×15 and a horizontal body force in the study of effects of different body forces



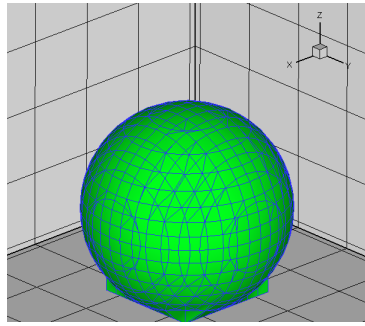
(a) $\theta = 45^\circ$

(b) $\theta = 90^\circ$

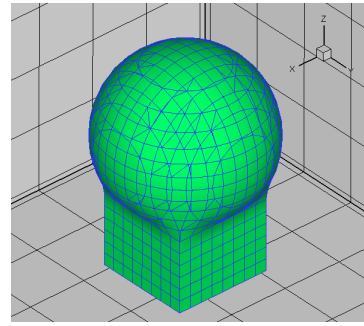


(c) $\theta = 135^\circ$

Fig. 4.21. Comparison of the liquid velocity evolution for flat and grooved walls (flat: line with symbol; grooved: line)

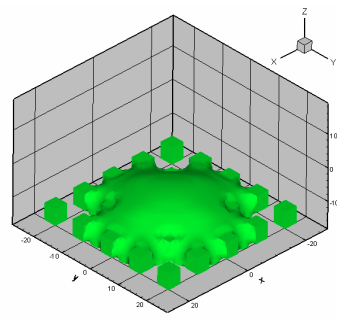


(a) Initial Configuration

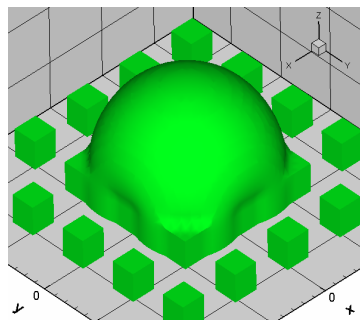


(b) Configuration after 10^4 steps

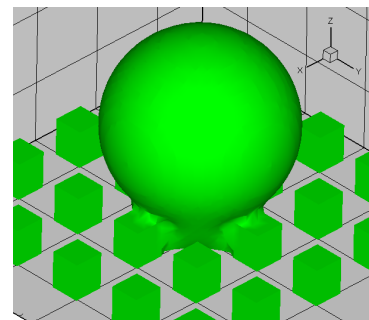
Fig. 4.22. Drop evolution near a single pillar



(a) $\theta \approx 45^\circ$

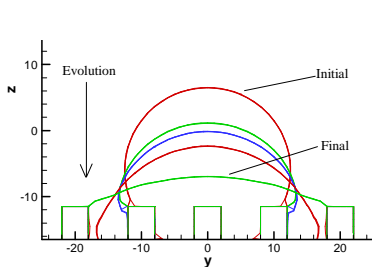


(b) $\theta = 90^\circ$

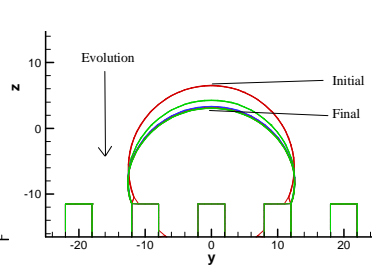


(c) $\theta \approx 135^\circ$

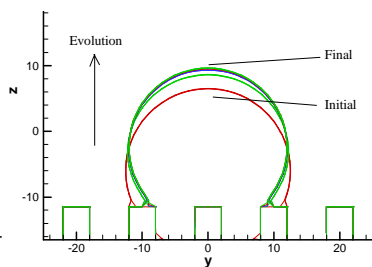
Fig. 4.23. Drop configurations on a pillar array after 10^5 time steps



(a) $\theta \approx 45^\circ$



(b) $\theta = 90^\circ$



(c) $\theta \approx 135^\circ$

Fig. 4.24. Interface evolutions in the middle $y - z$ plane every 2.5×10^4 time steps

Chapter V

Effect of Mobility in DIM Simulations of Binary Fluids¹¹

In Chapter II, some discussions were provided on the convergence of the diffuse interface method (DIM) to sharp interface solutions, and it was also mentioned that for small scale fluid systems the conditions for the convergence (i.e., both the interface thickness and the mobility approach zero) may not always hold. In this chapter, the role of the mobility in DIM simulations of binary fluids is investigated using the lattice Boltzmann implementation. The specific model employed is FE2-LBM-B. Emphasis will be placed on its effect near the solid boundaries, presumably at very small scales.

5.1 Brief review on mobility in DIM simulations of binary fluids

Recall that in DIM, the underlying governing equations consist of the Navier-Stokes equations for mass and momentum conservations, and the CHE for the evolution of the order parameter. The CHE is a convection-diffusion equation that is quite similar to the pure advection equation (without the diffusion term) in the LS and VOF methods (note that more strictly, these methods also allow certain diffusions, but they are just numerical and have no physical meanings). As compared with LS and VOF, the explicit inclusion of the diffusion term in the CHE, with its magnitude being proportional to the mobility M , provides a physical relaxation mechanism for the concentration. Such a mechanism provides flexibility for DIM to accommodate

¹¹ Materials in this chapter have been published in J. J. Huang, C. Shu and Y. T. Chew. International Journal for Numerical Methods in Fluids, 60, pp. 203-225 (2009).

various singularities, for instance, the pressure jump across a curved interface and the stress singularity in CL dynamics (Jacqmin 1999, 2000).

Previously a few analyses have been given about the role of mobility, both as a computational parameter related to asymptotics of numerical methods and as a physical one involving diffusion properties in mixing, coalescence and CL problems. Jacqmin (1999) found, by some theoretical analysis and numerical investigations, that the mobility should be bounded between $O(\varepsilon^2)$ and $O(\varepsilon)$ (here ε being the dimensionless interface thickness) in order to carry out an appropriate DIM simulation that approximates the sharp interface solutions. Jacqmin (2000) also provided detailed analysis on the inner regions surrounding a TPL and identified a length scale (here denoted as l_{CL}) for such small regions related to the dynamic viscosity and the mobility, $l_{CL} \propto \sqrt{\eta M}$. Similarly, Chen et al. (2000) reported a length scale in the moving CL problems for the dissipative relaxation of the concentration determined by the interfacial thickness, the concentration diffusivity and the boundary velocity. Kendon et al. (2001) addressed the significance of using an appropriate mobility, similar to the conclusion reached by Jacqmin (1999), in the LBM framework; they also addressed the difficulty to use a concentration-dependent mobility in LBM. Briant & Yeomans (2004) studied the CL dynamics using LBM and derived a length scale proportional to $M^{1/4}$ for the region in which the diffusive effects are significant and argued that their results matches the classical work using a slip length model. Inamuro et al. (2004) found, by using a LBM, that in bubble rising problems, the mobility affects the coalescence of two bubbles. Vladimirova & Mauri (2004), and more recently, Lamorgese & Mauri (2006), showed some DIM simulations of droplet coalescences when the system is suddenly changed from two-

to one- phase region; results from both investigations led to the conclusion that different mobilities (Peclet numbers in their original papers) may cause qualitatively different mixing outcome. Khatavkar et al. (2006) also discussed the scaling issues in DIM and pointed out that it is necessary to know how to adapt the mobility in accordance with the artificial enlargement of the interface thickness so as to capture the bulk flow phenomena. Zheng et al. (2006) discovered that, similar to the findings by Inamuro et al. (2004), large mobility expedites the merging processes of two neighbouring bubbles.

5.2 Aims of this chapter

Obviously the mobility is an important parameter in the study of MPMC fluid systems by DIM. However, the effects of mobility in various flows may be diverse and they certainly deserve further investigations, either as a physical property or as a numerical parameter in DIM.

Before discussing specific aims of this chapter, it is helpful to first examine two basic types of MPMC flows. According to the driving mechanism, the MPMC flows may be categorized into: (1) mechanically driven; (2) chemically driven (also called “capillarity-driven”). The first type includes the commonly encountered shear driven and body force driven flows. In the second type, the order parameter field is different from the equilibrium state and there exist chemical potential gradients in the system. In this chapter, the effects of mobility in both types of flows will be studied. In the first type, a droplet sitting on a substrate subject to a shear flow will be investigated. In the second type, the cases include droplet dewetting in hydrophobic surfaces, and droplets on chemically heterogeneous surfaces. All of these cases involve the CL.

Thus, the relation between the mobility and the CL velocity, and comparisons between the DIM and the slip model used in other methods will be discussed as well.

For simplicity yet without losing the core physics, only binary fluid systems with the same density and viscosity are considered here (as assumed in FE2-LBM). The macroscopic governing equations are given by Eqs. (1.1, a-c), and their dimensionless forms are Eqs. (1.2, a-c) (for even more details, refer to Eqs. (3.1) and (3.2) as well).

5.3 Sitting droplet subject to a shear flow

First, a droplet sitting on a substrate subject to a shear flow is studied. The initial setup is shown in Fig. 5.1. The two walls are separated by a distance H . The lower wall is kept stationary, and the upper wall moves toward right with a constant speed U . This induces a linear shear flow field that pulls the droplet towards right. Periodic boundary conditions are applied in x -direction. It was found in the simulations that under a small shear rate (here a small U if H is kept constant) the droplet deforms slowly first, then starts to move, and finally ceases to deform when reaching a certain shape with a constant moving speed U_d .

The common parameters for the simulations are listed in Table 5.1. The mesh is 100×50 . The initial droplet radius is set to be $R_d = 25$ and the initial droplet center is $(X_C, Y_C) = (50, 0)$. Both the upper and lower walls are neutral wetting. For $U = 0.01$ with different mobilities \tilde{M} in the range $[0.5, 20]$, the final droplet configurations do not differ very much (as seen in Fig. 5.2 for two typical cases with $\tilde{M} = 0.5$ and $\tilde{M} = 10$), but the steady state droplet velocities may differ significantly (see Fig. 5.3).

To check how the droplet velocity varies with the mobility, U_d is plotted as a function of \tilde{M} in Fig. 5.4. Note that the \tilde{M} axis uses the “log” scale. From Fig. 5.4, it seems that there exist three regimes for the $U_d - \tilde{M}$ relation within the explored range: (1) $0.5 \leq \tilde{M} \leq 2$; (2) $2 < \tilde{M} \leq 4$; (3) $4 < \tilde{M} \leq 20$. In each regime, U_d may be approximately expressed as a linear function of $\ln \tilde{M}$, for instance,

$$U_d = k_1 \ln \tilde{M} + k_2 \quad (5.1)$$

where k_1 and k_2 are some constants. For the above three regimes, the constants k_1 are measured and estimated to be 1.144, 0.889 and 0.752 respectively. The change in this constant may be caused by the change of the droplet shape (though relatively small) and consequently the dynamics. Since the lower wall is stationary and the droplet keeps a fixed shape upon reaching steady states, U_d is actually the slip velocity of the CLs. Thus, here the variation of slip velocity with the mobility has been measured (though for this specific problem only). Finally, to obtain an impression about the flows around the droplet, a snapshot of the steady state flow field (with the velocity in x – direction being relative to the droplet, i.e., in a frame moving with the droplet) is shown in Fig. 5.5. From Fig. 5.5, it is seen that far away above the droplet, the shear flow is only slightly disturbed; as the flow approaches the droplet, the streamlines are increasingly deformed. Finally, in the lower region containing the droplet, two circulations are observed: one is inside the droplet and the other is outside and relatively flat (note that in Fig. 5.5 it is separated into two parts on the left and right sides of the droplet which can be connected together because the periodic boundary conditions are applied in the horizontal direction).

5.4 Chemically driven binary fluids

Last section discusses about the effects of mobility in mechanically driven binary fluid systems. In this section, similar systems, but now driven by the imbalance of the chemical potential field, are investigated.

5.4.1 Droplet dewetting

First, droplet dewetting on a flat wall with spatially homogeneous wettability is studied. The lower wall is originally neutral wetting ($\tilde{\omega} = 0$, $\theta = 90^\circ$) and the droplet takes a semi-circular (in 2D) or hemispherical (in 3D) shape when in equilibrium.

5.4.1.1 Two-dimensional droplet dewetting

A 2D problem is considered first. The domain size is 100×50 for all cases. The initial droplet radius is set to be $R_d = 20$ and the droplet center is $(X_c, Y_c) = (50, 0.5)$. Note that the concentration field may need some time to reach equilibrium state after the initialization with the function $\phi = \tanh\left[\sqrt{(x - X_c)^2 + (y - Y_c)^2} / (W/2)\right]$. But since $\theta = 90^\circ$, it is assumed that the difference between the two states is small and the process for the droplet to evolve toward equilibrium is neglected.

At the beginning, the lower wall is abruptly changed to be very hydrophobic characterized by a large static CA ($\tilde{\omega} = -0.5865$, $\theta \approx 150^\circ$, which results in an initial CA difference $\Delta\theta = 150^\circ - 90^\circ = 60^\circ$). Such a change is similar to the situation in the electro-wetting experiment by Pollack et al. (2000) when a voltage is suddenly applied. In fact, researchers have invented some intriguing methods to modify the wall wettability such as shedding ultraviolet light or blue light onto a photoresponsive

surface (Ichimura et al. 2000). Another interesting way to achieve such a setup is given by Habenicht et al. (2005) which may deserve certain attention here due to the similarity between their observations and part of the simulation results that will be shown below. In that work, initially there were some triangular gold nanostructures on graphite; then, laser was applied to melt these structures which turned into liquid and the molten nanodroplets experienced a dewetting process. When they maintained the liquid form for sufficiently long time, such nanodroplets might jump off the surface.

Before the results are shown, several quantities are firstly defined, which reflect some characteristics of this problem. The first two are the average center y -coordinate (y_d) and the average vertical velocity (v_d) of the droplet, calculated by

$$y_d = \sum_{i,j} y_{i,j} N(\phi_{i,j}) / \sum_{i,j} N(\phi_{i,j}), \quad v_d = \sum_{i,j} v_{i,j} N(\phi_{i,j}) / \sum_{i,j} N(\phi_{i,j}) \quad (5.2a, b)$$

where the function $N(\phi)$ is defined as in Eq. (4.9) of last chapter. Besides them, the total kinetic energy of the droplet and that of the whole field calculated by

$$KE_d = \sum_{i,j} (1/2) |\vec{u}_{i,j}|^2 N(\phi_{i,j}), \quad KE_{total} = \sum_{i,j} (1/2) |\vec{u}_{i,j}|^2 \quad (5.3a, b)$$

are also monitored. To better appreciate the evolutions of the small regions around the three-phase point, the dynamic CA θ_{dyn} is extracted from the phase field. The calculation follows the formula by Ding & Spelt (2007a),

$$\theta_{dyn} = (180/\pi) \arccos[-(\vec{n} \cdot \nabla \phi) / |\nabla \phi|] \quad (5.4)$$

Two points to note are in order for Eq. (5.4). Firstly, the interface spans a few grid points, thus several values for θ_{dyn} are found across the interfacial region; but only the maximum one, which is the most accurate, is taken. Secondly, when the droplet is away from the surface after dewetting, θ_{dyn} is simply set to be 180° for convenience.

The last quantity to be calculated is R_x (as already defined in Subsection 3.4.3 in Chapter III). From R_x , the CL velocity V_{CL} is calculated by simple differentiation with respect to time. For instance, the CL velocity at time step t^n , V_{CL}^n , is obtained as,

$$V_{CL}^n = (R_x^n - R_x^{n-1})/\delta_t \quad (5.5)$$

where R_x^n (R_x^{n-1}) is the value recorded at t^n (t^{n-1}).

Some other parameters for simulations are listed in Table 5.2. Note that these parameters are in LU. For a general case, the kinematic viscosity ν and the surface tension σ may be calculated from the given Reynolds number Re and Capillary number Ca . However, for the present case, the characteristic velocity (maximum vertical velocity of droplet) is not known before the simulation. Thus, ν and σ are specified, which can be used to compute Re and Ca once the maximum vertical velocity of the droplet is obtained from the simulation.

Fig. 5.6 compares two series of snapshots of the droplet shapes every 10^3 steps for $\tilde{M} = 5$ and $\tilde{M} = 15$. For both cases, when the wettability is abruptly changed, the droplet begins to contract, approaching the equilibrium configuration; after some time the droplet shrinks to such a shape that corresponds to a CA larger than the static equilibrium one. After that, two different outcomes occur: if the mobility is small ($\tilde{M} = 5$), the droplet spreads after this overshoot, and thereafter experiences some oscillations on the wall until it obtains the shape of static equilibrium; by contrast, if the mobility is large enough ($\tilde{M} = 15$), the droplet jumps off the wall, oscillates as well but completely inside the ambient fluid and finally takes a circular shape. This resembles the experimental findings by Habenicht et al. (2005) to a large extent.

The dynamic CAs at the time steps shown in Fig. 5.6 are provided in Fig. 5.7. In all the three cases, the dynamic CA starts from about 90° in accordance with the initial condition. In the early stage, there are rather small differences between them: the dynamic CA just increases quickly to approach the equilibrium CA; after it approaches to the equilibrium one, it decreases slowly and then increases again. Significant differences occur between $t = 3 \times 10^3$ and 4×10^3 , after which the CA in the case with the largest mobility becomes 180° whereas for the other two it experiences some oscillations before returning to the equilibrium state.

In Fig. 5.8, the evolution of the droplet center and velocity in the vertical direction is given for $\tilde{M} = 5, 10$ and 15 . In agreement with the direct observations, when the mobility is small ($\tilde{M} = 5, 10$) y_d shows some oscillations before it finally reaches a constant value (~ 13) corresponding to the equilibrium configuration; but if $\tilde{M} = 15$, y_d almost keeps increasing until it becomes constant (~ 24) when all the kinetic energy has been dissipated. Based on the maximum droplet velocity ($v_d^{\max} \sim 0.004$), the Reynolds number and the capillary number are estimated to be $Re = v_d^{\max} R_d / \nu \sim 16$ and $Ca = (\rho_c \nu) v_d^{\max} / \sigma \sim 0.004$. In addition, the Cahn number is $Ch = W / R_d = 0.15$. Here the characteristic length is chosen as the drop radius. If it is chosen as the domain size, then the Cahn number will be 0.03. The Peclet number, $Pe = v_d^{\max} R_d^2 / [(1/2)\tilde{M}\delta_i] \sigma$, is within range of $42.7 \leq Pe \leq 128$ (dependent on M).

Fig. 5.9 compares the evolution of the kinetic energy of the droplet as well as the whole flow field under the three mobilities. From Fig. 5.9 it is seen that for all cases, the kinetic energy increases quickly at the initial stage, reaches a maximum and then

decays quickly. This corresponds to the transformation of the chemical potential energy (due to the initial non-equilibrium configuration) of the concentration field into kinetic energy of the flow field, and then vice versa. The larger the mobility is, the higher the extreme kinetic energy can reach. This may suggest that the mobility facilitates the release of the potential energy at the beginning, possibly due to the increase of CL velocity with increasing mobility. After this stage, the kinetic energy decays due to dissipation effects. It is interesting to note that, contrary to the maximum in the initial stage, the next-to-maximum of the kinetic energy decreases when the mobility increases. This is probably due to the fact that the dissipation by molecular diffusion increases with larger mobility and it becomes more significant in the later stages. Finally it is observed that the droplet experiences more oscillations if it is completely immersed in the ambient fluid than when it still stays attached on the wall. This is reasonable because the wall tends to exert larger retardating force on it.

Fig. 5.10 shows the evolutions of R_x on the wall from $t = 0$ to 2.5×10^4 for the three cases. This figure may illustrate the different evolutions of the droplet in a clearer way. It is found that R_x initially experiences some oscillations for $\tilde{M} = 5$ and 10 , and finally approaches a finite value (~ 8) corresponding to the configuration with static CA; when $\tilde{M} = 15$, R_x keeps decreasing and becomes zero at about $t = 3.6 \times 10^3$ which indicates that the droplet completely “jumps up”.

As mentioned earlier, the CL velocity, V_{CL} , can be obtained by differentiating R_x with respect to time. Its evolution is plotted in Fig. 5.11. Similar to the dynamic CA, the evolutions of V_{CL} in the early stage for different cases are rather close. But there

are some differences at the beginning: the magnitudes of V_{CL} at $t = 10$ for $\tilde{M} = 5, 10$ and 15 are $0.01103, 0.01771$ and 0.02264 respectively. For the case of $\tilde{M} = 15$, $|V_{CL}|$ displays a plunge before the droplet moves away from the wall (at about $t = 3.6 \times 10^3$). The reason may be related to the singularity that occurs at this specific stage. After that, $|V_{CL}|$ is not well defined; thus in Fig. 5.11 only the period during which the droplet was attached to the wall is shown. For the other two cases ($\tilde{M} = 5$ and 10), some oscillations and then a tendency to reach equilibrium are found, as expected from the evolution of R_x .

To obtain the critical value for mobility, many simulations have been carried out. Fig. 5.12 shows the evolutions of R_x from $t = 3000$ to 5500 for a series of mobility across the critical value. From this figure, it is seen that the critical \tilde{M} lies in between 10 to 10.1 (by a rough estimation, one may take $\tilde{M}_{cr} \approx 10.05$).

In addition, from this set of numerical experiments, the initial CL velocity (at $t = 10$) as a function of the mobility has been extracted (see Fig. 5.13). It is observed that the relation may be roughly described by a linear function ($V_{CL} \propto \tilde{M}$). However, it should be noted that this relation may hold only within a certain range of \tilde{M} and at the early stage of dewetting, plus under the capillary number regime investigated. At late stages, it may not hold because of the change of the droplet shape and other non-linear factors.

Finally, it would be interesting to compare the above results with the work by Fetzer et al. (2005), in which the dewetting process of a thin liquid film was studied both experimentally and by using a lubrication model with a slip condition. The radius of the hole and the rim profile were mainly investigated. It was found that two different lubrication models can result from slip lengths different by order of magnitude. That is quite similar to the present findings though here the dewetting of semi-circular droplets is investigated.

In the droplet dewetting process, the initial CA difference $\Delta\theta$ and the surface tension σ are certainly the two important factors. The variation of the critical mobility \tilde{M}_{cr} with $\Delta\theta$ (at a fixed σ), as well as its variation with σ (with $\Delta\theta$ fixed) are worth studying. Series of simulations varying θ while fixing σ (and vice versa) were carried out to find \tilde{M}_{cr} to the accuracy of 0.1, and the average value was chosen as the critical one (similar to the above case in which $\tilde{M}_{cr} \approx 10.05$).

Fig. 5.14 shows the variation of \tilde{M}_{cr} with $\Delta\theta$ (while the surface tension is fixed as $\sigma = 0.005$). The results are from eleven series of tests with the lower wall CA varying from 150° to 160° (at 1° interval). Note that the \tilde{M}_{cr} axis is plotted using log scale. It is seen that as the CA difference increases, the \tilde{M}_{cr} decreases which means that the droplet jumps off the surface easier. This can be understood from the direct physical analysis. Large $\Delta\theta$ is equivalent to large initial potential energy or driving force, thus bifurcation may still happen even when the slip on the wall (related to the mobility) is weak under such conditions. Another trend is that when $\Delta\theta$ decreases, \tilde{M}_{cr} seems to increase faster and faster (i.e., the rate of increase becomes larger as well). In Fig.

5.14, \tilde{M}_{cr} is in log scale and the data distribution seems to be close to one straight line (the dashed line drawn for reference) for relative small $\Delta\theta$ (roughly $\Delta\theta < 65^\circ$). It is close to another straight line (e.g., the dash-dot one) for relative large $\Delta\theta$ (roughly $\Delta\theta > 65^\circ$). For $\Delta\theta < 65^\circ$, one may deduce that \tilde{M}_{cr} may increase exponentially as $\Delta\theta$ decreases. In the simulations with $\Delta\theta = 55^\circ$ ($\theta = 145^\circ$) the bifurcation could no longer be observed, i.e., no matter how the mobility was varied, the droplet always stayed on the lower wall after the dewetting process. This indicates that at this CA, \tilde{M}_{cr} (if any) already exceeds the one that would guarantee numerical stability. At the other end, for $\Delta\theta > 65^\circ$, \tilde{M}_{cr} seems to decrease at a slower rate as $\Delta\theta$ increases.

The effect of the surface tension σ on \tilde{M}_{cr} can be found in Fig. 5.15. Five series of simulations with σ from 0.003 to 0.005 (at an interval of 0.0005) were performed at $\Delta\theta = 65^\circ$ (i.e., θ fixed to be 155°). Both \tilde{M}_{cr} and σ axes are plotted in log scale. It is found that the points are almost on a straight line (the dashed one). This suggests that the two may be related by $\tilde{M}_{cr} = C_2\sigma^{-C_1}$ where C_1 and C_2 are positive constants. It is obvious that \tilde{M}_{cr} decreases when σ increases. From the trend, it is possible that \tilde{M}_{cr} could go beyond the value that allows numerical stability as σ further decreases (to be far below 0.003); and for very large σ (to be much larger than 0.005), the droplet might jump away from the wall for any (numerically allowed) value of \tilde{M} (just like the situation for the $\tilde{M}_{cr} - \Delta\theta$ relation). However, the investigations of the two extremes are not within the scope of the present work. Besides, the $\tilde{M}_{cr} - \sigma$

relation deduced from Fig. 5.15 may not hold when $\Delta\theta$ varies. What it will be like as $\Delta\theta$ changes is left for future study.

5.4.1.2 Three-dimensional droplet dewetting

In addition to the 2D study, a few 3D dewetting simulations, which are supposedly to be closer to the real situations, have also been performed. The domain size is $90 \times 90 \times 50$, the initial droplet radius is set to be $R_d = 15$ and the droplet center is at $(X_C, Y_C, Z_C) = (45, 45, 0.5)$. The viscosity ν , the interface width W and other parameters remain the same as in the 2D study except that the surface tension is now smaller ($\sigma = 0.002$) (see Table 5.2). Like the 2D case, periodic boundary condition is implemented at all boundaries. Two values for the lower wall CA (145° and 150°) were tested. In both cases, bifurcations depending on the mobility were observed. For a brief capture, the final states for the case of $\theta = 145^\circ$ with the mobility being 4.5 and 5 are shown in Fig. 5.16. In Fig. 5.16(a), the droplet stays on the wall whereas it jumps off the surface in Fig. 5.16(b). The bifurcation diagrams in terms of the evolution of R_x (similar to the 2D definition, but now taken in the central $x-z$ plane) are given in Fig. 5.17. For the 3D case, the critical mobility \tilde{M}_{cr} is only found to the accuracy of 0.5. Using an estimation based on the average of the two mobilities across the critical one, \tilde{M}_{cr} would be 4.75 and 2.25 for $\theta = 145^\circ$ and 150° respectively. For the four cases ($\theta = 145^\circ$: $\tilde{M} = 4.5, 5$; $\theta = 150^\circ$: $\tilde{M} = 2, 2.5$), the recorded maximum droplet velocities in the z -direction (w_d^{\max}) (note that w_d is defined in a way similar to Eq. (5.2b)) are in the range from 0.0032 to 0.0034 (the mid-value 0.0033 is taken for convenience). Based on $w_d^{\max} \sim 0.0033$, the Reynolds

number and the capillary number are roughly given by $Re = w_d^{\max} R_d / \nu \sim 9.9$ and $Ca = (\rho_c \nu) w_d^{\max} / \sigma \sim 0.00825$. Besides, the Cahn number is $Ch = W / R_d = 0.2$, and the Peclet numbers, $Pe = w_d^{\max} R_d^2 / [(1/2) \tilde{M} \delta_i] \sigma$, are 371.25, 297, 165 and 148.5 respectively for $\tilde{M} = 2, 2.5, 4.5$ and 5. By comparing Fig. 5.17 with Fig. 5.12, one can see clearly that the 3D results do confirm the finding in the 2D study. That is, there is a critical mobility for bifurcation with a given CA.

5.4.2 Droplets on a chemically heterogeneous wall

Next some results about the mobility effects on 3D droplets on a flat wall with chemical heterogeneity are presented. The computations were done in a domain of size $50 \times 50 \times 25$ confined between two parallel walls at $z = 0$ and $z = 25$. On the other four sides, periodic boundary conditions were used; hence in equivalence a series of droplets are simulated and the neighboring droplets may coalesce with each other under certain conditions. Similar to the above cases of droplet dewetting, the initial conditions are given for the walls being neutral wetting and the droplets take hemispherical shape in equilibrium. The droplet radius is $R_d = 16.5$ and the droplet center is $(X_C, Y_C, Z_C) = (25, 25, 0)$. The wall at $z = 25$ is always kept neutral wetting. At the initial stage on the wall at $z = 0$, a narrow hydrophobic ($\tilde{\omega} = -0.432$, $\theta \approx 130^\circ$) stripe of width 6 is suddenly created near the center line of $x = 25$ (with slight asymmetry: 0.5 toward left) and all other parts are suddenly made hydrophilic ($\tilde{\omega} = 0.335$, $\theta \approx 60^\circ$) by some means (see Fig. 5.18; note that to better illustrate the situation, the right half ($50 \leq x \leq 100, 0 \leq y \leq 50, 0 \leq z \leq 25$), identical to the left, has been added). Some other parameters for simulations are listed in Table 5.3. For this problem, an average droplet velocity magnitude is defined by

$$|\vec{u}|_d = \sqrt{2 \sum_{i,j,k} (1/2) |\vec{u}_{i,j,k}|^2 N(\phi_{i,j,k}) / \sum_{i,j,k} N(\phi_{i,j,k})} \quad (5.6)$$

where the function $N(\phi)$ is defined as before.

The evolution of this system is monitored every 10^3 steps. Fig. 5.19 shows the snapshots of the system evolutions for $\tilde{M} = 2$ and $\tilde{M} = 20$. Note that the data for the right half ($50 \leq x \leq 100, 0 \leq y \leq 50, 0 \leq z \leq 25$) is duplicated from that for the left half in order to illustrate the evolution more clearly. It is easily seen that fundamental difference can be observed as a result of the change in mobility. Because the two cases evolved with different characteristic time, the snapshots were taken every 10^4 steps for $\tilde{M} = 2$ whereas the interval was 4×10^3 for $\tilde{M} = 20$. The evolutions of the average droplet $|\vec{u}|_d$ (as defined by Eq. (5.6)) are shown in Fig. 5.20. The observed maximum values of the droplet velocity, $|\vec{u}|_d^{\max}$, were 0.0017 and 0.0018 for $\tilde{M} = 2$ and $\tilde{M} = 20$ respectively. Their average, 0.00175, may be taken to roughly estimate the dimensionless numbers as, $Re = |\vec{u}|_d^{\max} R_d / \nu = 5.775$, $Ca = (\rho_c \nu) |\vec{u}|_d^{\max} / \sigma = 0.00875$, $Ch = W/R_d = 0.18$, and $Pe = |\vec{u}|_d^{\max} R_d^2 / [(1/2)\tilde{M}\delta_t] \sigma = 476.4$ for $\tilde{M} = 2$ and 47.64 for $\tilde{M} = 20$.

For both cases, the droplets are driven by the chemical heterogeneities towards the equilibrium configurations which minimize the total energy of the system. Probably due to the slight asymmetry in the position of the hydrophobic stripe, the droplets tend to move toward right; thus for each droplet the right tip is an advancing point and the left, receding. When the mobility is small, the droplets move much slower (smaller CL velocity). Note that both the advancing and receding speeds are small. But the

advancing point of the left droplet moves slower than the receding velocity of the right droplet and it is not able to catch up and coalesce with the right one; the droplets just experience some contractions when moving across the hydrophobic stripes and finally stay on the hydrophilic areas. If the mobility becomes much larger, the CL velocities of both the advancing and receding points increase. It seems that the increment in the advancing speed of the left droplet is more significant than that of the receding one of the right droplet. As a result, the left catches up with the right and merges with it. Eventually the all-connected large drop was again broken into small droplets staying on the hydrophilic parts separated by the hydrophobic stripes. It is noted that the two different processes are reflected in Fig. 5.20 as well. When the droplet was simply driven to the hydrophilic part without being splitted ($\tilde{M} = 2$), $|\vec{u}|_d$ had only two peaks; but when the droplet experiences the merging-and-splitting process ($\tilde{M} = 20$), $|\vec{u}|_d$ showed three peaks and decayed to zero much faster. Obviously, for this problem there should also be some critical value of the mobility which differentiates the two routes. However, it may require a lot of simulation efforts to obtain this value for the 3D cases and this is left for future work.

5.5 Summary and some remarks

In this chapter, the effects of the mobility on both mechanically and chemically driven droplets have been studied in the DIM framework. For the interfacial flows, the degree of non-equilibrium in the order parameter function is probably highest in the interfacial regions. Thus, the mobility is expected to play its role mostly in these regions as well. Near solid walls, such regions are limited to just the small areas near the CLs. It is the solution in such areas that determines the slip velocity and also the transformation rate of surface energy into the fluid interfacial energy (and, most

probably, further into the kinetic energy of the droplets or films). For both types of MPMC flows, the change of slip velocity with the mobility has been found under certain conditions. Through extensive numerical investigations of the droplet dewetting process (both 2D and 3D) and a preliminary 3D study of droplets on heterogeneous surfaces, it has been discovered that the mobility can decide the evolutionary routes and final equilibrium states (Huang et al. 2009b). The variations of the critical mobility with the driving “force” magnitude (initial CA difference) and surface tension have been obtained from the 2D study. These findings are expected to give some useful hints to future study of MPMC flows with CLs using DIM.

Table 5.1. Common parameters for simulations of a sitting droplet subject to a shear flow

Parameters	Value
Surface Tension	0.0025
Interface Width	3
Kinematic Viscosity	0.05
Wall Wettability (CA)	90°

Table 5.2. Common parameters for simulations of droplet dewetting

Parameters	Value
Surface Tension (2D / 3D)	0.005 / 0.002
Interface Width	3
Kinematic Viscosity	0.005
Upper Wall Wettability (CA)	90°

Table 5.3. Common parameters for simulations of droplets on heterogeneous substrates

Parameters	Value
Surface Tension	0.001
Interface Width	3
Kinematic Viscosity	0.005



Fig. 5.1. Initial condition for a sitting droplet under shear

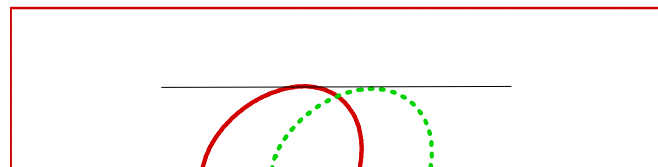


Fig. 5.2. Comparison of droplet configurations in steady state with different mobilities under small capillary numbers (solid: $\tilde{M} = 0.5$; dashed: $\tilde{M} = 10$) (note that the horizontal line is drawn just for reference)

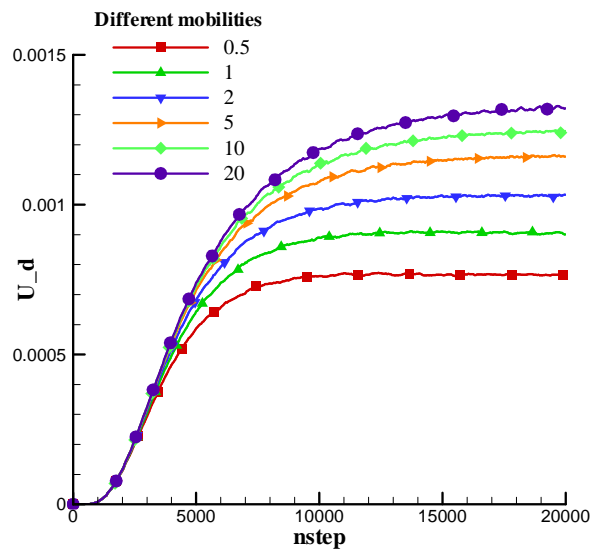


Fig. 5.3. Comparison of droplet velocity evolutions with different mobilities under small capillary numbers

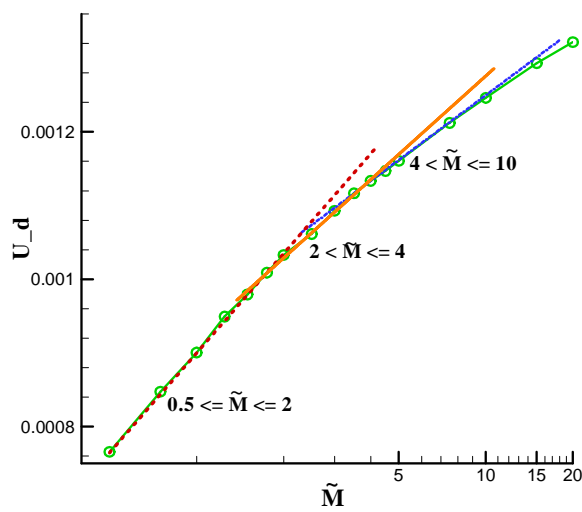


Fig. 5.4. Variation of the steady droplet velocity with the mobility \tilde{M} (note that the straight lines are drawn for reference)

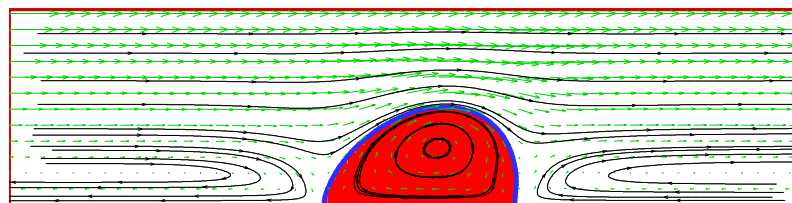
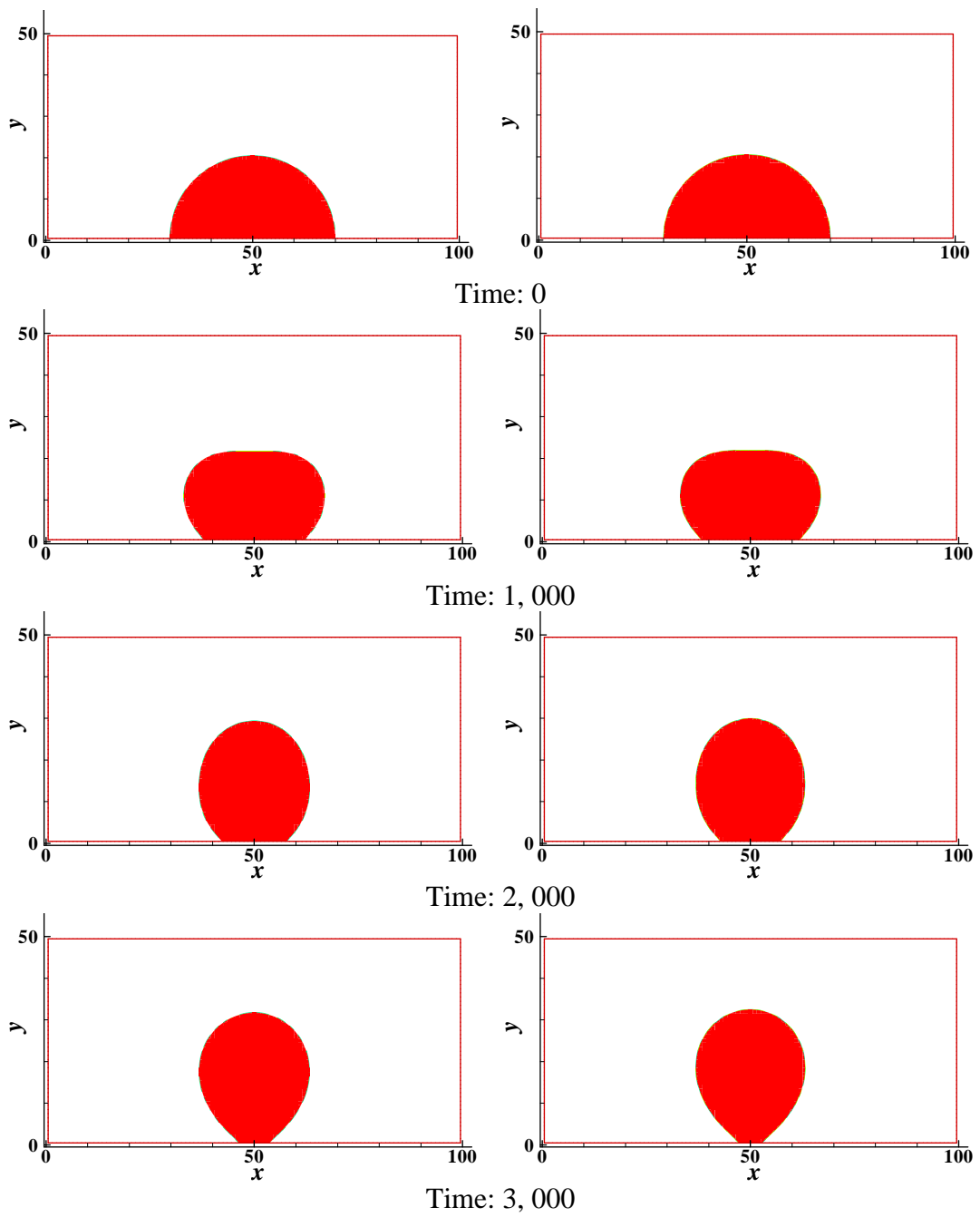


Fig. 5.5. Steady flow field (relative to the droplet) around a droplet for $\tilde{M} = 10$



(Fig. 5.6. to be continued)

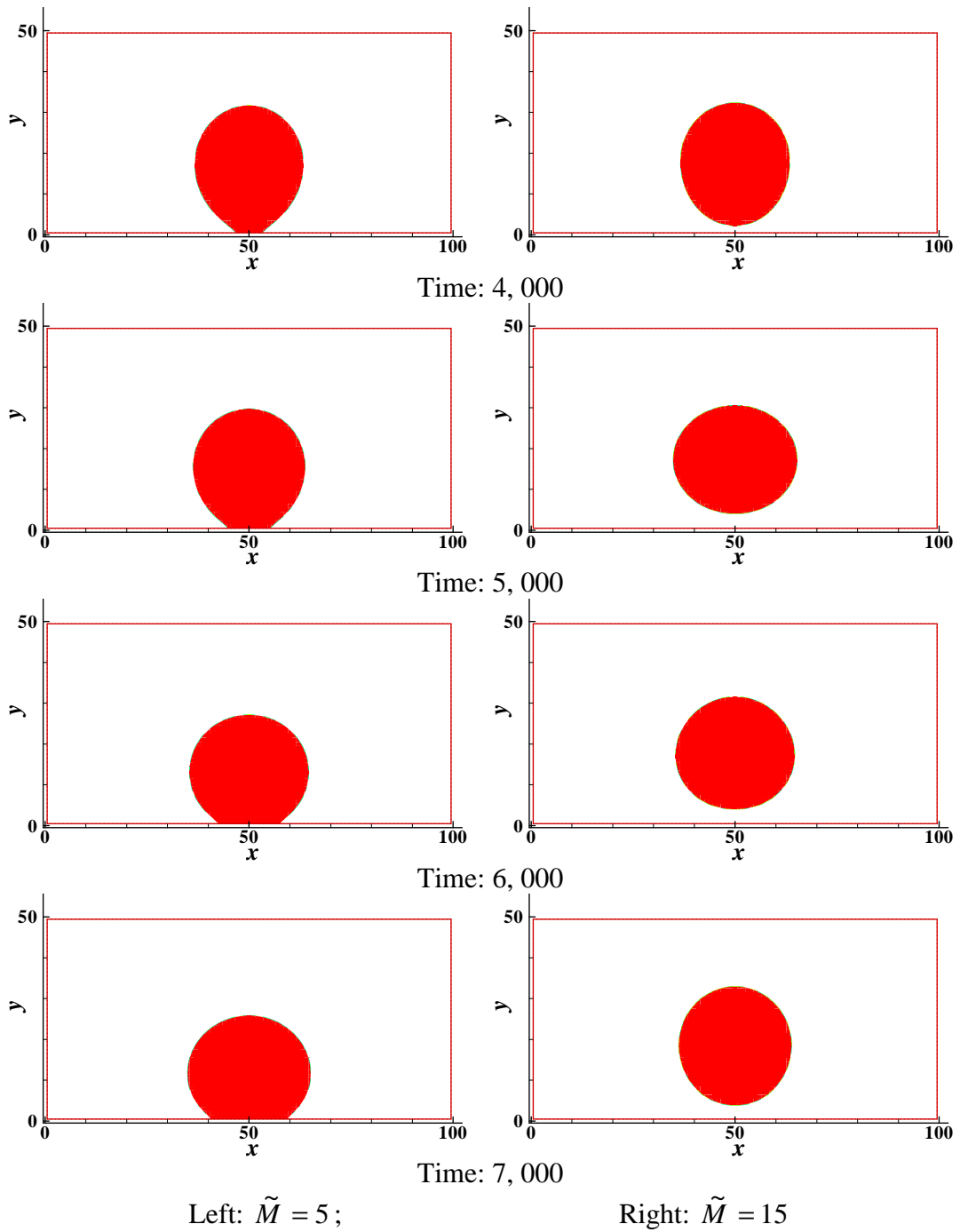


Fig. 5.6. Snapshots of droplet shapes every 10^3 steps after the wall wettability is suddenly switched from neutral wetting to very hydrophobic

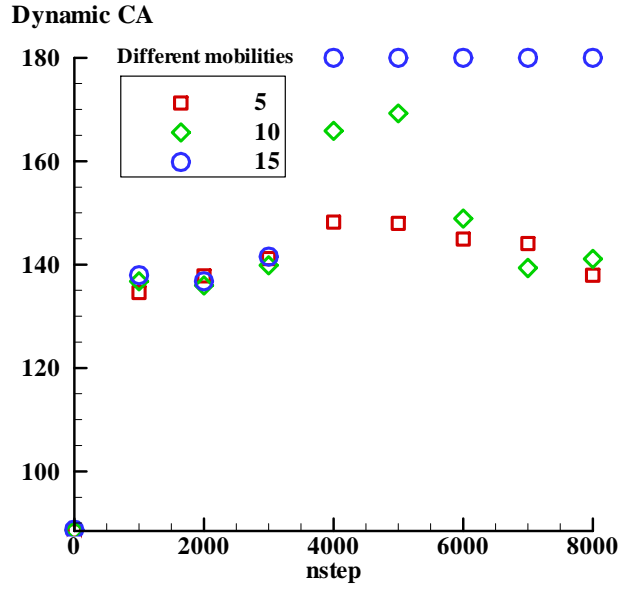


Fig. 5.7. Evolution of the dynamic CA at time intervals shown in Fig. 5.6

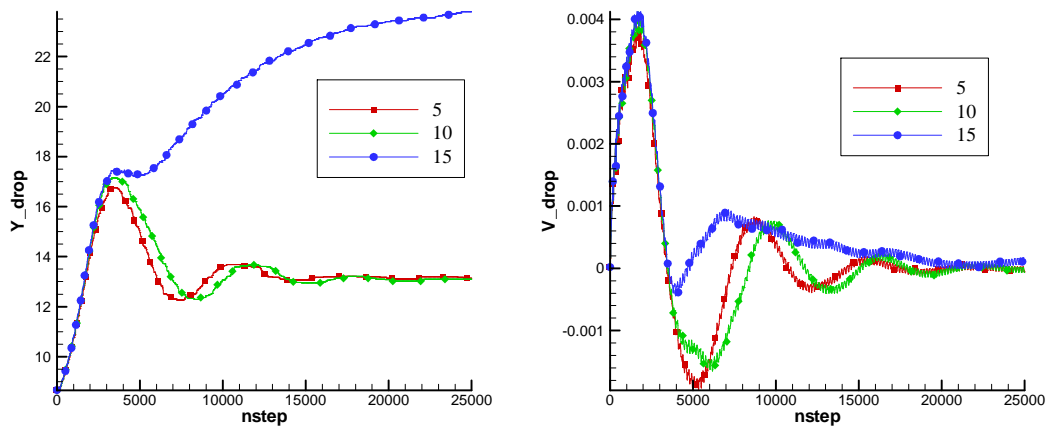


Fig. 5.8. Evolution of the average center y -coordinate (\bar{y}_{drop}) and the average vertical velocity (\bar{v}_{drop}) of the droplet under different mobilities

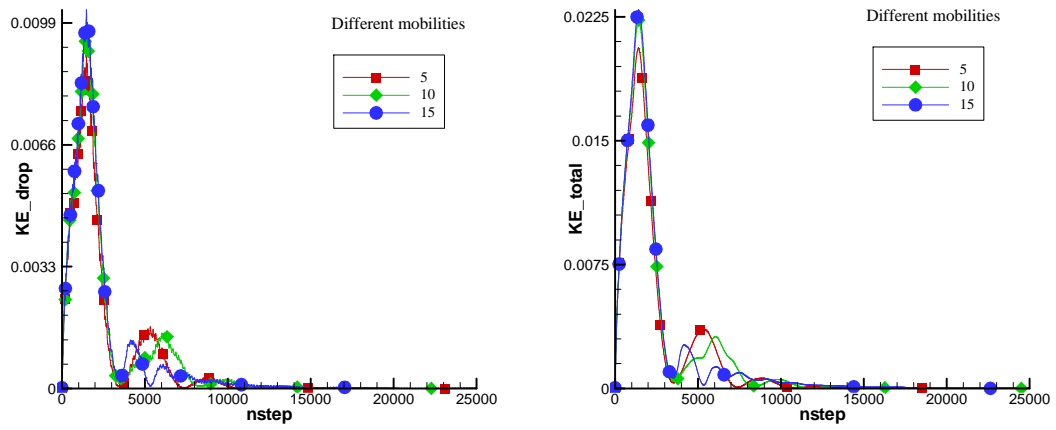


Fig. 5.9. Evolution of the kinetic energy of the droplet (KE_{drop}) and the whole flow field (KE_{total}) under different mobilities

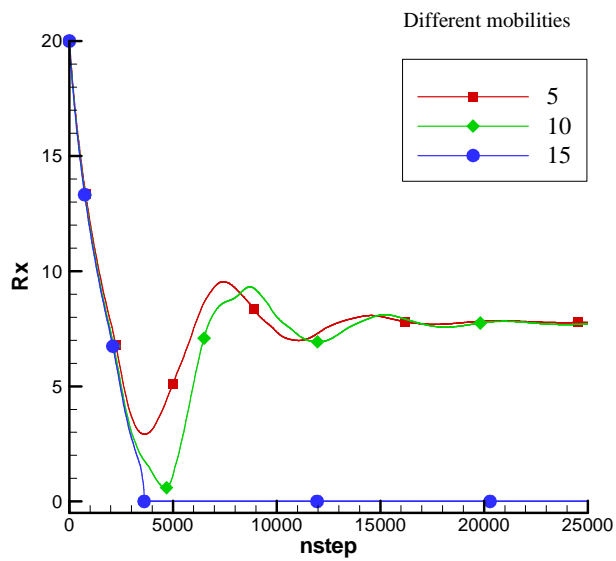


Fig. 5.10. Evolution of R_x on the wall for different mobilities

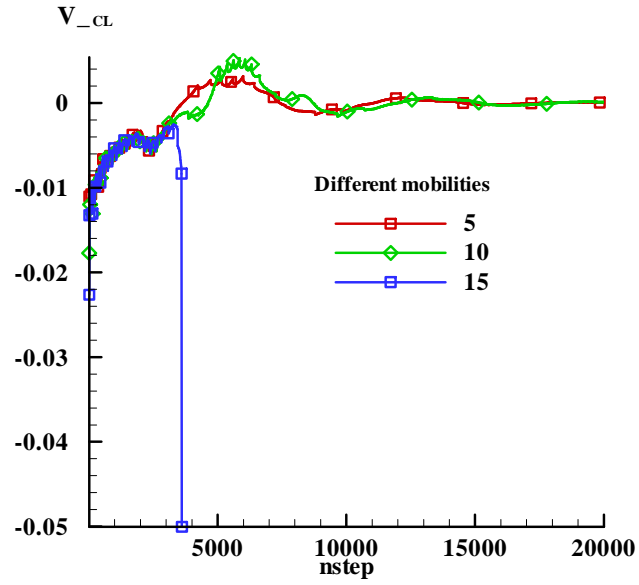


Fig. 5.11. Evolution of the CL velocity for different mobilities

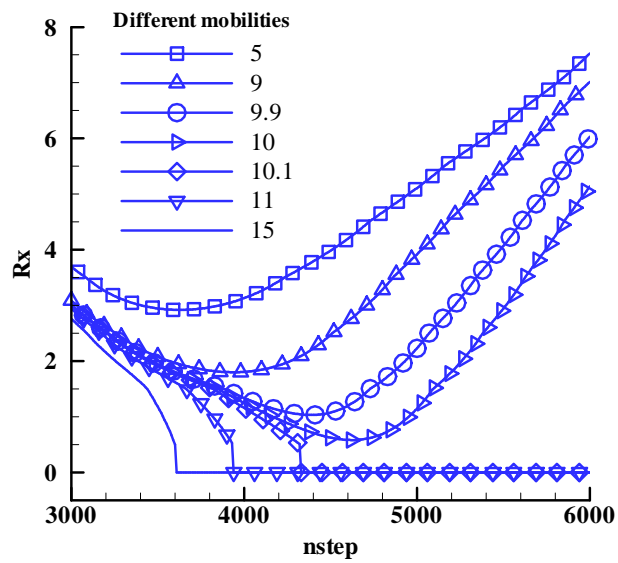


Fig. 5.12. Bifurcation diagram of the evolution of R_x under different mobilities

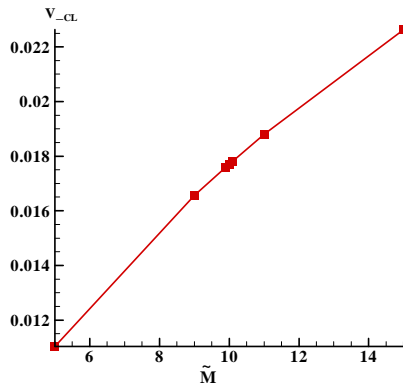


Fig. 5.13. Variation of the initial CL velocity with the mobility

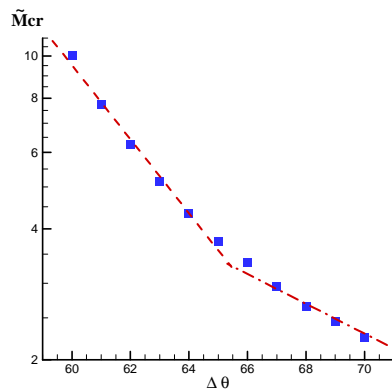


Fig. 5.14. Variation of the critical mobility with the initial CA difference (note that the dashed and the dash-dot lines are drawn for reference)

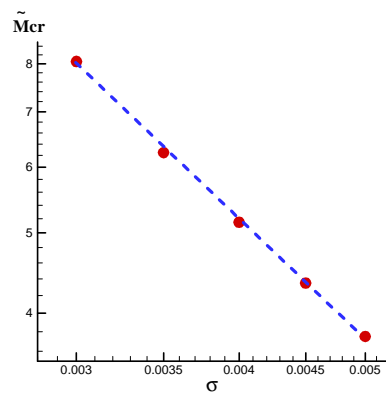


Fig. 5.15. Variation of the critical mobility with the surface tension (note that the dashed line is drawn for reference)

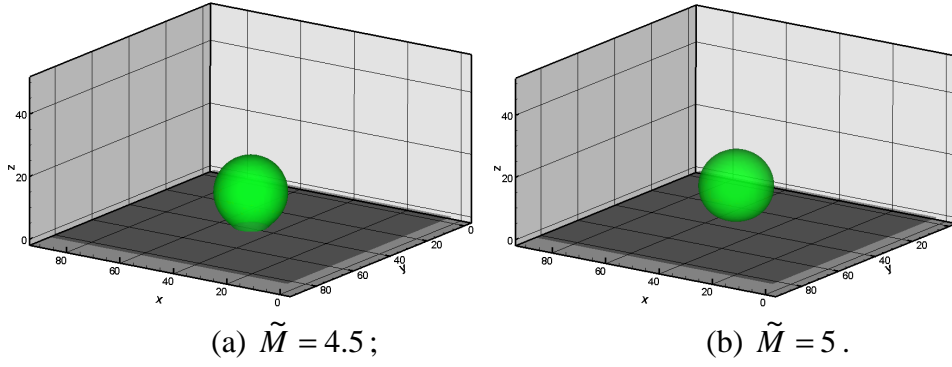


Fig. 5.16. Snapshots of the 3D droplet at the end of simulation (Time: 10, 000) for $\theta = 145^\circ$

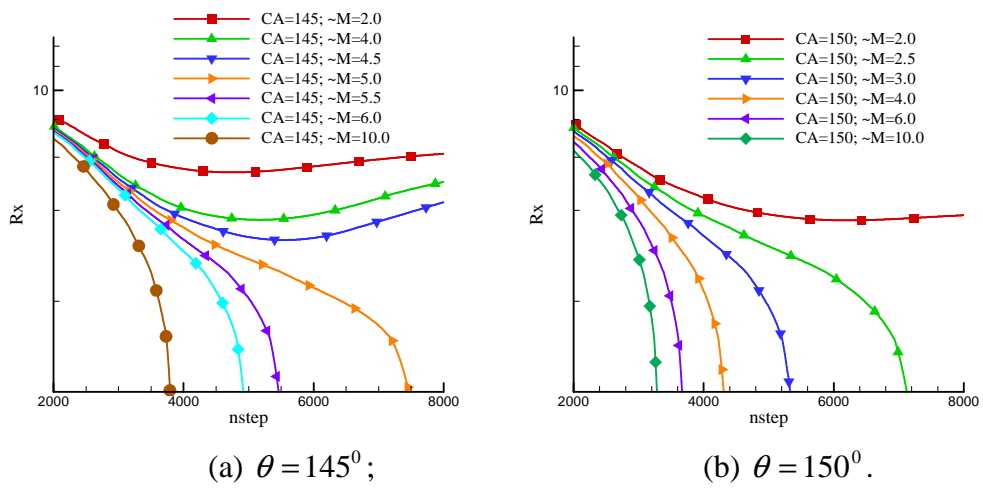


Fig. 5.17. Bifurcation diagram of evolution of R_x under different mobilities for a 3D droplet

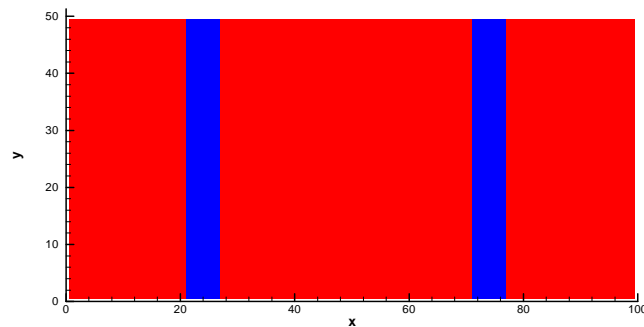


Fig. 5.18. Wettability distribution on the heterogeneous wall at $z = 0$ (slim stripe: hydrophobic; other parts: hydrophilic)

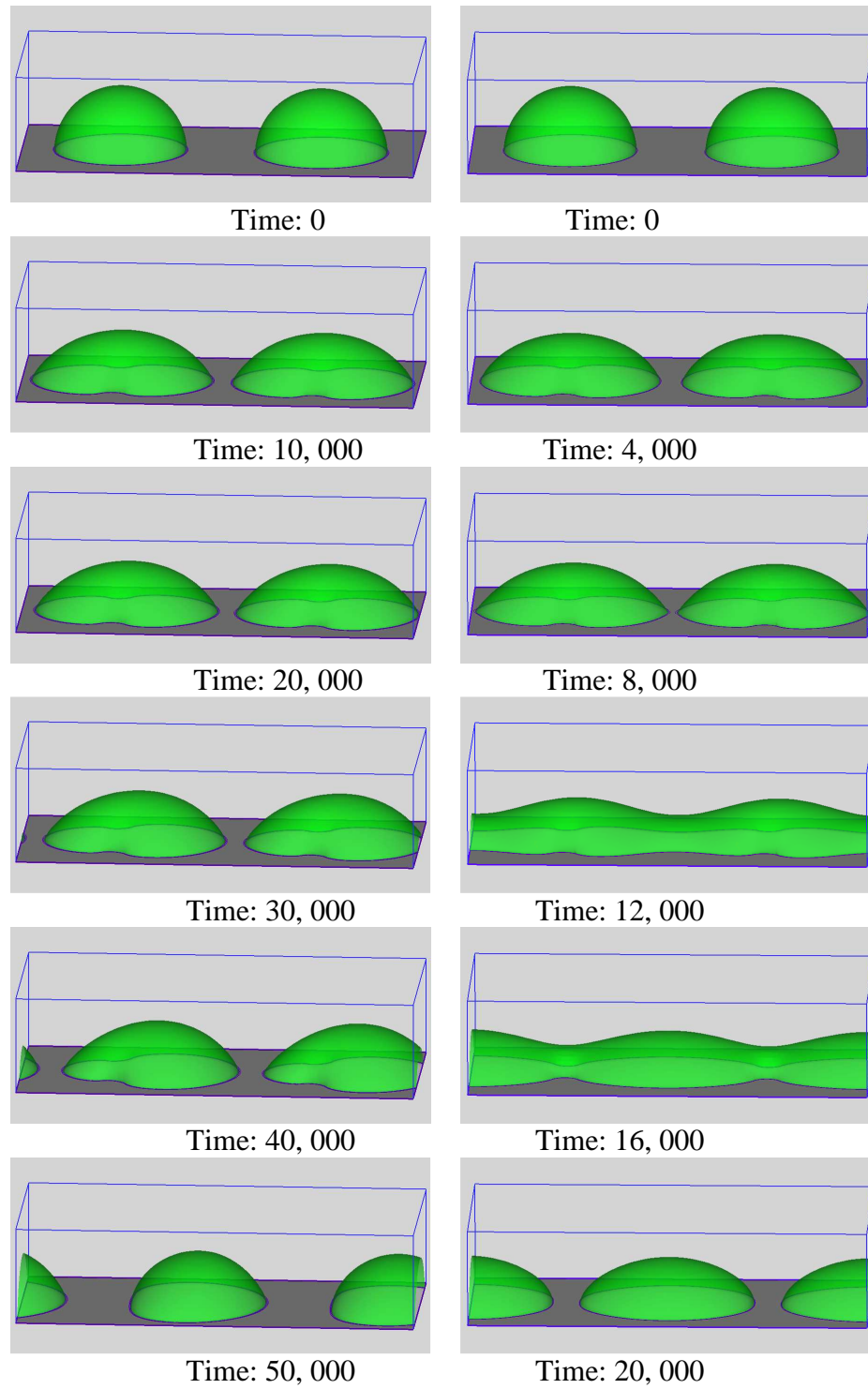


Fig. 5.19. Snapshots of droplet shapes for $\tilde{M} = 2$ (every 10^4 steps in left column) and for $\tilde{M} = 20$ (every 4×10^3 steps in right column) on chemically heterogeneous walls

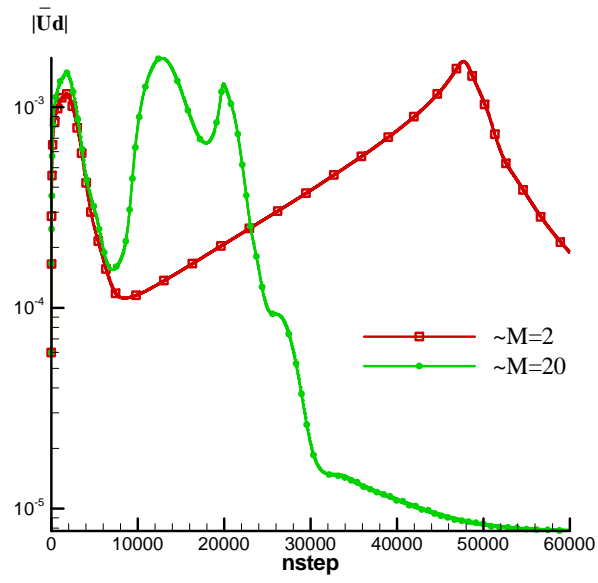


Fig. 5.20. Evolution of the average droplet velocity $|\bar{\mathbf{u}}|_d$ for $\tilde{M} = 2$ and $\tilde{M} = 20$

Chapter VI

Droplet Manipulation by Controlling Substrate Wettability¹²

In this chapter, a more realistic problem, namely the actuation and manipulation of droplets by surface modification, is studied by using FE2-LBM-B. Several designs of the controlling on the substrate wettability in both space and time are investigated and compared with each other in order to find an efficient way to direct droplet motions at small scales.

6.1 Droplet manipulation techniques in digital microfluidics

According to Stone et al. (2004), “devices and methods for controlling and manipulating fluid flows with length scales less than a millimeter” are referred to as microfluidics. Microfluidic devices offer the chance to revolutionize the way to perform various chemical and biological analyses (Squires & Quake 2005). The transport of fluid samples is one of the key steps for chemical synthesis and reactions. There are two types of microfluidic systems: one uses continuous flows, and the other uses discrete droplets (thus called “digital microfluidics”) (Pollack et al. 2002). Droplet manipulation is of fundamental importance in digital microfluidics. As stated at the beginning of this thesis, fluid flows in small devices are strongly affected by the boundary walls, and the wettability of the substrates can play a pivotal role in determining the flow pattern and the motions of the droplets in these devices. Thus, the droplet motions may be controlled through the wall wettability adjustment. Also

¹² Materials in this chapter have been published in J. J. Huang, C. Shu and Y. T. Chew. *Journal of Colloid and Interface Science*, 328, pp. 124-133 (2008).

noticeable is that recent developments in surface chemistry have enriched the methods to modify the substrate wettability, for instance by using light or controlling the temperature, which can be used to direct droplet motions at small scales (Liu et al. 2005). In parallel, applying controlled electrical fields has emerged as another promising way for droplet actuation by pseudo modification of the substrate wettability (Pollack et al. 2000, 2002). The underlying principles for driving droplets using these methods are similar, that is, to create some form of wettability gradient (WG) that further induces an imbalance of the forces acting on the droplets due to the system's tendency to approach a configuration with lower energy. Take a two-dimensional ribbon on a smooth substrate as an example. When the substrate has a small WG along the x – direction, the driving force can be found to be proportional to the gradient of the spreading parameter dS/dx , which might be related to the WG in analytical form (de Gennes et al. 2004). Note that here the spreading parameter is defined as $S \equiv \sigma_{sv} - (\sigma_{sl} + \sigma)$ (de Gennes et al. 2004) and “v” may denote “vacuum”, “air” or “another immiscible liquid”. For general situations in three dimensions, this force is a function of both the wettability distribution and the droplet shape (to be more specific, the TPL where each of the three phases meet the other two). When the FE theory including wetting (as described in Chapter II) is used, it has been shown that the substrate wettability can be solely characterized by a parameter $\tilde{\omega}$, where larger $\tilde{\omega}$ corresponds to more hydrophilic surface (smaller CA).

6.2 Simulations of droplet motion on substrates with spatiotemporally controlled wettability

Droplet behaviors on substrates with different wettability distributions are the main focus of this section. The wettability distributions are characterized by a constant

gradient (depicted by a linear function) or by a sharp gradient (depicted by a Heaviside function) of $\tilde{\omega}$. Intuitively, when an infinitesimally small droplet sits at a position with a constant WG, it may experience a constant driving force of finite magnitude toward the more wettable side. In contrast when the WG is sharp, such a force becomes infinitely large. In reality, these two types of WG are expected to result in different motion characteristics of the droplet. For the first one, the droplet velocity would be continuously increasing until the driving force is equal to the total viscous friction force; whereas for the second one, the droplet velocity would first increase to some peak value and then decay with time.

6.2.1 Descriptions of the problem and simulation

The detailed problem setups are given as follows. The initial condition is shown in Fig. 6.1: a stationary hemispherical droplet of diameter D_d sits on a smooth substrate at the bottom. Note that the hysteresis effects are assumed negligible, and so are the external body forces (gravitational, magnetic, etc.).

The domain size is $L_x \times L_y \times L_z = 4D_d \times 2D_d \times D_d$ and the initial droplet center is $(X_C, Y_C) = (D_d, D_d)$. Note that since the droplet is almost restricted to move on the substrate, only the (x, y) coordinates are concerned. Next, two types of bottom substrates with wettability distributions (in $\tilde{\omega}$) are introduced as shown in Fig. 6.2. In the first case, the WG is $\nabla \tilde{\omega} = d \tilde{\omega} / dx = (\tilde{\omega}_{\max} - \tilde{\omega}_{\min}) / (4D_d)$; in the second case, periodical abrupt jumps of $\tilde{\omega}$ (from $\tilde{\omega}_{\max}$ to $\tilde{\omega}_{\min}$, and vice versa) occur along the lines $x = nD_d$ ($n = 0, 1, 2, 3$), and $\tilde{\omega}$ is uniform in the patches separated by these lines. For both cases, the wettability variations are in the range $[\tilde{\omega}_{\min}, \tilde{\omega}_{\max}]$ where

$\tilde{\omega}_{\min} = -0.476$ approximately corresponds to a CA of $\theta_{phobic} \approx 135^\circ$ and $\tilde{\omega}_{\max} = 0.476$ corresponds to $\theta_{philic} \approx 45^\circ$.

The aim is to obtain continuous unidirectional droplet movement on these substrates. For the first case, this should be easy to achieve within the range of constant WG. But for the second case, the droplet initially sits across the two hydrophobic-hydrophilic patches and is expected to be pulled to the hydrophilic patch completely; after that it will meet the next hydrophobic patch and may be pinned at the transition line. To ensure continual motion, it is intuitively straightforward to switch the wettability of the patches to the opposite (e.g., in terms of the CA: $45^\circ \rightarrow 135^\circ$, $135^\circ \rightarrow 45^\circ$) at certain time, which bears some similarity to the principle used in the high energy particle accelerators or magnetic levitated high-speed train. However, this might not work for the “droplet accelerator” here under certain parameters (which will be shown later). Using very hydrophobic stripes to confine the droplet (similar to the idea used by Dupuis et al. (2005), Darhuber et al. (2003) and Kusumaatmaja & Yeomans (2007)) could help achieve this goal. Once the continuous droplet movement is realized in such a manner, it could possibly move much faster than on the substrate with constant WG. Hence, in addition to the two surface potential distributions in Fig. 6.2, a third case labeled (iii) with surface potential shown in Fig. 6.3 is included to illustrate the role of proper confinement by very hydrophobic stripes ($\tilde{\omega}_{conf} = -0.586$, $\theta_{conf} \approx 150^\circ$). In cases (ii) and (iii), the wettability is also periodically switched to the opposite at a frequency of $2\pi/T_{switch}$ (note: for case (iii) only the confined middle part of a width W_{conf} is switched).

Besides the bottom wall depicted above, it is assumed that there is a stationary wall with neutral wetting property ($\theta = 90^\circ$) on the top side and periodic boundary conditions are imposed on the other four sides. On the top and bottom walls, the half-way bounce back condition is used, and the wetting condition is implemented as described in Chapter II. The instantaneous droplet velocity $u_d(t)$ is calculated by simple averaging over the domain enclosed by the interface (similar to Eqs. (4.8) and (5.2b)), and the droplet position is calculated by integrating the droplet velocity as,

$$x_d(t) = x_d(t_0) + \int_{t_0}^t u_d(t) dt \quad (t \geq t_0) \quad (6.1)$$

where $x_d(t_0)$ is the starting position at time t_0 .

6.2.2 The parameters

Specific parameters are given as follows. The droplet diameter D_d is 45. Thus, the computational domain is $L_x \times L_y \times L_z = 180 \times 90 \times 45$. The surface tension σ is set to be 1.167×10^{-3} and the interface thickness spans about 3. The density and viscosity are assumed to be uniform everywhere ($\rho = 1$, $\nu = 0.005$) and the mobility \tilde{M} is fixed to be 10. The period for wettability switch in cases (ii) and (iii) is $T_{switch} = 18 \times 10^3$. The width of the confined part in case (iii) is $W_{conf} = 20$ (near to half of the droplet diameter). Based on the maximum velocities observed in the simulations, the Reynolds numbers ($Re = \rho U D_d / \eta$) are estimated to be in the range of $O(1) \sim O(10)$ and the Capillary numbers ($Ca = \eta U / \sigma$) are in the range of $O(10^{-3}) \sim O(10^{-2})$. When hydrophobic confinement was used, the droplet was allowed to first equilibrate for $T_{equil} = 9 \times 10^3$ time steps (i.e., to contract to stay between the confining stripes) during which the middle part was kept neutral wetting and the droplet did not move in the

x – direction (note that this period is excluded from the evolution of droplet velocity in the figures and is not counted, i.e., $t_0 = T_{equil}$ is chosen in this case); after that the sharp WG was applied and periodically switched. Some of the common parameters are summarized in Table 6.1.

6.2.3 Comparison of droplet motions under different controls

Fig. 6.4 shows the comparisons of the droplet velocity evolution and droplet velocity at different positions for the three cases. Note here only the velocity and position in the horizontal direction is studied. In Fig. 6.4(a) only the first 90×10^3 steps (i.e., $5T_{switch}$ for case (iii)) are plotted. The points “A”, “C”, “E” and “G” denote the time of the wettability switches for the first $3T_{switch}$ steps in (iii), and “B”, “D”, “F” are the mid points in each T_{switch} , which are also close to the peak values of the velocity. Their correspondents in the velocity-position graph are given in Fig. 6.4(b). In general, Fig. 6.4 is in accordance with the postulations given earlier. For case (i) (constant WG), the droplet is accelerated continuously but slowly, and the acceleration rate decreases with time; eventually it stops at the right end, as observed from Fig. 6.4(b), due to the pinning effect (note: periodic boundary condition used in the x – direction creates a jump in wettability at the two ends $x=0, L_x$). For case (ii) (sharp alternating WG), the droplet velocity only displays a surge for the first T_{switch} ; after that it varies slightly near zero, which means that the droplet almost stays at the same place (as seen from Fig. 6.4(b)). Overall, the droplet is transported fastest in case (iii) with both the hydrophobic confining stripes and the dynamic wettability switch. In each T_{switch} , the droplet velocity increases first (e.g., the paths “A”-“B”, “C”-“D”, “E”-“F”) and then decreases (e.g., the paths “B”-“C”, “D”-“E”, “F”-“G”). Note that

the variation of the droplet velocity in the first $3 \times T_{switch}$ steps shows some irregularities; but after the droplet adjusts its motion well, it becomes relatively more regular. In general, the trend agrees with that observed in the electrowetting experiment by Pollack et al. (2002) although the experimental setup is somewhat different. In spite of such oscillations, the droplet almost always keeps moving toward right and the average velocity over the whole period is much larger than that in case (i), leading to the rapid transport. More details on the droplet shape and the TPL for cases (ii) and (iii) are given below in an attempt to explain these observations better.

Fig. 6.5 shows the evolutions of the droplet shape and the TPL distribution in case (ii) for every 9×10^3 steps. Note that the substrate surface potential distribution (in $(-\tilde{\omega})$) is added as the background in each TPL distribution graph (“white” - hydrophilic; “light-green” - hydrophobic). It is seen that after the first 9×10^3 steps the droplet sticks to the second patch (initially hydrophilic) even when this patch is later switched to be hydrophobic. It is worth mentioning that several switch frequencies spanning a wide range have been tested and such a “stick-to-one-patch” phenomenon has always been observed. The reason may be that without the confining stripes the droplet spreads much more on the hydrophilic patch and the initial momentum along the x -direction is diverted to the other directions (y and z) due to the large pinning effect at the transition line where the wettability jump from hydrophilic to hydrophobic occurs. Subsequent changes of the wettability just cause the droplet to oscillate in the form of alternate spreading and dewetting, and this happens mostly in the z -direction on a single patch (see Figs. 6.5 (c-f)).

Similar snapshots for case (iii) are shown in Fig. 6.6. where the subfigures (a-e) correspond to the points “A” to “E” in Fig. 6.4. The blue parts in the TPL graphs

represent the very hydrophobic confining stripes. It is found that these confining stripes make the droplet contract and stay almost only in the middle part. Upon careful examinations of Fig. 6.6, it is interesting to observe that the motion takes the following steps. Initially the WG drives the lower part of the droplet, and under the action of surface tension, the upper part of the droplet is accelerated subsequently. Probably because of the lower friction at the fluid-fluid interface (as compared with the fluid-solid interface), this part obtains a larger average velocity. When the lower part is pinned at the transition line, the upper part continues moving forward and pulls the lower part to the next desirable position where it can absorb the energy from the wettability switch once more. Following this loop, the movement is sustained. Based on these observations, it seems that the continuous droplet movement critically depends on at least the following factors: (1) large WG; (2) proper confinement; (3) suitable droplet inertia. First, sufficiently strong wettability contrast provides large driving forces, thus results in the prompt acceleration of the droplet and makes inertia important. The function of the hydrophobic confining stripes is two folds: they not only prevent too much droplet spreading on the hydrophilic patch (as compared with case (ii)) but also reduce the pinning effect at the transition line. Finally the inertia of the droplet helps it overcome the energy barrier at the transition lines. It is worth mentioning that the functions of the WG and confining stripes are ultimately related to the TPL (including its length and its distribution on patches of different wettabilities). The TPL on different patches should be long enough for the droplet to gain sufficient driving force, and at the same time it should not be overly extended so that the pinning across the transition line does not prevent the droplet from reaching the next suitable position. Having said the advantages of the three factors, one should also be aware that they must be within certain ranges. Large WG would also lead to

very large energy barrier (or pinning effect). Strong confinement may reduce the driving force and if the flow is inertia-dominant, the surface tension would not play significant roles which may be unacceptable in the WG driven flows. In addition, the frequency of wettability switch should be important; so is the width of the middle part being confined. These two factors are further investigated in the following.

6.2.4 Effects of the switch frequency and confined stripe size

In the second and third type of surface control, the frequency of wettability switch, T_{sw} , should be important; and so is the width of the middle confined part, W_{conf} . More detailed studies of these two factors are reported in this subsection.

First, for a given W_{conf} (within the range that guarantees continuous droplet movement with a proper T_{sw}), varying T_{sw} is found to lead to several distinct droplet motions. Here a typical group of cases with $W_{conf} = 20$ are extensively discussed. Fig. 6.7 shows the droplet position evolution under a series of T_{sw} (12, 15, 16, 17, 18, 21, 22, 23, 24, 27) $\times 10^3$. When the frequency was excessively high (T_{sw} being small, e.g., $T_{sw}/10^3 = 12, 15$), the droplet was pulled back before it was able to move across the patch, and then it just moved backward and forward alternately in the x -direction near the wettability transition line. As T_{sw} increases (the frequency decreases) to a certain value (here around 16×10^3), the above problem disappears and the favorable continuous droplet movement is realized. The value (16×10^3) seems to be nearly optimal for this group of cases because further increasing T_{sw} leads to poorer performance (see the cases with $T_{sw}/10^3 = 17, 18, 21, 22$ even though the continuous

movement may be sustained). Note that the period was varied just at an interval of $\Delta T_{sw} = 10^3$. This applies for other cases shown below in search of the optimal period. Thus, “optimal” is meant only to such a degree of accuracy. For higher accuracy, more refined simulations are required. It is interesting to see that with even larger T_{sw} ($T_{sw}/10^3 = 23, 24, 27$), continuous movement is still achievable over certain time period; but the droplet may be in need of an initial adjustment (to first move backward and then forward, as for $T_{sw}/10^3 = 23$) or it may move in the opposite direction instead (for $T_{sw}/10^3 = 24, 27$). For all the three cases ($T_{sw}/10^3 = 23, 24, 27$), the droplet did not move as smoothly as in previous optimal or near-optimal cases, thus the transport efficiency was low. Another point to be mentioned is that when the frequency was too low (for $T_{sw}/10^3 = 27$), eventually the droplet would not receive timely energy input and got stuck at some position.

From the above it has been found that there seems to be a frequency range within which the desired movement can be achieved, and a possible optimum exists. Hence, it is worthy finding out in which way the droplet motions under different T_{sw} differ within such a range. Fig. 6.8 provides the evolution of the droplet velocity (see Fig. 6.8(a)) and the velocity at different positions (Fig. 6.8(b)) after the droplet has evolved into a stage of continuous movement for $T_{sw}/10^3 = 16, 17, 18$ with $W_{conf} = 20$. As already shown previously, the droplet has alternating accelerations and decelerations, but its velocity remains positive. It seems that the droplet gradually reaches a semi-steady state (in terms of one period averaging), but it reaches such a state relatively faster under larger T_{sw} . As T_{sw} increases, the maximum velocity the droplet achieved, U_{max} , remains almost unchanged (around 0.0035) whereas the

length of deceleration stage (the descending part) extends, and the minimum droplet velocity declines (e.g., in the last period shown in Fig. 6.8(a), it is about 0.0016, 0.0011 for $T_{sw}/10^3 = 16$ and 17 respectively, but only 0.0006 for $T_{sw}/10^3 = 18$). This delays the time for the droplet to reach the same position. Further examination of Fig. 6.8(b) reveals that the differences lie mostly in the late-deceleration and early-acceleration stages, and the velocity-position plots almost match each other for different T_{sw} over a large portion of the deceleration stage. This should be understandable because only the timing (not the place) to switch the surface wettability is considered. Also interesting is that in Fig. 6.8(b) the lines for different cases are somehow shifted closer than in Fig. 6.8(a).

In addition to the switch frequency, the width between the confining stripes also plays important roles in such systems as well. Several different values of W_{conf} have been tested, each with a series of switch frequency.

To study the effects of W_{conf} , a few cases for $W_{conf} = 30$ are presented below to compare with those in Fig. 6.8 with $W_{conf} = 20$. Note that the “local optimal” T_{sw} varies for different W_{conf} , and for $W_{conf} = 30$, numerical tests of different T_{sw} (varied by 10^3) show that now the optimum may be about $T_{sw}/10^3 = 13$. Fig. 6.9 gives the velocity-time and velocity-position plots for $T_{sw}/10^3 = 13, 14, 15$ with $W_{conf} = 30$. Fig. 6.9 generally shows some trends similar to Fig. 6.8. However, the amplitude of velocity oscillation for $W_{conf} = 30$ becomes much larger than that for $W_{conf} = 20$. The change in the oscillation amplitude is mainly due to the increase in the maximum

velocity (now $U_{\max} = 0.0045$ as compared with $U_{\max} = 0.0035$ for $W_{\text{conf}} = 20$), rather than due to the decrease of the minimum (though slight difference is still there).

Besides $W_{\text{conf}} = 30$, two other series with $W_{\text{conf}} = 24$ and $W_{\text{conf}} = 34$ have been run.

The respective optimal switch periods were found to be around $T_{\text{sw}}/10^3 = 14$ and 12.

Fig. 6.10 compares the evolution of droplet position with time for the four series

($W_{\text{conf}} = 20, 24, 30, 34$), each under its own optimal conditions ($T_{\text{sw}}/10^3 = 16, 14, 13,$

12 correspondingly). It is obvious that the droplet moves the fastest under $W_{\text{conf}} = 34$

with $T_{\text{sw}}/10^3 = 12$. However, as W_{conf} becomes larger, the speed of increment in the

transport capability seems to decrease, indicating that there may be an upper limit.

This trend is also seen in Fig. 6.11 which compares the velocity-position relations for

the four cases. Take the maximum droplet velocity U_{\max} at the last cycle shown in Fig.

6.11 for analysis. Simple calculations give the rates of change in maximum velocity

with respect to the change in W_{conf} , $\Delta U_{\max}/\Delta W_{\text{conf}}$, as follows: 1.175×10^{-4}

($W_{\text{conf}} = 20, 24$), 0.8×10^{-4} ($W_{\text{conf}} = 24, 30$) and 0.625×10^{-4} ($W_{\text{conf}} = 30, 34$).

Obviously, $\Delta U_{\max}/\Delta W_{\text{conf}}$ keeps decreasing. Subsequent tests with $W_{\text{conf}} = 40$

confirm indirectly the existence of such a limit since the desired droplet motion was

no longer observed with $W_{\text{conf}} = 40$ (not shown here). Thus, the critical width $W_{\text{conf}}^{\text{cr}}$

should have some value between 34 and 40 for the current investigation. Besides,

from Fig. 6.11, it is interesting to note that even when W_{conf} varies, the position where

U_{\max} is realized remains almost the same for all these cases.

The above observations quantitatively confirm some of the discussions in Subsection 6.2.3. That is, within a proper range, the longer the TPL near the WG (here the length is related to W_{conf}) is, the larger the driving force will be (as reflected from the maximum velocity). They also imply that as long as the continuous movement is achievable (or at least within the range tested, $20 \leq W_{conf} \leq 34$), the benefits due to the increase of W_{conf} seem to overtake the impedance effects caused by pinning (which also increases with W_{conf}). However, it is possible that the opposite might be true as W_{conf} further increases from some point up to W_{conf}^{cr} (though this range might be quite narrow). To find the “global optimal” parameters, careful adjustments and tests are required.

Finally, to have an overall picture on how the two factors, T_{sw} and W_{conf} , are related, the variation of the “local optimal” T_{sw} with W_{conf} is plotted in Fig. 6.12. Also shown in this figure is the change of the maximum droplet velocity, U_{max} , with W_{conf} , but of course in a different scale.

6.2.5 Effects of initial droplet position

For the above simulations with the third type of substrate control, the initial droplet center was set to be $(X_C, Y_C) = (D, D) = (45, 45)$ for which X_C coincides with the first wetting-non-wetting transition line. Under such a condition, the initial bottom area of droplet and the TPL on the wetting and non-wetting patches are equal. When the initial X_C is varied, they become unequal on the two contrasting patches and the droplet motion may be affected. A few simulations with different values of X_C

($X_C = 30, 34, 56, 60$) for one of the optimal parameter groups (for $X_C = 45$), namely $W_{conf} = 34$ and $T_{sw}/10^3 = 12$, have been carried out to investigate the initial position effect. For these cases, the change of X_C with respect to the original one ($X_C = 45$) are $\Delta X_C = -15, -11, 11, 15$ respectively.

Fig. 6.13 shows the droplet velocity evolution and Fig. 6.14 gives the change of droplet position with time for these cases. For better comparison, the case with $X_C = 45$ is also included in the figures. It is seen that the initial droplet position can become a determinant factor in deciding which direction the droplet would move. For the cases with $X_C = 30, 34$, there only exist some differences at the initial stage of acceleration (see Fig. 6.13) as compared with $X_C = 45$. After the initial adjustment, the droplet soon achieves the desirable state of continuously moving toward right. However, when $X_C = 60$, the initial adjustment stage is so different from the three cases that the droplet moves in the opposite direction after the initial stage. However, the average droplet velocity magnitude remains almost the same (around 0.004). Probably the most undesirable case is the one with $X_C = 56$. For such an initial position, the desired droplet motion cannot be realized and the droplet just oscillates near the second wetting-non-wetting transition line located at $x = 90$ (see Fig. 6.14).

The effects of the initial position may be understood from the following aspects. Essentially, the continuous droplet motion critically depends on the synchronization of the droplet motion and the acceleration due to the wettability gradient. Change in the initial position affects the amount of acceleration the droplet gains during the first period. Since the wettability distribution and its switch obey some preset pattern, the

initial acceleration (in terms of amount and duration) may determine if the above-mentioned synchronization is achievable. Based on these results, it seems that even when X_c is moderately shifted toward the non-wetting patch (e.g., about one third of the diameter for the case $X_c = 30$, $\Delta X_c = -15$), such synchronization is still realizable. But when shifted to the other side, the droplet seems to be less predictable and can move in opposite direction (as for $X_c = 60$, $\Delta X_c = 15$). The above conclusion is based on 4 case studies. A complete understanding of initial position effect may need more simulations and even under more parameter groups for W_{conf} and T_{sw} . This is left for future endeavor.

6.3 Some further discussions and remarks

In essence, the above workable scheme of driving droplets makes use of some kind of resonance effect (specifically, by matching the wettability switch frequency with the frequency of the droplet motion as determined by its inertia effect). It would be interesting to compare the present work with that by Daniel et al. (2005). In that work, the droplet motion was induced by asymmetric lateral vibrations of the substrate which was uniformly non-wetting. Thus, that scheme was purely mechanical. However, there are some similar aspects between the two. First, both schemes depend on the droplet inertia, thus the Reynolds number must not be too low. Second, both found different types of droplet motion under different “forcing” applied and possible optimal frequencies were identified. One possible advantage of the present scheme is that by tuning the frequency properly it is easier for the droplet to avoid backward motions (i.e., to retain positive velocities), which seems to be difficult when the substrate is vibrated back and forth. Of course in the present work only a scheme of

driving droplet is proposed by numerical simulations, and the means of switching the wettability is not specified yet. This is different from the work by Daniel et al. (2005) which also provides experimental demonstration.

Besides the above comparisons, some limitations of the present work may need to be addressed. Firstly, it is assumed that the patch size was almost the same as the droplet diameter. Thus, for a given substrate the above way of manipulation may apply for droplets of sizes within certain range. However, if the optical method is used to modify the wettability, as in the work by Ichimura et al. (2000), the restriction may be alleviated provided that the lighting sources can be flexibly fabricated; but at present there still seem to be difficulty in achieving a fast wettability switch using such kind of methods. Secondly, in this study, the substrates were assumed to be ideally smooth and hysteretic effects were neglected. Under many real situations when the substrates possess some microscopic chemical and/or topographical heterogeneity, it is harder to drive the droplet, and there may be a corresponding hysteresis in the droplet motion in response to the wettability switch. This issue was well elaborated by Walker & Shapiro (2006). Thus, future improvements of the present simulation model are necessary in order to take this effect into account. Nevertheless, the basic principles obtained in the current work should still apply. Another note is that it is most desirable to dynamically changing the wettability of the patches using some feedback systems to capture the instant position and shape of the droplet (perhaps more accurately, the information of the three-phase line). If such systems are successfully fabricated and integrated into microfluidic devices, it would become much easier and more flexible to manipulate the droplets through controlling surface wettabilities.

6.4 Summary

To summarize, the diverse behaviors of droplets on chemically-patterned substrates have been studied by LBM. Three types of wettability distributions (and temporal variations for two of them) of the substrate have been tested. It has been found that under certain conditions, the droplet displays rapid continuous unidirectional movement. The TPL has been identified to be especially important in affecting the droplet motion based on the observations under small scales. Besides, the droplet inertia has also been found necessary for the desirable outcome. For the most favorable setup, the trend of the “optimal” frequency variation with the size of the confined stripe has been roughly obtained. Within all the frequency-stripe size pairs, there seems to be a best one under a specific condition (e.g., surface tension and WG, etc.) (Huang et al. 2008). The effect of initial droplet position has also been studied preliminarily and it was discovered that the initial position would affect the droplet motion critically within certain range. The effects of many other factors, such as the fluid viscosity and droplet size, would require further studies. Nevertheless, the present findings would be helpful in giving some guidelines on manipulating droplets by surface wettability control in lab-on-a-chip systems.

Table 6.1. Common parameters for the droplet manipulation problem

Parameters	Value
Surface Tension	0.001167
Interface Width	3
Kinematic Viscosity	0.005
Domain Size	$180 \times 90 \times 45$
Droplet diameter	45

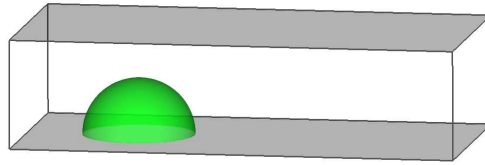


Fig. 6.1. Initial condition and problem setup for droplet manipulation

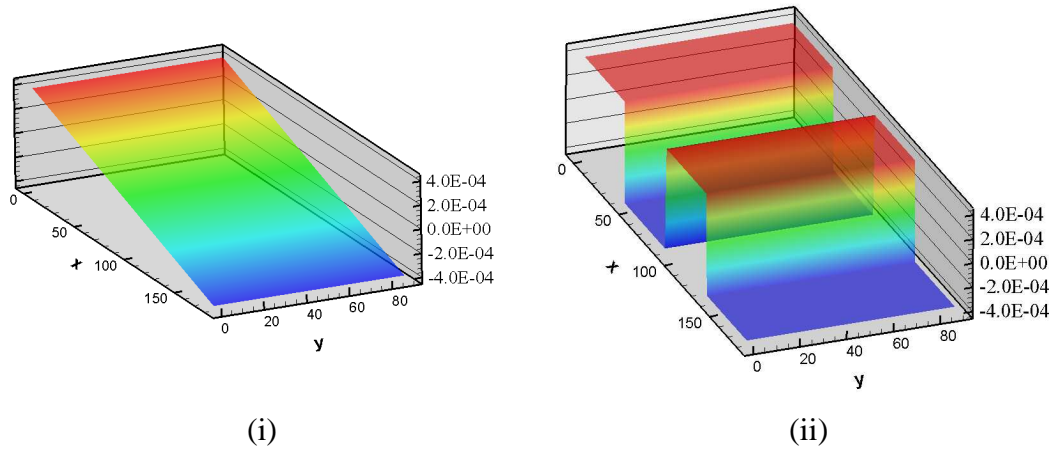


Fig. 6.2. Two types of surface potential distribution (in $-\tilde{\omega}$) of the substrate: (i) $\tilde{\omega}$ varies linearly from non-wetting to wetting ($d\tilde{\omega}/dx = \text{const}$); (ii) the substrate is made of alternating non-wetting-wetting patches of equal length ($d\tilde{\omega}/dx \rightarrow \pm\infty$ at the transition lines $x = nD$ ($n = 0,1,2,3$) and vanishes otherwise).

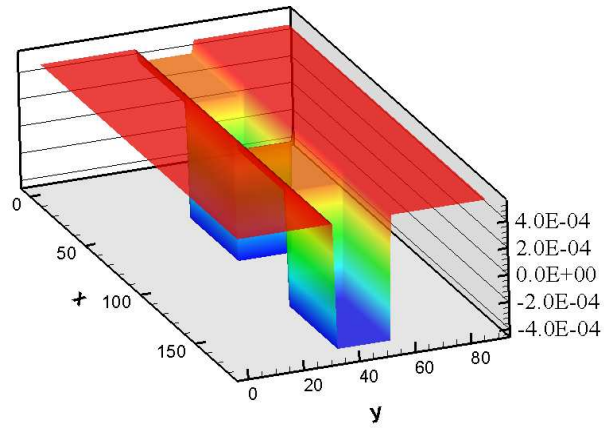
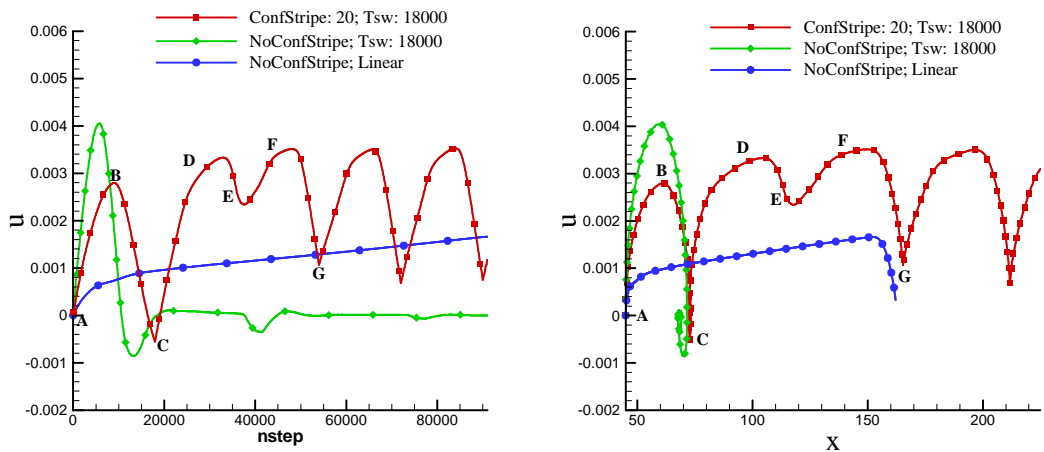


Fig. 6.3. The surface potential distribution (in $-\tilde{\omega}$) of the substrate in case (iii): similar to (ii) except that additional very non-wetting stripes are used to confine the droplet to move on the middle part of width W_{conf} .



(a) Droplet Velocity v.s. Time Step

(b) Droplet Velocity v.s. Droplet Position

Fig. 6.4. Evolution of the droplet velocity and the velocities at different positions

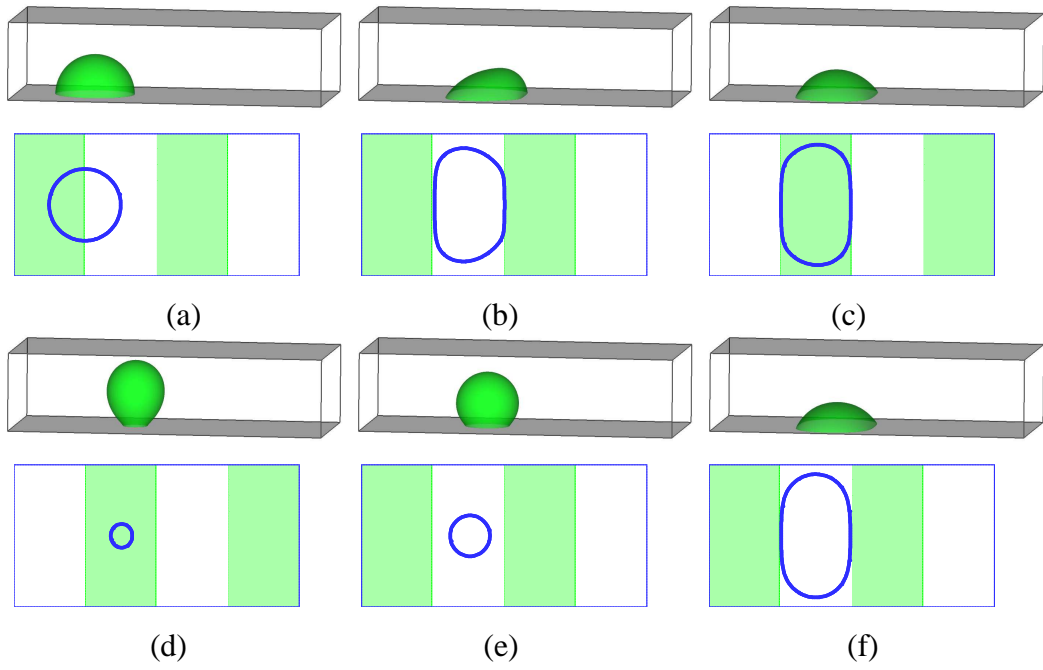


Fig. 6.5. The droplet shape and the TPL distribution every 9×10^3 steps for case (ii)

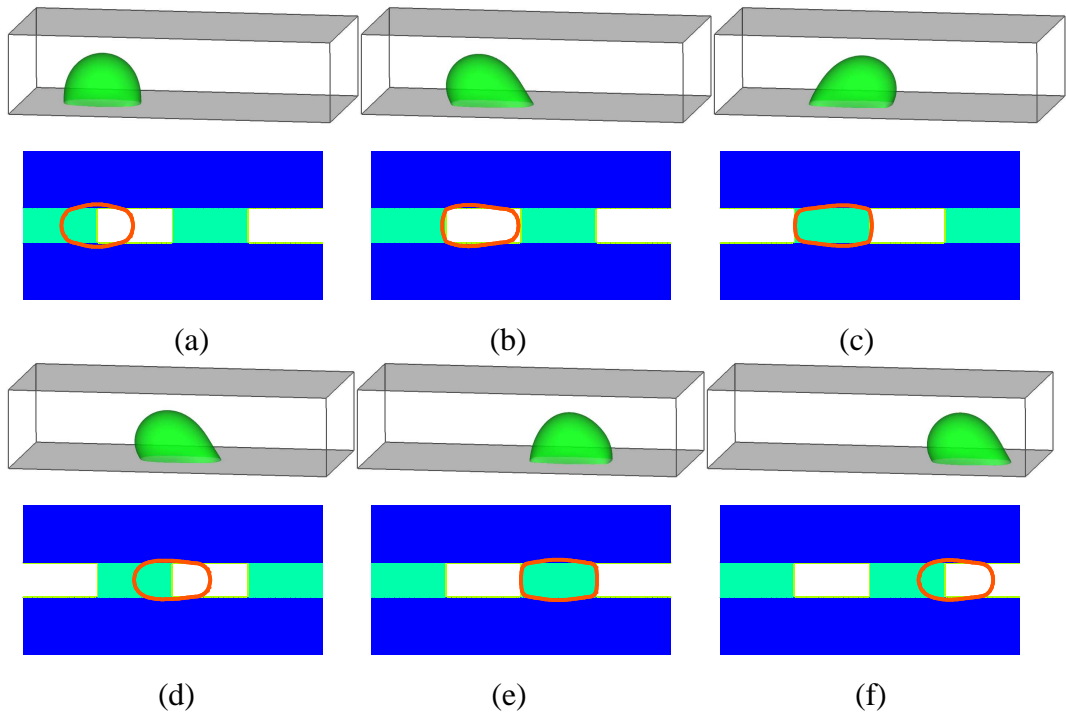


Fig. 6.6. The droplet shape and the TPL distribution every 9×10^3 steps for case (iii)

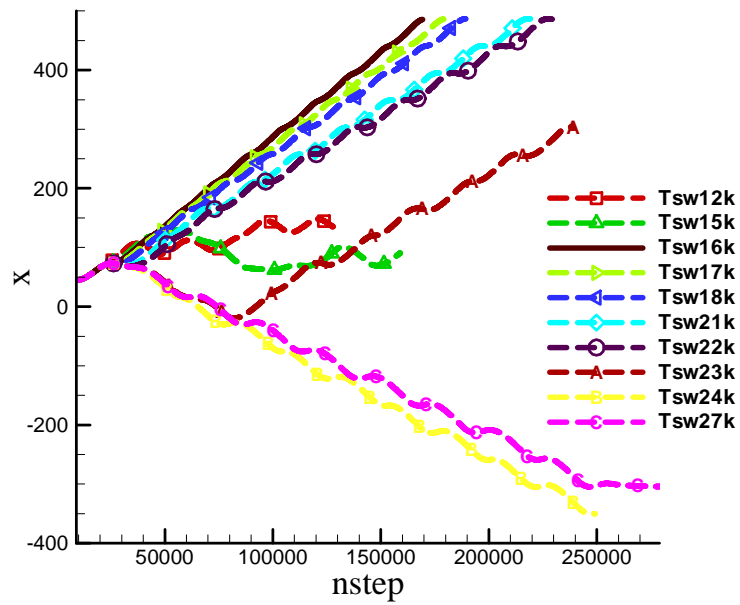


Fig. 6.7. Droplet position evolution $x_d(t)$ under different T_{switch} (12, 15, 16, 17, 18, 21, 22, 23, 24, 27($\times 10^3$)) with $W_{conf} = 20$

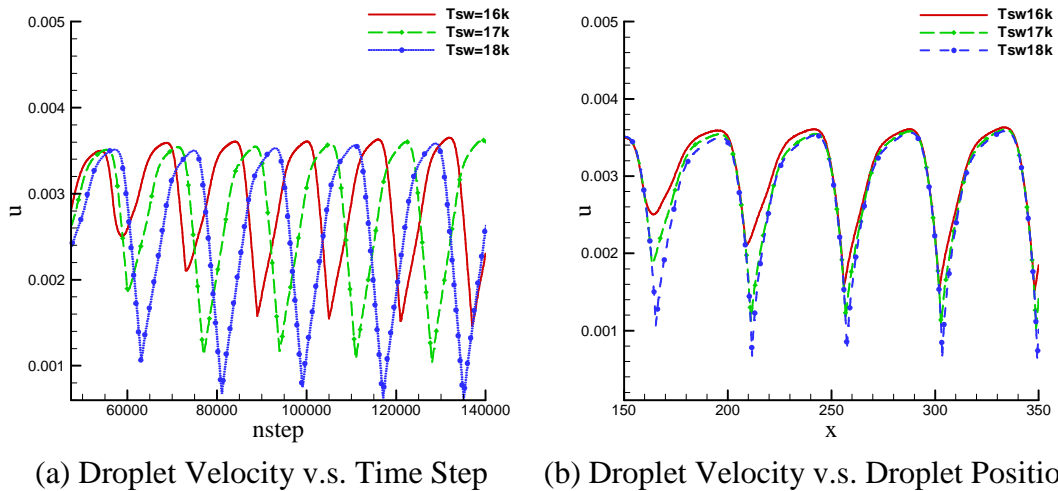


Fig. 6.8. Evolution of the droplet velocity and the velocities at different positions (after achieving continuous motions) under different T_{switch} (16, 17, 18($\times 10^3$)) with $W_{conf} = 20$

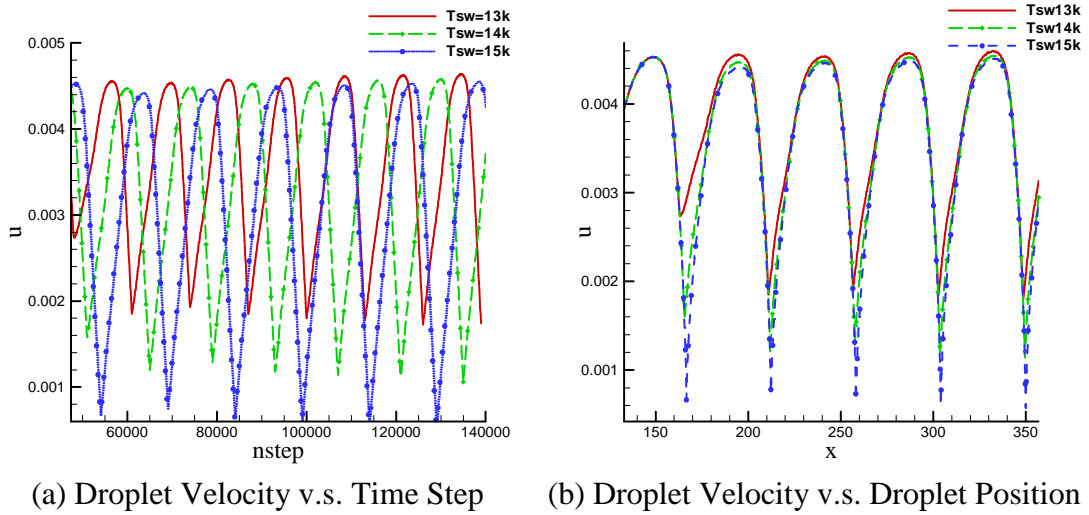


Fig. 6.9. Evolution of the droplet velocity and the velocities at different positions (after achieving continuous motions) under different T_{switch} (13, 14, 15($\times 10^3$)) with $W_{conf} = 30$

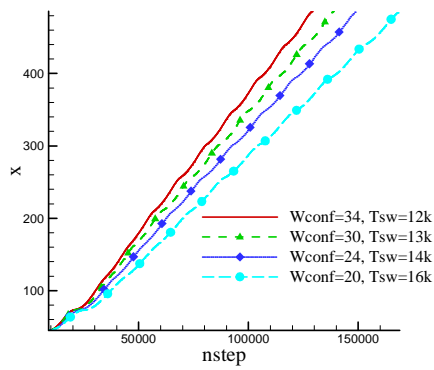


Fig. 6.10. Comparison of droplet position evolutions under four “local-optimal” conditions

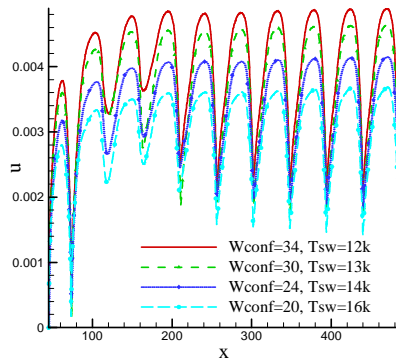


Fig. 6.11. Comparison of droplet velocity at different positions under four “local-optimal” conditions

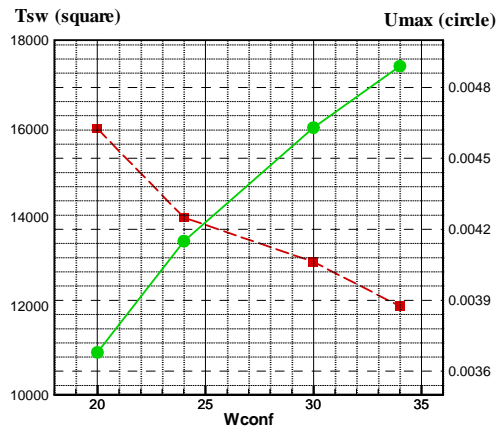


Fig. 6.12. Variations of the “local-optimal” period for wettability switch T_{switch} and the respective maximum droplet velocity U_{max} with the size of confined stripe W_{conf}

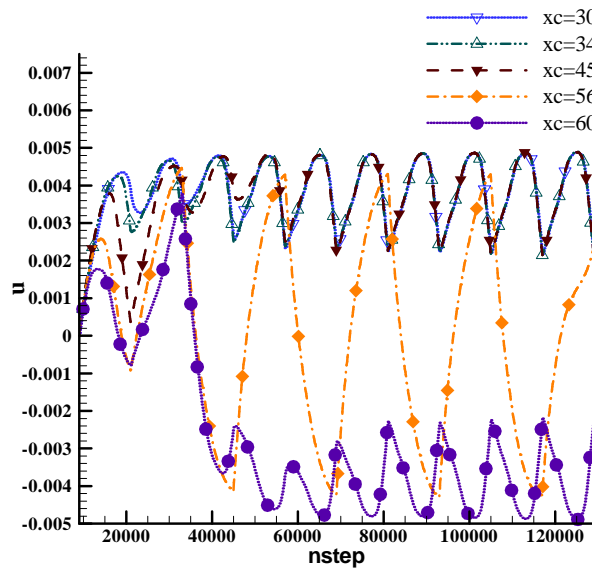


Fig. 6.13. Comparison of droplet velocity evolutions for different initial droplet positions $X_C = 30, 34, 45, 56, 60$

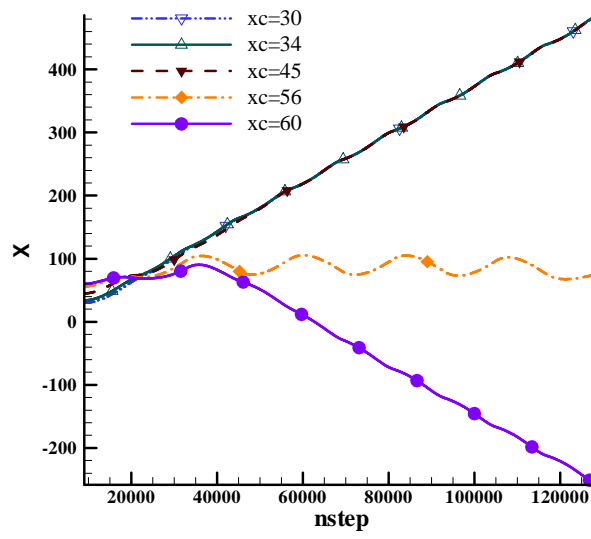


Fig. 6.14. Comparison of droplet position evolutions for different initial droplet positions $X_C = 30, 34, 45, 56, 60$

Chapter VII

***Bubble* Entrapment during Droplet Impact¹³**

In this chapter, droplet impact on dry surfaces is studied by using FE2-LBM-B with specific focus on the entrapment of *bubbles* during such processes. Numerous 3D simulations are performed and several types of entrapment are found under specific impact conditions. Dissections of the entrapment processes are carried out, and detailed analyses of the flow fields and interface motions are provided at selected moments for certain cases. The effects of various factors, including the Reynolds number, the Weber number and the surface wettability are analyzed. Finally, the impact condition to prevent entrapment is preliminarily estimated in terms of the Ohnesorge number upon examination of numerous simulations.

7.1 Introduction on bubble entrapment in droplet impact

Droplet-surface interactions are commonly encountered in many industry applications (e.g., ink-jet printing and surface coating). Depending on the impact conditions, various outcomes such as deposition, splashing, breaking-up and rebounding, may be observed (Yarin 2006). Besides, a special phenomenon, namely the entrapment of bubbles, may occur under certain specific conditions (Chandra & Avedisian 1991, Pasandideh-Fard et al. 1996, Thoroddsen & Sakakibara 1998, Fujimoto et al. 2000, Mehdi-Nejad et al. 2003, Thoroddsen et al. 2005, Khatavkar et al. 2007b). Chandra & Avedisian (1991) provided probably the earliest report of a kind of entrapment in

¹³ Materials in this chapter have been published in J. J. Huang, C. Shu and Y. T. Chew. Lattice Boltzmann study of bubble entrapment during droplet impact. (International Journal for Numerical Methods in Fluids, in press)

droplet-surface collision experiments. Later, Pasandideh-Fard et al. (1996) successfully captured it by numerical simulations using a VOF method. Thoroddsen & Sakakibara (1998) also managed to observe similar entrapment in their experimental study and gave more detailed theoretical explanations on its formation. After that, several specific studies, exclusively devoted to entrapped bubbles, appeared in the literature (Fujimoto et al. 2000, Mehdi-Nejad et al. 2003, Thoroddsen et al. 2005). Fujimoto et al. (2000) investigated experimentally a water droplet in air hitting a solid surface and reported a type of bubble entrapment due to an initial ring-shape contact. Mehdi-Nejad et al. (2003) simulated bubble entrappings for three types of impacting droplets in air (water, n-heptane and molten nickel) by using a VOF method. Excellent agreements were obtained between their numerical results and previous experimental photographs. The mechanism for the entrapment in that study was similar to that of Fujimoto et al. (2000). That is, a high pressure region develops under the central part of the gap between the droplet and the solid surface, which distorts the droplet interface and causes the ring-shape-like contact. Thoroddsen et al. (2005) showed time-resolved observations of the air disk entrapped resembling the above by using an ultra-high-speed video camera. Their work spanned a wide range of impacting conditions and a special type of compound droplet (liquid-in-air-in-liquid-in-air) was reported. Quite recently, Khatavkar et al. (2007b) used an axisymmetric DIM model to study droplet impact on a smooth, flat, and homogeneous surface, and successfully captured diverse impact behaviors under different conditions, including entrapped bubbles. Besides air-liquid systems, it is interesting to note that the entrapment phenomena also occur in immiscible binary fluids such as an oil-water system. In the work by Staicu & Mugele (2006), oil film entrapment due to

electrowetting and its destabilization (into micro droplets) was shown and the formation of these micro droplets was also analyzed theoretically.

Droplet-surface interactions are in general important in many practical applications. As noted by Thoroddsen et al. (2005), the study of entrapment is becoming even more important recently because of some quite new applications involving droplet impact, such as the fabrication of large displays and polymeric circuits through printing processes. In these applications, it is usually desirable to prevent the entrapment from occurring. Besides, the entrapment in systems other than air-liquid is relatively less studied. Thus, there is still a demand of more entrapment study in droplet impact under various conditions. For both the air-liquid and oil-water systems, the entrapment processes are determined by the interface motions and the underlying mechanisms are most likely the same. Here in this thesis the focus is exclusively on binary fluid systems with the ambient fluid having the same density and viscosity as the enclosed one. Thus, “bubble” does not actually mean air bubbles in a liquid; instead it is used to denote more general cases in which one fluid is surrounded by another (immiscible fluid). The model used here is a fully three-dimensional version of FE2-LBM-B. As compared with previous numerical studies of entrapment by Pasandideh-Fard et al. (1996), Mehdi-Nejad et al. (2003), and Khatavkar et al. (2007b), a unique feature of this work is that the simulations are fully three-dimensional other than axisymmetric. This feature is essential to capture some real 3D phenomena (further details to be given later).

7.2 Problem description and simulation setup

The basic simulation setup is shown in Fig. 7.1 (for illustration). All the following cases are 3D and have moderately large domain sizes ($L_x \times L_y \times L_z = 180 \times 180 \times 100$ or $240 \times 240 \times 120$). The quantities are given in LU. It is worth noting that no simplifications are made by assuming axisymmetric conditions; instead, a box domain is used and periodic conditions are applied for the four side planes. As compared with the axisymmetric simulations, such periodic conditions somehow introduce asymmetry along two angle groups ($0^\circ, 90^\circ, 180^\circ, 270^\circ$) and ($45^\circ, 135^\circ, 225^\circ, 315^\circ$) in the azimuthal direction. Although in many cases the impact process is almost axisymmetric, the introduced asymmetry becomes critical in some of them when the entrapped ring evolves into four or eight bubbles due to the interface instability. Such phenomena due to asymmetry cannot be captured in axisymmetric models. Initially, a droplet with a radius R_d is put at the center ($(X_C, Y_C) = (L_x/2, L_y/2)$), close to the bottom wall ($Z_C = R_d + 6$, i.e., the lowest point of the droplet is 6 away from the wall), and also a velocity U_z (with a negative value) is given in the z direction. Under such conditions, there are still certain symmetries, namely, symmetries about the middle $x-z$ and $y-z$ planes. Thus, in the simulation, only a quarter of the domain is actually used and it is noted that in the figures shown below, data in the other parts are duplicated according to the symmetric conditions. The surface tension is σ . For this particular problem, the Reynolds and Weber numbers are defined as,

$$\text{Re} = 2R_d |U_z| / \nu, \quad (7.1)$$

$$\text{We} = 2R_d \rho |U_z|^2 / \sigma \quad (7.2)$$

For droplet impact dynamics, the Ohnesorge number is often used. It is defined as

$$Oh = \rho\nu / \sqrt{\rho\sigma(2R_d)} \quad (7.3)$$

As given in Chapter I, Oh can also be written as $Oh = We^{1/2} Re^{-1}$.

The impact velocity U_z is either -0.01 or -0.05 (thus the nearly-incompressible condition for LBM is satisfied), the radius R_d is equal to 30, 40 or 50, the viscosity ν takes either 0.005 or 0.02, and the surface tension is fixed to be 0.001. The interface thickness is roughly 3 and the mobility is 0.5 (provided that $\tau_g = 1$). The Cahn number ($Ch = W/(2R_d)$) takes one of the following values, 0.05, 0.0375 and 0.03 (corresponding to the above three drop radii respectively). The Peclet number ($Pe = U_z(2R_d)^2/M\sigma$) will be given for each specific case later. Besides, the CA (in static equilibrium) for the bottom wall is θ , having one of the following three values: 75° , 90° and 105° .

7.3 Results and discussion

Next, four different types (I-IV) of entrapment due to different impact conditions (Re and We), as well as surface wettabilities (θ), are reported and analyzed. Three of them are distinctive and another one may be viewed as a combination of two of them. It is worth mentioning that numerous cases have been investigated and the cases presented here are picked from them as typical representations of various entrapment phenomena. The evolution of the interfaces in the middle $x-z$ plane, as well as the TPLs in the bottom $x-y$ plane are examined. Some types may contain more than one case. In the middle $x-z$ planes, the instantaneous velocity fields are also overlaid to provide more insights into the whole fluid motion and its interaction with

the interfaces. For a clear overview, key parameters for all cases are listed in Table 7.1 and some other simulation parameters are given in Table 7.2.

7.3.1 Types I and II: Entrapment during slow impact

In the first and second types, the impact velocity is relatively small ($U_z = -0.01$) and the Weber number is also small (≤ 10).

For the first type, two cases are presented with drop radius $R_d = 40$ and 30 ($We = 8$ and 6 , $Re = 160$ and 120 , respectively). The nominal Peclet numbers based on initial velocity are 1.28×10^5 and 7.2×10^4 . The CA is $\theta = 90^\circ$. In both of them, initially the droplet approaches the wall slowly. During this period, the droplet deforms and becomes relatively flat (especially when near the solid wall), and a gap of roughly equal height develops. After certain time, part of this gap is enclosed by the droplet and the wall, somehow forming a flat disk. But once the droplet touches the wall (here in the form of a ring, see Fig. 7.2), the TPLs move in such a way that the droplet configuration corresponds to the equilibrium CA, as required by the force balance. Since the Weber number is small, the surface tension effect tends to be dominant in this type. The two cases in Type I are slightly different, as seen from the snapshots taken in the middle $x-z$ plane at $t = 18000$ (see Figs. 7.3 and 7.4). Note that the length scale for the snapshots of the middle $x-z$ plane in these two figures is different from that in the bottom plane in Fig. 7.2. Besides, the time periods for significant variations in the two planes are not the same; therefore the snapshots in the middle plane do not exactly match those at the bottom. This also applies for other figures shown later.

The Weber number of Case 1 is slightly larger ($We = 8$) than Case 2 ($We = 6$) because of the change of the droplet radius. This makes the size of the entrapped disk in Case 1 become larger and hence more unstable. It is observed that the central part of the upper surface of the disk is bended toward the wall in Case 1, whereas in Case 2 the entrapped part quickly assumes a spherical shape. Figs. 7.5 and 7.6 give closer views of the flow fields near the contact line regions for the two cases, at two selected moments of interest ($t = 18000$ and $t = 24000$). It is easy to see that there exist three major vortices in Case 1 at $t = 18000$. The outer lower one is due to the spreading motion which appears to be the most dominant one at this stage. It is interesting to note that similar pattern has been reported elsewhere (see Fig. 3 in the work by Ding & Spelt (2007b)) during initial droplet spreading. Besides this major one, there is an inner lower one that seems to be caused by contraction of the entrapped bubble. Finally, on the upper side there is another vortex. Its formation may be understood as follows: as the outer contact line (ring) moved outward, the outer interface was highly bended and a capillary wave propagated upwards, causing that part to move upward temporarily; at the same time the outer fluid was moving downward to fill in the vacant space. Such a mutual motion led to this third vortex. After this stage was over, the whole system became closer to equilibrium, the motions became mild and the vortices disappeared (as found at $t = 24000$ in Fig. 7.5).

In Case 2 at $t = 18000$, the outer spreading motion seems to be in an earlier stage as the outer lower vortex appears to be less violent and much lower (closer to the contact line, see Fig. 7.6); and there is no inner vortex observed probably because the entrapped bubble did not start to contract yet. As time progressed, the outer lower vortex moved upward whereas a small inner vortex came into being around the

entrapped bubble (as seen at $t = 24000$ in Fig. 7.6). For the two cases, the evolution of the entrapped bubble diameter (diameter of the inner circle in the bottom plane D_{in}) and the spreading process (as reflected from the outer circle in the bottom plane D_{out}) were also monitored (see Fig. 7.7).

Based on the observations, it may be deduced that when the droplet radius is increased, the initial entrapped disk size is expected to be enlarged as well. One possible further consequence is that beyond certain value, the central part will pinch off and generate a child droplet, as found by Thoroddsen et al. (2005). For such cases, the propagation of the capillary wave from the circumference to the center has to be fast enough so that the pinch-off can occur timely; otherwise the parent droplet will contact the wall from the center and spread out, as shown below in the second type.

In the second type, the Weber number and Reynolds number are a little larger than in the first type, due to the increase of the droplet radius. Now the drop radius is $R_d = 50$, and the Weber number is $We = 10$, and the corresponding Reynolds number is $Re = 200$. The Peclet number is $Pe = 2 \times 10^5$. For this type, there are also two cases presented here. These two cases are different only in the CA ($\theta = 90^\circ$ and 75°). Typical results are shown in Figs. 7.8-7.11.

For this type the initial disk of surrounding fluid under the droplet has such large volume that the surface tension is not strong enough to pull the fluid together to form a dome. Thus, the disk collapses from the center (see the snapshots at $t = 18000$ in Figs. 7.8 and 7.9, and that at $t = 16000$ in Fig. 7.11). After the central tip contacts the wall, spreading occurs from there and the flat disk becomes an entrapped ring (see the

snapshot at $t = 22000$ in Fig. 7.9, and that at $t = 18000$ in Fig. 7.11). Under the specific simulation conditions (with four corners and four sides), the ring is not stable and may either evolve into four separate bubbles (for the case of $\theta = 90^\circ$; see Fig. 7.9) distributed along the two diagonal lines, i.e., in the North-East (NE), North-West (NW), South-West (SW) and South-East (SE) directions; or it may become eight isolated bubbles of two sizes (for the case of $\theta = 75^\circ$; see Fig. 7.11) that are distributed, in addition to the above four directions, in four more directions (North (N), West (W), South (S) and East (E)).

From Fig. 7.11, it is obvious that the bubbles that only appear after increasing the surface hydrophilicity in N, W, S and E directions are relatively smaller than the other four in the NE, NW, SW and SE directions. For Type II, some enlarged views of the flow fields near the contact lines are also provided in Figs. 7.12 and 7.13 for Cases 1 and 2, respectively. Again the outer vortex, which probably initiated from the outer contact line (ring), is observed at $t = 18000$ and $t = 24000$ for both cases.

From Fig. 7.12 (at $t = 18000$), besides the vortex, the approaching of the bent interface toward the wall is also obvious. Such motion later led to the entrapped ring ($t = 22000$ in Fig. 7.9). Also from Fig. 7.12 (at $t = 24000$) the diversion of the downward moving fluid inside the droplet due to the outer spreading and the inner contraction of the entrapped ring is also easily observed. Due to the decreased contact angle in Case 2, the whole progress is “ahead of” that in Case 1, as reflected from the vortex positions in Fig. 7.13. It is interesting to note the two different stages of contraction of the entrapped bubble in Fig. 7.13: at $t = 18000$ it was still in a ring shape (see Fig. 7.11), the inner side contact angle was not in its equilibrium and the

fluid motion was outward; at $t = 24000$ it was already a separated bubble but still in an elongated shape (see Fig. 7.11 again), and the main motion was upward so that a spherical shape would be established (as observed at $t = 26000$ in Fig. 7.11).

The mechanism of entrapment in the first and second types is very similar to those reported by Chandra & Avedisian (1991), Pasandideh-Fard et al. (1996), Thoroddsen & Sakakibara (1998), Fujimoto et al. (2000), and Mehdi-Nejad et al. (2003). In both types, a high pressure region is developed under the droplet, which delays or even prevents the central part from contacting the wall. Fig. 7.14 shows the total pressure distributions at $t = 6000$ along the center line at the bottom plane for all the cases in Types I and II. Note that here the total pressure is defined as

$$p_{tot} = \rho c_s^2 + \left\{ [\phi \psi'(\phi) - \psi] - \left(\kappa \phi \nabla^2 \phi - \frac{1}{2} \kappa |\nabla \phi|^2 \right) \right\} \quad (7.4)$$

and it is related to the full pressure tensor (see Eqs. (2.85) and (2.76) in Chapter II) as

$$\vec{P}^{th} = p_{tot} \vec{I} + \kappa [(\nabla \phi) \otimes (\nabla \phi) - |\nabla \phi|^2 \vec{I}] \quad (7.5)$$

Also note that the pressure in Fig. 7.14 is a relative value (with respect to a reference one at the corner of the simulation box farthest away from the center), and only the left half parts are shown for clarity. It is easily seen that the pressure at the center is the highest in all the cases. For the two cases in Type 2, the pressure distributions almost overlap with each other completely. This is expected because the two cases are differentiated by the contact angle, and at $t = 6000$, the droplet did not touch the wall yet.

The differences between the present work and previous work are possibly due to the initial conditions. In the present work, the droplet was initialized to be spherical and

only a few lattice sites away from the wall, and a uniform velocity was assigned to it. The falling stage is rather short and the droplet deformation in this stage is relatively small (as compared to previous experimental work). This can lead to a different shape of its bottom surface, which indeed affects the impacting process.

7.3.2 Type III: Entrapment during fast impact

The third type of entrapment is completely different from the above two. In this type the Weber number is one order of magnitude larger though the Reynolds number is kept the same order. The initial impact velocity is now $U_z = -0.05$ and the droplet radius is $R_d = 30$. Besides the viscosity is increased to $\nu = 0.02$. These values give $We = 150$ and $Re = 150$. The Peclet number is $Pe = 3.6 \times 10^5$. The CA is $\theta = 105^\circ$.

The evolutions in the middle $x-z$ plane as well as in the bottom plane are given in Fig. 7.15. The initial contact between the droplet and the wall is similar to the second type (the droplet interface at the bottom has a convex shape). However, due to the dominating inertial effect (over the surface tension effect), the droplet spreads so fast that the interface near the TPL does not have sufficient time to bend to form a ring. After the droplet reaches the maximum radius in the spreading, it retracts back to the center under the action of the surface tension. Note that the average interface curvatures in the outer regions are in general smaller than those in the inner regions, and it seems to be easier to bend an interface with smaller curvatures (similar to the cases for elastic membranes). Thus, the outer regions suffer more from the surface tension, and the interfaces there retract faster than in the inner regions. This essentially contributes to the entrapment of *bubble* at the center. In this type, the final stable state is a compound droplet (e.g., oil-in-water-in-oil). Such a type of

entrapment was also reported by Khatavkar et al. (2007b) under a Reynolds number 130 and CA 120° . Note that the Webber number was much lower (1.5) in the work by Khatavkar et al. (2007b), and other simulation conditions differ from the present one as well (e.g., the density ratio and viscosity ratio). Probably these differences affect mainly the time scale of the impact process but not the interface shape evolutions because a large degree of similarity is easily found between the figure series in the left column of Fig. 7.15 and those in the right most column of Fig. 14 in the work by Khatavkar et al. (2007b).

Here a note about the snapshots at $t = 12,000$ may be in order. On the view at the bottom plane, there is a ring; but when viewed at the middle $x-z$ plane, the part enclosed by the ring actually corresponds to an isolated small cap (thin film). Probably because it was too thin to be resolved by the numerical model, it disappeared after a few time steps. Such a phenomenon is possibly due to the property of the phase field model; similar observations have also been reported and discussed by Khatavkar et al. (2007b), Khatavkar et al. (2005), and Yue et al. (2007).

7.3.3 Type IV: Hybrid type entrapment

Parameters in the fourth type are the same as in the third one ($U_z = -0.05$, $R_d = 30$, $\nu = 0.02$, $We = 150$, $Re = 150$, $Pe = 3.6 \times 10^5$) except that the CA is different ($\theta = 90^\circ$). As may be expected, an entrapment similar (but not identical) to the third type occurs in this case as well. However, at the same time, it also has some entrapment features of the second type though it appears only transiently (see Fig. 7.16). This is clearly seen in the snapshot of the bottom plane at $t = 18000$ which has a small circle at the center and a ring at the peripheral part. The central circle is

caused by both the dewetting of the thin film resulted from the initial spreading and the retraction process under the action of surface tension. The formation of the outer ring is the same as Type II. However, the local scale of the entrapped ring was too small, thus it disappeared after some time (similar to the disappearance of the thin cap in Type III discussed above). The final equilibrium state is almost the same as in Type III except that the local CAs are different. Nevertheless, as a good example, this case has demonstrated how the wall wettability affects the entrapment process.

7.3.4 Preliminary look at the entrapment condition

In the above, some of the cases were crudely differentiated by “slow” and “fast” for convenience. It may be more appropriate to look at the Reynolds and Webber numbers, and also the wall wettability (CA). However, from the above cases, one may only see the variation of entrapment type with given parameters and has no information on whether entrapment will occur under certain conditions.

As noted previously, in fact many simulations have been carried out and they spanned a much wider parameter regime. In many others, which are not shown here, the simulation parameters are quite different and the entrapment phenomena may or may not occur. It should be helpful to look at the whole parameter regime to obtain some clues on the conditions that facilitate the entrapment. Fig. 7.17 shows the points on the $Re-We$ and $Oh-We$ maps for all cases that have been studied. Those with entrapment are shown in “hollow diamonds” and the above cases are highlighted by “big circles”. From Fig. 7.17 it seems that entrapment phenomenon may occur over a wide range of Reynolds and Webber numbers, but tends not to happen when the Ohnesorge number is large (for all the cases with entrapment observed in our

simulations, $Oh < 0.2$). Of course, it is still too preliminary to use this as a criterion due to the limited number of cases investigated. Besides, as discussed above, the CA is also an important parameter and could play a determinant role under certain Reynolds and Weber numbers. Finally, it is expected that other surface properties, such as roughness and chemical heterogeneity which may be essential for CA hysteresis, will affect the droplet impact process and can be advantageous for entrapment to occur. Such factors are not considered in the current work and are left for future study.

7.4 Summary

To summarize, the phenomena of bubble entrapment have been studied in the course of a droplet impact upon a dry surface. Under different We , Re numbers and the wall wettabilities, four types of entrapment have been observed. The detailed dynamics of such processes have been analyzed. For small We and Re numbers, bubble entrapment is more likely due to the development of a high pressure region which further leads to a negative curvature of the lower droplet surface. Some direct numerical evidences have been supplemented for such a mechanism. Although the mechanism is similar to some other work, new pattern evolutions on the wall have been observed and analyzed. For large We and Re numbers, the lower droplet surface has positive curvature at the time of contact, and such entrapments either occur near the TPL when the spreading of the droplet slows down sufficiently and the action of surface tension takes over, or at the center during the retraction stage after a dewetting process; depending on the wall wettability, a hybrid form of entrapment combining the two may take place. Based on the simulations carried out, it appears that large Ohnesorge number might prevent the entrapment from occurring.

Table 7.1: Key parameters for the cases in Types I-IV of bubble entrapment

Type	U_z	R	ν	We	Re	Oh	θ	Domain size
I	1	-0.01	40	0.005	8	160	0.0177	180×180×100
	2		30		6	120	0.0204	
II	1	-0.01	50	0.005	10	200	90°	240×240×120
	2						75°	
III	-0.05	30	0.02	150	150	0.0816	105°	180×180×100
IV	-0.05	30	0.02	150	150	0.0816	90°	180×180×100

Table 7.2: Some simulation parameters for all cases in Types I-IV

Type	σ	W	M	Ch	Pe
I	1	0.001	3	0.5	0.0375
	2				7.2×10 ⁴
II	1	0.001	3	0.5	2×10 ⁵
	2				
III	0.001	3	0.5	0.05	3.6×10 ⁵
IV	0.001	3	0.5	0.05	3.6×10 ⁵

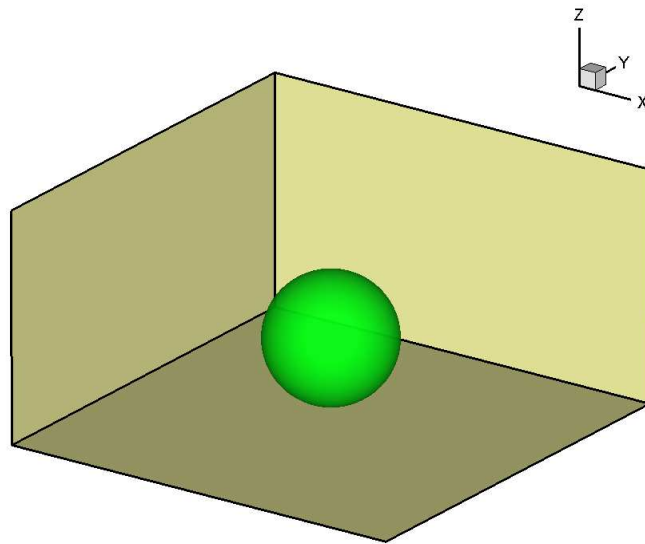


Fig. 7.1. Illustration of the initial condition of droplet impact

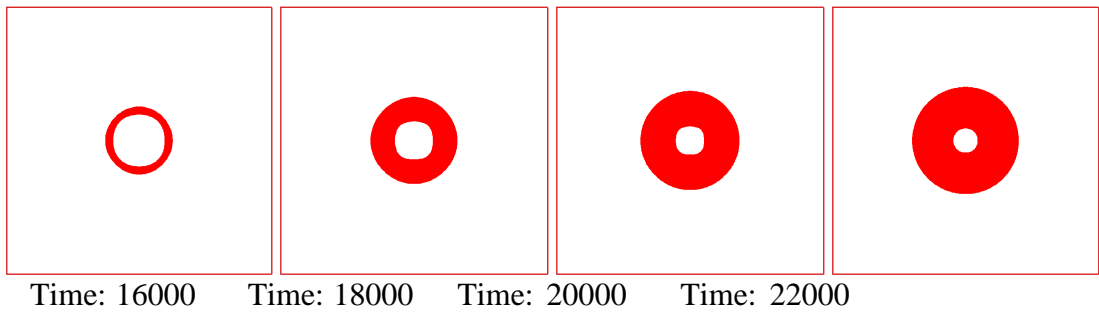


Fig. 7.2. Snapshots of the bottom plane (Type I; Case 1)

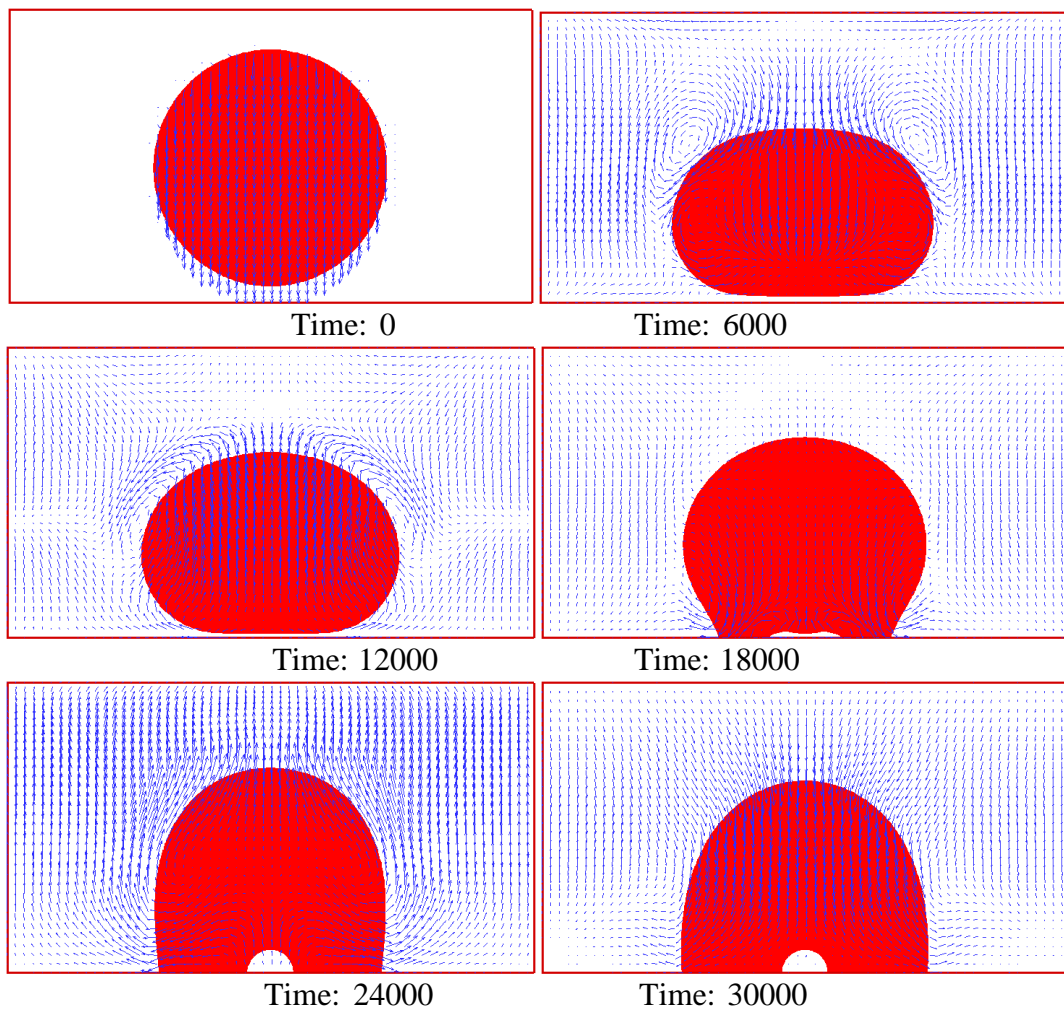


Fig. 7.3. Snapshots of the middle $x-z$ plane (Type I; Case 1) (note that for display convenience the scale of Fig. 7.3 for middle planes is different from that in Fig. 7.2 for bottom planes though they are taken from the same process, and this scale difference in display applies for Figs. 7.8 & 7.9, and Figs. 7.10 & 7.11 as well)

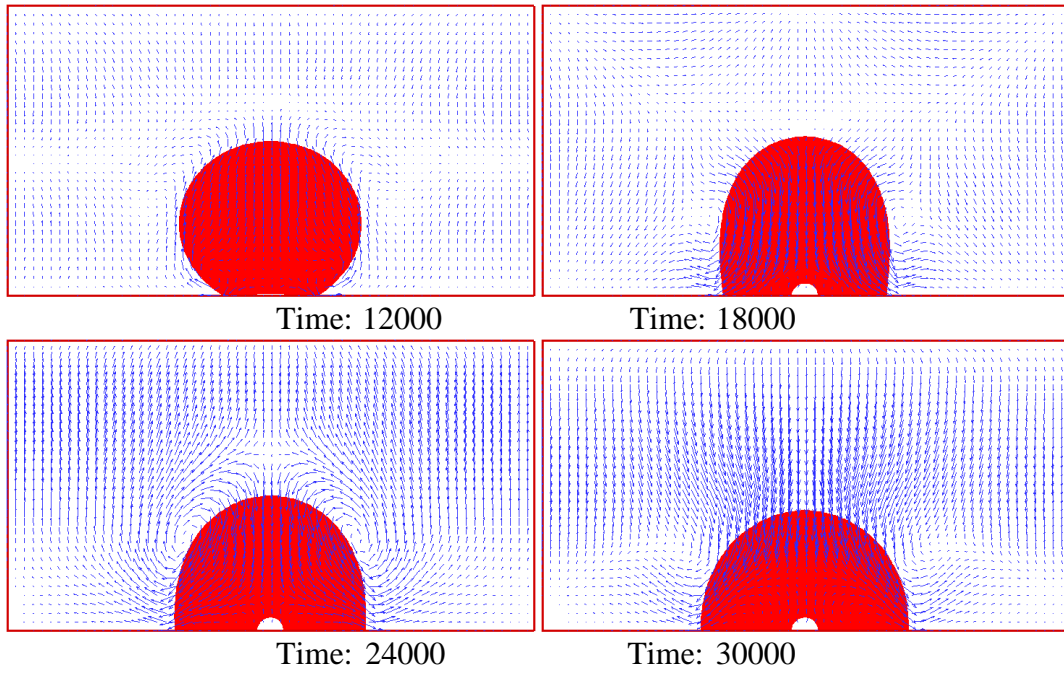


Fig. 7.4. Snapshots of the middle $x - z$ plane (Type I; Case 2)

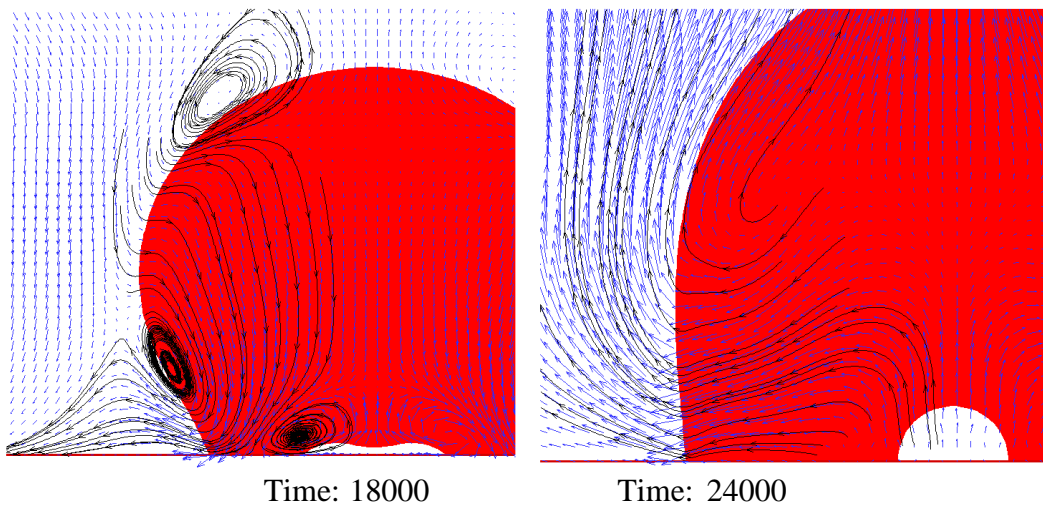


Fig. 7.5. Enlarged views of the flow fields in the middle $x - z$ plane at selected time (Type I; Case 1)

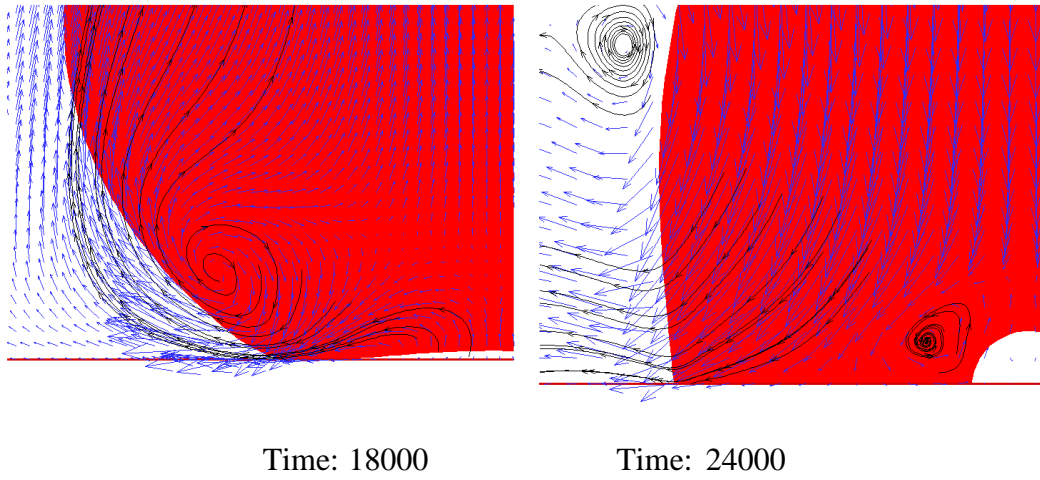


Fig. 7.6. Enlarged view of the flow fields in the middle $x-z$ plane at selected time (Type I; Case 2)

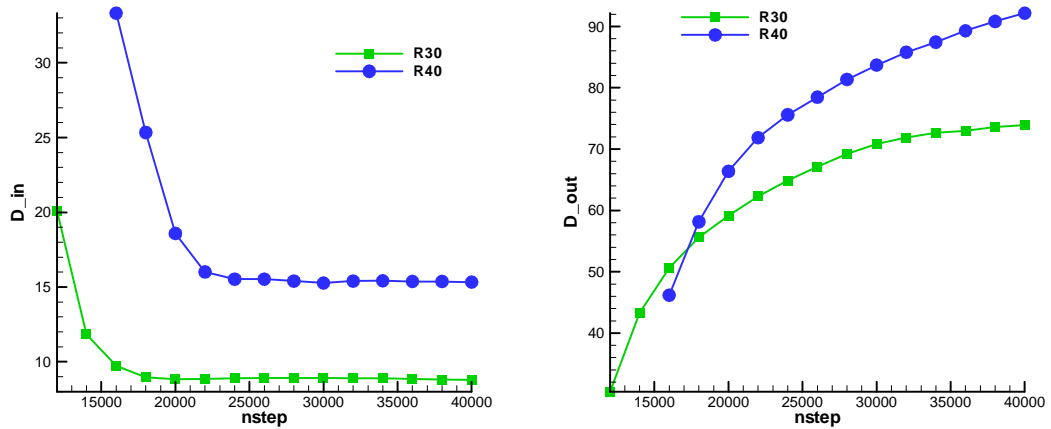


Fig. 7.7. Evolution of the inner and outer diameter of the circles on the bottom plane (Type I; Cases 1 & 2)

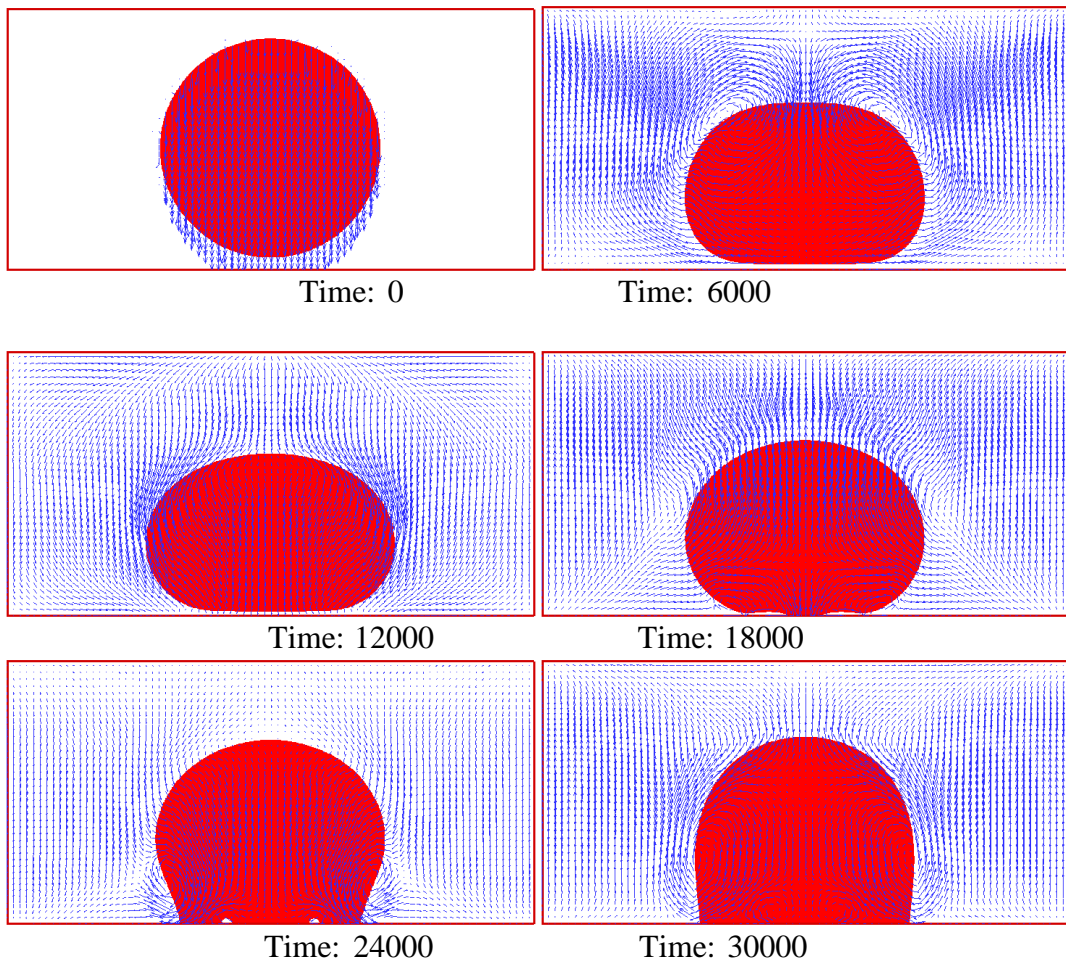


Fig. 7.8. Snapshots of the middle $x-z$ plane (Type II; Case 1)

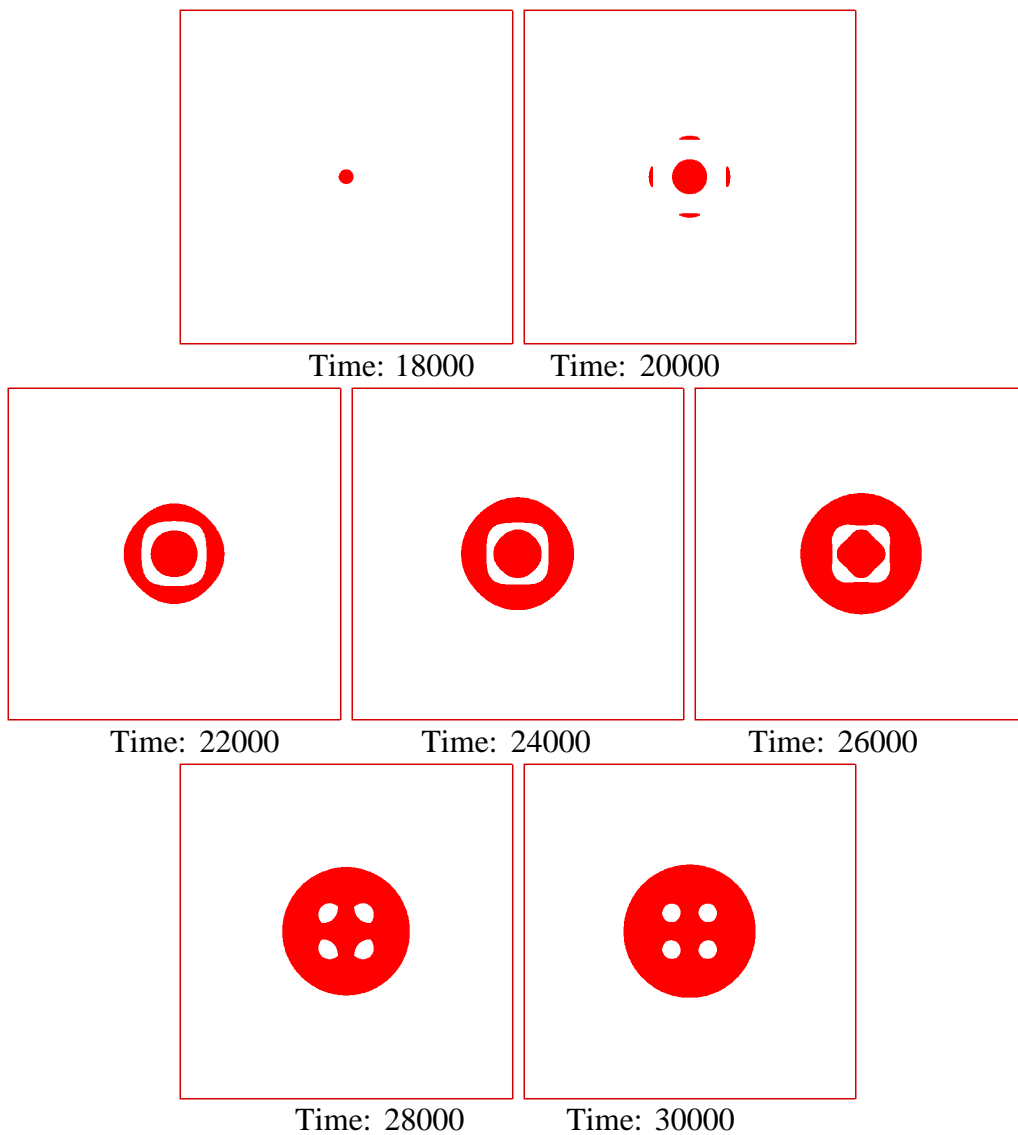


Fig. 7.9. Snapshots of the bottom plane (Type II; Case 1)

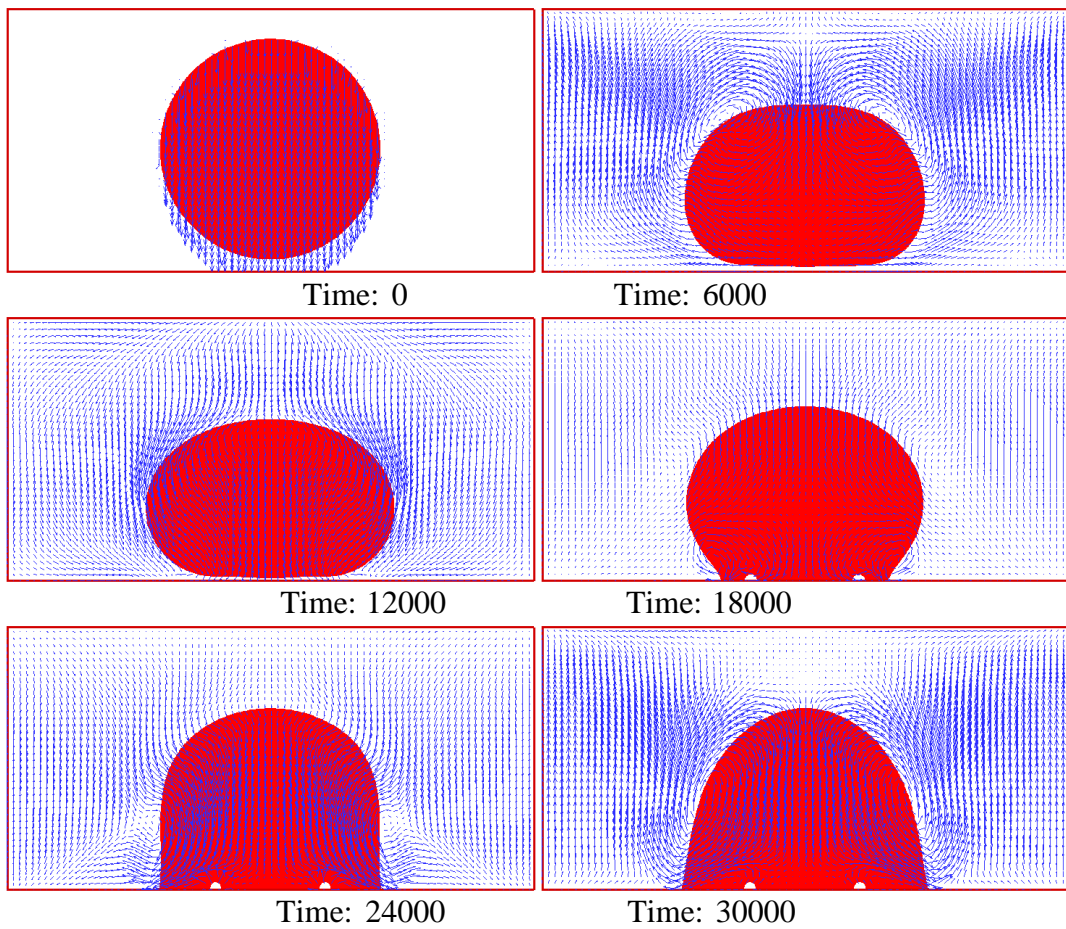


Fig. 7.10. Snapshots of the middle $x-z$ plane (Type II; Case 2)

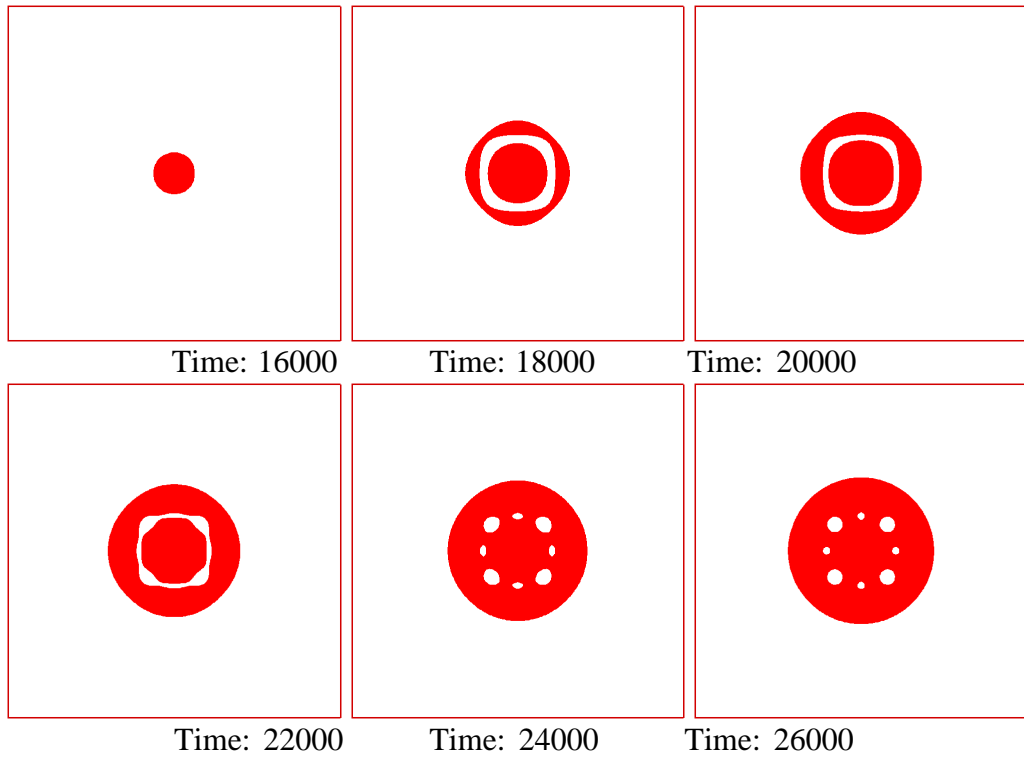


Fig. 7.11. Snapshots of the bottom plane (Type II; Case 2)

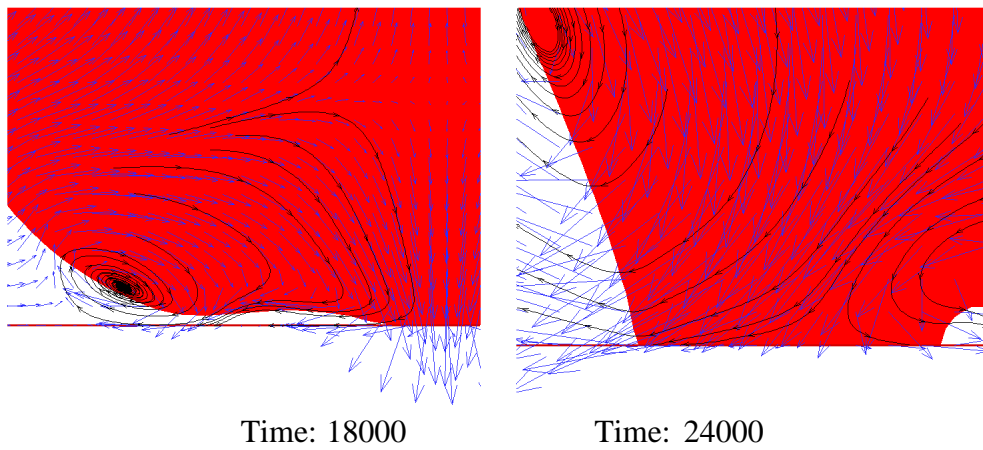


Fig. 7.12. Enlarged view of the flow fields in the middle $x-z$ plane at selected time (Type II; Case 1)

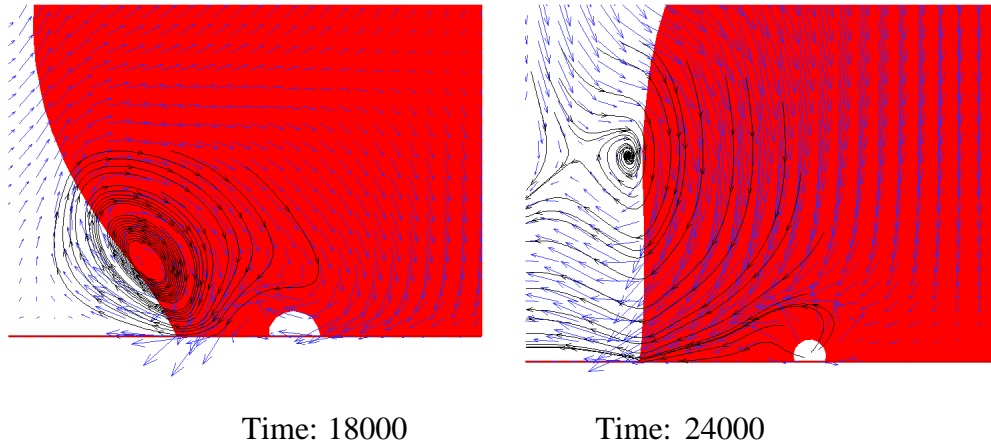


Fig. 7.13. Enlarged view of the flow fields in the middle $x - z$ plane at selected time (Type II; Case 2)

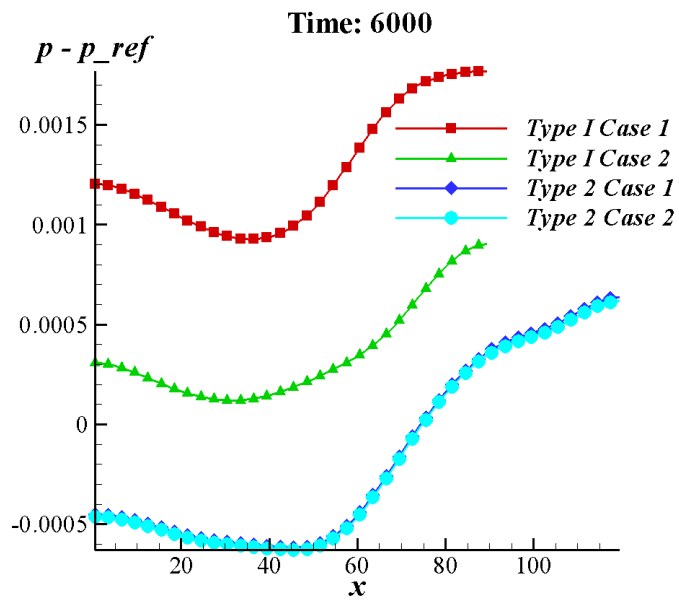
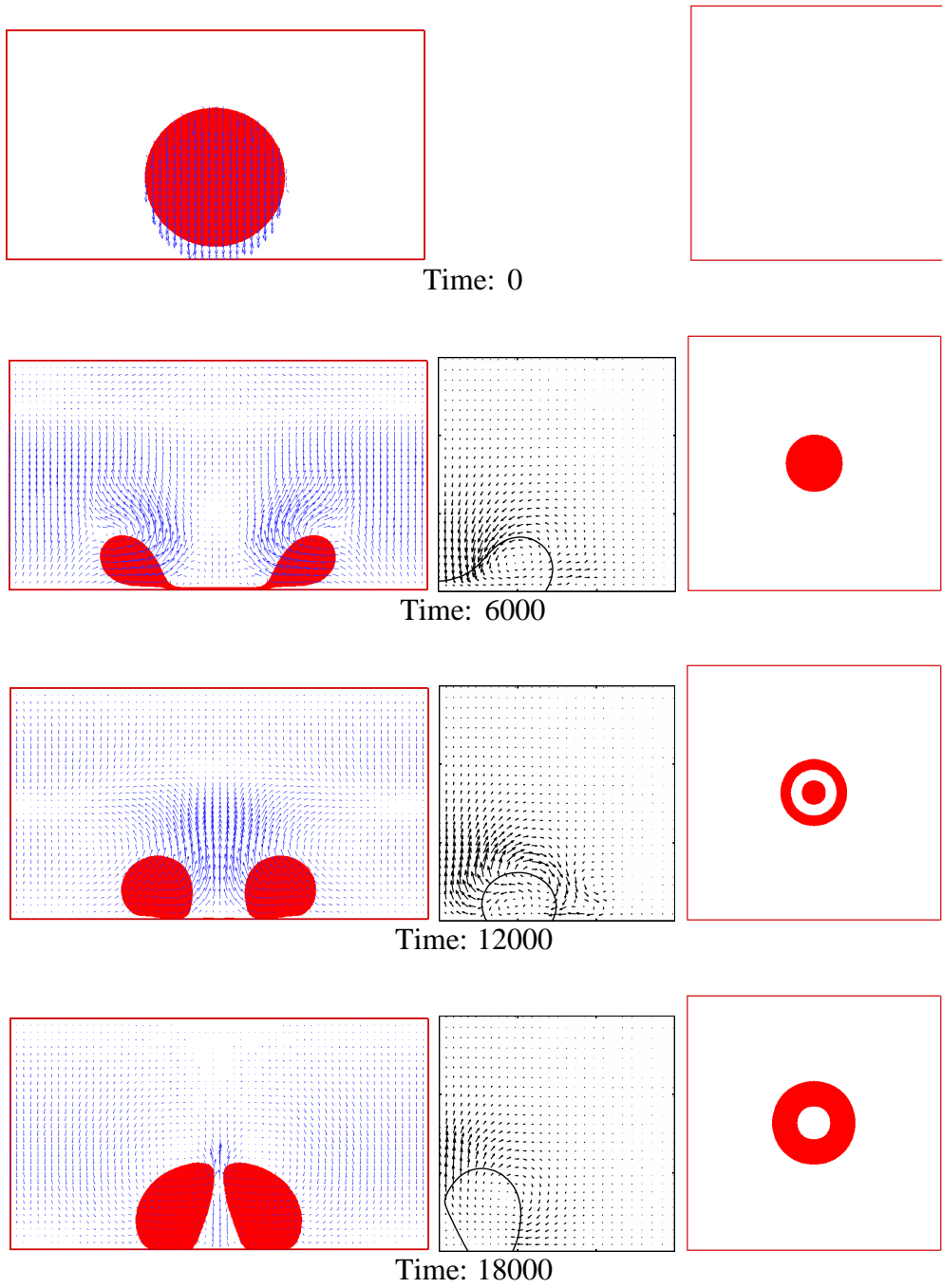


Fig. 7.14. Pressure distribution along the center line at the bottom plane for Types I and II



(Fig. 7.15: To be continued)

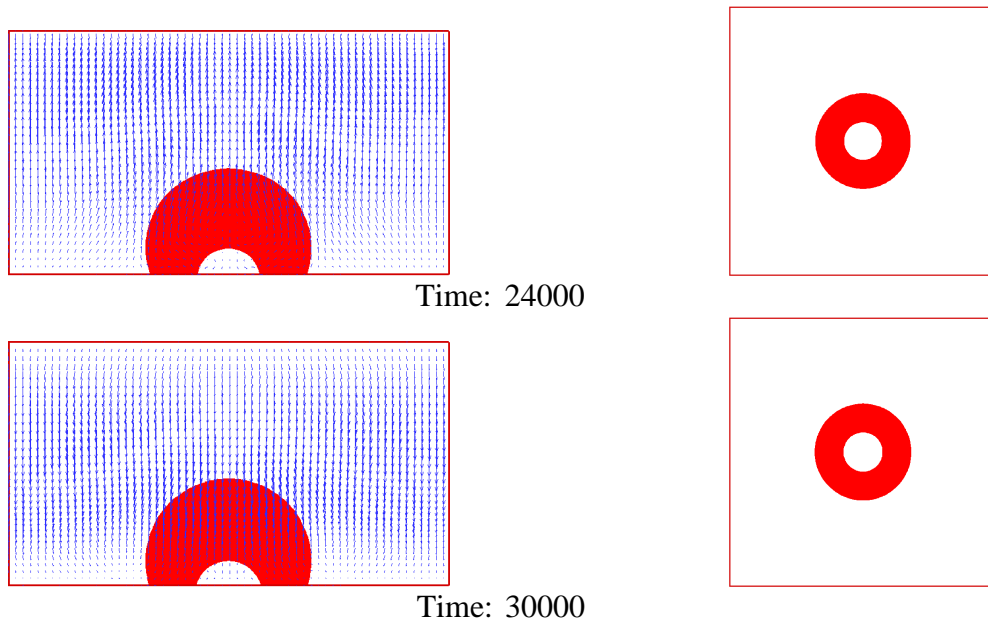
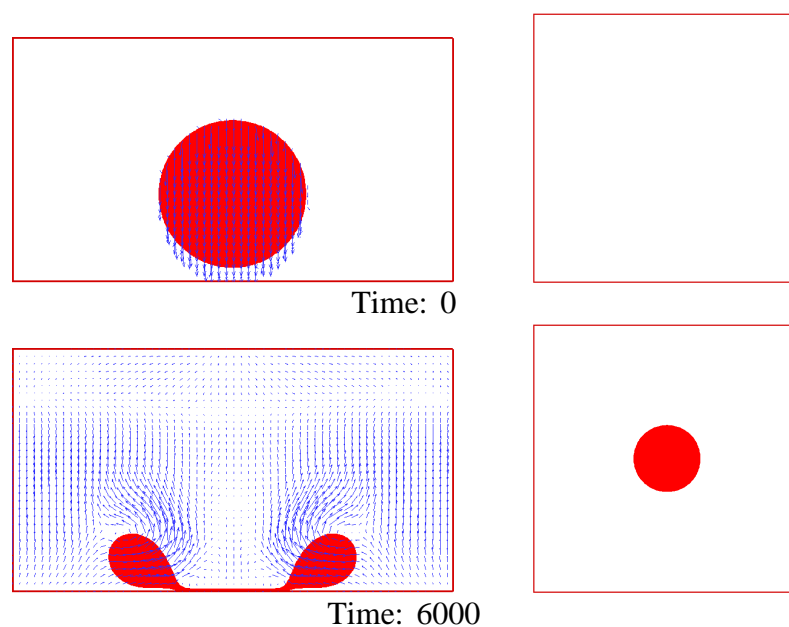


Fig. 7.15. Snapshots of the middle $x-z$ plane (left column) and the bottom plane (right column) (Type III) (for convenience of display the scales for the left and right columns are not the same; this applies for Fig. 7.16 below as well); the middle column shows some snapshots at certain time from the right most column of Fig. 14 in the work by Khatavkar et al. (2007b) (selected based on the similarity of interface shape, not the exact time)



(Fig. 7.16: To be continued)

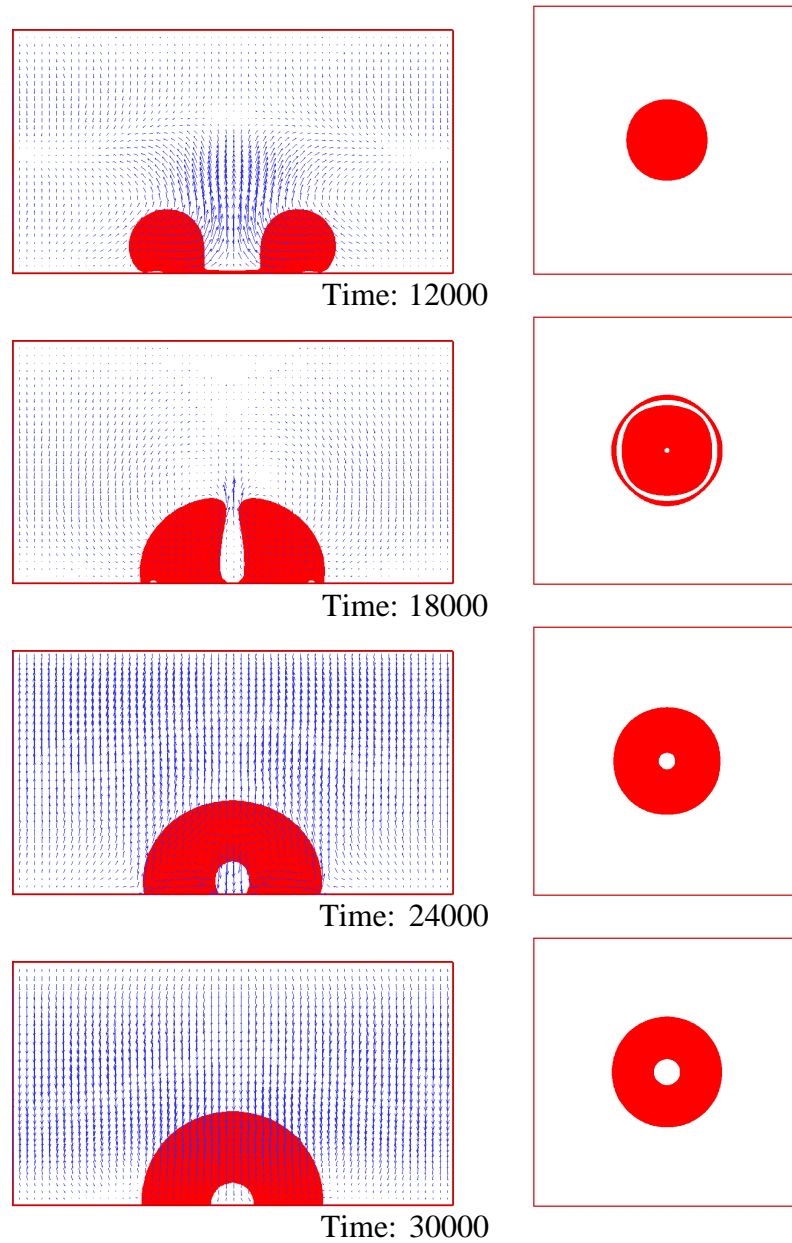


Fig. 7.16. Snapshots of the middle $x-z$ plane (left column) and the bottom plane (right column) (Type IV)

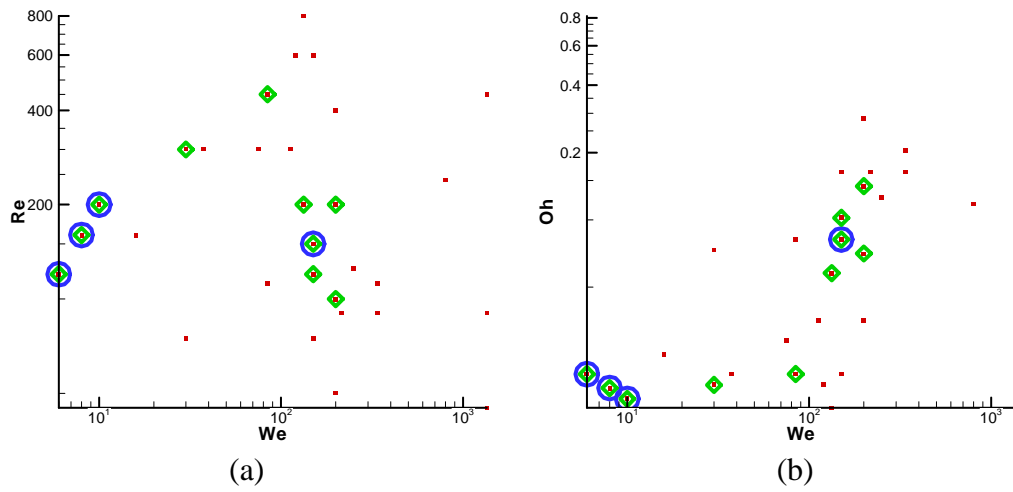


Fig. 7.17. $Re-We$ and $Oh-We$ maps for all droplet impact cases studied (both axes in log scale; small “dot”: all cases; “hollow diamond”: cases with entrapment; “big circle”: cases analyzed in detail)

Chapter VIII

Conclusion and Future Work

In this thesis, LBM has been applied to investigate near-wall MPMC flows, mostly at small scales. The effects of various important factors, such as the surface wettability and topography, and the mobility, have been studied for several different types of problems. Besides, a prototype of droplet manipulation by controlling substrate wettability has been devised and explored, and droplet impact on a surface has also been investigated with special concentration on the entrapment phenomena.

8.1 The effects of surface topography and wettability

First, the surface topography and wettability were found to strongly affect the droplet motions driven by a body force in a 2D microchannel with a smooth neutral-wetting upper wall and a rough lower wall (with varying geometry and wettability). As the hydrophobicity of the rough wall increases, the droplet tends to experience less drag. This agrees with the intuitive expectations. One noticeable discovery was that when the rough wall was sufficiently hydrophobic, the droplet attached completely to the upper side, thus benefiting greatly from the lubrication layer formed under it. This could be attributed to the pinning effect when the droplet entered the rough region. Another important finding was that even when the rough wall was hydrophilic, the droplet might move over the rough surface with an apparent hydrophobic CA. This confirms previous theoretical postulations of the “roughness induced non-wetting” phenomenon (Herminghaus 2000). Such an interesting phenomenon occurs only when the groove geometry and surface wettability satisfy certain conditions. Through a few

series of simulations, the critical values for the contact angle, groove width and depth were obtained, and the interface motions under sub-critical and super-critical conditions were clearly demonstrated. However, for a better understanding of similar phenomena in real life, for example, water droplets on lotus leaves, 3D simulations should be carried out. Due to the enormous time required to carry out meaningful 3D simulations, only a limited number of 3D cases for droplet motion on rough surfaces were investigated with the surface geometry fixed. Nevertheless, the preliminary results are satisfactory to reflect at least the effects of wettability when a complex textured surface is present. Overall, the research in this part represents a major step toward the better understanding of coupled effects of surface geometry and wettability under dynamic conditions at small scales.

8.2 The mobility effects

Secondly, the mobility in DIM was found to play a significant role in flows at low Re and Ca involving CLs by using a LBM implementation. The relation between the mobility and CL velocity was obtained for both a steady shear driven, and an unsteady capillarity driven flow. In the latter type, a droplet was driven by the abrupt change in the substrate wettability from neutral wetting to hydrophobic, and the mobility was found to determine whether or not the droplet would jump off the wall. The possible reason is that the mobility controls the diffusion in the regions around CLs which is critical for the slip velocity, and further affects the rate of energy transformation (from the system's FE to the droplet's kinetic energy). When the mobility becomes larger, the slip velocity increases correspondingly and it becomes easier for the droplet to leave the wall. Such observations agree qualitatively with previous experimental observations by Habenicht et al. (2005) and also theories

employing slip velocity models by Fetzer et al. (2005), though the problem setups were different. The bifurcation diagrams for the dewetting droplets (both 2D and 3D) were obtained through numerous simulations under different mobilities. In another 3D study of droplets on a chemically heterogeneous surface characterized by alternating hydrophobic-hydrophilic patches, it was found that the mobility determined whether the droplet was transferred completely to the hydrophilic patch, or was split in half and merged with neighbouring droplets. Such an observation could also be attributed to the relations between the mobility and the slip velocities of CLs. It is noted that all the above investigations considered only geometrically smooth surfaces. It would be interesting to include the roughness and check how the mobility affects the dynamics under such more complex situations. However, it is not explored in this study due to the considerable time and efforts required. Although the cases studied here seem to be relatively simple, they have provided direct and important illustrations of the mobility-dependant bifurcations in MPMC systems, and are expected to provide some useful implications for future numerical study in microfluidics.

8.3 Droplet manipulation by surface wettability control

Thirdly, a prototype of droplet manipulation system using proper spatio-temporal control in substrate wettability was devised and simulated. Several systems with different wettability distributions were studied and compared in detail and an efficient scheme was identified. It used hydrophobic patches to confine the droplet from two sides and also dynamically switched alternating hydrophobic-hydrophilic patches under the droplet. Such a scheme essentially realized some kind of “resonance” between the droplet motion and the wettability switch. Only if the wettability switch period approximately matched that of the droplet to move across one unit could rapid

unidirectional transport of the droplet result; otherwise the droplet stopped at one patch and oscillated in the normal direction in response to the periodic wettability switch. Relations between two key parameters in this scheme, namely the period of switching the wettability and the size of the confinement, were studied through a number of simulations. The variations of the extreme droplet velocity with them were obtained as well. However, in these simulations the CA hysteresis effect was not considered. Further studies including fairly efficient CA hysteresis modeling should be quite valuable since they may provide results closer to experiments. Nonetheless, this work gives very useful information about the key factors in the design and control of the substrates in digital microfluidics.

8.4 Bubble entrapment during droplet impact

Finally, the formation of entrapped *bubbles* during the course of a droplet impact upon a homogeneous surface was studied, and several types of entrapment were discovered, depending on We and Re , and the surface wettability. Different mechanisms for entrapment were identified, and they agree with previous numerical or experimental studies. For one of them, a few new entrapment phenomena were captured with the fully 3D model (which is impossible for previous axisymmetric models). Based on numerous simulation results, it was proposed that as the Ohnesorge number increases the probability of entrapment may be reduced. It is noted that the total number of simulations was still limited due to the high computational cost, and it is possible that future studies under different conditions could uncover new types of entrapment. Besides, similar to the study of droplet manipulation, the hysteresis effect was neglected, the inclusion of which could reveal more diverse entrapment phenomena beyond those reported here. However, it can be concluded that this

research extends broadly our understanding of the entrapment phenomena, and possesses certain reference values for some recent industrial applications, such as making large displays by ink-jet printing, in which bubble entrapment is undesirable.

8.5 Concluding remarks and future work

Several issues related to this thesis are not completely understood or developed, and further investigations should be conducted. They may be categorized into “problem-related” and “simulation-related”.

Some of the problem-related topics were already mentioned before, and here they are summarized and also extended. First, further investigations are recommended to find the critical aspect ratios under various conditions such as different Capillary numbers, wall wettabilities and droplet sizes for the droplet moving over grooved wall. The study of the Lotus Effect is still preliminary and it would be interesting to construct walls with double structures that mimic the real micro and nano structures on a lotus leaf. Considerable 3D simulations would be necessary to completely resolve this intriguing phenomenon. It is fair to say that it remains a very challenging problem in the near future due to the multiple scales of the surface and their complicated effects on the flow. Second, there is still much space left on devising smart ways to actuate and manipulate tiny droplets. For example, the following questions should deserve further studies: (1) how to set the degree of contrast in the wettability of different patches; (2) how the droplet size (relative to the patch size) affects the outcome; (3) how to take into account the hysteresis effects of surfaces manufactured by different methods or under different conditions. Besides, the even simpler yet fundamentally important problem, i.e., the CL motion on smooth substrates, requires considerable

work though there are many previous studies using either experimental or simulation approaches. For instance, in addition to the viscosity and mobility, it is also interesting to simulate how the wettability affects the slip velocity. Finally, many parameters and factors in droplet impact remain to be explored. Besides the hysteresis effect, the ratios of density and viscosity of the two fluids, and the variation of the surface either geometrically or chemically, may be investigated.

The first simulation-related issue is about the development of LBM for multi-phase flows with large density ratios. As mentioned in Chapters I and II, LBM for multi-phase flows needs a more rigorous foundation. Many papers in this subject do not distinguish single component two phase systems from two component fluids, and they use two sets of distribution functions for the hydrodynamic fields and the indicator function respectively (He et al. 1999, Inamuro et al. 2004, Lee & Lin 2005, Zheng et al. 2006). The usual air-water system is, in fact, obviously not a single component system. It might be more appropriate to use the mass fraction or mole fraction as the indicator function for such a system. Many problems in large density ratio models arise probably due to the attempt to extend the theory for single component fluid systems near critical points to regimes far away from critical points, which may not be admissible. Thus, it is suggested to base the models on more solid theories for binary fluids such as the one by Lowengrub & Truskinovsky (1998). The second is to extend the lower limit of the viscosity (in equivalence, the lower limit of Ca for small scale MPMC systems, and the upper limit of Re for macroscopic flows). In Chapter III, it was mentioned that the models using multiple relaxation times may help in this aspect. MRT models may achieve this by employing suitable separate relaxation times for the moments of the distribution functions and decoupling the hydrodynamic moments

from those higher order moments (Lallemand & Luo 2000). However, the benefits might be limited: MRT models work better than BGK models simply because they eliminate some unwanted effects of high order moments on the lower ones, but they can not actually improve the evolutions of lower order moments. In addition to MRT models, suitable turbulence modeling could help to some extent for high Re flows. However, considerable efforts for model development are still required for extremely low Ca flows. Thirdly, it is very desirable to incorporate some sophisticated mesh adaptation techniques for the study of MPMC problems involving interfaces. For uniform grids, the interfaces are usually unavoidably enlarged. When the grid is refined in interfacial regions, both the accuracy and efficiency of the simulations can be improved.

To conclude, the small scale MPMC flows near substrates are becoming more and more important as the focus on micro- and nano- fluidic devices increases. It is an exciting opportunity to explore this field, but it is also challenging due to the need to integrate the knowledge dispersed in many relevant fields (e.g., the physics of condensed matter, electronics, magnetism and optics, physical chemistry and fluid dynamics). Many more efforts are required to understand the *small* world completely so that the physics unique at these scales can be fully utilized.

References

- D. M. Anderson, G. B. McFadden, and A. A. Wheeler. Diffuse-interface methods in fluid mechanics. *Annu. Rev. Fluid Mech.*, 30:139, 1998.
- J.-L. Barrata and L. Bocquet. Influence of wetting properties on hydrodynamic boundary conditions at a fluid-solid interface. *Faraday Discussions*, 112:119, 1999.
- W. Barthlott and C. Neinhuis. Purity of the sacred lotus, or escape from contamination in biological surfaces. *Planta*, 202:1, 1997.
- R. Benzi, L. Biferale, M. Sbragaglia, S. Succi, and F. Toschi. Mesoscopic modeling of a two-phase flow in the presence of boundaries: The contact angle. *Phys. Rev. E*, 74:021509, 2006.
- P. L. Bhatnagar, E. P. Gross, and M. Krook. A model for collision processes in gases. i. small amplitude processes in charged and neutral one-component systems. *Phys. Rev.*, 94:1, 1954.
- A. J. Briant, P. Papatzacos, and J. M. Yeomans. Lattice Boltzmann simulations of contact line motion in a liquid-gas system. *Phil. Trans. R. Soc. Lond. A*, 360:485, 2002.
- A. J. Briant, A. J. Wagner, and J. M. Yeomans. Lattice Boltzmann simulations of contact line motion. I. liquid-gas systems. *Phys. Rev. E*, 69:031602, 2004.
- A. J. Briant and J. M. Yeomans. Lattice Boltzmann simulations of contact line motion. ii. binary fluids. *Phys. Rev. E*, 69:031603, 2004.
- A. B. D. Cassie and S. Baxter. Wettability of porous surfaces. *Trans. Faraday Soc.*, 40:546, 1944.

- S. Chandra and C. T. Avedisian. On the collision of a droplet with a solid surface. *Proc. R. Soc. London A*, 432: 13, 1991.
- S. Chapman. *The mathematical theory of non-uniform gases: an account of the kinetic theory of viscosity, thermal conduction, and diffusion in gases*. Cambridge University Press, Cambridge; New York, 1990.
- H.-Y. Chen, D. Jasnow, and J. Vinals. Interface and contact line motion in a two phase fluid under shear flow. *Phys. Rev. Lett.*, 85:1686, 2000.
- S. Chen and G. D. Doolen. Lattice Boltzmann method for fluid flows. *Annu. Rev. Fluid Mech.*, 30:329, 1998.
- Y.-T. Cheng and D. E. Rodak. Is the lotus leaf superhydrophobic? *Appl. Phys. Lett.*, 86:144101, 2005.
- S. Daniel, M. K. Chaudhury, and P.-G. de Gennes. Vibration-actuated drop motion on surfaces for batch microfluidic processes. *Langmuir* 2 (9):4240, 2005.
- A. A. Darhuber and S. M. Troian. Principles of microfluidic actuation by modulation of surface stresses. *Annu. Rev. Fluid Mech.*, 37:425, 2005.
- A. A. Darhuber, J. P. Valentino, J. M. Davis, S. M. Troian, and S. Wagner. Microfluidic actuation by modulation of surface stresses. *Appl. Phys. Lett.*, 82:657, 2003.
- P.-G. de Gennes, F. Brochard-Wyart, and D. Quere. *Capillarity and Wetting Phenomena: Drops, Bubbles, Pearls, Waves*. Springer, 2004.
- P. J. Dellar. Bulk and shear viscosities in lattice Boltzmann equations. *Phys. Rev. E*, 64:31203, 2001.
- H. Ding and P. D. M. Spelt. Wetting condition in diffuse interface simulations of contact line motion. *Phys. Rev. E*, 75:046708, 2007a.

H. Ding and P. D. M. Spelt. Inertial effects in droplet spreading: a comparison between diffuse-interface and level-set simulations. *J. Fluid Mech.*, 576:287, 2007b.

A. Dupuis, E. M. Kotsalis, and P. Koumoutsakos. Coupling lattice Boltzmann and molecular dynamics models for dense fluids. *Phys. Rev. E*, 75:046704, 2007.

A. Dupuis, J. Lopolds, D. G. Bucknall, and J. M. Yeomans. Control of drop positioning using chemical patterning. *Appl. Phys. Lett.*, 87:024103, 2005.

A. Dupuis and J. M. Yeomans. Modeling droplets on superhydrophobic surfaces: Equilibrium states and transitions. *Langmuir*, 21:2624, 2005.

W. E and B. Engquist. Multiscale modeling and computation. *NOTICES OF THE AMS*, 50:1062, 2003.

J. D. Eick, R. J. Good, and A. W. Neumann. Thermodynamics of contact angles. II. Rough solid surfaces. *J. Colloid Interface Sci.*, 53(2):235, 1975.

R. Fetzer, K. Jacobs, A. Munch, B. Wagner, and T. P. Witelski. New slip regimes and the shape of dewetting thin liquid films. *Phys. Rev. Lett.*, 95:127801, 2005.

E. G. Flekkoy and P. V. Coveney. From molecular dynamics to dissipative particle dynamics. *Phys. Rev. Lett.*, 83:1775, 1999.

H. Fujimoto, H. Shiraishi, and N. Hatta. Evolution of liquid-solid contact area of a drop impinging on a solid surface. *Int. J. Heat Mass Transfer*, 43:1673, 2000.

R. Furstner, W. Barthlott, C. Neinhuis, and P. Walzel. Wetting and self cleaning properties of artificial superhydrophobic surfaces. *Langmuir*, 21:956, 2005.

R. D. Groot and P. B. Warren. Dissipative particle dynamics: Bridging the gap between atomistic and mesoscopic simulation. *J. Chem. Phys.*, 107:4423, 1997.

A. K. Gunstensen and D. H. Rothman. A Galilean-invariant immiscible lattice gas. *Physica D*, 47:53, 1991.

- Z. Guo and T. S. Zhao. Finite-difference-based lattice Boltzmann model for dense binary mixtures. *Phys. Rev. E*, 71:026701, 2005.
- A. Habenicht, M. Olapinski, F. Burmeister, P. Leiderer, and J. Boneberg. Jumping nanodroplets. *Science*, 309:2043, 2005.
- B. He, J. Lee, and N. A. Patankar. Contact angle hysteresis on rough hydrophobic surfaces. *Colloids and Surfaces A: Physicochem. Eng. Aspects*, 248:101, 2004.
- X. He, S. Chen, and R. Zhang. A lattice Boltzmann scheme for incompressible multiphase flow and its application in simulation of Rayleigh-Taylor instability. *J. Comput. Phys.*, 152:642, 1999.
- X. He, G. D. Doolen, and T. Clark. Comparison of the lattice Boltzmann method and the artificial compressibility method for Navier-Stokes equations. *J. Comput. Phys.*, 179:439, 2002.
- X. He and L.-S. Luo. Lattice Boltzmann model for the incompressible Navier-Stokes equation. *J. Stat. Phys.*, 88:927, 1997b.
- X. He and L.-S. Luo. Theory of the lattice Boltzmann method: From the Boltzmann equation to the lattice Boltzmann equation. *Phys. Rev. E*, 56:6811, 1997a.
- X. He, L.-S. Luo, and M. Dembo. Some progress in lattice Boltzmann method. part I. nonuniform mesh grids. *J. Comput. Phys.*, 129:357, 1996.
- S. Herminghaus. Roughness-induced non-wetting. *Europhys. Lett.*, 52:165, 2000.
- J. J. Huang, C. Shu, and Y. T. Chew. Numerical investigation of transporting droplets by spatiotemporally controlling substrate wettability. *J. Colloid Interface Sci.*, 328:124, 2008.
- J. J. Huang, C. Shu, and Y. T. Chew. Lattice Boltzmann study of droplet motion inside a grooved channel. *Phys. Fluids*, 21:022103, 2009a.

- J. J. Huang, C. Shu, and Y. T. Chew. Mobility-dependent bifurcations in capillarity-driven two-phase fluid systems by using a lattice Boltzmann phase-field model. *Int. J. Numer. Meth. Fluids*, 60:203, 2009b.
- K. Ichimura, S.-K. Oh, and M. Nakagawa. Light-driven motion of liquids on a photoresponsive surface. *Science*, 288:1624, 2000.
- T. Inamuro, T. Ogata, S. Tajima, and N. Konishi. A lattice Boltzmann method for incompressible two-phase flows with large density differences. *J. Comput. Phys.*, 198:628, 2004.
- D. Jacqmin. Calculation of two-phase Navier-Stokes flows using phase-field modeling. *J. Comput. Phys.*, 155:96, 1999.
- D. Jacqmin. Contact-line dynamics of a diffuse fluid interface. *J. Fluid Mech.*, 402:57, 2000.
- R. E. Johnson and R. H. Dettre. Contact angle hysteresis. I. Study of an idealized rough surface. *Adv. Chem. Ser.*, 43:112, 1964.
- J. L. Jones, M. Lal, J. N. Ruddock, and N. A. Spenley. Dynamics of a drop at a liquid/solid interface in simple shear fields: A mesoscopic simulation study. *Faraday Discussions*, 112:129, 1999.
- J. Jopp, H. Grull, and R. Yerushalmi-Rozen. Wetting behavior of water droplets on hydrophobic microtextures of comparable size. *Langmuir*, 20:10015, 2004.
- V. M. Kendon, M. E. Cates, I. Pagonabarraga, and J.-C. D. and P. Bladon. Inertial effects in three-dimensional spinodal decomposition of a symmetric binary fluid mixture: a lattice Boltzmann study. *J. Fluid Mech.*, 440:147, 2001.
- V. V. Khatavkar, P. D. Anderson, P. C. Duineveld, and H. H. E. Meijer. Diffuse Interface Modeling of Droplet Impact on a Pre-Patterned Solid Surface. *Macromol. Rapid Commun.*, 26:298, 2005.

- V. Khatavkar, P. Anderson, and H. Meijer. On scaling of diffuse-interface models. *Chemical Engineering Science*, 61:2364, 2006.
- V. V. Khatavkar, P. D. Anderson, and H. E. H. Meijer. Capillary spreading of a droplet in the partially wetting regime using a diffuse-interface model. *J. Fluid Mech.*, 572:367, 2007a.
- V. V. Khatavkar, P. D. Anderson, P. C. Duineveld, and H. E. H. Meijer. Diffuse-interface modelling of droplet impact. *J. Fluid Mech.*, 581:97, 2007b.
- J. Kim. A continuous surface tension force formulation for diffuse-interface models. *J. Comput. Phys.*, 204:784, 2005.
- H. Kusumaatmaja and J. M. Yeomans. Controlling drop size and polydispersity using chemically patterned surfaces. *Langmuir*, 23:956, 2007.
- P. Lallemand and L.-S. Luo. Theory of the lattice Boltzmann method: Dispersion, dissipation, isotropy, Galilean invariance, and stability. *Phys. Rev. E*, 61:6546, 2000.
- A. G. Lamorgese and R. Mauri. Mixing of macroscopically quiescent liquid mixtures. *Phys. Fluids*, 18:044107, 2006.
- M. Latva-Kokko and D. H. Rothman. Static contact angle in lattice Boltzmann models of immiscible fluids. *Phys. Rev. E*, 72:046701, 2005.
- T. Lee and C.-L. Lin. A stable discretization of the lattice Boltzmann equation for simulation of incompressible two-phase flows at high density ratio. *J. Comput. Phys.*, 206:16, 2005.
- C. Liu and J. Shen. A phase field model for the mixture of two incompressible fluids and its approximation by a Fourier-spectral method. *Physica D*, 179:211, 2003.
- G. R. Liu and M. Liu. *Smoothed particle hydrodynamics: a meshfree particle method*. World Scientific Pub., 2003.

- M. Liu, P. Meakin, and H. Huang. Dissipative particle dynamics simulation of fluid motion through an unsaturated fracture and fracture junction. *J. Comput. Phys.*, 222:110, 2007a.
- M. Liu, P. Meakin, and H. Huang. Dissipative particle dynamics simulation of multiphase fluid flow in microchannels and microchannel networks. *Phys. Fluids*, 19:033302, 2007b.
- Y. Liu, L. Mu, B. Liu, and J. Kong. Controlled switchable surface. *Chem. Eur. J.*, 11:2622, 2005.
- J. Lowengrub and L. Truskinovsky. Quasi-incompressible Cahn-Hilliard fluids and topological transitions. *Proc. R. Soc. Lond. A*, 454:2617, 1998.
- M. Lundgren, N. L. Allan, and T. Cosgrove. Molecular dynamics study of wetting of a pillar surface. *Langmuir*, 19:7127, 2003.
- M. Lundgren, N. L. Allan, and T. Cosgrove. Modeling of wetting: a study of nanowetting at rough and heterogeneous surfaces. *Langmuir*, 23:1187, 2007.
- L.-S. Luo. Unified theory of lattice Boltzmann models for Nonideal gases. *Phys. Rev. Lett.*, 81:1618, 1998.
- L.-S. Luo and S. S. Girimaji. Theory of the lattice Boltzmann method: Two-fluid model for binary mixtures. *Phys. Rev. E*, 67:036302, 2003.
- A. Marmur. The lotus effect: Superhydrophobicity and metastability. *Langmuir*, 20:3517, 2004.
- M. E. McCracken and J. Abraham. Multiple-relaxation-time lattice-Boltzmann model for multiphase flow. *Phys. Rev. E*, 71:036701, 2005.
- G. McHale, N. J. Shirtcliffe, S. Aqil, C. C. Perry, and M. I. Newton. Topography driven spreading. *Phys. Rev. Lett.*, 93:036102, 2004b.

- G. McHale, N. J. Shirtcliffe, and M. I. Newton. Contact-angle hysteresis on superhydrophobic surfaces. *Langmuir*, 20:10146, 2004a.
- V. Mehdi-Nejad, J. Mostaghimi, and S. Chandra. Air bubble entrapment under an impacting droplet. *Phys. Fluids*, 15(1):173, 2003.
- R. Mei, L.-S. Luo, and W. Shyy. An accurate curved boundary treatment in the lattice Boltzmann method. *J. Comput. Phys.*, 155:307, 1999.
- R. R. Nourgaliev, T. N. Dinh, T. G. Theofanous, and D. Joseph. The lattice Boltzmann equation method: theoretical interpretation, numerics and implications. *Int. J. Multiphase Flow*, 29:117, 2003.
- S. Osher and R. Fedkiw. *Level sets methods and dynamic implicit surfaces*. Springer, 2002.
- P. Papatzacos. Macroscopic two-phase flow in porous media assuming the diffuse-interface model at pore level. *Transport Porous Med.*, 49:139, 2002.
- M. Pasandideh-Fard, Y. M. Qiao, S. Chandra, and J. Mostaghimi. Capillary effects during droplet impact on a solid surface. *Phys. Fluids*, 8(3):650, 1996.
- N. A. Patankar. On the modeling of hydrophobic contact angles on rough surfaces. *Langmuir*, 19:1249, 2003.
- N. A. Patankar. Mimicking the lotus effect: Influence of double roughness structures and slender pillars. *Langmuir*, 20:8209, 2004.
- M. G. Pollack, R. B. Fair, and A. D. Shenderov. Electrowetting-based actuation of liquid droplets for microfluidic applications. *Appl. Phys. Lett.*, 77:1725, 2000.
- M. G. Pollack, A. D. Shenderov, and R. B. Fair. Electrowetting-based actuation of droplets for integrated microfluidics. *Lab Chip*, 2:96, 2002.
- K. N. Premnath and J. Abraham. Three-dimensional multi-relaxation time (MRT) lattice-Boltzmann models for multiphase flow. *J. Comput. Phys.*, 224:539, 2007.

- D. C. Rapaport. *The art of molecular dynamics simulation*. Cambridge University Press, 1995.
- S. Reddy, P. R. Schunk, and R. T. Bonnecaze. Dynamics of low capillary number interfaces moving through sharp features, *Phys. Fluids* 17:122104, 2005.
- M. Renardy, Y. Renardy, and J. Li. Numerical simulation of moving contact line problems using a volume-of-fluid method. *J. Comput. Phys.*, 171:243, 2001.
- M. Sbragaglia, R. Benzi, L. Biferale, S. Succi, and F. Toschi. Surface roughness-hydrophobicity coupling in microchannel and nanochannel flows. *Phys. Rev. Lett.*, 97:204503, 2006.
- M. Sbragaglia and S. Succi. Analytical calculation of slip flow in lattice Boltzmann models with kinetic boundary conditions. *arXiv*, page 0410039, 2004.
- R. Scardovelli and S. Zaleski. Direct numerical simulation of free-surface and interfacial flow. *Annu. Rev. Fluid Mech.*, 31:567, 1999.
- R. Seemann, M. Brinkmann, E. J. Kramer, F. F. Lange, and R. Lipowsky. Wetting morphologies at microstructured surfaces. *PNAS* 102(6):1848, 2005.
- X. Shan and H. Chen. Lattice Boltzmann model for simulating flows with multiple phases and components. *Phys. Rev. E*, 47:1815, 1993.
- X. Shan and H. Chen. Simulation of nonideal gases and liquid-gas phase transitions by the lattice Boltzmann equation. *Phys. Rev. E*, 49:2941, 1994.
- C. Shu, Y. T. Chew, and X. D. Niu. Least-squares-based lattice Boltzmann method: A meshless approach for simulation of flows with complex geometry. *Phys. Rev. E*, 64:045701, 2001.
- P. A. Skordos. Initial and boundary conditions for the lattice Boltzmann method. *Phys. Rev. E*, 48:4823, 1993.

- P. D. M. Spelt. A level-set approach for simulations of flows with multiple moving contact lines with hysteresis. *J. Comput. Phys.*, 207:389, 2005.
- P. D. M. Spelt. Shear flow past two-dimensional droplets pinned or moving on an adhering channel wall at moderate Reynolds numbers: a numerical study. *J. Fluid Mech.*, 561:439, 2006.
- T. M. Squires and S. R. Quake. Microfluidics: Fluid physics at the nanoliter scale. *Rev. Mod. Phys.*, 77:977, 2005.
- A. Staicu and F. Mugele. Electrowetting-induced oil film entrapment and instability. *Phys. Rev. Lett.*, 97:167801, 2006.
- J. D. Sterling and S. Chen. Stability analysis of lattice Boltzmann methods. *J. Comput. Phys.*, 123:196, 1996.
- H. A. Stone, A. D. Stroock, and A. Ajdari. Engineering flows in small devices: Microfluidics toward a lab-on-a-chip. *Annu. Rev. Fluid Mech.*, 36:381, 2004.
- S. Succi. *The Lattice Boltzmann Equation for Fluid Dynamics and Beyond*. Clarendon Press, New York, 2001.
- M. R. Swift, E. Orlandini, W. R. Osborn, and J. M. Yeomans. Lattice Boltzmann simulations of liquid-gas and binary fluid systems. *Phys. Rev. E*, 54:5041, 1996.
- M. R. Swift, W. R. Osborn, and J. M. Yeomans. Lattice Boltzmann simulation of nonideal fluids. *Phys. Rev. Lett.*, 75:830, 1995.
- A. Tartakovsky and P. Meakin. Modeling of surface tension and contact angles with smoothed particle hydrodynamics. *Phys. Rev. E*, 72:026301, 2005.
- S. T. Thoroddsen, T. G. Etoh, K. Takehara, N. Ootsuka, and Y. Hatsuki. The air bubble entrapped under a drop impacting on a solid surface. *J. Fluid Mech.*, 545:203, 2005.

- S. T. Thoroddsen and J. Sakakibara. Evolution of the fingering pattern of an impacting drop. *Phys. Fluids*, 10(6): 1359, 1998.
- S. O. Unverdi and G. Tryggvason. A front-tracking method for viscous, incompressible, multi-fluid flows. *J. Comput. Phys.*, 100:25, 1992.
- S. van der Graaf, T. Nisisako, C. G. P. H. Schroen, R. G. M. van der Sman, and R. M. Boom. Lattice Boltzmann simulations of droplet formation in a t-shaped microchannel. *Langmuir*, 22:4144, 2006.
- R. Verberg, C. M. Pooley, J. M. Yeomans, and A. C. Balazs. Pattern formation in binary fluids confined between rough, chemically heterogeneous surfaces. *Phys. Rev. Lett.*, 93:184501, 2004.
- N. Vladimirova and R. Mauri. Mixing of viscous liquid mixtures. *Chemical Engineering Science*, 59:2065, 2004.
- S. W. Walker and B. Shapiro. Modeling the fluid dynamics of electrowetting on dielectric (EWOD). *J. Microelectromech. Syst.*, 15 (4):986, 2006.
- R. N. Wenzel. Surface roughness and contact angle. *J. Phys. Colloid Chem.*, 53:1466, 1949.
- A. L. Yarin. Drop Impact Dynamics: Splashing, Spreading, Receding, Bouncing... *Annu. Rev. Fluid Mech.*, 38:159, 2006.
- Z. Yoshimitsu, A. Nakajima, T. Watanabe, and K. Hashimoto. Effects of surface structure on the hydrophobicity and sliding behavior of water droplets. *Langmuir*, 18:5818, 2002.
- D. Yu, R. Mei, and W. Shyy. Improved treatment of the open boundary in the method of lattice Boltzmann equation. *Progress in Computational Fluid Dynamics*, 5:3, 2005.
- P. Yue, C. Zhou, and J. J. Feng. Spontaneous shrinkage of drops and mass conservation in phase-field simulations. *J. Comput. Phys.*, 223:1, 2007.

P. Yue, C. Zhou, J. J. Feng, C. F. Ollivier-Gooch, and H. H. Hu. Phase-field simulations of interfacial dynamics in viscoelastic fluids using finite elements with adaptive meshing. *J. Comput. Phys.*, 219:47, 2006.

J. Zhang, B. Li, and D. Y. Kwok. Mean-field free-energy approach to the lattice Boltzmann method for liquid-vapor and solid-fluid interfaces. *Phys. Rev. E*, 69:032602, 2004.

J. Zhang and D. Y. Kwok. Contact line and contact angle dynamics in superhydrophobic channels. *Langmuir*, 22:4998, 2006.

H. W. Zheng, C. Shu, and Y. T. Chew. A lattice Boltzmann model for multiphase flows with large density ratio. *J. Comput. Phys.*, 218:353, 2006.

Appendix

Chapman-Enskog Expansion and Macroscopic Equations

The Chapman-Enskog multiscale expansion procedure as applied to the FE2-LBM-B is detailed in the following.

Recall that for FE2-LBM-B the two sets of LBEs are given by Eqs. (2.99) and (2.89),

$$f_i(\bar{x} + \bar{e}_i \delta_t, t + \delta_t) - f_i(\bar{x}, t) = -\left(f_i(\bar{x}, t) - f_i^{eq}(\bar{x}, t)\right)/\tau_f + \delta_t w_i \bar{e}_{i\alpha} (\mu \partial_\alpha \phi)/c_s^2$$

$$g_i(\bar{x} + \bar{e}_i \delta_t, t + \delta_t) - g_i(\bar{x}, t) = -\left(1/\tau_g\right) \left[g_i(\bar{x}, t) - g_i^{eq}(\bar{x}, t)\right]$$

and the multiscale expansions are applied to them as in Eqs. (2.103-2.107),

$$f_i(\bar{x} + \bar{e}_i \delta_t, t + \delta_t) = f_i(\bar{x}, t) + \varepsilon (\partial_t + e_{i\alpha} \partial_\alpha) f_i + \frac{1}{2} \varepsilon^2 (\partial_t + e_{i\alpha} \partial_\alpha) (\partial_t + e_{i\beta} \partial_\beta) f_i + O(\varepsilon^3)$$

$$f_i = f_i^{eq} + \mathcal{E} f_i^{(1)} + O(\varepsilon^2)$$

$$g_i(\bar{x} + \bar{e}_i \delta_t, t + \delta_t) = g_i(\bar{x}, t) + \varepsilon (\partial_t + e_{i\alpha} \partial_\alpha) g_i + \frac{1}{2} \varepsilon^2 (\partial_t + e_{i\alpha} \partial_\alpha) (\partial_t + e_{i\beta} \partial_\beta) g_i + O(\varepsilon^3)$$

$$g_i = g_i^{eq} + \mathcal{E} g_i^{(1)} + O(\varepsilon^2)$$

$$\partial_t = \partial_{t_0} + \varepsilon \partial_{t_1} + O(\varepsilon^2)$$

with $\varepsilon = \delta_t$ being small compared to the macroscopic time scales.

The LBE for the distribution function f_i used for the hydrodynamics fields is studied first. After the expansion, the LHS of Eq. (2.99) becomes

$$\varepsilon (\partial_{t_0} + e_{i\alpha} \partial_\alpha) f_i^{eq} + \varepsilon^2 \left[\partial_{t_1} f_i^{eq} + (\partial_{t_0} + e_{i\alpha} \partial_\alpha) f_i^{(1)} + \frac{1}{2} (\partial_{t_0} + e_{i\alpha} \partial_\alpha) (\partial_{t_0} + e_{i\beta} \partial_\beta) f_i^{eq} \right] + O(\varepsilon^3),$$

and the RHS,

$$-\frac{1}{\tau_f}(\mathcal{E}f_i^{(1)} + \varepsilon^2 f_i^{(2)}) + O(\varepsilon^3) + \varepsilon \left(\frac{1}{c_s^2} \mu w_i e_{i\alpha} \partial_\alpha \phi \right).$$

By matching the terms at different orders of ε , one gets

$$(\partial_{t_0} + e_{i\alpha} \partial_\alpha) f_i^{eq} = -\frac{1}{\tau_f} f_i^{(1)} + \frac{1}{c_s^2} \mu w_i e_{i\alpha} \partial_\alpha \phi \quad \text{at } O(\varepsilon) \quad (\text{A1})$$

$$\partial_{t_1} f_i^{eq} + (\partial_{t_0} + e_{i\alpha} \partial_\alpha) f_i^{(1)} + \frac{1}{2} (\partial_{t_0} + e_{i\alpha} \partial_\alpha) (\partial_{t_0} + e_{i\beta} \partial_\beta) f_i^{eq} = -\frac{1}{\tau_f} f_i^{(2)} \quad \text{at } O(\varepsilon^2) \quad (\text{A2})$$

Substituting (A1) into (A2), one obtains

$$\partial_{t_1} f_i^{eq} + \frac{2\tau_f - 1}{2\tau_f} (\partial_{t_0} + e_{i\alpha} \partial_\alpha) f_i^{(1)} + \frac{1}{2} (\partial_{t_0} + e_{i\alpha} \partial_\alpha) \left(\frac{1}{c_s^2} \mu w_i e_{i\zeta} \partial_\zeta \phi \right) = -\frac{1}{\tau_f} f_i^{(2)} \quad (\text{A3})$$

Note that one can use the following solvability conditions for $f_i^{(k)}$ ($k = 1, 2, \dots$),

$$\sum_i f_i^{(k)} = 0 \quad (k = 1, 2, \dots) \quad (\text{A4})$$

$$\sum_i e_{i\alpha} f_i^{(k)} = 0 \quad (k = 1, 2, \dots) \quad (\text{A5})$$

and also the conditions for f_i and f_i^{eq} , as given by Eqs. (2.97 a, b, d) and (2.102),

$$\sum_i f_i^{eq} = \rho$$

$$\sum_i e_{i\alpha} f_i^{eq} = \rho u_\alpha$$

$$\sum_i e_{i\alpha} e_{i\beta} f_i^{eq} = \rho u_\alpha u_\beta + (\rho c_s^2 + \phi \mu) \delta_{\alpha\beta}$$

$$\sum_i e_{i\alpha} e_{i\beta} e_{i\gamma} f_i^{eq} = \rho c_s^2 (\delta_{\alpha\beta} u_\gamma + \delta_{\alpha\gamma} u_\beta + \delta_{\beta\gamma} u_\alpha)$$

with the equilibrium distribution function f_i^{eq} given by Eq. (2.100).

The zeroth and first order moments of (A1) lead to,

$$\partial_{t_0} \rho + \partial_\alpha (\rho u_\alpha) = 0 \quad (\text{A6})$$

$$\partial_{t_0}(\rho u_\alpha) + \partial_\beta \left\{ \rho u_\alpha u_\beta + (\rho c_s^2 + \phi \mu) \delta_{\alpha\beta} \right\} = \mu \partial_\alpha \phi \quad (\text{A7})$$

It is straightforward to prove that Eq. (A7) is equivalent to

$$\partial_{t_0}(\rho u_\alpha) + \partial_\beta \left\{ \rho u_\alpha u_\beta + \rho c_s^2 \delta_{\alpha\beta} \right\} = -\phi \partial_\alpha \mu \quad (\text{A8})$$

The moments of (A2) lead to,

$$\partial_{t_1} \rho + \frac{1}{2} \partial_\alpha (\mu \partial_\alpha \phi) = 0 \quad (\text{A9})$$

$$\partial_{t_1}(\rho u_\alpha) + \frac{2\tau_f - 1}{2\tau_f} \partial_\beta \Pi_{\beta\alpha}^{(1)} + \frac{1}{2} \partial_{t_0}(\mu \partial_\alpha \phi) = 0 \quad (\text{A10})$$

where the tensor $\Pi_{\beta\alpha}^{(1)}$ is defined as

$$\Pi_{\beta\alpha}^{(1)} = \sum_i e_{i\alpha} e_{i\beta} f_i^{(1)} \quad (\text{A11})$$

and can be calculated as

$$\begin{aligned} \Pi_{\beta\alpha}^{(1)} &= \sum_i e_{i\alpha} e_{i\beta} f_i^{(1)} = -\tau_f \sum_i e_{i\alpha} e_{i\beta} \left[(\partial_{t_0} + e_{i\gamma} \partial_\gamma) f_i^{eq} - \frac{1}{c_s^2} w_i e_{i\zeta} \mu \partial_\zeta \phi \right] \\ &= -\tau_f \left[\partial_{t_0} \sum_i (e_{i\alpha} e_{i\beta} f_i^{eq}) + \partial_\gamma \sum_i (e_{i\alpha} e_{i\beta} e_{i\gamma} f_i^{eq}) - \frac{1}{c_s^2} \mu \partial_\zeta \phi \left(\sum_i w_i e_{i\zeta} e_{i\alpha} e_{i\beta} \right) \right] \\ &= -\tau_f \left\{ \partial_{t_0} [\rho u_\alpha u_\beta + (\phi \mu + \rho c_s^2) \delta_{\alpha\beta}] + \partial_\gamma [\rho c_s^2 (\delta_{\alpha\beta} u_\gamma + \delta_{\alpha\gamma} u_\beta + \delta_{\beta\gamma} u_\alpha)] \right\} \\ &= -\tau_f \left\{ \partial_{t_0} (\rho u_\alpha u_\beta + \rho c_s^2 \delta_{\alpha\beta}) + \partial_\gamma [\rho c_s^2 (\delta_{\alpha\beta} u_\gamma + \delta_{\alpha\gamma} u_\beta + \delta_{\beta\gamma} u_\alpha)] \right\} - \tau_f \partial_{t_0} (\phi \mu \delta_{\alpha\beta}) \\ &= -\tau_f \rho c_s^2 (\partial_\alpha u_\beta + \partial_\beta u_\alpha) + \tau_f \phi (u_\alpha \partial_\beta \mu + u_\beta \partial_\alpha \mu) + \tau_f \partial_\gamma (\rho u_\alpha u_\beta u_\gamma) - \tau_f \partial_{t_0} (\phi \mu \delta_{\alpha\beta}) \end{aligned}$$

where the properties of the lattice tensors and Eqs. (A6) and (A7) have been used.

Then, Eq. (A10) becomes

$$\begin{aligned} \partial_{t_1}(\rho u_\alpha) - \partial_\beta \left\{ \rho c_s^2 \left(\tau_f - \frac{1}{2} \right) (\partial_\alpha u_\beta + \partial_\beta u_\alpha) \right\} + \partial_\beta \left\{ \left(\tau_f - \frac{1}{2} \right) \phi (u_\alpha \partial_\beta \mu + u_\beta \partial_\alpha \mu) \right\} \\ + \partial_\beta \left[\left(\tau_f - \frac{1}{2} \right) \partial_\gamma (\rho u_\alpha u_\beta u_\gamma) \right] - \partial_\beta \partial_{t_0} \left\{ \left(\tau_f - \frac{1}{2} \right) \phi \mu \delta_{\alpha\beta} \right\} + \frac{1}{2} \partial_{t_0} (\mu \partial_\alpha \phi) = 0 \quad (\text{A12}) \end{aligned}$$

To obtain the macroscopic equations, one simply sums the equations at different orders together. When Eq. (A9) is multiplied by $\delta_t = \varepsilon$ and added to Eq. (A6), one gets

$$\partial_t \rho + \partial_\alpha (\rho u_\alpha) + \frac{1}{2} \delta_t \partial_\alpha (\mu \partial_\alpha \phi) = 0 \quad (\text{A13})$$

And similarly, when Eq. (A12) is multiplied by δ_t and added to Eq. (A6), it is easy to find,

$$\begin{aligned} & \partial_t (\rho u_\alpha) + \partial_\beta (\rho u_\alpha u_\beta + \rho c_s^2 \delta_{\alpha\beta}) - \partial_\beta \left\{ \rho c_s^2 \delta_t \left(\tau_f - \frac{1}{2} \right) (\partial_\alpha u_\beta + \partial_\beta u_\alpha) \right\} \\ & + \delta_t \partial_\beta \left\{ \left(\tau_f - \frac{1}{2} \right) \phi (u_\alpha \partial_\beta \mu + u_\beta \partial_\alpha \mu) \right\} + \partial_\beta \left[\left(\tau_f - \frac{1}{2} \right) \delta_t \partial_\gamma (\rho u_\alpha u_\beta u_\gamma) \right] \\ & - \delta_t \partial_\alpha \partial_{t_0} \left\{ \left(\tau_f - \frac{1}{2} \right) \phi \mu \right\} + \frac{1}{2} \delta_t \partial_{t_0} (\mu \partial_\alpha \phi) = -\phi \partial_\alpha \mu \end{aligned} \quad (\text{A14})$$

The term $\partial_\alpha (\mu \partial_\alpha \phi)$ in Eq. (A13) is multiplied by δ_t , and the chemical potential μ is a small quantity. Therefore, it may be neglected and the equation is approximately

$$\partial_t \rho + \partial_\alpha (\rho u_\alpha) = 0 \quad (\text{A15})$$

which is exactly the continuity equation.

Similar arguments apply for the terms $\delta_t \partial_\alpha \partial_{t_0} \left\{ \left(\tau_f - \frac{1}{2} \right) \phi \mu \right\}$ and $\frac{1}{2} \delta_t \partial_{t_0} (\mu \partial_\alpha \phi)$ in Eq.

(A14). The term $\rho u_\alpha u_\beta u_\gamma$ in Eq. (A14) is of order $O(Ma^3)$. The term

$\delta_t \partial_\beta \left\{ \left(\tau_f - \frac{1}{2} \right) \phi (u_\alpha \partial_\beta \mu + u_\beta \partial_\alpha \mu) \right\}$ also includes δ_t , and besides $\phi (u_\alpha \partial_\beta \mu + u_\beta \partial_\alpha \mu)$ is

of order $O(Ma)$ as compared with $\phi \partial_\alpha \mu$ on the RHS. Hence, they may all be

neglected and Eq. (A14) approximately becomes

$$\partial_t(\rho u_\alpha) + \partial_\beta(\rho u_\alpha u_\beta + \rho c_s^2 \delta_{\alpha\beta}) - \partial_\beta \left\{ \rho c_s^2 \delta_t \left(\tau_f - \frac{1}{2} \right) (\partial_\alpha u_\beta + \partial_\beta u_\alpha) \right\} = -\phi \partial_\alpha \mu \quad (\text{A16})$$

If the dynamic viscosity is introduced as $\eta = \rho c_s^2 \delta_t \left(\tau_f - \frac{1}{2} \right)$, Eq. (A16) becomes,

$$\partial_t(\rho u_\alpha) + \partial_\beta(\rho u_\alpha u_\beta + \rho c_s^2 \delta_{\alpha\beta}) - \partial_\beta \left\{ \eta (\partial_\alpha u_\beta + \partial_\beta u_\alpha) \right\} = -\phi \partial_\alpha \mu \quad (\text{A17})$$

This is just the momentum equation.

Next, the LBE for the distribution function g_i used for the indicator function is studied. After the expansion of Eq. (2.89) and the match of terms at different orders, one obtains,

$$(\partial_{t_0} + e_{i\alpha} \partial_\alpha) g_i^{eq} = -\frac{1}{\tau_g} g_i^{(1)} \quad \text{at } O(\varepsilon) \quad (\text{A18})$$

$$\partial_{t_1} g_i^{eq} - \left(\tau_2 - \frac{1}{2} \right) (\partial_{t_0} + e_{i\alpha} \partial_\alpha) (\partial_{t_0} + e_{i\beta} \partial_\beta) g_i^{eq} = -\frac{1}{\tau_g} g_i^{(2)} \quad \text{at } O(\varepsilon^2) \quad (\text{A19})$$

The zeroth moments of Eqs. (A18) and (A19) are

$$\partial_{t_0} \phi + \partial_\alpha (\phi u_\alpha) = 0 \quad (\text{A20})$$

$$\begin{aligned} & \partial_{t_1} \phi - \left(\tau_g - \frac{1}{2} \right) [\partial_{t_0} \partial_{t_0} \phi + \partial_\alpha \partial_{t_0} (\phi u_\alpha)] \\ & - \left(\tau_g - \frac{1}{2} \right) [\partial_\beta \partial_{t_0} (\phi u_\beta) + \partial_\alpha \partial_\beta (\tilde{M} \mu \delta_{\alpha\beta} + \phi u_\alpha u_\beta)] = 0 \end{aligned} \quad (\text{A21})$$

where the following solvability conditions for $g_i^{(k)}$ ($k = 1, 2, \dots$),

$$\sum_i g_i^{(k)} = 0 \quad (k = 1, 2, \dots) \quad (\text{A22})$$

$$\sum_i e_{i\alpha} g_i^{(k)} = 0 \quad (k = 1, 2, \dots) \quad (\text{A23})$$

and the conditions for g_i^{eq} , as given by Eq. (2.98),

$$\begin{aligned}\sum_i g_i^{eq} &= \phi \\ \sum_i e_{i\alpha} g_i^{eq} &= \phi u_\alpha \\ \sum_i e_{i\alpha} e_{i\beta} g_i^{eq} &= \tilde{M} \mu \delta_{\alpha\beta} + \phi u_\alpha u_\beta\end{aligned}$$

have been used. From Eq. (A20), one gets

$$\partial_{t_0} \partial_{t_0} \phi + \partial_\alpha \partial_{t_0} (\phi u_\alpha) = \partial_{t_0} (\partial_{t_0} \phi + \partial_\alpha (\phi u_\alpha)) = 0 \quad (\text{A24})$$

Then, Eq. (A21) is simplified as

$$\partial_{t_1} \phi = \left(\tau_g - \frac{1}{2} \right) \tilde{M} \partial_{\alpha\alpha} \mu + \left(\tau_g - \frac{1}{2} \right) \partial_\beta \left[\partial_{t_0} (\phi u_\beta) + \partial_\alpha (\phi u_\alpha u_\beta) \right] \quad (\text{A25})$$

By using Eqs. (A6), (A8) and (A20), one can find that

$$\partial_{t_0} (\phi u_\beta) + \partial_\alpha (\phi u_\alpha u_\beta) = \frac{\phi}{\rho} \left[-\partial_\alpha (\rho c_s^2) - \phi \partial_\alpha \mu \right] \quad (\text{A26})$$

In Eq. (A25), the two terms are after the differential operator ∂_β . Assuming that these high order derivatives can be omitted, one simplifies Eq. (25) as

$$\partial_{t_1} \phi = \left(\tau_g - \frac{1}{2} \right) \tilde{M} \partial_{\alpha\alpha} \mu \quad (\text{A27})$$

When Eq. (A27) is multiplied by δ_t and added to Eq. (A20), one gets,

$$\partial_t \phi + \partial_\alpha (\phi u_\alpha) = \left(\tau_g - \frac{1}{2} \right) \tilde{M} \delta_t \partial_{\alpha\alpha} \mu \quad (\text{A28})$$

If the mobility is introduced as $M = \left(\tau_g - \frac{1}{2} \right) \tilde{M} \delta_t$, Eq. (A16) becomes,

$$\partial_t \phi + \partial_\alpha (\phi u_\alpha) = M \partial_{\alpha\alpha} \mu \quad (\text{A28})$$

This is the approximate Cahn-Hilliard equation.

To summarize, the continuity equation, the momentum equation and the Cahn-Hilliard equation have been obtained as Eqs. (A15), (A17) and (A28) respectively.

Vita

NAME: HUANG, JUNJIE

DATE OF BIRTH: 3 SEP 1980

PLACE OF BIRTH: JIANGSU, CHINA

I was born in Jiangsu province of China in 1980. I obtained my *B. Eng.* degree in 2002 from Tsinghua University in Beijing. From 2003 to 2007 I studied as a *Ph.D.* student in the Department of Mechanical Engineering at the National University of Singapore. The following are the publications related to my *Ph.D.* work:

1. Y. T. Chew, **J. J. Huang**, C. Shu and H. W. Zheng. Investigation of multiphase flows near walls with textures by the lattice Boltzmann method. *Proceedings of "Enhancement and Promotion of Computational Methods in Engineering and Science X"*, Aug. 21-23, 2006, Sanya, China (Springer Berlin Heidelberg)
2. **J. J. Huang**, C. Shu, Y. T. Chew and H. W. Zheng. Numerical study of 2D multiphase flows over grooved surface by lattice Boltzmann method. *International Journal of Modern Physics C*, 18 (4), pp. 492-500 (2007).
3. **J. J. Huang**, C. Shu and Y. T. Chew. Numerical investigation of transporting droplets by spatiotemporally controlling substrate wettability. *Journal of Colloid and Interface Science*, 328, pp. 124-133 (2008).
4. **J. J. Huang**, C. Shu and Y. T. Chew. Lattice Boltzmann study of droplet motion

inside a grooved channel. *Physics of Fluids* 21, pp. 022103 (2009).

5. **J. J. Huang**, C. Shu and Y. T. Chew. Mobility-dependent bifurcations in capillarity-driven two-phase fluid systems by using a lattice Boltzmann phase-field model. *International Journal for Numerical Methods in Fluids*, 60, pp. 203-225 (2009).
6. **J. J. Huang**, C. Shu and Y. T. Chew. Lattice Boltzmann study of bubble entrapment during droplet impact. (*International Journal for Numerical Methods in Fluids*, in press)